A Ph.D. Dissertation on

MULTI-BODY DYNAMIC ANALYSIS AND VIBRATION CONTROL OF HORIZONTAL AXIS WIND TURBINE

submitted by

Arka Mitra

(176104102)

under the supervision of

Dr. Arunasis Chakraborty

DEPARTMENT OF CIVIL ENGINEERING

INDIAN INSTITUTE OF TECHNOLOGY GUWAHATI

December, 2024

Certificate

It is certified that the work contained in the dissertation entitled **"Multi Body Dynamic Analysis and Vibration Control of Horizontal Axis Wind Turbine"**, by **Arka Mitra (176104102)** for the partial fulfillment of the requirements for the award of the *Doctor of Philosophy* (*Ph.D.*) in *Civil Engineering* with the specialization in *Structural Engineering* at the *Indian Institute of Technology Guwahati, India* is an authentic work. This dissertation has been performed under my sole supervision and not submitted elsewhere to award a degree.

Date: 03/12/2024.

Dr. Arunasis Chakraborty
Professor
Department of Civil Engineering
Indian Institute of Technology Guwahati
Guwahati - 781039, India

Acknowledgements

I extend my heartfelt gratitude to my research supervisor and mentor, *Dr. Arunasis Chakraborty*, for welcoming me as his student. Throughout my Ph.D. journey, his encouragement, support, and motivation have propelled me to surpass my expectations. Dr. Chakraborty's profound knowledge and expertise have been a constant source of inspiration in my research endeavors and personal growth. Working under his guidance has been an immense honor and privilege. His constructive feedback on my presentations and writings has significantly honed my skills over time. I am deeply appreciative of his patience, empathy, and friendship, which provided the ideal environment for me to work.

My sincere thanks go to the members of the Doctoral Committee, *Prof. Anjan Dutta*, *Prof. Sajal K. Deb*, *Dr. Atanu Banerjee*, and my supervisor for their invaluable critiques, suggestions, and encouragement that steered my progress. Special thanks to the faculty of Civil Engineering and the staff for making my time at this institution memorable. The financial support from the Department of Civil Engineering, Indian Institute of Technology Guwahati, India, has been crucial for my research, and I am very grateful for it.

I am thankful to my seniors, *Dr. Amit Kumar Rathi*, *Dr. Swaroop Mahato*, and *Dr. Pranjan Tamuly*, for their motivation, insightful discussions, and support. My gratitude also extends to my colleagues, especially *Dr. M. M. Sajeer*, *Dr. Sourav Das*, *Ms. Yamini Giridharan*, *Dr. Saptarshi Sarkar*, and *Mr. Debasis Panda*, for their technical assistance and companionship that made my journey enjoyable. I look forward to seeing all my friends and colleagues achieve great success.

A special acknowledgment to my family, whose unwavering support and motivation were crucial in completing my thesis. My parents deserve special mention for their lifelong encouragement of my education. My elder sister's motivation, guidance, and financial support have been invaluable throughout my career. Lastly, immense gratitude for my wife, my steadfast pillar of support, whose understanding and encouragement have been my constant source of strength.

Arka Mitra

Date: 2^{nd} December, 2024

Arka Mitra
(176104102)
Department of Civil Engineering
Indian Institute of Technology Guwahati
Guwahati - 781039, India

To those whose unwavering support and

endless encouragement made this journey possible

Abstract

Horizontal axis wind turbines have gained prominence in the recent past as an efficient power-generating device, particularly in areas with abundant wind resources. Varying forces on turbines influence wind farm power production and efficiency in different geographical regions. These wind turbines are categorized as onshore and offshore based on their locations, with onshore being more accessible and easily connected to local power grids. However, onshore wind speeds fluctuate due to geographical features, requiring detailed analysis to ensure consistent wind availability and minimal impact on settlements and the environment. In contrast, offshore turbines are more profitable in the long run due to factors like steady wind flow, ample space for large wind farms, and less noise pollution. Yet, offshore construction, installation, and grid connection costs depend on water depth and distance from the shore. Despite offering more power than onshore turbines of similar size, offshore turbines face a harsher environment, demanding rigorous design for safe and sustained operation. Structural vibrations are significant in the marine environment due to combined wind and wave effects.

Today's multi-mega Watt wind turbines have long, slender, and flexible blades and towers, which experience significant vibration due to aerodynamic, hydrodynamic, and seismic loads. The blades are generally made of composite layups with cambered airfoil sections, which induce elastic and dynamic coupling between bending and torsional modes. In addition to these phenomena, the aerodynamic pitching moment also arises due to the offset of the blade pitch axis from the aerodynamic centre. With this in mind, a complete multi-body dynamic aero-servo-elastic model of a horizontal axis wind turbine, including bending-torsion coupling in blades, is developed in Kane's framework using MATLAB®.

The TurbSim package from the National Renewable Energy Laboratory (NREL) is used to simulate the three-dimensional wind field passing through the rotor plane, and the aerodynamic loads are calculated using a modified Blade Element Momentum Theory (BEMT). In offshore environments, wind turbines are exposed to wave currents in addition to aerodynamic loads. These wave loads are simulated using Morison's equation, with wave time histories generated from the Pearson-Moskowitz spectrum for two-dimensional wave propagation. The response of a benchmark wind turbine is validated with FAST and HAWC2. The model is then utilized to develop efficient control strategies designed for various turbine components depending on their location (i.e., onshore and offshore).

The effect of elastodynamic bending-torsion coupling in blades mentioned earlier is investigated thoroughly in this study. The dynamic coupling is found to be particularly detrimental at higher wind speeds than the rated value. On the other hand, elastic bending torsion coupling can have both beneficial and adverse effects on the dynamic response of the turbine depending on its direction (i.e., twist-to-feather and twist-to-stall). Hence, proper design and implementation of structural layup can enhance the aerodynamic performance of the blade. The optimal design of the composite fibre orientation of a benchmark turbine blade is presented to show its beneficial effects in load/response mitigation.

Monopile-supported offshore wind turbines are common in shallow waters, which require intricate design models to accommodate their size, power, and environmental conditions. This involves developing a detailed multi-body dynamic model by incorporating Soil-Structure Interaction (SSI) as it is crucial for accurate dynamic analysis. A benchmark turbine at the North Sea is modeled using Kane's method, analyzing each soil layer and the system's dynamic response through coupled analysis. Fatigue life is assessed according to International Electrotechnical Commission (IEC) 61400-3 standards using a rainflow algorithm, which accounts for both short-term stress and long-term serviceability. The study also develops the design curves for specific power ratings, ensuring structural integrity over the turbine's lifespan.

Besides monopiles, small vibrations in the tower can cause a detrimental effect on the drive-train assembly located at the nacelle. Hence, the study continued to investigate efficient control strategies for the vibration control of wind turbine towers. A wavelet-based strategy for fore-aft vibration control of onshore horizontal axis wind turbine towers is presented in this study. For this purpose, an active tuned mass damper is combined with an aero-servo-elastic turbine model in the multi-body framework. The combined system is exposed to turbulent wind and seismic ground motion to investigate the controller performance in extreme operating conditions. The optimal tuning is achieved by frequency-dependent gain scheduling via wavelet transform. Numerical studies demonstrate the advantage of the proposed gain scheduling over classical Linear Quadratic Regulator (LQR). The efficiency of the proposed algorithm is verified using different flow conditions and seismic input, where the performance is compared with benchmark results.

On the contrary, spar-type floating wind turbines exposed to marine environments experience significant vibration due to hydrodynamic loads, which is more prominent under wind-wave misalignment. This unavoidable vibration can induce significant damage to sensitive electro-mechanical components, leading to downtime for maintenance. With this in view, the present study proposes a modified spar-torus combination by introducing a spring and dashpot in between to work as an isolator. First, a comprehensive mathematical model for this offshore multi-body system is developed using Kane's approach with proper aero-elastic and hydrodynamic simulation. The response of the modified spar-torus combination is demonstrated, highlighting the efficiency and advantage of the proposed vibration isolation. Different sea states and wind conditions are simulated to investigate the performance envelope of the proposed controller for spar-type floating wind turbines.

This study also investigates the use of a double-pitched rotor with two different pitch angles to address power fluctuation and rotor vibration in modern horizontal-axis wind turbines. The model of a double-pitched turbine operating in both onshore and offshore environments is developed in the multi-body dynamic framework. Three control algorithms are developed: an optimal Proportional Integral Derivative (PID), a weight-optimized LQR, and a wavelet-based LQR. Gain scheduling in these algorithms is optimized through multi-objective optimization based on rotor speed error and structural vibration. The algorithms outperform a generalized full-blade single-pitch baseline control, as demonstrated using benchmark data from a 5MW turbine. The performance of these algorithms is evaluated under various flow conditions and wind-wave misalignments, with benchmark results serving as a basis for comparison.

List of Publications

Journal Articles:

1. Mitra, A., Sarkar, S., Chakraborty, A. and Das, S., 2021. Sway vibration control of floating horizontal axis wind turbine by modified spar-torus combination, *Ocean Engineering*, 219, p.108232.
2. Sajeer, M., Mitra, A. and Chakraborty, A., 2021. Multi-body dynamic analysis of offshore wind turbine considering soil-structure interaction for fatigue design of monopile, *Soil Dynamics and Earthquake Engineering*, 144, p.106674.
3. Mitra, A. and Chakraborty, A., 2022, Multi-Objective Optimization of Composite Airfoil Fiber Orientation Under Bending-Torsion Coupling for Improved Aerodynamic Efficiency of Horizontal Axis Wind Turbine Blade, *Journal of Wind Engineering and Industrial Aerodynamics*, 221, p.104881.
4. Mitra, A., Yamini G. and Chakraborty A., 2022, Wavelet linear quadratic regulator based gain scheduling for optimal fore-aft vibration control of horizontal axis wind turbine tower using active tuned mass damper, *Structural Control and Health Monitoring*, 29(11), p.e3055.
5. Mitra, A. and Chakraborty, A. 2023, Wavelet LQR Based Gain Scheduling for Power Regulation and Vibration Control of Floating Horizontal Axis Wind Turbine with Double-Pitched Rotor, *Wind Energy and Engineering Research*, 1, p.100001.
6. Mitra, A. and Chakraborty, A. 2024, Aerodynamic Load Control of Large Scale Horizontal Axis Wind Turbines with Double Pitched Rotor under Extreme Wind Conditions. (Under review).
7. Mitra, A. and Chakraborty, A. 2024, Multi-Objective Optimal PID Controlled Double Pitch Rotor for Power Regulation and Vibration Control of Horizontal Axis Wind Turbine. (Manuscript under-preparation).
8. Mitra, A. and Chakraborty, A. 2024, A Comprehensive Review on Active Vibration Control of Wind Turbine Towers Using Tuned Mass Damper. (Manuscript Under-preparation).

Book Chapter:

1. Mitra, A., Sarkar S., and Chakraborty, A. 2023, Multi-Body Dynamic Analysis of Onshore Horizontal Axis Wind Turbine. *Non-Destructive Testing and Condition Monitoring Techniques in Wind Energy, Wind Energy Engineering, p51–397. Academic Press.*

Related Publications:

1. Sajeer, M., Mitra, A. and Chakraborty, A., 2020. Spinning finite element analysis of longitudinally stiffened horizontal axis wind turbine blade for fatigue life enhancement. *Mechanical Systems and Signal Processing*, 145, 106924.

Contents

List of Figures

List of Tables

List of Abbreviations

ANN	Artificial Neural Networks
API	American Petrolium Institute
ARE	Algebric Riccati Equation
ATMD	Active Tuned Mass Damper
BEM	Blade Element Momentum
BEMT	Blade Element Momentum Theory
BVA	Ball Vibration Absorber
CFD	Computational Fluid Dynamics
DBD	Dielectric Barrier Discharge
DEL	Damage-equivalent Load
DES	Damage-equivalent Stress
DNV	Det Norske Veritas
DOFs	Degrees of Freedom
DRE	Differential Riccati Equation
FEA	Finite Element Analysis
FEM	Finite Element Method
FLAP	Force and Load Analysis Program
FSI	Fluid-Structure Interaction
FWT	Floating Wind Turbine
GA	Genetic Algorithm
HAWT	Horizontal Axis Wind Turbine
IEC	International Electrotechnical Commission
IPCC	Intergovernmental Panel on Climate Change
JONSWAP	Joint North Sea Wave Project
LQG	Linear Quadratic Gaussian
LQR	Linear Quadratic Regulator
ML	Machine Learning
MIMO	Multiple-Input Multiple-Output
MSTC	Modified Spar-Torus Combination

NQR	Nonlinear Quadratic Regulator
NREL	National Renewable Energy Laboratory
PI	Proportional Integral
PID	Proportional Integral Derivative
PM	Pearson-Moskowitch
PCE	Polynomial Chaos Expansion
RMS	Root Mean Square
RSS	Rotationally Sampled Spectrum
SISO	Single-Input Single-Output
SLS	Serviceability Limit State
SMA	Shape Memory Alloy
SNL	Sandia National Laboratory
SSI	Soil-Structure Interaction
STC	Spar-Torus Combination
TLCD	Tuned Liquid Column Damper
TLD	Tuned Liquid Damper
TMD	Tuned Mass Damper
TVA	Tuned Vibration Absorber
UD	Uni Directional
VAWT	Vertical Axis Wind Turbine
VD	Viscous Damper
WEC	Wave Energy Converter

List of Symbols

P	Power
ρ_a	Density of air
A_r	Rotor area
C_p	Power coefficient
V_w	Wind velocity
P_e	Ultimate power output
η_e	Electrical Inefficiency
η_m	Mechanical Inefficiency
$\mathbf{u}$	Degrees of freedom vector
u_i	i^{th} degree of freedom
$\hat{x}_i$	i^{th} component of global inertial coordinate system
$\hat{a}_i$	i^{th} component of tower global coordinate system
$\hat{b}_i$	i^{th} component of tower top coordinate system
$\bar{b}_i$	i^{th} component of tower elementwise fixed coordinate system
$\hat{c}_i$	i^{th} component of yaw/nacelle coordinate system
$\hat{d}_i$	i^{th} component of low-speed shaft tilt and skew coordinate system
$\hat{e}_i$	i^{th} component of low-speed shaft azimuthal coordinate system
$\hat{f}_{k,i}$	i^{th} component of k^{th} blade's global coordinate system
$\hat{g}_{k,i}$	i^{th} component of k^{th} blade's coned coordinate system
$\hat{h}_{k,i}$	i^{th} component of k^{th} blade's pitched coordinate system
$\hat{i}_{k,i}$	i^{th} component of k^{th} blade's nodal twist coordinate system
$\tilde{b}_{k,i}$	i^{th} component of k^{th} blade's elementwise fixed coordinate system
$\tilde{a}_{ek,i}$	i^{th} component of k^{th} blade's nodal aerodynamic coordinate system
c_k	Location of centre of mass of k^{th} body
x_k	Coordinate system attached to the centre of mass of k^{th} body
$\mathbf{F_i}$	Generalized active force vector for i^{th} DOF
$\mathbf{F_i^*}$	Generalized inertia force vector for i^{th} DOF
$\mathbf{r_{c_k}}$	Position vector of centre of mass of k^{th} body
$\mathbf{v_{c_k}}$	Linear velocity of centre of mass of k^{th} body
$\omega_{\mathbf{x_k}}$	Angular velocity of centre of mass of k^{th} body

$\mathbf{a_{c_k}}$	Linear acceleration of centre of mass of k^{th} body
$\alpha_{\mathbf{x_k}}$	Angular acceleration of centre of mass of k^{th} body
$\mathbf{v_{i,c_k}}$	Partial linear velocity of centre of mass of k^{th} body
$\omega_{\mathbf{i,x_k}}$	Partial angular velocity of centre of mass of k^{th} body
$\mathbf{F_{c_k}}$	External active force at the centre of mass of k^{th} body
$\mathbf{M_{x_k}}$	External active moment at the centre of mass of k^{th} body
m_k	Mass of k^{th} body
$\mathbf{\bar{I}_k}$	Inertia dyadic of k^{th} body
q_i	Generalized speed corresponding to i^{th} DOF
$\mathbf{F^*_{i,tw}}$	Generalized inertia force vector for tower DOFs
$\mathbf{F^*_{i,na}}$	Generalized inertia force vector for nacelle DOFs
$\mathbf{F^*_{i,hu}}$	Generalized inertia force vector for hub DOFs
$\mathbf{F^*_{i,gn}}$	Generalized inertia force vector for generator DOFs
$\mathbf{F^*_{i,ls}}$	Generalized inertia force vector for low-speed shaft DOFs
$\mathbf{F^*_{i,yb}}$	Generalized inertia force vector for yaw bearing DOFs
$\mathbf{F^*_{i,b_k}}$	Generalized inertia force vector for k^{th} blade DOFs
$\mathbf{F_{i,tw,el}}$	Elastic force vector for tower DOFs
$\mathbf{F_{i,b_k,el}}$	Elastic force vector for k^{th} blade DOFs
$\mathbf{F_{i,ls,el}}$	Elastic force vector for low-speed shaft DOFs
$\mathbf{F_{i,yb,el}}$	Elastic force vector for yaw bearing DOFs
$\mathbf{F_{i,tw,d}}$	Damping force vector for tower DOFs
$\mathbf{F_{i,b_k,d}}$	Damping force vector for k^{th} blade DOFs
$\mathbf{F_{i,ls,d}}$	Damping force vector for low-speed shaft DOFs
$\mathbf{F_{i,yb,d}}$	Damping force vector for yaw bearing DOFs
$\mathbf{F_{i,tw,ae}}$	Aerodynamic force vector for tower DOFs
$\mathbf{F_{i,b_k,ae}}$	Aerodynamic force vector for k^{th} blade DOFs
$\mathbf{F_{i,tw,gv}}$	Gravity force vector for tower
$\mathbf{F_{i,b_k,gv}}$	Gravity force vector for k^{th} blade
$\mathbf{F_{i,na,gv}}$	Gravity force vector for nacelle
$\mathbf{F_{i,hu,gv}}$	Gravity force vector for hub
$\mathbf{F_{i,gn}}$	Active force vector due to generator torque
$\mathbf{F_{i,br}}$	Active force vector due to shaft brake
$\mathbf{F_{i,eq}}$	Seismic forces acting at the tower base DOFs
$[\mathbf{M(u,t)}]$	Mass matrix of the multi-body system
$\{\mathbf{\bar{F}(\dot{u},u,t)}\}$	Generalized force vector of the multi-body system
g	Acceleration due to gravity
$\phi^{FA}_{i,tw}$	i^{th} mode shape of the tower in the fore-aft direction
$\phi^{SS}_{i,tw}$	i^{th} mode shape of the tower in the side-to-side direction
$S^{FA}_{i,j;tw}$	Quadratic axial shortening effect due to i^{th} and j^{th} mode shape of the tower in the fore-aft direction

$S^{SS}_{i,j;tw}$	Quadratic axial shortening effect due to i^{th} and j^{th} mode shape of the tower in the side-to-side direction
H_{tw}	Height of the tower from its base
μ_{tw}	Distributed mass per unit length of the tower
$k^{FA}_{i,j;tw}$	Generalized stiffness of the tower in the fore-aft direction obtained from i^{th} and j^{th} mode shape
$k^{SS}_{i,j;tw}$	Generalized stiffness of the tower in the side-to-side direction obtained from i^{th} and j^{th} mode shape
$f^{FA}_{i,tw}$	i^{th} modal frequency of the tower in the fore-aft direction
$f^{SS}_{i,tw}$	i^{th} modal frequency of the tower in the side-to-side direction
$\xi^{FA}_{i,tw}$	i^{th} modal damping ratio of the tower in the fore-aft direction
$\xi^{SS}_{i,tw}$	i^{th} modal damping ratio of the tower in the side-to-side direction
G_{br}	Gearbox ratio
G_{dir}	Generator direction
ϕ_{i,b_k}	i^{th} twisted shape function of the k^{th} blade in the out-of-plane direction
φ_{i,b_k}	i^{th} twisted shape function of the k^{th} blade in the in-plane direction
γ^{F}_{i,b_k}	i^{th} node shape of the k^{th} blade in the flapwise direction
γ^{E}_{i,b_k}	i^{th} node shape of the k^{th} blade in the edgewise direction
γ^{T}_{i,b_k}	i^{th} node shape of the k^{th} blade in the torsional direction
$S_{i,j;b_k}$	Quadratic axial shortening effect due to i^{th} and j^{th} mode shape of the k^{th} blade
θ_s	Local structural twist angle of the blade nodes
X_{b_k}	Nodal position vector of the k^{th} blade along $\hat{h}_k, 1$ axis
Y_{b_k}	Nodal position vector of the k^{th} blade along $\hat{h}_k, 2$ axis
θ_{t,b_k}	Nodal torsional twist vector of the k^{th} blade with respect to $\hat{h}_k, 3$ axis
X'_{b_k}	Nodal slope vector of the k^{th} blade with respect to $\hat{h}_k, 2$ axis
Y'_{b_k}	Nodal slope vector of the k^{th} blade with respect to $\hat{h}_k, 1$ axis
R_{b_k}	Length of the k^{th} blade
μ_{b_k}	Distributed mass per unit length of the k^{th} blade
$k^{F}_{i,j;b_k}$	Generalized stiffness of the k^{th} blade in the flapwise direction obtained from i^{th} and j^{th} mode shape
$k^{E}_{i,j;b_k}$	Generalized stiffness of the k^{th} blade in the edgewise direction obtained from i^{th} and j^{th} mode shape
$k^{T}_{i;b_k}$	Generalized stiffness of the k^{th} blade in the torsional direction obtained from i^{th} mode shape
$k^{FE}_{i,j;b_k}$	Coupled bending stiffness between i^{th} flapwise and j^{th} edgewise mode
$k^{FT}_{i,j;b_k}$	Generalized coupled stiffness between i^{th} flapwise and j^{th} torsional mode
$k^{ET}_{i,j;b_k}$	Generalized coupled stiffness between i^{th} edgewise and j^{th} torsional mode
$\lambda^{FT}_{b_k}$	Flap-twist coupling coefficient
$\lambda^{ET}_{b_k}$	Edge-twist coupling coefficient
$g^{FT}_{b_k}$	Coupled flap-torsional stiffness
$g^{ET}_{b_k}$	Coupled edge-torsional stiffness
f^{F}_{i,b_k}	i^{th} modal frequency in the flapwise direction
f^{E}_{i,b_k}	i^{th} modal frequency in the edgewise direction
f^{E}_{i,b_k}	i^{th} modal frequency in the torsional direction
ξ^{F}_{i,b_k}	i^{th} modal damping ratio in the flapwise direction

ξ^{E}_{i,b_k}	i^{th} modal damping ratio in the edgewise direction
ξ^{T}_{i,b_k}	i^{th} modal damping ratio in the torsional direction
S_u	Single-sided power spectrum of the wind speed fluctuations
κ_u	Autocorrelation function of the wind speed fluctuations
L	The integral length scale of turbulence
$\bar{v}$	Mean wind speed
σ_v	Standard deviation of the wind speed
Φ_{opt}	Optimal inflow angle
θ_p	Blade pitch angle
c	Chord length of the airfoil section
Ω	Rotational speed of the rotor
α	Angle of attack
V_x	Wind velocity component in normal direction
V_y	Wind velocity component in tangential direction
v_{rel}	Relative flow velocity
a'	Axial induction factor
a''	Tangential induction factor
F_L	Lift force
F_D	Drag force
M_p	Pitching moment
F_N	Normal force
F_T	Tangential force
C_L	Lift force coefficient
C_D	Drag force coefficient
C_M	Pitching moment coefficient
N_b	Number of blades
$f^{\text{hub}}_{\text{loss}}$	Hub loss coefficient
$f^{\text{tip}}_{\text{loss}}$	Tip loss coefficient
σ_p	Local solidity
a_c	Flow induction factor
V_{ci}	Cut-in wind speed
V_r	Rated wind speed
V_{co}	Cut-out wind speed
Ω_{ci}	Cut-in rotor speed
Ω_r	Rated rotor speed
u_R	Tower base relative displacement with respect to ground
K_p	Stiffness of ground oscillator
C_{d_p}	Damping coefficient of ground oscillator
T_{gn}	Generator torque

T_{aero}	Aerodyanmic torque
P_0	Rated power of the turbine
Ω_0	Rated generator speed of the turbine
K_P	Proportional Gain
K_I	Integral gain
K_D	Derivative gain
G_K	Gain correction factor
θ_K	Blade pitch angle at which pitch sensitivity is doubled from its value at the rated condition
U_{B1_OOP}	Blade 1 tip out-of-plane displacement
U_{B1_IP}	Blade 1 tip in-plane displacement
U_{B1_T}	Blade 1 tip torsional rotation
U_{TFA}	Tower top fore-aft displacement
U_{TSS}	Tower top side-to-side displacement
θ_{1,b_k}	Fibre angle at the top composite layer of the blade skin
θ_{2,b_k}	Fibre angle at the bottom composite layer of the blade skin
$\mathbf{F_{i,tw,hy}}$	Hydrodynamic force vector for monopile-tower DOFs
$K^e_{n_e}$	Soil-monopile element stiffness matrix
n_e	Element number
E_p	Young's modulus and
E_s	Soil modulus based on the p-y curve
I_p	Second moment of area of the monopile element
l_e	Element length
A_L	Factor for accounting different loading cases
k_{in}	Initial modulus of the subgrade reaction
p_u	Ultimate bearing capacity of soil at a depth H_{so}
H_{so}	Height of the soil strata
D_p	Diameter of the monopile
γ_s	Effective soil weight
C_a	Coefficient of active earth pressure
ϕ	Angle of internal friction of soil
K_{ps}	Rankine's passive earth pressure coefficient
$S(f_i, \theta_j)$	Directional JONSWAP spectrum
θ_j	The direction of wave propagation
H_w	Wave amplitude
$\epsilon_{j,k}$	Uniformly distributed phase angle between 0 to 2π
k_j	Wave number corresponding to the frequency f_j
σ_{L}	Total normal stress at any point on the monopile cross-section
V_{fx}	Shear force along the $\hat{x}_3$ axis
V_{fy}	Shear force along the $\hat{x}_1$ axis

V_{fz}	Axial force along the $\hat{x}_2$ axis
A_{cr}	Cross-sectional area of the pile
M_x	Bending moment in the $\hat{x}_3$ axis
M_y	Bending moment in the $\hat{x}_1$ axis
M_z	Torsional moment
x_c	Position of monopile outer surface in the $\hat{x}_3$ axis
y_c	Position of monopile outer surface in the $\hat{x}_1$ axis
I_x	Moment of inertia of the cross-section about $\hat{x}_3$ axis
I_y	Moment of inertia of the cross-section about $\hat{x}_1$ axis
J	Polar moment of inertia of the cross-section
τ	Total shear stress
β_τ	Angle between the point at which the internal stress is estimated and the total internal shear vector
m	Slope of the S-N curve
σ_{ji}^m	Mean stress of the i^{th} cycle in the j^{th} time-history
σ_{ji}^a	Alternating stress of the i^{th} cycle in the j^{th} time-history
σ_{ji}^{ae}	Equivalent alternating stress
σ^{mf}	Fixed mean stress
σ^u	Ultimate strength of the material
D_j^{ST}	Damage accumulated from the j^{th} stress time-history
n_{ji}	Rainflow cycle count
N_{ji}	Allowable number of load cycles corresponding to the i^{th} stress reversal
D^L	Damage accumulation during the lifetime
f_{av}	Availability factor of the wind turbine
f_j^L	Scaling factor for the j^{th} time series to account for the probability of occurrence.
$\sigma_{DE_j}^{ST}$	Short-term DES
f^{eq}	Frequency of DES
T_j	Total time duration of the jth time-history
σ_{DE}^L	Lifetime DES
y_N	Lateral deformation after the N cycle
y_1	Static displacement corresponding to the first cycle
ϵ_N^{PL}	Strain accumulation after N cycles
ϵ_1	Strain in the first cycle of loading.
ϵ_N^{LL}	Accumulated strain computed through logarithmic relation
F_d	Factor accounting for soil density
F_i	Factor accounting for monopile installation method
F_l	Factor accounting for cyclic load ratio
L_p	Length of the monopile
L_c	Characteristic length of the monopile
n_h	Coefficient of the subgrade reaction

ϵ_{PN}	Accumulated strain after the N cycles in stiffness degradation method
ϵ_{P1}	Accumulated strain after the 1^{st} cycle in stiffness degradation method
E_{SN}	Young modulus of soil at the N^{th} load cycle
E_{S1}	Young modulus of soil at the 1^{st} load cycle
X_c	Characteristic cyclic stress ratio
U_{NacYaw}	Nacelle rotation in yaw
U_{DrTr}	Drive-train (low-speed shaft) torsional deformation
$\dot{U}_{GeAz}$	Rotational speed of the low-speed shaft
u^m_{fa}	Monopile trajectory at mudline in fore-aft direction
u^m_{ss}	Monopile trajectory at mudline in side-to-side direction
u^p_{fa}	Platform motion in the fore-aft direction
u^p_{ss}	Platform motion in the side-to-side direction
θ^p_{fa}	Rotation of wind turbine at platform level in fore-aft direction
θ^p_{ss}	Rotation of wind turbine at platform level in side-to-side direction
θ_{ma}	Wind-wave misalignment angle
t_p	Thickness of the monopile surface
D_w	Depth of water level
$\mathbf{F^*_{i,s}}$	Generalized inertia force vector for spar DOFs
$\mathbf{F_{i,s,hy}}$	Hydrodynamic force vector for spar DOFs
$\mathbf{F_{i,s,mr}}$	Mooring force vector for spar DOFs
$\mathbf{F_{i,s,gv}}$	Gravity force vector for spar DOFs
S_{PM}	Pierson Moskowitch spectrum
H_s	Significant wave height
T_p	Peak wave period
f_p	Peak wave frequency
C_A	Added mass coefficient
C_{Mf}	Fluid inertia coefficient
C_{Dr}	Viscous drag coefficient
D_s	Diameter of the spar
v^f_i	Velocity of fluid along i^{th} spar DOF
a^f_i	Acceleration of fluid along i^{th} spar DOF
ρ	Density of water
N_c	Number of nodes in mooring cable
$U_{s\_Su})$	Spar translation in surge
U_{s_Sw}	Spar translation in sway
U_{s_R}	Spar rotation in roll
U_{s_P}	Spar rotation in pitch
$\mathbf{F_{i,tmd,gv}}$	Gravity force vector for the TMD
$\mathbf{F_{i,tmd,el}}$	Elastic force vector for the TMD

$\mathbf{F_{i,tmd,d}}$	Damping force vector for the TMD
$\mathbf{F_{i,tmd,act}}$	Generalized active force on the TMD exerted by the actuator
K_{tmd}	Generalized stiffness of the TMD
ξ_{tmd}	Critical damping ratio of the TMD
f_{tmd}	Natural frequency of the TMD
$f_{act,FA}$	Actuation force in the fore-aft direction
$U(t)$	State vector
$F_c(t)$	Control input
$F(t)$	External disturbance
$A_s(t)$	System matrix
$B_c(t)$	Control force correlation matrix
$B_F(t)$	External disturbance correlation matrix
$Y(t)$	Measurement vector
Q	LQR weight matrix on the states
R	LQR weight matrix on the control force
S^f	Terminal weight matrix
λ	Co-state vector
G_{LQR}	LQR feedback gain matrix
W_ψ	Continous wavelet transform
$\psi(t)$	Wavelet basis function
a	Scale or dilation parameter in wavelet transform
b	Translational or position parameter in wavelet transform
$\tilde{\psi}(t)$	Wavelet dual of the basis function
$\mathrm{H}(\omega)$	Heaviside step function
β	Compactness parameter of Morse wavelet
ν	Symmetry parameter of Morse wavelet
$\mathbf{F_{i,tr,gv}}$	Gravity force vector for the torus
$\mathbf{F_{i,tr,el}}$	Elastic force vector for the torus
$\mathbf{F_{i,tr,d}}$	Damping force vector for the torus
$\mathbf{F_{i,tr,hy}}$	Generalized hydrodynamic force on the torus
K_{tr}	Generalized stiffness of the torus
ξ_{tr}	Critical damping ratio of the torus
f_{tr}	Natural frequency of the torus
$\theta_{p,1}$	Blade pitch angle at the root
$\theta_{p,2}$	Blade pitch angle at the tip
$K_{P,i}$	Proportional gain for the i^{th} pitch actuator
$K_{I,i}$	Integral gain for the i^{th} pitch actuator
α_i	Gain distribution factor for the i^{th} pitch actuator
γ	Length ratio for the double-pitched rotor

Chapter 1

Introduction

The need for electrical energy has grown exponentially due to socio-economic growth worldwide. However, rising concerns about climate change due to the ever-increasing carbon footprint and gradual depletion of fossil fuels have pushed mankind to opt for alternative renewable energy sources (e.g., solar, wind, and wave) for power generation. In general, wind power is one of the most popular, abundant, renewable, widely spread, and clean energy sources. It reduces greenhouse gas emissions as opposed to fossil-fuel-derived electricity. People have been using wind power for grinding, sailing boats, and pumping water for almost 3000 years. Windmills have been an integral part of many communities since the beginning of 1200 BC. It converts inbound wind energy (i.e., kinetic energy) into electrical energy or mechanical power.

Wind flows due to the unequal heating of the atmosphere by the sunlight, apart from other factors. Air movement is augmented by differences in atmospheric forces (e.g., pressure, Coriolis effect, inertial, and frictional forces) caused by fluctuations in atmospheric heat. The Intergovernmental Panel on Climate Change (IPCC) has predicted a rise in mean sea level due to global warming [7,8], emphasizing the need for carbon-free alternate energy sources. Large-scale wind farms provide electricity to national grids, whereas small individual turbines can light up rural areas or grid-isolated locations. Due to these reasons, their relevance is expanding day by day.

The kinetic energy of wind turns a rotor attached to a slow-moving shaft of a turbine. The spinning rotor turns the generator through a linking shaft and gearbox to generate power. Thus, wind turbines are divided into two categories based on their rotational axis. As the name suggests, Horizontal Axis Wind Turbine (HAWT) revolves around their horizontal axis, while Vertical Axis Wind Turbine (VAWT) spins around their vertical axis. The rotor blades of a horizontal axis turbine span perpendicular to the wind flow. HAWTs are the most common form of wind turbine and are available in various shapes and sizes. The two types of HAWTs are upwind turbines, with the rotor facing the inflowing wind, and downwind turbines, with the rotor behind the tower. Most HAWTs are now designed as upwind turbines with a yaw mechanism to face the incoming wind to avoid the tower shadow effect.

A horizontal axis wind turbine has five essential components: rotor blades, rotor hub, nacelle, tower, and footing. The size of the blade determines how much wind energy can be converted into power. These blades have an aerodynamic profile and are made of materials with a high strength-to-weight ratio. The tip speed ratio, number of blades, and blade profile greatly influence power output. The nacelle contains a gearbox and generator that convert the shaft power into electricity. The tower provides the necessary height for the rotor to overcome obstacles that produce turbulence at lower elevations. A HAWT can have any number of blades; however, a three-bladed rotor is most effective [9]. The tip speed ratio varies with the number of blades. Therefore, a system with fewer blades can rotate faster to capture the same amount of energy provided by more blades. Previous studies have shown that a three-bladed system can produce less vibration and noise than one or two blades. Apart from the appropriate tip speed ratio, the pitch controller present in a modern rotor allows it to operate over the full range of wind flow, making it more efficient than VAWT.

VAWTs, on the other hand, are smaller and easier to build, carry, and install. As a result, it has lower startup and ongoing costs. Furthermore, while VAWT does not require a yaw mechanism and can operate at low wind speeds, they still require a small amount of power to initiate rotation. It is environmentally friendly and may be deployed near human settlements with minimal land use and noise. There are three types of VAWT available in the market: Savonius, Giromill, and Darrieus. In general, horizontal axis turbines are more common since they can produce more power and are economically viable for a large settlement. These turbines can be erected on land or in the sea, provided the region has consistent wind flow throughout the year.

Wind turbine blades have aerodynamic properties similar to airplane wings. The airfoil design causes a velocity difference on either side due to pressure difference, following Bernoulli's principle. The net lift force that turns the blade is caused by the differential pressure on either side of the rotor plane. Thus, the power generated by a wind turbine is given by

$$P = \frac{1}{2}\rho_a A_r C_p {V_w}^3 \tag{1.1}$$

where P represents power, ρ_a denotes air density, A_r indicates rotor area, C_p symbolizes the power coefficient, and V_w represents incoming wind velocity. The power coefficient is the ratio of the power extracted to the available power. German scientist Albert Betz proved that the maximum power coefficient of an ideal wind turbine is 59.3%, i.e., the maximum amount of energy that can be generated provided there are no mechanical and electrical losses [9]. In general, the power coefficient of an actual wind turbine is roughly 35 $\sim$ 40%. It is expressed as a function of tip speed ratio and blade pitch angle, which is adjusted in real-time to maintain stable power output, i.e., optimum C_p. Thus, the power losses owing to electrical and mechanical inefficiencies (i.e., η_e and η_m, respectively) are taken into account when determining the ultimate power output, which is given by

$$P_e = \eta_e \eta_m P \tag{1.2}$$

Eq. 1.1 reveals that the power output of a wind turbine is proportional to the rotor area and the cube of the inflowing wind velocity. It indicates that site selection demands a detailed feasibility study, i.e., the availability of adequate wind resources within a given geographical set-up. Wind properties alter with time and space. Hence, geographical variations and climate change directly impact wind flow. Besides wind speed,

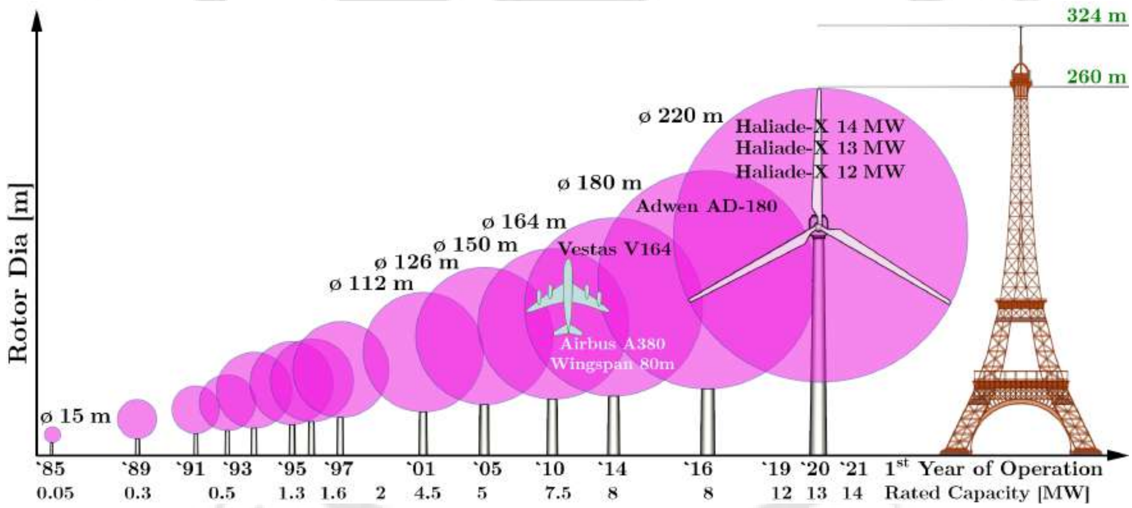

Figure 1.1: Evolution of horizontal axis wind turbines

the power output of a wind turbine also depends on the rotor size. Due to this reason, the blade length has continuously grown to generate more power. In this context, recent advancements in material technology have helped build large rotors. For example, the Haliade-X 12 MW, the World's largest wind turbine, has a rotor diameter of 220 m [10, 11]. This three-bladed offshore turbine has been deployed in Rotterdam Port, Netherlands, since 2019.

The evolution of wind turbines in size and power generation is shown in Fig. 1.1. In general, the turbine blade revolves at an average of 10 $\sim$ 20 rpm. As the rotor speed increases, HAWT is known to produce noise. As a result, larger turbines produce more noise, which is noticeable in its neighborhood. The energy loss produced by friction and blade oscillation affects the power efficiency of a wind turbine. It also damages the blade, necessitating frequent maintenance. Also, aerodynamic and other environmental loads (i.e., gravitational, seismic, and hydrodynamic) cause significant vibration. Therefore, high-fidelity modeling, analysis, and efficient control are essential for the safe and long-term operation of any horizontal axis wind turbine.

1.1 Literature Review

The increasing demand for renewable energy, specifically carbon-free sources, has been consistently on the rise. The current utilization of wind energy is a result of sustained research and development efforts over the past decades, instilling confidence in its efficacy. However, a significant challenge in the technological evolution of wind energy lies in the structural aspects supporting the rotor and other electrical components throughout their operational lifespan. This includes the platform, tower, drive-train, and blades, which undergo structural vibrations when exposed to various environmental loads such as wind, seismic forces, or hydrodynamics. Therefore, the precise modeling and analysis of these components are crucial to capture their structural behaviors. On the other hand, minimizing vibration levels is a fundamental requirement for ensuring the safety and sustainability of the entire power generation unit. Due to this reason, the development of a robust and accurate mathematical model of operating wind turbines in a multi-body framework is the motivation behind this thesis work. The study also places emphasis on the on vibration control of different structural components and its impact, such as enhancing fatigue life and regulating power output. The ensuing subsections provide insights into the current state-of-the-art in modeling HAWTs, fatigue design, structural loads, and the control of vibrations in various turbine components.

1.1.1 Multi-Body Dynamic Modeling of HAWT with Bending-Torsion Coupling in Blades

Modern wind turbines, being a significant source of renewable energy, have also evolved with bigger sizes and more power ratings to keep up with the ever-increasing demand. The blades of these turbines are large and flexible, constructed using materials with a high strength-to-weight ratio to retain their aerodynamic performance. These blades undergo excessive deformation under turbulent wind, and hence, their design demands precise modeling and analysis. Due to this reason, the development of a robust and accurate mathematical model of operating wind turbines in a multi-body framework has always remained an open area of research for scientists and engineers. The behavior of a dynamic system can be characterized by a set of governing differential equations that encompass inertial, damping, and elastic forces, in addition to external disturbances. These equations can be derived either through the analytical approach (continuous parameter model) or the numerical method (finite element or vector approach). Consequently, a physical system can be represented as either a continuous or discrete system. In computational applications, continuous systems are typically approximated as discrete or lumped parameter models for ease of analysis. Creating a finite element model for the entire wind turbine system is computationally demanding. Therefore, numerous researchers have opted for reduced-order models of wind turbines, incorporating mode shapes obtained from finite element models. In a reduced-order model, only a few significant modes of the blade and tower are considered for analysis. Burton et al. [9] outlined a systematic procedure for developing a discrete reduced-order wind turbine model and conducted the dynamic analysis. They derived an approximate expression for mass-proportional or equivalent modal aerodynamic damping of the turbine. Additionally, they illustrated the change in natural frequencies with an increase in the turbine's rotational speed using a Campbell diagram for a 40 m blade. In this context, Kane's approach [12] provides a significant computational advantage for such multi-body dynamic analysis as the number of degrees of freedom can be minimized for a large structure, e.g., wind turbine [13–15].

Wind turbine blades are modeled as a rotating cantilever beam that primarily vibrates in flapwise and edgewise directions under aerodynamic loading. As the length increases, these ultra-light blades also experience torsional vibration due to aerodynamic pitching moment, which often interacts with bending deformation. The reason behind this structural behavior can be classified into two primary sources - (i) elastic coupling and (ii) dynamic coupling. The elastic coupling can arise due to the non-anti-symmetric layout of the materials in an airfoil, which is reflected in the offset of the shear centre with respect to the centre of gravity. On the other hand, dynamic coupling originates due to the offsets of the centre of gravity from the blade pitch axis and aerodynamic centre. In addition to these effects, the aerodynamic pitching moment changes the instantaneous twist angle of an airfoil that develops torsion. An earlier study on coupled flapwise/edgewise bending and torsion of a rotating blade was carried out in the late fifties by Houbolt and Brooks [16], where they included the effect of offsets between neutral, elastic, and mass axes of an airfoil but neglected second-order non-linear effects. Their work provided the basic mathematical framework, which led to much research on this topic in the following years. For example, Hodges and Dowell [17] derived a set of non-linear equations for coupled flap-lag-torsional vibration of a rotor, which was modeled as a slender, flexible, homogeneous, and isotropic beam undergoing moderate deformation. This model was further developed using geometrically exact beam theories, which enabled the study of the kinematics of a rotor as an Euler-Bernoulli beam undergoing large deformation [18] and pre-twist [19]. In the late eighties, Panda and Chopra [20] highlighted the impact of bending-torsion coupling on rotor instability. Later, Chandra and Chopra [21] proposed a mathematical model of rotating blades using the theory of thin-walled elastic beams to model bending-torsion coupling. Here, it may be mentioned that many previous studies on rotor dynamics under this coupling were based on Rayleigh-Ritz or Lagrange formulations [22, 23]. For example, Banerjee [24] developed an exact dynamic stiffness matrix approach using twisted Timoshenko beams for free vibration analysis, including rotatory inertia and shear deformation. In a different study, Banerjee and Su [25] used the same formulation for composite beams considering geometrical and material coupling between bending and torsional deformation originating from the unbalanced in ply orientation and lamina thickness. Finally, they used the Wittrick–Williams algorithm to determine the natural frequencies and mode shapes of an aircraft wing [26]. Unlike non-rotating beams, the natural frequencies of a rotating beam are affected by its *rpm*. Hence, the variations of modal parameters of a rotating pre-twisted beam were investigated by many researchers [27–29]. Zhao and Wu [30] investigated the coupled vibration characteristics of rotating cantilever beams in 3D, considering Coriolis forces and steady-state axial deformation. Their study indicated that Coriolis terms did not have a significant effect on the edgewise bending frequency. In this context, flap-lag-torsional coupling played a vital role in rotor dynamics as Castillo et al. [31] demonstrated. They also studied the effects of boundary conditions (i.e., free-hinged, spring-hinged, or hinge-less) on rotor dynamics under elastic and inertial coupling besides gyroscopic actions. Oh and Yoo [32] proposed efficient modeling for vibration analysis of a rotor considering bending, extension, and torsional couplings. They investigated the effects of sectional parameters, e.g., elastic offsets, pre-twist angle, structural coupling, and rotational speeds on its modal characteristics.

In recent years, Hafeez et al. [33] developed a mathematical model for a flexible rotating beam using nonlinear coupled partial differential equations, which accounted for the effect of mass and shear center offsets on the coupled axial-bending-torsional vibrations of the blade. Nonlinear aeroelastic models of the blades were also studied by Bichou et al. [34] to investigate the coupled vibration characteristics of the system. In general, the blades are susceptible to flutter even below their linear-flutter speed, particularly near cut-out conditions with increased blade size and rotor speed. Kessentini et al. [35] developed a mathematical model to study the coupled interaction of blades and towers of a horizontal-axis wind turbine. They observed that small tower vibrations could induce significant blade vibration, which indicated the requirement for detailed modeling and control. Kang et al. [36] investigated dynamic instability caused by tower-blade interaction and rigid nacelle using a simplified two-dimensional coupled model. However, their model did not consider the dynamic bending-torsional coupling in blades and the drive-train generator interactions often encountered in a wind turbine. These components, along with the applied control systems of a wind turbine, can cause significant dynamic interactions and, therefore, need to be modeled thoroughly.

In general, the aeroelastic behavior of composite turbine blades can be complex and requires detailed investigation before implementation. Rafiee et al. [37] investigated such behavior using 3D finite element analysis based fluid-structure interaction of a full-scale composite blade. They observed that blade deformations could impact the power generation capabilities, particularly in higher wind speeds where instabilities could occur. Here, it may be noted that bending-torsion coupling affects aerodynamic stability, which is a significant concern in the aero and wind turbine industry. High bending-torsion coupling coefficients can induce flutter instability in large blades. Stäblein et al. [38] investigated this feature to quantify the critical root bending moment in a flap-twist to feather coupled blade. Hence, efficient blade design to reduce structural stresses on the turbine has always been an open problem for researchers. These design modifications and vibration control techniques implemented by the previous studies did not consider the effect of bending-torsion coupling in detail, affecting the controller's performance. However, it should be noted that bending-torsion coupling is not always detrimental for a rotor. It can help in aerodynamic load alleviation if appropriately designed. Lobitz and Laino [39] demonstrated this feature and its beneficial effects. They studied a torsionally coupled fixed-rpm rotor subjected to a stochastic wind spectrum and observed that a high twist-to-feather coupling coefficient reduces the rotor's loads and fatigue damage significantly, over the entire range of wind loading. Gözcü and Kayran [40] used dynamic super-element to model the coupled motion of a turbine blade to demonstrate its load reduction capabilities. They demonstrated that the damage equivalent loads could be reduced in the crucial connection points of the complete wind turbine system, not just in the blades, with the introduction of bending-torsion coupling. Hayat et al. [41] analyzed classical flutter performance of National Renewable Energy Laboratory (NREL)-5MW blade considering bending-torsion coupling arising from layup unbalances. They observed that a change in fibre orientation could decrease the flutter speed considerably and suggested stiffer carbon fibre composites to induce high structural coupling to improve its performance. Later, Shakyaet al. [42] studied the same behavior of composite wind turbine blades. Their work showed that up to 100% increase of critical flutter speed was possible due to the coupled flap-torsional stiffness originating from the unbalance in the composite layup.

1.1.2 Modeling and Fatigue Design of Monopile Supported Offshore Turbines

Over the last decade, offshore wind turbines also witnessed significant growth in their size to meet the power demand. Offshore wind turbines boast several benefits, including a consistent and prolonged wind flow, as well as expansive utilization of space within the marine environment. Shallow-water offshore turbines, typically situated at depths ranging from 30m to 50m, are primarily erected on monopile supports. In contrast, deep-water offshore turbines, found in depths exceeding 120m, rely on floating spars anchored to the seafloor through mooring cables. As turbine size and power ratings escalate, the load-carrying capacity of monopiles must proportionately increase to accommodate these larger and more powerful turbines. The intricate design of these structures necessitates a sophisticated model for the entire multi-body rotating system, where Soil-Structure Interaction (SSI) plays an important role. Various methods are proposed in the literature to model the soil-structure interaction. For example, a closed-form expression for finding the fundamental frequency of a wind turbine tower under SSI was developed and experimentally validated by Adhikari and Bhattacharya [43]. Finite element analysis of monopile-supported offshore wind turbines is a popular approach, where soil properties are modeled by linear or non-linear springs [44]. The dynamic interaction results in an increased response of the combined system. Zuo et al. [45] modeled the NREL 5 MW benchmark wind turbine in the finite element framework using ABAQUS software and observed a significant reduction of the tower natural frequencies due to SSI. They also noticed that blade and tower responses increased with rotor speed. Thus, monopile design without considering blade rotation led to gross underestimation that could subsequently affect the structure. Bisoi and Haldar [46] studied soft-soft and soft-stiff monopile design and checked the overall safety against serviceability and fatigue limit states. They observed that the length of the monopile below its critical depth had a negligible impact on its design.

Rong et al. [47] derived an analytical formula for the natural frequency of monopile-supported wind turbine using the Euler-Bernoulli beam model with p-y curves for foundation stiffness. In this context, different aspects of offshore foundation design may be found in Bhattacharya [48]. This book explains the importance of soil-structure interaction and multiple methods to evaluate the foundation stiffness. It also provides a comprehensive review of different methods used for long-term behavior estimation. Banerjee et al. [49] modeled the effect of foundation flexibility using an equivalent spring-dashpot model for monopile below the mudline. They carried out dynamic analysis using four different soil conditions and observed that the total displacement at the tower top increased with reduced shear wave velocity, especially for lower soil stiffness. Kementzetzidis et al. [50] studied different geotechnical aspects of monopile foundation using 3D non-linear finite element analysis with a significant emphasis on the robustness of soft-stiff design, particularly in the extreme weather. In this context, the impact load test on pile [51, 52] is a standard tool to estimate its stiffness and in-situ frequency response function for finite element modeling.

Developing new methodologies to improve the bearing capacity using stiffeners to avoid the abnormal size of monopile was proposed by Li et al. [53]. In general, fatigue design focuses on the short-term effects, while long-term effects are equally crucial for serviceability. Katsikogiannis et al. [54] studied the stress due to axial force and bi-directional bending moments for damage estimation. They compared the sensitivity of three soil modeling techniques (viz. macro-element model, linear elastic stiffness model with soil damping and p-y curves) under wind-wave misalignment. Their study concluded that significant fatigue damage might occur for misalignment greater than 30°.

In general, the soil type around the monopile affects its design life. Schafhirt et al. [55] investigated this influence on long-term performance due to cyclic loading. They modeled soil-structure interaction by non-linear p-y curves to estimate the fatigue life using the mudline bending moment, which was affected by the softening of the surrounding soil. Besides spring stiffness, aero-elastic and hydrodynamic damping play a significant role in fatigue life and cost-effective design [56, 57]. In this context, current industry standards are often inadequate [58] for the upcoming large turbines due to their simplified approach for stiffness and damping characterization and wind-wave modeling in the light of misalignment and soil-structure interaction. These shortcomings often lead to underestimation of fatigue damage accumulation and subsequent design life of the foundation. Marino et al. [59] compared the linear and non-linear wave models for fatigue load estimation. They concluded that the linear wave model underestimated fatigue load in the non-operating (or parked) condition, where hydrodynamic loads predominate. Simultaneously, the non-linear wave model was less critical in normal operating conditions, where aerodynamic loads dictated the design. Risi et al. [60] investigated the performance of offshore wind turbines under extreme events, e.g. earthquakes along with wind and wave loads. In their study, a finite element model of an offshore wind turbine was developed for seismic fragility analysis to investigate its vulnerability, particularly under crustal earthquakes in soft soils. Loken and Kaynia [61] estimated the fatigue life of monopile and caisson foundation of offshore wind turbines using the mudline bending moment, which concluded that fixed bottom boundary condition over-estimated the design length.

Monopiles in the marine environment are often subjected to stress reversal caused by the environmental loads. Thus, fatigue crack propagation in these structures is the subject of various studies [62, 63], where residual stress has a significant role in the performance of welds and connections. In this context, structural loads in the marine environment are highly uncertain. Hence, stochastic analysis of monopile has remained a significant area of research, where the overall reliability index is often quantified by approximate models [64] or Monte Carlo simulation [65]. Haldar et al. [66] studied the stochastic response of monopile-supported offshore wind turbine in clay using non-linear p-y curves. They observed that the increase in embedded length reduced the mean of maximum tilt at the mudline, while marginally influencing its fatigue life. Teixeira et al. [67] used kriging for stress-cycle analysis of offshore wind turbines at a reduced computational cost without compromising its accuracy. Velarde et al. [68] conducted a sensitivity analysis of fatigue loads due to uncertainty in environmental, structural, and geotechnical parameters. They observed that the uncertainties in turbulence intensity and wave load had a significant influence on fatigue loads. For further reading on this aspect, a comprehensive review of stochastic fatigue damage analysis for offshore wind turbines may be found in Jimenez-Martinez [69].

1.1.3 Modeling and Dynamic Analysis of Spar-type Floating Offshore Turbines

Spar-type floating wind turbines operate in deep-water offshore environments. They consist of mooring supports, a floating spar, a long and flexible tower supporting the nacelle, and a rotor at the top. Unlike onshore turbines, which are exposed to turbulent wind, the primary source of vibration for these types of offshore floating turbines is the hydrodynamic load. In this structural set-up, small vibrations of the spar (i.e. tower base) due to sea waves can cause an amplified response at the nacelle (i.e. tower top). It is more pronounced under wind-wave misalignment, which is often reflected in the side-to-side response of the tower or nacelle.

Moreover, the power capacity of deep-water offshore wind turbines has increased rapidly in the recent past with larger rotor diameters and taller towers to capture more wind energy. Modeling these ultra-large machines and their supporting structures is extremely challenging. Various methods have been adopted for this purpose by many researchers, in order to characterize the multi-body dynamics including aero-servo-elastic coupling [70–72]. The modeling is more complex for Floating Wind Turbine (FWT), which needs to include the dynamics of the floater and mooring mechanism. O'Brien et al. [73] have presented a review of commercially available software packages and codes for this purpose with a major emphasis on modeling in the light of Fluid-Structure Interaction (FSI). Ageze et al. [74] have studied different aero-elastic simulation tools available for wind turbine analysis. They have also compared the results of a benchmark wind turbine considering FSI with different aero-elastic codes. Ullah et al. [75] have studied the effect of hydrostatic nonlinearity in the case of high amplitude motions of spar-type FWT with a mathematical model based on the Newton-Euler approach. Their study has indicated that non-linear hydrostatic behavior can increase significantly increase roll and pitch moments (almost 40-50%), while marginally affecting the heave force. In this context, one of the most popular and widely used simulation tools is FAST (Fatigue, Aerodynamics, Structures, and Turbulence), by NREL, USA [76]. However, this open-source package is under development and has many limitations. Being an emerging area with immense potential for sustainable development, the wind energy industry is constantly growing to meet the ever-increasing demand for more efficient solutions.

Due to this reason, research activities in the recent past have been focused on different aspects of efficient modeling, analysis, and design of wind turbines. For example, Li et al. [77] have explored the effects of the yaw error and wind-wave misalignment on the dynamics and power generation of floating turbines using FAST. Their study indicates that yaw error can result in reduced power generation without adverse effects, while wind-wave misalignment significantly affects the dynamics of the structure. Kyle et al. [78] have investigated the propeller and vortex ring states of the NREL 5MW floating turbine when subjected to strong waves and low wind using Computational Fluid Dynamics (CFD) analysis. Their study has shown that negative thrust can occur in regions of high twist angles. Li et al. [79] have also studied the dynamics of a semi-submerged offshore wind turbine subjected to turbulent wind flow to investigate the effects of wind shear, turbulence intensity, and coherence on the responses of the turbine structure in another work. They have noticed that increased turbulence can create violent shaking of the platform, which, in turn, increases structural loads on the turbine significantly. They have suggested the use of a partial coherence structure to ensure the safety of the wind turbine. Liu et al. [80] have analyzed the reliability of floating wind turbines considering wind and wave loads with no misalignment between them. They have observed that edgewise blade response can be considerably larger in offshore turbines compared to its onshore counterpart, thereby adversely affecting the fatigue life at the blade root. Chevillottete et al. [81] have tested the fatigue life of polyamide-based mooring cables for supporting offshore wind turbines and claimed significant enhancement of the fatigue life of braided nylon ropes by enhancing fibre coatings with modified rope construction. Pham et al. [82] have discussed the reliability-based modeling and service life monitoring strategy for mooring cables with remedial measures at the design level to improve the dynamics of floating turbines.

1.1.4 Environmental Loads

Wind turbines are exposed to various external forces depending on the operating environmental conditions, as shown in Fig. 1.2, where the blades and the tower are subjected to aerodynamic loads due to inflowing wind, on the other hand, the spar is exposed to hydrodynamic loads arising from the ocean waves and anchoring cables. Therefore, an accurate estimation of these loads is essential for the design of wind turbine components.

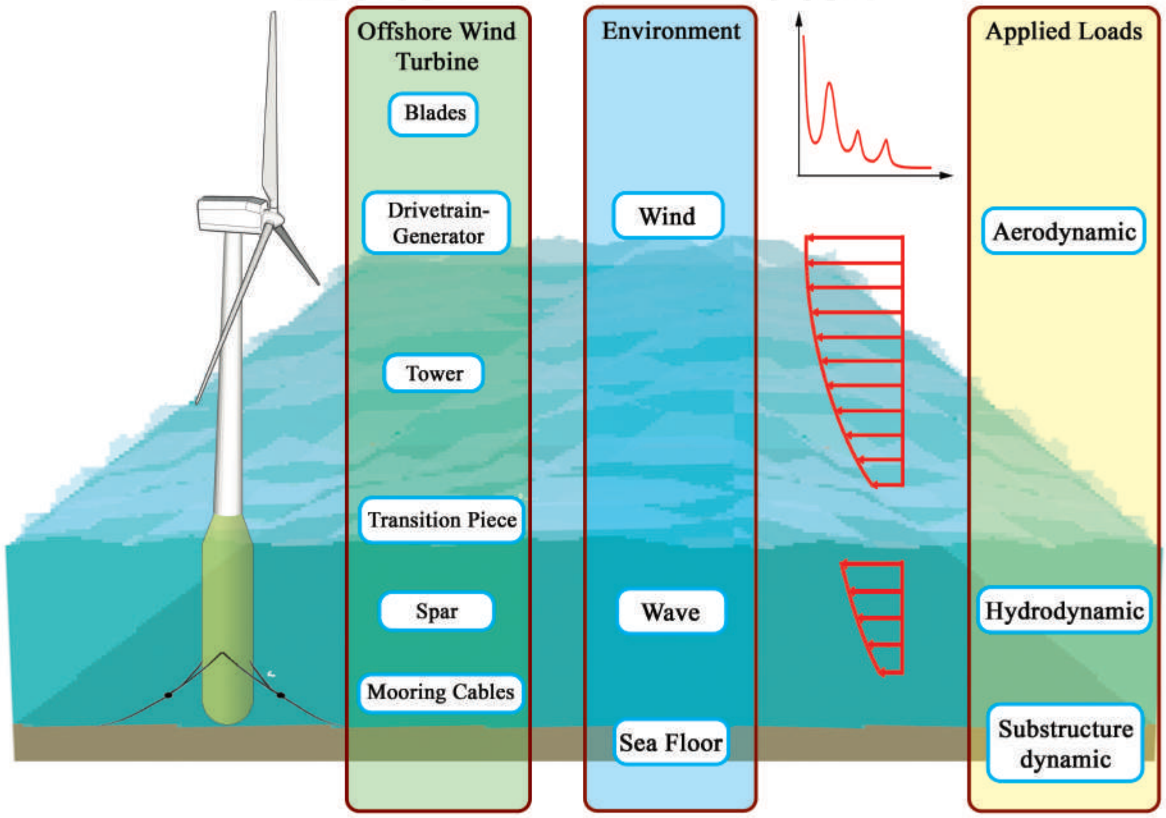

Figure 1.2: Floating Offshore wind turbine and its components.

Estimating aerodynamic loads relies on the consideration of environmental factors. IECWind [83] and TurbSim [84, 85] stand out as widely adopted tools for such simulations, both originating from the NREL. IECWind generates a deterministic wind flow under extreme conditions (e.g., gusts, directional shifts, coherent gusts with directional changes) specified in IEC 61400-1 [86] and IEC 61400-3 [87]. In contrast, TurbSim models the stochastic, full-field, three-dimensional turbulent components of wind speed. Following the simulation of the wind field, the estimation of aerodynamic loads is accomplished by considering the airfoil and geometric characteristics of a blade facing the incoming wind. In 1984, Thresher et al. [88] introduced a Force and Load Analysis Program (FLAP), employing a quasi-steady linear aerodynamic model. This model accounted for wind shear, tower shadow effects, and gravity loads, and utilized a power law to estimate the mean wind velocity above the ground. Initially designed to estimate time-dependent aerodynamic forces for a rigid-hub case, the program was later adapted for a teetering-hub scenario, incorporating pinned boundary conditions to address asymmetric bending modes [89].

Over the past decade, the exploration of wind turbine blade flow behavior through Computational Fluid Dynamics (CFD) has captivated the attention of researchers [90,91]. Duque et al. [92] introduced a CFD code integrated with a turbulence model based on the Reynolds Averaged Navier-Stokes equations. Goundarzi [93] conducted an extensive review of both Blade Element Momentum (BEM) theory and CFD analysis. Advocating for a more precise and computationally efficient approach, he proposed a CFD-BEM hybrid method for estimating aerodynamic loads. Despite the appeal of CFD, BEM theory remains the predominant tool for evaluating aerodynamic forces on rotating blades due to its efficiency and simplicity, outshining alternatives like CFD. The National Renewable Energy Laboratory (NREL) developed AeroDyn [94], a software employing BEM theory to estimate aerodynamic loads from simulated wind fields. BEM theory assumes the independence of aerodynamic forces on blade elements and relies solely on lift and drag coefficients, but several corrections have been proposed in the literature to enhance its accuracy [95–98]. However, the limitations of BEM theory become evident when the axial induction factor surpasses 0.5, rendering the relation between axial induction factor and thrust coefficient invalid. To address this, Glauert [95] proposed an empirical relationship based on experimental data, though it lacks accommodation for tip and hub losses. Buhl [96] later extended this empirical solution, incorporating corrections for tip and hub losses. Despite these enhancements, the traditional BEM theory, which iteratively solves induction factors, often encounters numerical convergence issues. Addressing these issues, Ning [99] introduced a modified BEM approach with guaranteed convergence. In Ning's method, the optimal flow angle is evaluated instead of induction factors, segmenting the BEM equation into three regions (momentum, empirical, and propeller break) to enhance convergence. Ning's approach incorporates Buhl's empirical relationship with various corrections, providing a more accurate solution to the aerodynamic load estimation challenge.

Numerous wind turbines are frequently erected in offshore environments, subjecting them to loads induced by ocean waves. Ocean wave profiles are typically simulated based on the zero-mean Gaussian stationary power spectrum, which correlates energy with crucial parameters influencing wave formation, such as fetch length and effective depth. Pearson and Moskowitch [100] introduced a mathematical formulation, the Pearson-Moskowitch (PM) spectrum, designed to fit the frequency spectrum for a fully developed sea state. However, fully developed sea states occur only when sustained wind speeds persist over an extensive fetch length, which is often not the case and can result in an exaggerated peak in the frequency spectrum.

In response to this limitation, Hasselmann et al. [101] devised an enhanced spectrum known as the Joint North Sea Wave Project (JONSWAP) spectrum, derived from actual wave measurements. This spectrum builds upon the PM spectrum, introducing a normalizing parameter and frequency-dependent peak enhancement factor to model large waves more accurately. After simulating the wave time history, hydrodynamic loads acting on the structure are estimated using Morison's equation [87]. Recognizing the interplay of wind and wave loading, Jamieson et al. [102] emphasized the significance of concurrently considering these factors in the design of offshore structures. Isolating one load case from the other can lead to overly conservative design practices. Hence, a comprehensive model of the environmental loads and the turbine is essential for accurate aero-servo-elastic simulation of the dynamics of such turbines.

1.1.5 Vibration Control

Wind turbines undergo considerable vibrations throughout their operational lifespan, prompting the exploration of diverse strategies and devices in the literature to optimize turbine performance. Vibration control in wind turbine systems encompasses the alleviation of vibrations in the foundation, tower or nacelle, drivetrain, and rotor blades. Notably, large rotor blades predominantly experience vibrations in both the flapwise and edgewise directions. The airfoil shapes of turbine blades are meticulously optimized to minimize drag and maximize lift. This optimization results in a configuration where flapwise motion encounters substantial aerodynamic damping, leading to large amplitude deformations along this direction. However, these deformations exhibit a significant static component due to the non-zero mean of the upstream wind flowing towards the rotor plane. While aerodynamic damping effectively mitigates vibration in the flapwise direction, it merely reduces vibration to some extent without altering the mean component (i.e., static deformation) of the response. In contrast, edgewise motion experiences significantly less aerodynamic damping, resulting in smaller amplitude but high-frequency vibrations [103,104]. Under certain conditions, the edgewise direction may exhibit very low or negative damping, leading to potential instability [105]. Beyond the dominant blade modes, the dynamics of the tower in the fore-aft and side-to-side directions are coupled with the blades, introducing significant blade-tower interaction. Murtagh et al. [106] delved into the dynamics of wind turbines under blade-tower interaction, revealing that the displacement of the blade tip increased by up to 256% due to this interaction. Thus, tower vibration control is an essential component for safe and sustained operation. It helps to provide a stable platform at the tower top, which is a primary requirement for housing the generator, drive-train, and rotor assembly.

As a result, numerous researchers initially introduced traditional Tuned Vibration Absorbers (Tuned Vibration Absorbers (TVAs)) to diminish tower top motion and subsequently extended their application to alleviate blade vibrations. Tuned vibration absorbers, such as Tuned Mass Dampers (Tuned Mass Damper (TMD)) and Tuned Liquid Column Dampers (Tuned Liquid Column Damper (TLCD)), have been widely utilized as motion control devices in civil and mechanical systems since the early 20th century. The exploration of passive control techniques using these devices has been a focal point for structural control in both onshore and offshore wind turbines. Passive devices, including ball/roller dampers [107], tuned mass dampers [108], liquid dampers [109,110], and tuned liquid column dampers [111–113], offer simplicity as they operate without external power and real-time monitoring. Recent studies have extensively examined tower vibration control using passive devices, with TMD and TLCD emerging as the most commonly proposed devices. TMD and TLCD have found applications beyond wind turbines, for instance, Ricciardelli et al.[114] developed a semi-active TMD for wind-induced vibration control in a 64-story building. TMD is also being adopted by the wind turbine industry for commercial use [115–117]. Positioned within the nacelle, TMD is designed to match the fundamental frequency of the tower, effectively absorbing significant energy from the primary structure (i.e., HAWT) through resonance. Murtagh et al. [118] implemented a passive TMD at the tower top to mitigate its fore-aft motion, achieving around a 20% reduction in tower tip displacement. Colwell and Basu [112] investigated the effectiveness of TLCD for tower vibration control, placing it at the tower's summit with a 1% mass ratio tuned to 99.2% of the fundamental frequency. Their study, considering wind and wave loading through the Kaimal spectrum and JONSWAP wave spectrum, respectively, demonstrated a 55% reduction in peak displacement. Notably, these studies often overlooked the aerodynamics of the blades.

Lackner and Rotea [108] delved into the efficacy of passive Tuned Mass Dampers (TMD) in controlling vibrations in offshore wind turbines, utilizing a more realistic aeroelastic code, FAST (Fatigue, Aerodynamics, Structures, and Turbulence). Expanding on this work, Lackner and Rotea [119] developed a simulation tool for TMD-based passive, active, and semi-active control systems for offshore floating wind turbines. In a recent investigation, Zhang et al. [107] explored the performance of a Ball Vibration Absorber (Ball Vibration Absorber (BVA)) for controlling vibrations in the tower of offshore wind turbines, utilizing both numerical and experimental models. Shake table tests on a scaled wind turbine model demonstrated the effectiveness of BVA. Rezaee et al. [120] conducted a comparative study on various vibration control devices, including TMD, Tuned Liquid Dampers (Tuned Liquid Damper (TLD)), Tuned Liquid Column Dampers (TLCD), and Viscous Dampers (Viscous Damper (VD)), to reduce tower top displacement and acceleration. While VD exhibited superior performance, its implementation required additional design considerations. Most studies in the literature focused on unidirectional control. However, Sun and Jahangiri [121] explored the vibration control of offshore wind turbines using a bi-directional pendulum TMD under misaligned wind, wave, and seismic loadings. Comparing the results with conventional unidirectional TMD, they observed a noteworthy 10% improvement in vibration control for the same mass ratio. The model developed by Lackner and Rotea [108] was further modified by Asareh and Prowell [122] to incorporate seismic excitation. As TMD primarily relies on resonance, its performance is significant if the fundamental mode of the tower is excited (i.e., the frequency to which the device is tuned). The studies mentioned above mostly focused on a single TMD along a particular direction, which was further augmented with additional TMD in orthogonal directions for both onshore and offshore turbines [123, 124]. TMD was also used on offshore platforms in addition to nacelle [125–127] to mitigate wave-induced vibrations where wind-wave misalignment played a significant role. Besides the position of this control device inside a wind turbine, its architecture was also investigated by many researchers. For example, a single pendulum TMD was developed that could control vibrations in two orthogonal directions [128]. Enevoldsen and Mork [129] optimized mass-damper properties to reduce the dynamic response and fatigue loads on wind turbine towers. Their model of a 500 KW turbine showed that the tower design became more economical with the inclusion of mass dampers inside the nacelle. Chen et al.[130] suggested a combination of tuned mass damper and particle damper to suppress the wind-induced tower vibration. The damper efficiency during emergency shutdown and regular operation was investigated. In another study [131], they used shake table experiments to explore the impact of design characteristics (such as the sensitivity of controller frequency, mass ratio, and the number of steel balls per container). Gerges and Vickery [132] studied the performance of a non-linear TMD to mitigate wind-induced vibrations of a slender tower in its side-to-side directions. They validated the accuracy of their model using wind tunnel test data. In general, the performance of TMD is mainly governed by the optimal tuning of its parameters, which is difficult to derive in close form for a multi-body dynamic system having time-varying system matrices, e.g., wind turbine. Moreover, passive TMDs offer sub-optimal performance while experiencing random excitations when the input frequency does not coincide with tower mode.

To address this issue, researchers have shifted their attention to developing semi-active or active control systems that can operate in more challenging environments. The recent advancement in actuator technology has made this transition (i.e., active control from its primitive passive version) smooth and feasible. Numerical studies employing FAST revealed that an active TMD outperformed its passive counterpart, resulting in a remarkable 30% or more reduction in fore-aft displacement. Fitzgerald and Basu [133] employed Active Tuned Mass Damper (ATMD) for controlling tower out-of-plane vibrations, considering foundation damage due to soil stiffness degradation. With a 20% reduction in soil stiffness leading to a 45% increase in peak-to-peak vibration of the tower/nacelle without the controller, the ATMD intervention achieved a 52% reduction. Hemmati and Oterkus [134] investigated the performance of a semi-active TMD for vibration control of a monopile-supported offshore wind turbine exposed to combined wind, waves, and seismic loading. They tuned the device to the fundamental frequency of the tower, and the sub-optimally performed passive TMD was augmented with additional actuator force in the semi-active framework. Due to this reason, semi-active TMD performed better than its passive version. The overall performance of a semi-active TMD was further enhanced in the active mode [135], where actuators were used to provide additional force in real time. Lackner and Rotea [119] studied the performance of active TMD (ATMD) to regulate the fore-aft vibration of an offshore wind turbine tower supported on a barge. In this work, a family of controllers were designed using H_∞ algorithm with multivariable loop shaping for turbulent wind and wave excitations. Thus, real-time optimal tuning helped to maintain the controller performance over a wider operating range [136].

In this aspect, Magnetorheological (MR) fluid possesses an intelligent characteristic wherein its viscosity rises in response to the application of a magnetic field. Other advanced control algorithms such as Linear Quadratic Regulator (LQR) or Linear Quadratic Gaussian (LQG) were also implemented in such active controllers. Saptarshi et al. [137] employed magneto-rheological fluid within a Tuned Liquid Column Damper (TLCD) for semi-active vibration control of the tower within the LQR framework. Hu and He [138] proposed an active stroke-limited Hybrid Mass Damper (HMD) using LQR control strategy for floating turbines. They observed that the hybrid version of the damper in active mode performed better under stochastic wind loads modeled by Weibull distribution. Martynowicz and Rosòl [139] proposed a magneto-rheological tuned vibration absorber where an LQG control algorithm was implemented to mitigate tower vibration. In this approach, the quadratic cost function was developed using the states and control forces to find the optimal actuator force. Better control was achieved due to this reason, which was otherwise difficult in passive or semi-active mode. Fitzgerald et al. [140] also found the same, i.e., an ATMD could improve the reliability of a wind turbine tower against fore-aft vibration.

Contrary to onshore turbines, floating offshore wind turbines experience tower vibration due to the combined effect of hydrodynamic and aerodynamic loads. In order to control such vibrations, Madsen et al.[141] have experimentally studied different close and open-loop control strategies on the scaled model of a 10MW turbine supported by tension leg platforms. They have noticed that the surge motion of the turbine governs the tension in the mooring cables. At the same time, negative aerodynamic damping of the controller can increase the vibration leading to higher responses in the surge, which can cause increased stresses and failure of the supporting structures. Han and Nagamune [142] have studied platform position control in offshore wind farms to mitigate the effect of aerodynamic wakes considering disturbances in the wind and wave loading. Their study has shown that the use of a linear quadratic integrator control algorithm adequately designed to achieve the targeted platform positions can maximize the power output by substantially reducing the wake effects. Sun [143] has investigated the performance of semi-active tuned mass dampers for vibration mitigation of floating turbines considering wind-wave misalignment. Sun and Jahangiri [121] have proposed a 3D pendulum-type tuned mass damper to control bi-directional responses (i.e. fore-aft and side-to-side) of mono-pile supported offshore turbine tower considering wind-wave misalignment and seismic loading. He et al.[144] have used tuned mass damper to control the vibrations of offshore wind turbines, where artificial fish swarm algorithm. The results of this study have shown improvements in the overall response and a significant reduction of standard deviations of the power generation. However, the tuned mass damper can create adverse effects and increase the response of several components, particularly under wind-wave misalignment. Also, one of the significant problems with tuned mass dampers is housing a large mass within the tower or nacelle, which has limited space. Due to this fact, new ideas and techniques are coming up very often, and industries have also embraced some of these options for further development [145]. For example, Spar-Torus Combination (STC) has been proposed by Muliawan et al.[146], where a donut-shaped Wave Energy Converter (WEC) is attached to the spar-type floating wind turbine (FWT). Although the torus designed in this format does not help in controlling spar vibration, its performance in trapping additional wave energy is impressive. Later, other studies have investigated its effect on the structural responses and power generation in both operational and extreme sea conditions [147–149]. These studies have observed that combining a torus with a spar can increase power production. However, it can also increase forces in mooring lines with additional bending moments in the tower, causing new challenges in design against ultimate limit state and fatigue. Wan et al. [150] have conducted laboratory tests on the possible slamming effect and green water effect of STC. Their studies have shown that submerging the torus in case of extreme sea conditions can reduce the forces induced in the mooring lines and also the bending moments in the tower. Ren et al. [151] has developed a new concept by combining WEC in the tension leg platform (TLP) of a floating wind turbine. Dynamic responses of the combined system have been studied numerically and experimentally with a scaled model that has a fair agreement. Although the primary focus of these studies is on harnessing wave energy in operational sea states, the use of torus to control the response has not been investigated. Yue et al. [152] have studied the positive effects of installing a heave plate in the spar of floating offshore wind turbines. Their study has shown that the effect of a heave plate depends on its position of installation (i.e. if it is located in the upper part of the spar, then the pitching motions and vibrations of the platform can be reduced substantially). Sant et al. [153] has introduced a new concept of including compressed air energy storage into the spar-type offshore wind turbine platforms. The numerical simulation conducted in ANSYS-Aqua has shown the possibility of integrating it with the spar without causing any adverse effect on the overall structural dynamics. Choung et al. [154] have estimated the fatigue damage of mooring lines for combined WEC and floating platforms, ignoring turbulence. Ren et al. [155] have estimated the long-term performances and fatigue life of STC using a simplified thrust model of wind loading. They have also developed two different survival modes to reduce long-term fatigue damage and extreme responses.

Apart from the tower, wind turbine blades are also subject to various dynamic forces that can induce vibrations, including turbulent wind flows, changes in wind speed and direction, and gravitational loads. These vibrations, if not adequately controlled, can lead to fatigue, damage, and fluctuations in the power output, reducing the turbine's operational life and increasing maintenance and repair costs. Additionally, prolonged exposure to large-amplitude vibrations during the turbine's service life can often result in structural failure of the blade. In this context, blade vibration control can be segmented into two different classes depending on the solution strategy. The first option is to enhance blade performance using different passive or semi-active devices, e.g., tuned liquid column dampers [156, 157], and semi-active fuzzy controlled MR dampers [158]. These devices are tuned to absorb energy from the primary structure, i.e., the blade in this case. Biglari and Fakhari [159] proposed shunt damping for edgewise blade vibration control, which primarily relied on non-linear aerodynamic damping in real time. Besides these devices, active tendons are also embedded in the blade [160–162] to enhance its stiffness. These tendons are made of smart materials, e.g., shape memory alloy [163,164] whose super-elastic property helps to generate actuation force that opposes blade deformation. Thus, active tendon not only reduces blade vibration but also enhances its reliability as a natural consequence [165]. Previous studies have also shown that the aerodynamic performance of wind turbine blades can be improved by inducing bend-twist coupling in a twist-to-feather direction [166]. As mentioned earlier, Hayat et al. [41] investigated the flutter instability characteristics of a bending-torsion coupled blade under quasi-steady aerodynamics. However, the authors did not consider the interaction of the bend-twist coupled blade with other turbine DOFs.

The second category of controller primarily relies on flow control using different options to alleviate the aerodynamic load on the rotor. The examples of this class are yaw control [167], active morphing [168], trailing edge flaps [169], Dielectric Barrier Discharge (DBD) plasma actuators [170], and most importantly, pitch control [171–173]. These options utilize wind flowing over the airfoil to tune the lift force, leading to less vibration. Among these control options, modern wind turbines primarily rely on pitch controllers to maintain constant power output when operating above their rated condition. It is a key element of wind turbine technology that contributes to the production of secure, effective, and sustainable electricity production. In this option, maximizing energy output with minimum fluctuation and safeguarding the turbine from damage is achieved by altering the blade pitch angle. It enhances the ability to harness wind energy effectively, thereby increasing its overall power production and lifespan. It also helps avoid overworking during heavy wind, which may result in mechanical/electrical failure and other problems. In this process, the aerodynamic load is attenuated by pitching the blades (either collectively or individually) to feather or stall positions depending upon the instantaneous wind flow. It primarily focuses on power regulation (i.e., maintaining the generator speed) while alleviating the aerodynamic load on the rotor. Different pitch control strategies have been developed for mitigating the trailing edge noise of wind turbine blades [174], fatigue loads, and tower vibrations [175]. A full-blade pitch controller of a modern turbine is a complex mechanism, requiring precise estimation of the actuator force to turn the blade. Moreover, the actuator demand (and subsequent power requirement) of a full-blade pitch controller increases with its rotor size, which is susceptible to deformation resulting in stress development at critical locations. Therefore, the demand for an efficient pitch control strategy has increased significantly with the growth of wind turbines in terms of their power output and size.

Thus, numerous studies have been carried out over the past few decades focusing on high-fidelity models of different control algorithms for wind turbines [176–180]. All these options utilize wind flowing over the airfoil, i.e., tuning the lift force, which is ultimately reflected in less vibration. Many researchers have explored various pitch control strategies for wind turbines [181–183], with Proportional Integral Derivative (PID)-based designs being the most common approach. In this context, the PID based pitch control algorithm [184,185] is also a popular option in the industry due to its simplicity and robustness. Staino and Basu [186] proposed a combination of active tendons and blade-pitch control strategy for simultaneous minimization of blade vibrations and power regulation. Fuzzy logic-based active pitch control [187–189], memory-based pitch control [190], and individual blade pitch control [191–193] are different options available in the literature. As the wind speed increases and direction changes (e.g., extreme hurricane-induced loads), the combined action of yaw and blade pitch control becomes a reliable option. Manikandan and Saha [194] suggested a novel sub-optimal control based on a Nonlinear Quadratic Regulator (NQR) for offshore systems. In this regard, fault-tolerant pitch control [195] is an option often suggested by researchers and engineers for extreme operating conditions. Tutivén et al. [195] introduced a super-twisting algorithm to increase the blade performance in fault-free and faulty conditions. These fault-tolerant pitch control systems received the attention of many researchers for blade load alleviation. For example, Noshirvani et al. [196] used Kalman filters for fractional-order terminal sliding mode control with a precise estimation of actuator force. Their method maintained the stability of the pitching system in finite time while reducing chattering. Other examples of advanced control used in controlling the blade pitch angle of wind turbines are Linear Quadratic Regulator (LQR) and Linear Quadratic Gaussian (LQG), Least Mean Square (LMS), and Sliding Mode Control (SMC), among many others. For instance, Basu and Nagarajaiah [197] proposed a wavelet-based LQR strategy for linear time-invariant systems, incorporating a switching scheme to adjust the gain matrix based on signal strength within a predetermined duration. Fitzgerald et al. [198] employed a similar algorithm to implement active pitch control using discrete wavelets, which split the states into two components and applied different weights to control efforts close to the structural frequency. The performance of this controller was compared to a baseline Proportional Integral (PI) and LQR-based pitch controllers, which were outperformed due to efficient frequency-based gain scheduling. Sarkar et al. [199] further improved this algorithm by developing an individual pitch controller for a spar-supported offshore wind turbine, ensuring stability and reducing platform pitch and roll motion. However, it was observed that this improved structural response resulted in increased deviation from the rated rotor speed, leading to higher power fluctuation.

In this context, double-pitched smart rotors have been developed in the recent past [200] where the blades are divided into two segements; an inboard section whose pitch angle is controlled at the root and an outboard section with a different pitch angle near the free end, i.e., (tip-controlled rotor). The power output can be tuned by regulating the pitch angle of the outboard section using a separate actuator. Tip-controlled rotor offers better start-up and shutdown abilities, faster control, lower weight, and more liberty in airfoil selection compared to a single-pitched rotor [201,202]. Afjeh and Keith [203] characterized the performance of tip-controlled rotors using a simplified flow model where a system of trailing vortex lines emerging from the junction of the bounded vortex system of the blade was used to model the wake and compared it with experimental results. Agarwala and Ro [204] investigated blade performance considering different pitch angles at the tip. Chen et al. [205] demonstrated the efficiency of a double-pitched system in active flutter control. The length of the tip portion was optimized along with the chord-wise position of the actuator for maximum output. Bernhard and Chopra [206] modeled the actuator of a double-pitched rotor with an active blade tip. They used a special beam element following Vlasov's theory and validated using free-vibration and static response of a scaled model. In general, a tip-controlled blade results in a better overall design and lower power fluctuation. Xie et al. [207] introduced a folding blade design for horizontal-axis wind turbines. This design involved a stall-regulated root blade section and a folding tip blade section with an inclined fold axis, which altered the lift force and moment arm, resulting in changes in power output. They also developed a blade folding actuation mechanism using a servo motor and worm gear with a servo system featuring double feedback loops for blade fold angle control. Industry-level partial pitch wind turbines include models like the 2.5 MW MOD-2, developed by Boeing Engineering and Construction Co. in the early 1980s [208] which had a controllable tip, also Denmark's Nibe A turbine and Envision two-bladed partial-pitch turbine installed in Thyborøn in 2012. Regarding patents, US Patent US20120288371A1 [209] outlines a partial pitch turbine and control strategy that helps to mitigate loads on the blade root and achieve a more stable power curve. Another US Patent, US9732730B2 [210], discloses the design of a double-pitch turbine resting on a floating foundation. Similarly, German Patent DE 917540 [211] revealed a partial-pitch wind turbine rotor capable of producing power at nominal levels over a defined wind speed range. These advancements in rotor blade design and control mechanisms indicate the continuous evolution of innovative approaches to enhance wind turbine performance and efficiency.

1.2 Gap Areas and Motivation

The review of the present state-of-art on modeling the dynamics of HAWT is presented in §1.1.1. The aerodynamic and other environmental loads (i.e., gravitational, seismic, and hydrodynamic) cause significant vibration. The energy loss produced by friction and blade oscillation affects the power efficiency of a wind turbine. It also damages the blade, necessitating frequent maintenance. Therefore, high-fidelity modeling and analysis are essential for the safe and long-term operation of any horizontal-axis wind turbine. In general, the aeroelastic behavior of composite turbine blades can be complex and requires detailed investigation before implementation. Although numerous studies were carried out in the recent past to develop modeling techniques for bending-torsionally coupled rotors, it has remained an open problem. The state-of-art in §1.1.1 indicates that while high-fidelity aero-servo-elastic modeling and design of wind turbine blades, including bend-twist coupling, have been significantly advanced by models such as Siemens-Gamesa's BHawC [212] and DTU's HAWC2 [213], there remains room for further development in integrating these capabilities into other multi-body dynamic frameworks with lesser DOFs. Also, efficient blade design to reduce structural stresses on the turbine has always been an open problem for researchers. Several studies were focused on maximizing the flutter speed of turbine blades using bending-torsion coupling. As a matter of fact, flutter is not critical under normal operating conditions for an optimally designed rotor. In this context, modern wind turbines have increasingly integrated these techniques to enhance blade performance under normal operating conditions and other modes that risk resonance-induced vibrations. Extreme loads can occur under fault conditions, as outlined in IEC-specific design load cases (e.g., DLC2.1, DLC2.4, and DLC6.1 and DLC6.2 for edgewise extreme loads) and through the extrapolation of loads over long-term operation [214]. However, the present study focuses on optimizing the fibre orientations of blade skin to maximize the beneficial twist-to-feather coupling mechanism for improved dynamic performance of the horizontal axis wind turbine blade under normal operations.

The literature on various methods to model soil-structure interaction and dynamics of monopile-supported offshore turbines are presented in §1.1.2. The literature review clearly shows the importance of incorporating the effect of soil-structure interaction and its coupling with other turbine DOFs in terms of fatigue design and long-term behavior analysis of monopile-supported offshore wind turbines. These studies use models which can be broadly classified into two major subgroups - (i) static or quasi-static analysis with soil springs, where the turbines and blades are lumped at the tower-top, and (ii) dynamic analysis using software, e.g. FAST [76], Bladed [215], 3DFloat [216], HAWC2 [213]. Since monopile fatigue analysis depends on stress reversal, the first category models have inherent limitations as they do not consider blade dynamics. Although blade and drivetrain dynamics are modeled in the software, they have scope for further improvements for more accurate modeling with SSI in the multi-body dynamic framework. Similarly, existing models of deep-water offshore turbines don't consider bending-torsion coupling in blades and its intricate interaction with other turbine components. Also, the existing models are incapable of implementing advanced control algorithms and devices to investigate their effectiveness in mitigating structural vibrations and power fluctuations. With this in mind, this study aims to model the dynamics of the HAWT system in a multi-body dynamic framework using Kane's method [12]. Here, the model proposed by Jonkman et al. [13] and Sarkar et al. [199] is further improved to include bending-torsion coupling in blades, soil-structure interaction in monopile, and the intricate coupling between different turbine DOFs under various environmental loads. The model is also capable of incorporating advanced control strategies for several turbine components and asses their performance through time-history simulation.

The literature review presented in §1.1.5 outlines the evolution of different control devices used to mitigate the vibrations of several turbine components as well as power fluctuations in the generator. These studies showed that tuned mass dampers, in general, offered impressive performance in both passive and active/semi-active modes. Due to these reasons, it is one of the most widely explored devices in the industry. With the improvement of actuators, active controllers using various optimization strategies were extensively investigated. In this context, estimating optimal control forces in real-time offers several challenges, particularly for a system whose coefficient matrices are time-dependent. The problem becomes complicated if the system is exposed to an input with time-varying frequency content, e.g., an earthquake. Although previous researchers developed the wavelet-LQR technique, their treatment of the LQR algorithm had some heuristic approximation. For example, time-varying system matrices were arbitrarily replaced by constant values in the LQR format over a finite time horizon without appropriately modifying the objective function and associated Riccati equation. These proposals of wavelet-based LQR algorithm did not account for time-varying system matrices and used an approximate value of these matrices while estimating the optimal control force. Moreover, the objective function over a finite time window ignored the terminal boundary conditions leading to an approximate Algebric Riccati Equation (ARE). Therefore, the control was not optimal in the true sense and offered the scope for further development. Due to this reason, tuning an active mass damper in the wavelet-LQR framework has remained an open problem for vibration control of wind turbine towers.

The literature presented on offshore turbines clearly outlines that spar-type floating turbines have proved themselves as a viable option for deep-sea wind farms. The availability of strong wind for longer duration in the marine environment makes them more profitable in the long run. However, they are exposed to a significant level of vibration due to the combined action of aero-hydrodynamic loads. The review clearly outlines the need for vibration control of a floating wind turbine tower under different operational conditions. In this context, previous studies have proposed different strategies for vibration control, but it has remained an open problem. In this context, STC shows promising results in terms of power generation due to wave energy conversion. However, STC, in its present form, does not offer significant vibration control. This motivates to investigate the design of a spar-type floater by modifying the torus to act as a vibration isolator to mitigate tower vibrations in deep water offshore turbines.

The literature review presented on the available pitch control strategies outlines the need for robust vibration control of wind turbine rotors and power fluctuations. All these studies on blade pitch control were aimed at load reduction and improving power production. The control strategies varied from simple Single-Input Single-Output (SISO) PI controllers to advanced Multiple-Input Multiple-Output (MIMO) controllers utilizing fuzzy logic or model predictive control. However, these strategies often encounter a trade-off between power production and structural load reduction due to conflicting requirements [199]. Also, previous studies have employed simplified models for blades and towers, limiting the accuracy of their findings [198, 217]. Furthermore, developing control strategies for offshore wind turbines poses additional challenges, as the stability of the entire system, including platform roll and pitch, must be considered. Moreover, large rotors experience bending-torsion coupling, further complicating the analysis and controller design. Although previous studies developed different strategies for this purpose, issues related to power fluctuation and blade vibration control have continued to persist. In this context, a double-pitch rotor offers promising results in terms of power regulation, actuator demand, and structural vibration control. Despite the fact that tip-controlled blades have significant potential benefits, there has been limited research dedicated to exploring their advantages. Specifically, there is a lack of in-depth investigation into vector approach-based high-fidelity multi-body dynamic modeling incorporating bending-torsion coupling. Modeling the complex interactions between blade bending and torsional deformations, which is unavoidable in ultra-large flexible rotors, is essential to simulate tip-controlled blades' behavior accurately. Besides accurate modeling, comprehensive performance analysis and optimal design for double-pitched rotors offer different challenges, which motivates the present study. Moreover, the optimal tuning of the pitch angles for double-pitched rotors suitable for time-varying systems like floating wind turbines has not been investigated before. Given these gaps in the existing research, the objectives of the present study are identified below.

1.3 Objectives

The outlined gap areas distinctly highlight the scope of research concerning the modeling, fatigue analysis, and vibration control of wind turbine components, including towers, blades, drive-trains, and support structures, across various operating scenarios. This underscores the imperative for continued investigation into this field to devise more effective engineering solutions. The dynamic analysis of wind turbine blades under bending-torsion coupling and aerodynamic pitching moment is of utmost importance to be included in the mathematical model. Although prior research has successfully incorporated bend-twist coupling in blade modeling using advanced aerodynamic models with high degrees of freedom and in Lagrangian framework [213], the challenge of combining this with complete system modeling in a vector approach-based multi-body dynamic framework, particularly for aero-servo-elastic simulations, continues to be an area of active research. The present work builds on prior efforts [217, 218] by the addition of the bending-torsion coupling in the blades, soil-structure interaction in monopile foundations, active and passive TMD for onshore turbine's tower vibration control, floating turbine along with its control, and blade-pitch control systems with different control options for both cases (single-pitch system and partial-pitch system). It is the primary motivation behind the present work to meet the following objectives

- Develop a combined model of a horizontal axis wind turbine (i.e., blade, drive-train, and tower) in a multi-body dynamic framework considering elastic and dynamic bending-torsion coupling. For this purpose, Kane's approach is proposed to be adopted in this study, where the effects of different pitch angles, yaw angles, and generator torque controllers are included in the modeling.
- Study the coupled behavior over the complete operating range of the turbine. Identify different effects

(both beneficial and adverse) of these coupling and highlight their impact on the design and safety of the turbine blades.

- Conduct multi-objective optimization considering bending-torsion coupling to minimize the peak dynamic responses of different turbine DOFs to find the Pareto optimal distribution of the composite fibre orientation angle in the blade skin.

The literature review explicitly underscores the significance of incorporating fatigue design and analyzing the long-term behavior of monopile-supported shallow water offshore wind turbines with a focus on Soil-Structure Interaction. While previous software models have addressed blade and drivetrain dynamics, there remains a substantial opportunity for refinement. Enhancing accuracy through more sophisticated modeling of SSI within a multi-body dynamic framework, especially with effective integration with other turbine components, is a clear avenue for further development. Thus, the following objectives are proposed to be investigated

- Develop a multi-body dynamic model of a monopile-supported offshore wind turbine considering soil-structure interaction, where all the states are integrated as a tightly coupled system. Multiple soil layers are proposed to be characterized by their respective non-linear load-deformation curves. The dynamic equilibrium equations are developed following Kane's approach, where Winkler's beam formulation models the soil-pile interaction.

- Investigate the impact of generalized stress-based formulation for fatigue design using the 3D multi-body dynamic model and compare it with a moment-based approach. For this purpose, estimate the longitudinal stress at different locations from the bi-directional bending moment and axial force acting on the monopile foundation.

- Once the stress-based cycle counts are ready, the short-term damage in each load case and its accumulation over the design life are estimated to find the fatigue life. The damage-equivalent stress is proposed to be evaluated, which is useful for the load test of monopiles.

- Finally, the long-term serviceability of the combined system at the mudline is proposed to be investigated, followed by the sensitivity analysis for various parameters, e.g. diameter, thickness, and water depth. The study suggests the site-specific design curves that help the planning and foundation design of similar systems.

Regarding the mitigation of seismic responses in onshore wind turbine towers, optimizing an active mass damper within the wavelet-LQR framework continues to be an unresolved issue. With this in view, tower vibration control in its two orthogonal directions under extreme conditions (i.e., the combined action of wind and earthquake) is proposed to be addressed in this paper. A modified wavelet-LQR-based gain scheduling considering the frequency content of the input and feedback is proposed here. As a result, the aims of this work are as follows

- Develop a multi-body dynamic model of an onshore wind turbine considering aero-servo-elastic coupling with an active TMD attached to the nacelle. Kane's [12] approach is adopted to model the dynamics of the combined system with wind and seismic excitation.

- Develop a modified optimal wavelet-LQR control strategy for gain scheduling using frequency-dependent weight matrices for a time-varying system by solving the differential Riccati equation in backward translation. In this algorithm, the frequency content of the feedback is analyzed using continuous wavelet transformation, where the Morse wavelet is used as the basis function for gain-scheduling in the time-frequency domain.

- Compare the effectiveness of the proposed tuning of ATMD with classical LQR-based ATMD available in the literature. A sensitivity analysis is planned to study the performance envelope under different wind speeds and seismic loading covering the complete operational spectrum of a benchmark turbine.

On the other hand, the primary source of vibration in deep water offshore wind turbines stems from the combined effects of aerodynamic and hydrodynamic forces. In this scenario, STC demonstrates the potential for enhancing power generation through wave energy conversion. Nonetheless, the current iteration of STC falls short in providing effective vibration mitigation. This gap prompts an exploration into redesigning the spar-type floater, with modifications to the torus, to serve as a vibration isolator. Thus, the key objectives of this study are as follows

- Develop the concept of a modified spar-torus combination by introducing spring and dashpot for wave load isolation to improve the dynamics of spar-type floaters. This spring and dashpot in between spar and torus have the potential to isolate hydrodynamic loads from the spar, thereby, reducing its response significantly. The energy is dissipated as the torus is allowed to vibrate in the surge (i.e. along wind) and sway (i.e. side-to-side). As the wave loads are higher near the surface, an adequately designed torus is bound to provide significant vibration control, particularly under wind-wave misalignment.

- Formulate a detailed mathematical model using Kane's approach for a modified spar-torus combination attached to the mooring cables. This multi-body dynamic framework helps to reduce the degrees of freedom to its minimum while modeling the highly non-linear system of a floating turbine assembly.

- Demonstrate the performance of the proposed modified spar-torus combination under the different operational scenarios in the marine environment to examine its performance envelope, particularly in sway (i.e. side-to-side) direction, which is one of the main objectives of this work.

The literature review highlights the importance of robust pitch control for wind turbines. Despite previous research proposing various strategies, vibration control remains a persistent issue. One promising approach is the use of double-pitch rotors, which offer benefits in terms of vibration control, actuator demand, and power regulation. However, existing models for double-pitched turbines have many assumptions and limitations. Hence, a double-pitched system in its current form (both modeling and control strategy) needs further improvements for optimal performance. It motivates the present study to look into its analysis and design by developing a high-fidelity model with bending-torsion coupling. The study also aims to address multi-objective optimal control under different operating scenarios for onshore wind turbines whose major contributions are listed below.

- Develop a multi-body dynamic model of a horizontal axis wind turbine (blade, drive-train, and tower) with a double-pitched rotor considering dynamic bending-torsion coupling. In this study, Kane's approach is proposed for response simulation with different pitch angles at the rotor base and tip.

- Develop a centralized PID control algorithm and optimize its parameter (i.e. gain scheduling for two different pitch angles) using multiple objective functions based on rotor speed fluctuation and blade vibration under turbulent wind flow.

- Demonstrate the performance of the proposed PID control strategy under different conditions and investigate its sensitivity in mitigating power fluctuation and vibration control over the complete operating range of the turbine.

- Develop a centralized LQR control algorithm and optimize the control parameters for two different pitch angles using an objective function that minimizes rotor speed fluctuation and vibrations of the different structural components under the turbulent wind flow.

- Demonstrate the performance of the proposed LQR control strategy under different flow conditions. Investigate the sensitivity of the proposed control scheme, especially in mitigating structural vibrations, actuator demand, and rotor speed fluctuations (subsequently power generation), which are the primary goals of this study.

The complexity of a double-pitched rotor system increases when the system is subjected to inputs with time-varying frequency content, such as wind-wave interaction in the deep-water offshore environment. Besides structural modeling, pitch control plays a vital role in any modern offshore turbine. While previous studies have developed the wavelet-LQR technique, their treatment of the LQR algorithm in the wavelet domain adopts heuristic approximations. Consequently, optimal vibration control for a double-pitched rotor within the wavelet-LQR framework remains an open challenge. This motivates the present study to develop a high-fidelity model for double-pitched offshore turbines. The study also aims to design an optimal wavelet-LQR control strategy for different operating conditions. Thus, the objectives of this work are as follows

- Develop a detailed multi-body dynamic model of an offshore spar-type horizontal axis wind turbine (including blade, drive-train, tower, and spar). Introduce a double-pitched rotor, where the coupling between bending and torsion degrees of freedom is considered. The formulation is prepared to adopt Kane's approach while modeling the complex multibody system.

- Design an optimal wavelet-LQR control strategy for the double-pitched rotor, which is first introduced in this work. It involves frequency-dependent optimal gain-scheduling for two different pitch angles of the rotor. Propose, a modified wavelet-LQR based gain scheduling approach, incorporating optimal weight matrices and considering the frequency content of the feedback signal. An objective function aims to minimize rotor speed fluctuation and reduce the vibration of different structural components subjected to turbulent wind-wave loading.

- Assess the performance of the proposed control scheme in terms of mitigating structural vibrations of different components (e.g., blades and spar), reducing actuator demand, and minimizing rotor speed fluctuations (and, therefore, optimizing power generation) over the operating range (i.e., rated to cut-out condition) of the controller.

1.4 Organization of the Thesis

This thesis aims to develop an efficient multi-body dynamic model of a Horizontal Axis Wind Turbine with aero-servo-elastic coupling and subsequently use the model for fatigue analysis and control design of various turbine components for both onshore and offshore environments. An overview of the work is presented in this chapter, followed by a literature review covering their modeling, multi-body dynamics, simulation of loads, and vibration control mechanisms for various components. In this context, the structure of the rest of the thesis is detailed as follows

- In the 2nd Chapter, the multi-body dynamic model of onshore horizontal axis wind turbines is developed considering bending-torsion coupling in blades. The aero-elastic modeling of aerodynamic and seismic forces is also discussed in this chapter. The baseline control systems are also included in the modeling. Following this, the responses of a benchmark wind turbine are simulated using the model and validated against FAST and HAWC2 simulations. Finally, an innovative approach to designing the composite fibre angles in the blade skin is presented in light of the beneficial use of the bending-torsion coupling.

- The 3rd Chapter discusses the modeling of monopile-supported shallow water offshore turbines considering the effect of SSI. The model is subsequently validated with FAST. The developed model is further used to analyze short-term and long-term stress-reversal effects in monopile design and finally propose a site-specific fatigue design curve for their improved service life.

- The 4th Chapter extends the multi-body dynamic model to the deep-water offshore case. A spar-type floating offshore turbine is modeled in Kane's framework considering the rigid body displacements and rotations of its platform. The hydrodynamic and mooring forces associated with the offshore turbine are also modeled here. The time-history responses from the model are validated with benchmark responses obtained from FAST.

- In the 5th Chapter, the focus is given on controlling the tower vibration of onshore wind turbines with the help of a bi-directional active TMD installed in the nacelle. The mathematical model was subsequently modified to include the effect of the additional component (i.e., TMD) in the dynamic response of the system. Furthermore, these dynamic responses are also validated with responses obtained from FAST. The active TMD is designed with the help of a traditional LQR algorithm and a novel wavelet-based LQR algorithm to further improve its performance. Subsequently, the performance of the TMD in both passive and active operational modes is showcased through its capacity to mitigate tower vibration under seismic loading. Finally, a series of sensitivity analyses are conducted to illustrate the operational range and effectiveness of the proposed control mechanism.

- Chapter 6 investigates the performance of a proposed modified torus in controlling the tower and platform motions of a spar-type offshore wind turbine. The modified torus is connected to the spar with the help of springs and dashpots to effectively isolate the wave loads near the ocean surface. A complete sensitivity analysis is carried out to find out the performance envelope and parameter sensitivity of the proposed Modified Spar-Torus Combination (MSTC).

- Power regulation and Vibration control of onshore wind turbines with the help of double-pitched rotor is discussed in chapter 7. A detailed mathematical model of a double-pitched rotor-based onshore turbine with bending-torsion coupling in blades is presented here. The control mechanism for the two different pitch angles is designed with a multi-objective optimal PID algorithm and a weight-optimized

LQR algorithm to enhance its performance further. The enhanced performance envelope of the double-pitched rotor over its traditional single-pitch counterpart is analyzed for the complete operating range of the turbine.

- Based on the development of Chapter 7, the model of the double-pitched onshore turbine is further extended to deep-water offshore turbines in the 8^{th} Chapter. The effects of wind-wave interaction and the rigid body motions of the spar introduce time-dependent system matrices in the design of the controller. Hence, a wavelet-based gain scheduling is proposed for the weight-optimized LQR controller of the double-pitch system to counter the time-frequency content of the disturbance. The effectiveness and the performance envelope of the proposed control are studied in this chapter as well.

- Lastly, Chapter 9 wraps up with a concise discussion on the significant contributions of this study and potential directions for future research.

- An appendix is provided at the end with the relevant matrices used in the modeling to transform vectors between different coordinate systems.

Chapter 2

Multi-Body Dynamic Model of Onshore Wind Turbine with Bending-Torsion Coupling in Blades

2.1 Introduction

Modern wind turbines, being a significant source of renewable energy, have also evolved with bigger sizes and more power ratings to keep up with the ever-increasing demand. The blades of these turbines are large and flexible, constructed using materials with a high strength-to-weight ratio to retain their aerodynamic performance. They also undergo excessive deformation under turbulent wind, and hence, their design demands precise modeling and analysis to capture minute structural behavior. These blades are generally made of composite layups with cambered airfoil sections, which induce elastic and dynamic coupling between bending and torsional modes. In addition to these phenomena, the aerodynamic pitching moment also arises due to the offset of the blade pitch axis from the aerodynamic centre. With this in mind, this chapter focuses on developing a computationally efficient complete multi-body dynamic aero-servo-elastic model of an onshore horizontal axis wind turbine, including bending-torsion coupling and aerodynamic pitching moment. The mathematical model also includes different control systems found in commercial turbines (e.g., torque and pitch controllers). The 3D wind field is generated for turbulent flow, and the Blade Element Momentum (BEM) theory is used to model the aerodynamic forces. The responses of the coupled system are solved under different operational scenarios, which signify the impact of the aforementioned coupling. It is found to be particularly detrimental at higher wind speeds than the rated value. However, proper design and implementation of structural layup can enhance the aerodynamic performance of the blade. Finally, the optimal design of composite fibre orientation of a benchmark turbine blade is investigated to show its beneficial effects in load/response mitigation.

2.2 Mathematical Model

This section focuses on modeling an onshore horizontal-axis wind turbine in a multi-body framework. It comprises a tower, drive-train, and blades, as shown in Fig. 2.1, that are modeled independently and merged to form the combined system. The deformed shape of the turbine is described using 22 degrees of freedom (Degrees of Freedom (DOFs)), which are given by

$$\mathbf{u} = [\underbrace{u_1, ...u_3,}_{Base} \underbrace{u_4, ...u_7,}_{Tower} \underbrace{u_8,}_{Nacelle} \underbrace{u_9, u_{10},}_{Drive-train} \underbrace{u_{11}, ...u_{22}}_{Blades}]^T \tag{2.1}$$

The rotation at the base is not considered as the turbine modelled here is supported on a rigid foundation. As a result, the DOFs 1,2,3 in Eq. 2.1 indicate translational boundary conditions to accommodate seismic ground motions. The tower vibration is represented by the first two modes in its fore-aft and side-to-side

Table 2.1: Details of DOFs

Multibody Names	Components	DOFs	Local Coordinate	Remarks
Tower Base	Fore-aft translation	u_1	-	-
	Side-to-side translation	u_2	-	-
	Heave translation	u_3	-	-
Tower	1^{st} Fore-aft mode	u_4	$\hat{a}$	Tower global
	1^{st} Side-to-side mode	u_5	$\hat{b}$	Tower top
	2^{nd} Fore-aft mode	u_6	$\bar{b}$	Tower element fixed system
	2^{nd} Side-to-side mode	u_7		
Nacelle	Nacelle yaw	u_8	$\hat{c}$	Yaw
Drive-train	Generator azimuth	u_9	$\hat{d}$	Slow speed shaft tilt and skew
	Shaft torsional DOF	u_{10}	$\hat{e}$	Rotating slow speed shaft
Blade 1	1^{st} Flap mode	u_{11}	$\hat{f}_1$	Global
	1^{st} Edge mode	u_{12}	$\hat{g}_1,\hat{h}_1,\hat{i}_1$	Cone, Centroidal, Twist
	2^{nd} Flap mode	u_{13}	$\tilde{b}_1$, $\hat{a}_{e1}$	Element fixed system
	1^{st} Torsional mode	u_{14}		
Blade 2	1^{st} Flap mode	u_{15}	$\hat{f}_2$	Global
	1^{st} Edge mode	u_{16}	$\hat{g}_2,\hat{h}_2,\hat{i}_2$	Cone, Centroidal, Twist
	2^{nd} Flap mode	u_{17}	$\tilde{b}_2$, $\hat{a}_{e2}$	Element fixed system
	1^{st} Torsional mode	u_{18}		
Blade 3	1^{st} Flap mode	u_{19}	$\hat{f}_3$	Global
	1^{st} Edge mode	u_{20}	$\hat{g}_3,\hat{h}_3,\hat{i}_3$	Cone, Centroidal, Twist
	2^{nd} Flap mode	u_{21}	$\tilde{b}_3$, $\hat{a}_{e3}$	Element fixed system
	1^{st} Torsional mode	u_{22}		

directions, i.e., the following four DOFs. The nacelle yaw, drive-train torsion, and generator azimuth (i.e., slow-speed shaft) are modeled by a single degree of freedom for each of them. Finally, two flapwise, one edgewise, and one torsional mode are considered to simulate each blade. The details of these DOFs for different components are shown in Table 2.1.

The equations of motion are formulated by Kane's approach [12] using the kinematics of each component. The fixed global reference frame $\hat{x}$ for the complete system lies at the tower base. Besides this inertial frame, each component has its own global and local coordinates, as mentioned in Table 2.2. The positions of these coordinate systems are also shown in Fig. 2.1. One coordinate system can be converted to another using appropriate transformation [13], which is given in the Appendix.

The position vectors of each deformed component are specified using appropriate DOFs and coordinate systems to quantify their relative linear and angular velocities and accelerations. These are used to model various forces operating on each component as per Newton's law. Once the internal and external forces are determined, the equation of motion for the given holonomic multi-body dynamic system appears as [14,219]

$$\mathbf{F_i} - \mathbf{F_i^*} = 0 \quad for \quad i = 1, 2, ..., n \tag{2.2}$$

In the above equation, n represents the total number of DOFs (i.e., $n = 22$ in this case). $\mathbf{F_i}$ and $\mathbf{F_i^*}$ represent the generalized active and inertia forces, respectively. The generalized active forces in a N body dynamic

Components	Coordinate Systems	Representation	Origin	Remarks
Tower	Tower base	$\hat{a}$	Intersection of centre of tower base and platform support	Translates with platform
	Tower top	$\hat{b}$	On yaw axis at top of tower	Moves with the tower but does not yaw
	Tower element	$\bar{b}$	On each tower nodes	Moves with the deformed tower elements
Nacelle	Yaw	$\hat{c}$	Same as $\hat{b}$	Moves with the tower and yaw of nacelle
Drive-train	Slow-speed Shaft	$\hat{d}$	Intersection of rotor axis and $\hat{c}_2$-$\hat{c}_3$ plane of nacelle coordinate system	Skews and tilts with the shaft but does not spin with rotor
	Azimuth	$\hat{e}$	Same as shaft coordinate system	Spins with rotor
Blade	Global	$\hat{f}_k$	At blade roots	Spins with rotor
	Coned	$\hat{g}_k$	Same as $\hat{f}_k$	Cones with blade
	Pitched	$\hat{h}_k$	Same as $\hat{f}_k$	Pitches with blade
	Twisted	$\hat{i}_k$	On each blade nodes	Twisted with blade's structural twist
	Blade-element	$\tilde{b}_k$	Same as $\hat{h_k}$	Moves with the deformation of blade elements
	Aerodynamic	$\hat{a}_{ek}$	Same as $\hat{h_k}$	Used to calculate aeroelastic forces on the blades (normal and tangential to the rotor plane)

Table 2.2: Coordinate systems of different components

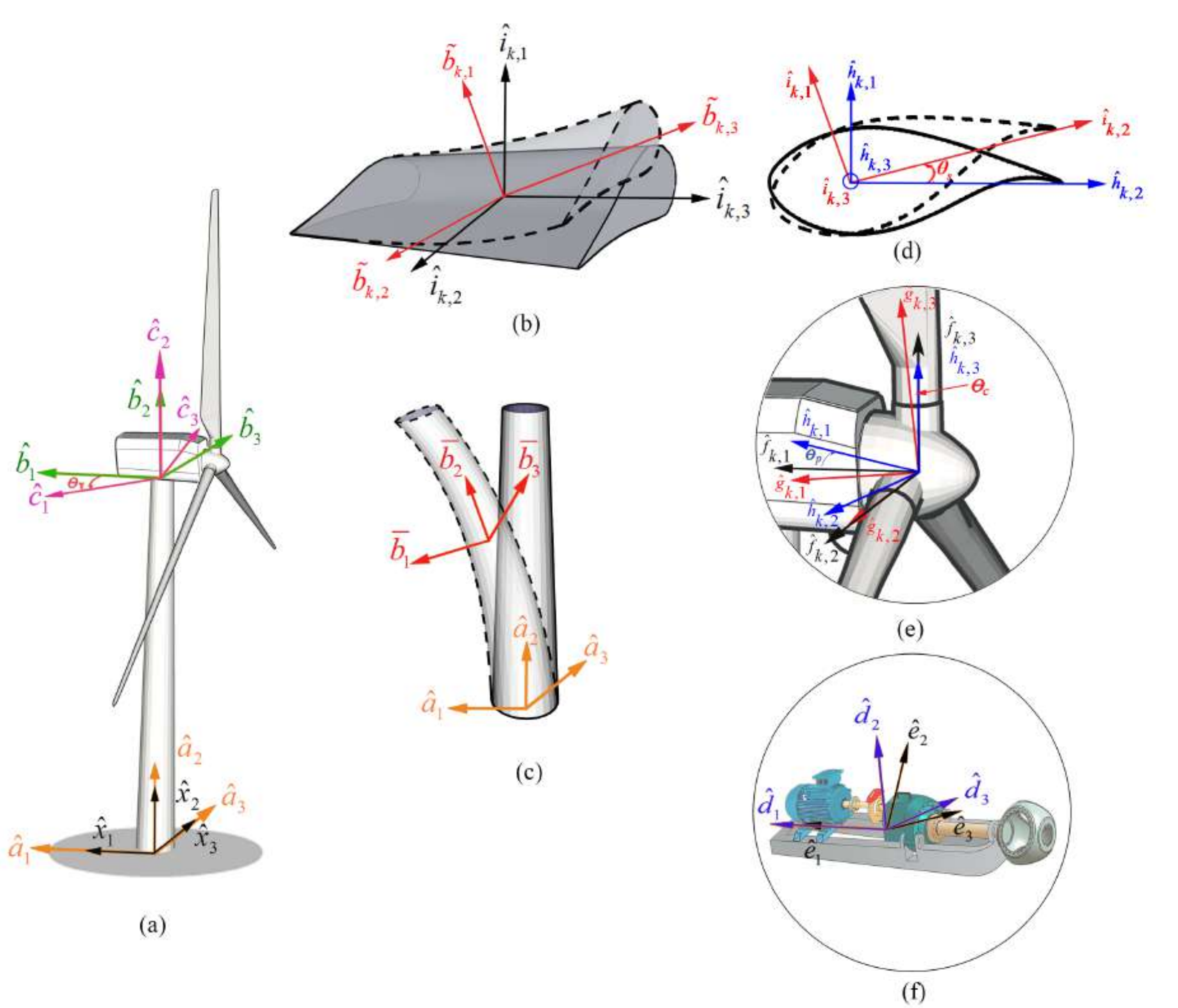

Figure 2.1: Schematic diagram of HAWT and associated coordinates; (a) combined multi-body system, (b) deformed blade element, (c) deformed tower, (d) local twist of blade, (e) cone and pitch & (f) drive-train and TMD

system ($N \neq n$) with a reference frame x_k for each body having the centre of mass at c_k, are given by

$$\mathbf{F_i} = \sum_{k=1}^{N} [\mathbf{v_{i,c_k}}.\mathbf{F_{c_k}} + \omega_{\mathbf{i,x_k}}.\mathbf{M_{x_k}}] \tag{2.3}$$

where $\mathbf{v_{i,c_k}}$ and $\omega_{\mathbf{i,x_k}}$ are partial linear and angular velocities, respectively, at the centre of mass of the k^{th} body. The external active forces and moments operating at c_k are represented by $\mathbf{F_{c_k}}$ and $\mathbf{M_{x_k}}$, respectively, in the above equation. Likewise, the generalized inertial force in Eq. 2.2 can be defined as

$$\mathbf{F_i^*} = \sum_{k=1}^{N} \left[\mathbf{v_{i,c_k}}.(m_k \mathbf{a_{c_k}}) + \omega_{\mathbf{i,x_k}}.(\bar{\mathbf{I}}_\mathbf{k}.\alpha_{\mathbf{x_k}} + \omega_{\mathbf{x_k}} \times \bar{\mathbf{I}}_\mathbf{k}.\omega_{\mathbf{x_k}})\right] \tag{2.4}$$

The generalized mass and moment of inertia dyadic of the k^{th} body are defined by m_k and $\bar{\mathbf{I}}_\mathbf{k}$, respectively, in the preceding equation. Total linear and angular velocities at c_k are represented by the sum of different partial velocities in this formulation, i.e.,

$$\mathbf{v_{c_k}} = \sum_{i=1}^{n} \mathbf{v_{i,c_k}}.q_i + \mathbf{v_{t,c_k}} \tag{2.5a}$$

$$\omega_{\mathbf{x_k}} = \sum_{i=1}^{n} \omega_{\mathbf{i,x_k}}.q_i + \omega_{\mathbf{t,x_k}} \tag{2.5b}$$

Thus, total velocity (i.e., linear and angular) has two significant components. The partial velocity (i.e., $\mathbf{v_{i,c_k}}$ or $\omega_{\mathbf{i,x_k}}$), which can be written as a linear summation, is the first part on the right-hand side. The remaining component (i.e., $\mathbf{v_{t,c_k}}$ or $\omega_{\mathbf{t,x_k}}$), on the other hand, is the partial velocity that does not obey superposition. In this formulation, q_i is the generalized speed, which is considered to be the first differential of DOF u_i with respect to time, i.e., $q_i = \dot{u}_i$ [12]. Using these descriptions of partial velocities, the following formulae can be derived for the total linear and angular accelerations of the k^{th} body

$$\mathbf{a_{c_k}} = \sum_{i=1}^{n} \left[\mathbf{v_{i,c_k}}.\ddot{u}_i + \frac{d}{dt}\left\{\mathbf{v_{i,c_k}}\right\}.\dot{u}_i \right] + \frac{d}{dt}\left\{\mathbf{v_{t,c_k}}\right\} \tag{2.6a}$$

$$\alpha_{\mathbf{x_k}} = \sum_{i=1}^{n} \left[\omega_{\mathbf{i,x_k}}.\ddot{u}_i + \frac{d}{dt}\left\{\omega_{\mathbf{i,x_k}}\right\}.\dot{u}_i \right] + \frac{d}{dt}\left\{\omega_{\mathbf{t,x_k}}\right\} \tag{2.6b}$$

It may be noted that the total accelerations (both linear and angular) in Eq. 2.6 have the same format as in Eq. 2.5. The governing equation of motion for the complete multi-body system in its global reference frame can be determined once the position vectors, velocities, and accelerations are modeled. The tower (tw), nacelle (na), generator (gn), low-speed shaft (ls), hub (hu), yaw bearing (yb), and three blades (b_k) make up the entire wind turbine structure. Therefore, $c_k = \{tw, na, hu, gn, ls, yb, b_1, b_2, b_3\}$ represents the two-letter acronym for the centre of gravity of these subsystems. Except for the low-speed shaft and yaw bearing (which move very slowly), each component contributes to the generalized inertia force. As a result, the total generalized inertia force can be expressed using the following equation

$$\begin{aligned}\mathbf{F_i^*} =& \mathbf{F^*_{i,tw}} + \mathbf{F^*_{i,na}} + \mathbf{F^*_{i,hu}} + \mathbf{F^*_{i,gn}} \\ &+ \cancelto{0}{F^*_{i,ls}} + \cancelto{0}{F^*_{i,yb}} + \mathbf{F^*_{i,b_1}} + \mathbf{F^*_{i,b_2}} + \mathbf{F^*_{i,b_3}}\end{aligned} \tag{2.7}$$

The generalized active force, which includes both internal and external conservative and non-conservative forces, acts on each sub-system in addition to the generalized inertia force in Eq. 2.7. Hence, elastic (el), damping (d), aeroelastic (ae), gravitational (gv), generator (gn), brake (br), and seismic (eq) forces can be modelled as

$$\begin{aligned}\mathbf{F_i} =& \mathbf{F_{i,tw,el}} + \mathbf{F_{i,b_1,el}} + \mathbf{F_{i,b_2,el}} + \mathbf{F_{i,b_3,el}} + \mathbf{F_{i,ls,el}} + \mathbf{F_{i,yb,el}} + \mathbf{F_{i,tw,d}} + \mathbf{F_{i,b_1,d}} \\ &+ \mathbf{F_{i,b_2,d}} + \mathbf{F_{i,b_3,d}} + \mathbf{F_{i,ls,d}} + \mathbf{F_{i,yb,d}} + \mathbf{F_{i,tw,ae}} + \mathbf{F_{i,b_1,ae}} + \mathbf{F_{i,b_2,ae}} + \mathbf{F_{i,b_3,ae}} + \mathbf{F_{i,tw,gv}} \\ &+ \mathbf{F_{i,na,gv}} + \mathbf{F_{i,hu,gv}} + \mathbf{F_{i,b_1,gv}} + \mathbf{F_{i,b_2,gv}} + \mathbf{F_{i,b_3,gv}} + \mathbf{F_{i,gn}} + \mathbf{F_{i,br}} + \mathbf{F_{i,eq}}\end{aligned} \tag{2.8}$$

Finally, the governing equation of motion can be obtained by substituting Eq. 2.7 and Eq. 2.8 into Eq. 2.2 and rearranging them in matrix form, which leads to the following equation

$$[\mathbf{M(u,t)}].\{\ddot{\mathbf{u}}\} + \left\{\bar{\mathbf{F}}(\dot{\mathbf{u}},\mathbf{u},\mathbf{t})\right\} = 0 \tag{2.9}$$

The inertial components form the mass matrix $[\mathbf{M(u,t)}]$ in the above equation. The remaining part, i.e., $\left\{\bar{\mathbf{F}}(\dot{\mathbf{u}},\mathbf{u},\mathbf{t})\right\}$ incorporates stiffness and damping besides externally applied forces. The complete derivation of each component in Eq. 2.9 for various subsystems is presented step-by-step in the following subsections.

2.2.1 Tower

The motion of the tower is derived from its base. The position vector r_{t_b} at the tower base t_b with respect to reference frame $\hat{x}$ is given by

$$\mathbf{r_{t_b}} = u_1.\hat{x}_1 - u_2.\hat{x}_3 + u_3.\hat{x}_2 \tag{2.10}$$

The linear velocity at t_b can be obtained by differentiating the position vector, i.e.,

$$\mathbf{v_{t_b}} = \dot{u}_1.\hat{x}_1 - \dot{u}_2.\hat{x}_3 + \dot{u}_3.\hat{x}_2 \tag{2.11}$$

Using the definition of generalized speed and rearranging Eq. (2.11) in the format of Eq. (2.5a) reveals that the terms not following linear superimposition is zero, i.e., $v_{t,t_b} = 0$ and the remaining components are given by

$$\mathbf{v_{i,t_b}} = \begin{cases} \hat{x}_1 & \text{for } \ i = 1 \\ -\hat{x}_3 & \text{for } \ i = 2 \\ \hat{x}_2 & \text{for } \ i = 3 \end{cases} \tag{2.12}$$

As no rotation is considered at the tower base, the total and partial angular velocities are zero. The tower is modeled as a hollow tapered flexible cantilever beam with distributed mass, stiffness, and cross-sectional characteristics. For this system, the following expression defines the position vector of a point at a height h from the base.

$$\begin{aligned} \mathbf{r_{tw}(h)} = & [\phi^{FA}_{1,tw}(h).u_4 + \phi^{FA}_{2,tw}(h).u_6].\hat{a}_1 + [h - 0.5\,\{S^{FA}_{1,1;tw}(h).u_4^2 \\ & + S^{FA}_{2,2;tw}(h).u_6^2 + 2S^{FA}_{1,2;tw}(h).u_4.u_6 + S^{SS}_{1,1;tw}(h).u_5^2 + S^{SS}_{2,2;tw}(h).u_7^2 \\ & + 2S^{SS}_{1,2;tw}(h).u_5.u_7\,\}].\hat{a}_2 + [\phi^{SS}_{1,tw}(h).u_5 + \phi^{SS}_{2,tw}(h).u_7].\hat{a}_3 \end{aligned} \tag{2.13}$$

The elements $\{.\}$ in the coefficient of $\hat{a}_2$ represents height contraction owing to bending in two modes [i.e., $\phi^{(.)}_{i,tw}$], where the superscripts FA and SS represent fore-aft and side-to-side directions, respectively. The term $S^{(.)}_{i,j,tw}(h)$ in Eq. 2.13 come from the i^{th} and j^{th} mode shapes [i.e., $\phi^{(.)}_{i,tw}$ and $\phi^{(.)}_{j,tw}$, respectively], which represent the axial shortening of the tower due to bi-axial bending [13] and can be expressed by the following equations

$$S^{FA}_{i,j;tw}(h) = \int_0^h \left[\frac{d\phi^{FA}_{i,tw}(\bar{h})}{d\bar{h}}.\frac{d\phi^{FA}_{j,tw}(\bar{h})}{d\bar{h}}\right] d\bar{h} \tag{2.14a}$$

$$S^{SS}_{i,j;tw}(h) = \int_0^h \left[\frac{d\phi^{SS}_{i,tw}(\bar{h})}{d\bar{h}}.\frac{d\phi^{SS}_{j,tw}(\bar{h})}{d\bar{h}}\right] d\bar{h} \tag{2.14b}$$

where $\bar{h}$ is a dummy variable representing the height of the tower. The total linear velocity at this location (h) may be derived by differentiating its position vector and adding it to the linear velocity at the tower base (v_{t_b}), i.e., $\mathbf{v_{tw}(h)} = \frac{d}{dt}\mathbf{r_{tw}(h)} + \mathbf{v_{t_b}}$. Consequently, the total angular velocity at the same position can be estimated using a small angle approximation, which has the following form

$$\omega_{\mathbf{tw}}(\mathbf{h}) = \left[\frac{d\phi^{SS}_{1,tw}(h)}{dh}.\dot{u}_5 + \frac{d\phi^{SS}_{2,tw}(h)}{dh}\dot{u}_7\right].\hat{a}_1 - \left[\frac{d\phi^{FA}_{1,tw}(h)}{dh}.\dot{u}_4 + \frac{d\phi^{FA}_{2,tw}(h)}{dh}\dot{u}_6\right].\hat{a}_3 \tag{2.15}$$

Here, it may be noted that total linear and angular velocities can be expressed in the same format as in Eq. 2.5a and Eq. 2.5b i.e., $\mathbf{v_{tw}(h)} = \sum_{i=1}^{n} \mathbf{v_{i,tw}(h)}.q_i + \mathbf{v_{t,tw}}(h)$ and $\omega_{\mathbf{tw}}(\mathbf{h}) = \sum_{i=1}^{n} \omega_{\mathbf{i,tw}}(\mathbf{h}).q_i + \omega_{\mathbf{t,tw}}(\mathbf{h})$. Clearly, the rigid body components [i.e., $\mathbf{v_{t,tw}(h)}$ and $\omega_{\mathbf{t,tw}}(\mathbf{h})$] are zero. These partial linear and angular velocities can be expressed using the generalized speed q_i, which have the following format

$$\mathbf{v_{i,tw}(h)} = \mathbf{v_{i,t_b}} + \begin{cases} \phi^{FA}_{1,tw}(h).\hat{a}_1 - [S^{FA}_{1,1,tw}(h).u_4 + S^{FA}_{1,2;tw}(h).u_6].\hat{a}_2 & \text{for } \ i = 4 \\ \phi^{SS}_{1,tw}(h).\hat{a}_3 - [S^{SS}_{1,1,tw}(h).u_5 + S^{SS}_{1,2;tw}(h).u_7].\hat{a}_2 & \text{for } \ i = 5 \\ \phi^{FA}_{2,tw}(h).\hat{a}_1 - [S^{FA}_{2,2,tw}(h).u_6 + S^{FA}_{1,2;tw}(h).u_4].\hat{a}_2 & \text{for } \ i = 6 \\ \phi^{SS}_{2,tw}(h).\hat{a}_3 - [S^{SS}_{2,2,tw}(h).u_7 + S^{SS}_{1,2;tw}(h).u_5].\hat{a}_2 & \text{for } \ i = 7 \end{cases} \tag{2.16a}$$

$$\omega_{\mathbf{i,tw}}(\mathbf{h}) = \begin{cases} -\frac{d\phi^{FA}_{1,tw}(h)}{dh}.\hat{a}_3 & \text{for } \ i = 4 \\ +\frac{d\phi^{SS}_{1,tw}(h)}{dh}.\hat{a}_1 & \text{for } \ i = 5 \\ -\frac{d\phi^{FA}_{2,tw}(h)}{dh}.\hat{a}_3 & \text{for } \ i = 6 \\ +\frac{d\phi^{SS}_{2,tw}(h)}{dh}.\hat{a}_1 & \text{for } \ i = 7 \end{cases} \tag{2.16b}$$

Once the partial linear and angular velocities are modeled, they can be further used to compute the total linear and angular accelerations as indicated in Eq. 2.6a and Eq. 2.6b, i.e., $\mathbf{a_{tw}(h)} = \sum_{i=1}^{7}[\mathbf{v_{i,tw}(h)}.\ddot{u}_i + \dot{\mathbf{v}}_{\mathbf{i,tw}}\mathbf{(h)}.\dot{u}_i]$ and $\alpha_{\mathbf{tw}}\mathbf{(h)} = \sum_{i=1}^{7}[\omega_{\mathbf{i,tw}}\mathbf{(h)}.\ddot{u}_i + \dot{\omega}_{\mathbf{i,tw}}\mathbf{(h)}.\dot{u}_i]$. Hence, the total generalized inertia force acting at the tower DOFs can be determined using the following equation

$$\mathbf{F^*_{i,tw}} = \int_0^{H_{tw}} \mu_{tw}(h).\mathbf{v_{i,tw}(h)}.\mathbf{a_{tw}(h)}.dh \;\; \text{for} \;\; i = 1...7 \tag{2.17}$$

where H_{tw} denotes the overall height of the tower and $\mu_{tw}(h)$ denotes its distributed mass per unit length. The mass matrix along the tower DOFs can be expressed as

$$\mathbf{M_{i,j;tw}(u,t)} = \int_0^{H_{tw}} \mu_{tw}(h).\mathbf{v_{i,tw}(h)}.\mathbf{v_{j,tw}(h)}.dh \quad \text{for} \;\; i,j = 1...7 \tag{2.18}$$

As a result, other components of the system matrices can be derived by rearranging Eq. 2.17, yielding the expression below

$$\bar{\mathbf{F}}^*_{\mathbf{i,tw}}(\dot{\mathbf{u}},\mathbf{u},\mathbf{t}) = \int_0^{H_{tw}} \mu_{tw}(h).\mathbf{v_{i,tw}(h)}.\left(\sum_{i=1}^{7}\frac{d}{dt}\left\{\mathbf{v_{i,tw}(h)}\right\}.\dot{u}_i\right).dh \quad \text{for} \;\; i = 1...7 \tag{2.19}$$

Thus, Eq. 2.18 together with Eq. 2.19 describes the generalized inertia force associated with tower DOFs.

The generalized active force (i.e., $\mathbf{F_i}$) on the respective structural component forms the remaining part of the governing differential equation, i.e., Eq. 2.2. They have two main components; internal reactions (i.e., elastic and damping forces) and externally applied forces (i.e., aerodynamic, gravitational, and brake forces acting on the yaw bearing). The potential energy contained in each component can be used to estimate the generalized elastic force, which is given by

$$\mathbf{F_{i,tw,el}}(\dot{\mathbf{u}},\mathbf{u},\mathbf{t}) = \begin{cases} -k^{FA}_{1,1;tw}.u_4 - k^{FA}_{1,2;tw}.u_6 & \text{for} \;\; i = 4 \\ -k^{SS}_{1,1;tw}.u_5 - k^{SS}_{1,2;tw}.u_7 & \text{for} \;\; i = 5 \\ -k^{FA}_{1,2;tw}.u_4 - k^{FA}_{2,2;tw}.u_6 & \text{for} \;\; i = 6 \\ -k^{SS}_{1,2;tw}.u_5 - k^{SS}_{2,2;tw}.u_7 & \text{for} \;\; i = 7 \end{cases} \tag{2.20}$$

In the above equation, $k^{FA}_{i,j;tw}$ and $k^{SS}_{i,j;tw}$ are the generalized stiffness of the tower, which can be obtained from the flexural rigidity [i.e., $EI^{FA}_{tw}(h)$ and $EI^{SS}_{tw}(h)$] and the mode shapes along the fore-aft and side-to-side directions [13], as expressed by the following equations

$$k^{FA}_{i,j;tw} = \int_0^{H_{tw}} EI^{FA}_{tw}(h).\frac{d^2\phi^{FA}_{i,tw}(h)}{dh}.\frac{d^2\phi^{FA}_{j,tw}(h)}{dh}dh \tag{2.21a}$$

$$k^{SS}_{i,j;tw} = \int_0^{H_{tw}} EI^{SS}_{tw}(h).\frac{d^2\phi^{SS}_{i,tw}(h)}{dh}.\frac{d^2\phi^{SS}_{j,tw}(h)}{dh}dh \tag{2.21b}$$

Additionally, $\mu_{tw}(h)$ along with a suitable mode shape, can be used to estimate the modal mass in the fore-aft and side-to-side directions. The modal frequencies of the tower can be evaluated using these parameters (i.e., $f^{FA}_{i,tw} = \frac{1}{2\pi}\sqrt{\frac{k^{FA}_{i,i;tw}}{m^{FA}_{i,i;tw}}}$ and $f^{SS}_{i,tw} = \frac{1}{2\pi}\sqrt{\frac{k^{SS}_{i,i;tw}}{m^{SS}_{i,i;tw}}}$).

The generalized damping forces acting on the tower can be represented using Rayleigh's model [220] i.e.,

$$\mathbf{F_{i,tw,d}}(\dot{\mathbf{u}},\mathbf{u},\mathbf{t}) = \begin{cases} -\frac{\xi^{FA}_{1,tw}.k^{FA}_{1,1;tw}}{\pi.f^{FA}_{1,tw}}.\dot{u}_4 - \frac{\xi^{FA}_{2,tw}.k^{FA}_{1,2;tw}}{\pi.f^{FA}_{2,tw}}.\dot{u}_6 & \text{for} \;\; i = 4 \\ -\frac{\xi^{SS}_{1,tw}.k^{SS}_{1,1;tw}}{\pi.f^{SS}_{1,tw}}.\dot{u}_5 - \frac{\xi^{SS}_{2,tw}.k^{SS}_{1,2;tw}}{\pi.f^{SS}_{2,tw}}.\dot{u}_7 & \text{for} \;\; i = 5 \\ -\frac{\xi^{FA}_{1,tw}.k^{FA}_{1,2;tw}}{\pi.f^{FA}_{1,tw}}.\dot{u}_4 - \frac{\xi^{FA}_{2,tw}.k^{FA}_{2,2;tw}}{\pi.f^{FA}_{2,tw}}.\dot{u}_6 & \text{for} \;\; i = 6 \\ -\frac{\xi^{SS}_{1,tw}.k^{SS}_{1,2;tw}}{\pi.f^{SS}_{1,tw}}.\dot{u}_5 - \frac{\xi^{SS}_{2,tw}.k^{SS}_{2,2;tw}}{\pi.f^{SS}_{2,tw}}.\dot{u}_7 & \text{for} \;\; i = 7 \end{cases} \tag{2.22}$$

Besides stiffness and damping, other external forces are acting on the tower. For example, the wind-induced aerodynamic force on the tower DOFs is given by

$$\mathbf{F_{i,tw,ae}}(\dot{\mathbf{u}}, \mathbf{u}, \mathbf{t}) = \int_0^{H_{tw}} [\mathbf{v_{i,tw}}(\mathbf{h}).\mathbf{F_{tw,ae}}(\mathbf{h}) + \omega_{\mathbf{i,tw}}(\mathbf{h}).\mathbf{M_{tw,ae}}(\mathbf{h})].dh \quad \text{for} \quad i = 4...7 \tag{2.23}$$

The aerodynamic force and moment acting at $\mathbf{r_{tw}}(\mathbf{h})$ from the tower base are represented by $\mathbf{F_{tw,ae}}(\mathbf{h})$ and $\mathbf{M_{tw,ae}}(\mathbf{h})$ in the above expression. Finally, the generalized active forces on the tower DOFs owing to gravity are given by

$$\mathbf{F_{i,tw,gv}}(\dot{\mathbf{u}}, \mathbf{u}, \mathbf{t}) = -\int_0^{H_{tw}} \mathbf{v_{i,tw}}(\mathbf{h}).\mu_{tw}(h).g.\hat{x}_2.dh \quad \text{for} \quad i = 4...7 \tag{2.24}$$

where g is the gravitational acceleration.

2.2.2 Nacelle and Bearing Assembly

The nacelle is a large mass on top of the tower as shown in Fig. 2.1, which is connected to the tower through the yaw bearing. It provides an enclosed space for the generator and drive-train assembly.

2.2.2.1 Yaw Bearing

The nacelle-drive train-rotor assembly is turned towards the in-flowing wind with the help of the yaw bearing. It changes direction slowly and hence does not add to the system inertia. It only provides stiffness and damping in the relevant rotational DOF (i.e., u_8 in this example). The following expressions can be used to model these active forces

$$\mathbf{F_{i,yb,el}}(\dot{\mathbf{u}}, \mathbf{u}, \mathbf{t}) = -k_{yb}(u_8 - u_8^{in}) \quad \text{for} \quad i = 8 \tag{2.25a}$$

$$\mathbf{F_{i,yb,d}}(\dot{\mathbf{u}}, \mathbf{u}, \mathbf{t}) = -c_{yb}.\dot{u}_8 \quad \text{for} \quad i = 8 \tag{2.25b}$$

where k_{yb} and c_{yb} are the spring stiffness and damping constant of the yaw bearing, respectively.

2.2.2.2 Nacelle

The nacelle can be described as a rigid mass at the top of the tower that houses the drive-train assembly. The linear and angular velocity and acceleration at its centre of mass can be evaluated using its position vector with respect to the centre point at the tower top. As a result, the position vector $\mathbf{r_{na}}$ is given by

$$\mathbf{r_{na}} = c_{na,x}.\hat{c}_1 + c_{na,z}.\hat{c}_2 + c_{na,y}.\hat{c}_3 \tag{2.26}$$

In this expression, $c_{na,x}$, $c_{na,z}$ and $c_{na,y}$ are the offsets of the nacelle centre of mass from the tower top. This position vector can be utilized to compute the overall linear and angular velocities at the nacelle centre of mass, i.e., $\mathbf{v_{na}} = \mathbf{v_{tw}}(\mathbf{H_{tw}}) + \omega_{\mathbf{na}} \times \mathbf{r_{na}}$ and $\omega_{\mathbf{na}} = \omega_{\mathbf{tw}}(\mathbf{H_{tw}}) + \dot{u}_8.\hat{c}_2$. Again, rearranging these equations in the form of Eq. 2.5a and Eq. 2.5b produce their respective partial forms, which are given below

$$\mathbf{v_{i,na}} = \mathbf{v_{i,tw}}(\mathbf{H_{tw}}) + \omega_{\mathbf{i,na}} \times \mathbf{r_{na}} \quad \text{for} \quad i = 1...8 \tag{2.27a}$$

$$\omega_{\mathbf{i,na}} = \begin{cases} \omega_{\mathbf{i,tw}}(\mathbf{H_{tw}}) & \text{for} \quad i = 1...7 \\ \hat{c}_2 & \text{for} \quad i = 8 \end{cases} \tag{2.27b}$$

The respective partial accelerations can now be determined by differentiating the linear and angular velocities, i.e. $\mathbf{a_{i,na}} = \frac{d}{dt}(\mathbf{v_{i,na}})$ and $\alpha_{\mathbf{i,na}} = \frac{d}{dt}(\omega_{\mathbf{i,na}})$. As stated earlier, these partial forms of velocities and accelerations can be used to obtain the generalized inertia force acting on the nacelle. Thus, following similar steps as discussed earlier, the mass matrix for nacelle has the expression below

$$\mathbf{M_{i,j;na}}(\mathbf{u}, \mathbf{t}) = m_{na}.\mathbf{v_{i,na}}.\mathbf{v_{j,na}} + \omega_{\mathbf{i,na}}.\bar{\mathbf{I}}_{\mathbf{na}}.\omega_{\mathbf{j,na}} \quad \text{for} \quad i,j = 1...8 \tag{2.28}$$

The rest of the generalized inertia force is obtained as

$$\begin{aligned}\bar{\mathbf{F}}^{*}_{\mathbf{i,na}}(\dot{\mathbf{u}},\mathbf{u},\mathbf{t}) =& m_{na}.\mathbf{v_{i,na}}.\left\{\sum_{i=1}^{8}\frac{d}{dt}(\mathbf{v_{i,na}}).\dot{u}_i\right\} \\ &+\omega_{\mathbf{i,na}}.\left[\bar{\mathbf{I}}_{\mathbf{na}}.\left\{\sum_{i=1}^{8}\frac{d}{dt}(\omega_{\mathbf{i,na}}).\dot{u}_i\right\}+\omega_{\mathbf{na}}\times\bar{\mathbf{I}}_{\mathbf{na}}.\omega_{\mathbf{na}}\right] \quad \text{for} \ \ i=1...8\end{aligned} \tag{2.29}$$

where m_{na} represents the nacelle mass and $\bar{\mathbf{I}}_{\mathbf{na}}$ is the corresponding inertia dyadic, i.e., $\bar{\mathbf{I}}_{\mathbf{na}} = [I_{na} - m_{na}(c^2_{na,x}+c^2_{na,y})].\hat{c}_2.\hat{c}_2$. The term I_{na} here refers to the nacelle inertia about its yaw axis. Finally, generalized active force on the nacelle coming from the gravitational field is given by

$$\mathbf{F_{i,na,gv}}(\dot{\mathbf{u}},\mathbf{u},\mathbf{t}) = -m_{na}.g.\mathbf{v_{i,na}}.\hat{x}_2 \quad \text{for} \quad i=1...8 \tag{2.30}$$

2.2.3 Drive-Train Model

The hub, generator, and low-speed shaft are the components that make up the whole drive-train assembly. The forces acting on these subsystems are described below.

2.2.3.1 Hub

The position vector at the apex of blade coning ($\mathbf{r_{ap}}$) is specified with respect to the centre point at the tower top, i.e. $\mathbf{r_{ap}} = c_{ap,x}.\hat{c}_1 + c_{ap,z}.\hat{c}_2 + c_{ap,y}.\hat{c}_3$. The offset of the corresponding point from the centre at the tower top is represented by $c_{ap,(.)}$ in this formulation. The position vector at the hub centre of mass is defined using the apex of blade coning as the reference point, i.e., $\mathbf{r_{hu}} = c_{hu,x}.\hat{d}_1 + c_{hu,z}.\hat{d}_2 + c_{hu,y}.\hat{d}_3$. The offset of the hub centre of mass [i.e., $c_{hu,(.)}$] from the rotor apex (ap) is used here. The angular velocity of the low-speed shaft (ls) governs the total angular velocity at the hub, which can be represented as $\omega_{\mathbf{hu}} = \omega_{\mathbf{ls}} = \omega_{\mathbf{na}} + (\dot{u}_9+\dot{u}_{10}).\hat{d}_1$. As a result, the partial angular velocities and accelerations at the hub and low-speed shaft are essentially equal, which may be expressed as

$$\omega_{\mathbf{i,hu}} = \omega_{\mathbf{i,ls}} = \begin{cases}\omega_{\mathbf{i,na}} & \text{for} \ \ i=1...8 \\ \hat{d}_1 & \text{for} \ \ i=9,10\end{cases} \tag{2.31a}$$

$$\alpha_{\mathbf{i,hu}} = \frac{d}{dt}(\omega_{\mathbf{i,hu}}) = \frac{d}{dt}(\omega_{\mathbf{i,ls}}) = \begin{cases}\frac{d}{dt}(\omega_{\mathbf{i,na}}) & \text{for} \ \ i=1...8 \\ \omega_{\mathbf{na}}\times\omega_{\mathbf{i,ls}} & \text{for} \ \ i=9,10\end{cases} \tag{2.31b}$$

The total linear velocity and accelerations at the hub in their partial forms are evaluated from the rotor apex, i.e., $\mathbf{v_{ap}} = \mathbf{v_{tw}}(\mathbf{H_{tw}}) + \omega_{\mathbf{ls}}\times\mathbf{r_{ap}}$. As a result, the partial linear velocity and acceleration at the rotor apex are expressed in the same way, as shown earlier, i.e.,

$$\mathbf{v_{i,ap}} = \mathbf{v_{i,tw}}(\mathbf{H_{tw}}) + \omega_{\mathbf{i,ls}}\times\mathbf{r_{ap}} \quad \text{for} \ \ i=1...10 \tag{2.32a}$$

$$\frac{d}{dt}(\mathbf{v_{i,ap}}) = \frac{d}{dt}\left\{\mathbf{v_{i,tw}}(\mathbf{H_{tw}})\right\} + \frac{d}{dt}(\omega_{\mathbf{i,ls}})\times\mathbf{r_{ap}} + \omega_{\mathbf{i,ls}}\times(\omega_{\mathbf{ls}}\times\mathbf{r_{ap}}) \quad \text{for} \ \ i=1...10 \tag{2.32b}$$

Similarly, the total linear velocity at the hub centre of mass can be evaluated, i.e., $\mathbf{v_{hu}} = \mathbf{v_{ap}} + \omega_{\mathbf{ls}}\times\mathbf{r_{hu}}$. Hence, the partial linear velocity and acceleration at the hub centre can be expressed as

$$\mathbf{v_{i,hu}} = \mathbf{v_{i,ap}} + \omega_{\mathbf{i,ls}}\times\mathbf{r_{hu}} \quad \text{for} \ \ i=1...10 \tag{2.33a}$$

$$\frac{d}{dt}(\mathbf{v_{i,hu}}) = \frac{d}{dt}(\mathbf{v_{i,ap}}) + \frac{d}{dt}(\omega_{\mathbf{i,ls}})\times\mathbf{r_{hu}} + \omega_{\mathbf{i,ls}}\times(\omega_{\mathbf{ls}}\times\mathbf{r_{hu}}) \quad \text{for} \ \ i=1...10 \tag{2.33b}$$

These partial velocities and accelerations can be used to obtain the generalized inertia forces, which lead to the following mass matrix

$$\mathbf{M_{i,j;hu}}(\mathbf{u},\mathbf{t}) = m_{hu}.\mathbf{v_{i,hu}}.\mathbf{v_{j,hu}} + \omega_{\mathbf{i,hu}}.\bar{\mathbf{I}}_{\mathbf{hu}}.\omega_{\mathbf{j,hu}} \quad \text{for } i,j = 1...10 \tag{2.34}$$

and the remaining part of the generalized inertia force is given by

$$\begin{aligned}\bar{\mathbf{F}}^{*}_{\mathbf{i,hu}}(\dot{\mathbf{u}},\mathbf{u},\mathbf{t}) =& m_{hu}.\mathbf{v_{i,hu}}.\left\{\sum_{i=1}^{10}\frac{d}{dt}(\mathbf{v_{i,hu}}).\dot{u}_i\right\} \\ &+ \omega_{\mathbf{i,hu}}.\left[\bar{\mathbf{I}}_{\mathbf{hu}}.\left\{\sum_{i=1}^{10}\frac{d}{dt}(\omega_{\mathbf{i,hu}}).\dot{u}_i\right\} + \omega_{\mathbf{hu}} \times \bar{\mathbf{I}}_{\mathbf{hu}}.\omega_{\mathbf{hu}}\right] \quad \text{for } i = 1...10\end{aligned} \tag{2.35}$$

where m_{hu} denotes the lumped hub mass, and $\bar{\mathbf{I}}_{\mathbf{hu}}$ denotes the hub inertia dyadic, i.e., $\bar{\mathbf{I}}_{\mathbf{hu}} = [I_{hu} - m_{hu}.c^2_{hu,x}].\hat{e}_2.\hat{e}_2$, where I_{hu} is the hub inertia about the rotor axis. The generalized active force on the hub due to gravity is given by

$$\mathbf{F_{i,hu,gv}}(\dot{\mathbf{u}},\mathbf{u},\mathbf{t}) = -m_{hu}.g.\mathbf{v_{i,hu}}.\hat{x}_2 \quad \text{for} \quad i = 1...10 \tag{2.36}$$

2.2.3.2 Generator and Shaft

Several elements determine the angular velocity of the generator, including gearbox ratio (G_{br}) and generator direction (G_{dir}), which may or may not spin in the same direction as the low-speed shaft. This model assumes, without loss of generality, that no friction develops inside the gears, implying 100% gearbox efficiency. If there is no gearbox, G_{br} can be set to 1, and G_{dir} value will be 1 for forwarding gear and -1 for reversing gear. The angular velocity of the generator ($\omega_{\mathbf{gn}}$) and its partial components are given by the following expression, where u_9 indicates the azimuth of the low-speed shaft.

$$\omega_{\mathbf{gn}} = \omega_{\mathbf{na}} + G_{br}.G_{dir}.\dot{u}_9.\hat{d}_1 \tag{2.37a}$$

$$\omega_{\mathbf{i,gn}} = \begin{cases} \omega_{\mathbf{i,na}} & \text{for } i = 1...8 \\ G_{br}.G_{dir}.\hat{d}_1 & \text{for } i = 9 \end{cases} \tag{2.37b}$$

As a result, the equation for the partial angular acceleration of the generator becomes

$$\frac{d}{dt}(\omega_{\mathbf{i,gn}}) = \begin{cases} \frac{d}{dt}(\omega_{\mathbf{i,na}}) & \text{for } i = 1...8 \\ \omega_{\mathbf{na}} \times \omega_{\mathbf{i,gn}} & \text{for } i = 9 \end{cases} \tag{2.38}$$

It is worth noting that the rate of change of angular momentum of the generator produces an additional torque that tries to spin the nacelle along with it. This torque, in addition to rotating the nacelle, is transmitted to the tower coupled with the torque from the low-speed shaft. As a consequence, the mass matrix and the remaining components of the total generalized inertia force can be written as

$$\mathbf{M_{i,j;gn}}(\mathbf{u},\mathbf{t}) = \omega_{\mathbf{i,gn}}.\bar{\mathbf{I}}_{\mathbf{gn}}.\omega_{\mathbf{j,gn}} \quad \text{for } i,j = 1...9 \tag{2.39a}$$

$$\bar{\mathbf{F}}^{*}_{\mathbf{i,gn}}(\dot{\mathbf{u}},\mathbf{u},\mathbf{t}) = \begin{cases} \omega_{\mathbf{i,gn}}.\left[\bar{\mathbf{I}}_{\mathbf{gn}}.\left\{\sum\limits_{i=1}^{8}\frac{d}{dt}(\omega_{\mathbf{i,na}}).\dot{u}_i\right\} + \omega_{\mathbf{gn}} \times \bar{\mathbf{I}}_{\mathbf{gn}}.\omega_{\mathbf{gn}}\right] & \text{for } i = 1...8 \\ \omega_{\mathbf{i,gn}}.\bar{\mathbf{I}}_{\mathbf{gn}}.\left\{\sum\limits_{i=1}^{9}\frac{d}{dt}(\omega_{\mathbf{i,na}}).\dot{u}_i\right\} & \text{for } i = 9 \end{cases} \tag{2.39b}$$

where $\bar{\mathbf{I}}_{\mathbf{gn}}$ is the inertia dyadic of the generator, i.e., $\bar{\mathbf{I}}_{\mathbf{gn}} = I_{gn}.\hat{d}_2.\hat{d}_2$. The high-speed shaft produces mechanical torque during power generation, which tries to resist its rotation. Mechanical brakes, similar to mechanical torque in a high-speed shaft, also provide torque along the same degrees of freedom. All of them contribute to the generalized active force, which can be described as

$$\mathbf{F_{i,gn}(\dot{u},u,t)} = \omega_{\mathbf{i,gn}}.\left[G_{dir}.T_{gn}(\dot{u}_9,t).\hat{d}_1 + G_{dir}.T_{br}(t).\hat{d}_1\right] \quad \text{for} \quad i=9 \tag{2.40}$$

where $T_{gn}(\dot{u}_9,t)$ denotes the load (i.e., positive power generation), while T_{br} in the above expression denotes the torque applied by the high-speed shaft brake, i.e., $T_{br}(t) = S_{br}.\tau(t)$. In this expression, S_{br} is the coefficient of a fully deployed high-speed shaft brake, and $\tau(t)$ is a function that determines the time between braking initiation and full deployment. Finally, elastic and damping forces acting on the low-speed shaft are evaluated from the potential energy, which are given by

$$\mathbf{F_{i,ls,el}(\dot{u},u,t)} = -k_{ls}.u_{10} \quad \text{for} \quad i=10 \tag{2.41a}$$

$$\mathbf{F_{i,ls,d}(\dot{u},u,t)} = -c_{ls}.\dot{u}_{10} \quad \text{for} \quad i=10 \tag{2.41b}$$

The torsional stiffness and damping constant of the low-speed shaft are represented by k_{ls} and c_{ls}, respectively, in the above equation.

2.2.4 Blade Model with Bending-Torsion Coupling

The blades are flexible rotating beams attached to the hub, which vibrates in flapwise, edgewise, and torsional directions. In this process, the coupling of different DOFs is mainly caused by the local twist and due to the offsets of the aerodynamic centre and elastic centre of the blade cross-section from its centre of gravity. The offset of the aerodynamic centre from the pitch axis gives rise to an aerodynamic pitching moment along with the lift and drag forces causing torsional vibration, which can significantly interact with bending deformations. This is aimed to be studied in this work, where the multi-body dynamics is modeled using Kane's approach.

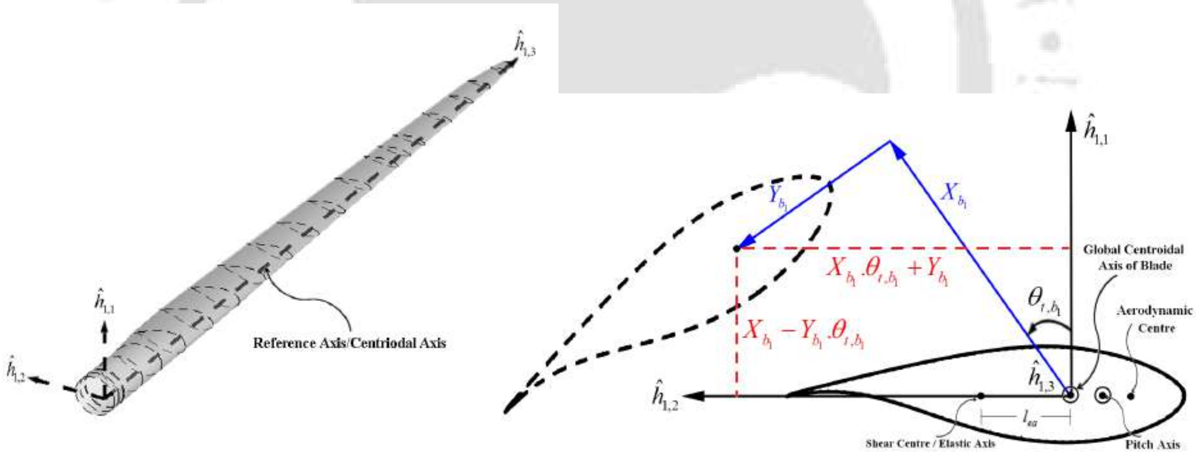

(a) (b)

Figure 2.2: Modeling of bend-twist coupling; (a) Blade reference axis, (b) Blade sectional view undergoing coupled deformation

The structural twist angle also induces coupling between the bending DOFs, and hence, the twisted mode shapes [i.e., ϕ_{i,b_1} and φ_{i,b_1}] are determined from the individual modes shapes in its flapwise and edgewise DOFs. Here, it should be noted that the effect of offsets of the centre of gravity and elastic centre of the blade sections from the reference axis is taken into account while determining the blade's individual flapwise and edgewise mode shapes. The twisted shape functions are obtained from the curvature of the flapwise and edgewise modes along the centroidal axis. For example, ϕ_{1,b_1} and ϕ_{2,b_1} in the out-of-plane direction originate from the components of 1^{st} and 2^{nd} flapwise modes, respectively, whereas ϕ_{3,b_1} in the same direction is the component of 1^{st} edgewise mode. Similarly, twisted shape functions φ_{i,b_1} (for i =1...3) in the in-plane direction are determined by projecting flapwise and edgewise modes. Hence, they can be written in the following form

$$\phi_1(p) = \int_0^p \int_0^r \left[\frac{d^2\gamma_1^F(\bar{r})}{d\bar{r}^2}\cos\{\theta_s(\bar{r})\}\right] d\bar{r}dr \tag{2.42a}$$

$$\phi_2(p) = \int_0^p \int_0^r \left[\frac{d^2\gamma_2^F(\bar{r})}{d\bar{r}^2} \cos\{\theta_s(\bar{r})\}\right] d\bar{r}dr \tag{2.42b}$$

$$\phi_3(p) = \int_0^p \int_0^r \left[\frac{d^2\gamma_1^E(\bar{r})}{d\bar{r}^2} \sin\{\theta_s(\bar{r})\}\right] d\bar{r}dr \tag{2.42c}$$

$$\varphi_1(p) = -\int_0^p \int_0^r \left[\frac{d^2\gamma_1^F(\bar{r})}{d\bar{r}^2} \sin\{\theta_s(\bar{r})\}\right] d\bar{r}dr \tag{2.42d}$$

$$\varphi_2(p) = -\int_0^p \int_0^r \left[\frac{d^2\gamma_2^F(\bar{r})}{d\bar{r}^2} \sin\{\theta_s(\bar{r})\}\right] d\bar{r}dr \tag{2.42e}$$

$$\varphi_3(p) = \int_0^p \int_0^r \left[\frac{d^2\gamma_1^E(\bar{r})}{d\bar{r}^2} \cos\{\theta_s(\bar{r})\}\right] d\bar{r}dr \tag{2.42f}$$

In this format, p and $\bar{r}$ are dummy variables representing the blade span while the terms $\gamma_i^F(\bar{r})$ and $\gamma_i^E(\bar{r})$ denote the i^{th} flapwise and edgewise modes, respectively. The term θ_s represents the local structural twist of the blade section. These dominant twisted modes determine the deformed position of the blade with respect to its centroidal axis. The nodal positions of the deformed blade from its reference axis are marked in Fig. 2.2. Here, the torsional twist is assumed to act against structural twist (i.e., torsion is trying to de-twist the blade). Hence, the position vector of a node of the 1^{st} blade located at a distance $(p + r_{hu})$ from its apex due to bi-axial bending and torsion can be written as

$$\begin{aligned}\boldsymbol{r_{b_1}(p)} =& \{X_{b_1}(p) - Y_{b_1}(p).\theta_{t,b_1}(p)\}.\hat{h}_{1,1} + \{X_{b_1}(p).\theta_{t,b_1}(p) + Y_{b_1}(p)\}.\hat{h}_{1,2} \\ &+ [p + r_{hu} - 0.5\{S_{1,1;b_1}(p).u_{11}^2 + S_{2,2;b_1}(p).u_{13}^2 + S_{3,3;b_1}(p).u_{12}^2 \\ &+ 2S_{1,2;b_1}(p).u_{11}.u_{13} + 2S_{1,3;b_1}(p).u_{11}.u_{12} + 2S_{2,3;b_1}(p).u_{13}.u_{12}\}].\hat{h}_{1,3}\end{aligned} \tag{2.43}$$

where $\theta_{t,b_1}(p)$ is the twist due to torsion while $X_{b_1}(p)$ and $Y_{b_1}(p)$ are the nodal positions of the blade along $\hat{h}_{1,1}$ and $\hat{h}_{1,2}$ axes, respectively without considering the effect of torsion [166]. They are given by

$$X_{b_1}(p) = \phi_{1,b_1}(p).u_{11} + \phi_{2,b_1}(p).u_{13} + \phi_{3,b_1}(p).u_{12} \tag{2.44a}$$

$$Y_{b_1}(p) = \varphi_{1,b_1}(p).u_{11} + \varphi_{2,b_1}(p).u_{13} + \varphi_{3,b_1}(p).u_{12} \tag{2.44b}$$

$$\theta_{t,b_1}(p) = \gamma_{1,b1}^T(p).u_{14} \tag{2.44c}$$

where $\gamma_{1,b1}^T(p)$ is the first torsional mode of the blade. In Eq. 2.43, $S_{i,j;b_1}$ represents the quadratic effects of bending modes, which determines axial shortening of the blade due to bi-axial bending [13] as also described for the tower. It can be expressed as

$$S_{i,j;b_1}(p) = \int_0^p \left[\frac{d\phi_{i,b_1}(r)}{dr}.\frac{d\phi_{j,b_1}(r)}{dr} + \frac{d\varphi_{i,b_1}(r)}{dr}.\frac{d\varphi_{j,b_1}(r)}{dr}\right] dr \tag{2.45}$$

The total angular velocity at the same point depends on the angular velocity of the low-speed shaft and the rate of change of slope of the deformed blade due to combined bending and torsion. Hence, using small-angle approximation, the angular velocity of the node at p can be expressed as

$$\boldsymbol{\omega_{b_1}(p)} = \boldsymbol{\omega_{ls}} - \left[\dot{X}'_{b_1}(p).\theta_{t,b_1}(p) + \dot{Y}'_{b_1}(p)\right].\hat{h}_{1,1} + \left[\dot{X}'_{b_1}(p) - \dot{Y}'_{b_1}(p).\theta_{t,b_1}(p)\right].\hat{h}_{1,2} + \dot{\theta}_{t,b_1}(p).\hat{h}_{1,3} \tag{2.46}$$

where the terms $\dot{X}'_{b_1}(p)$, $\dot{Y}'_{b_1}(p)$ and $\dot{\theta}_{t,b_1}(p)$ arise from the rate of change of slope due to bending and torsional velocity of the blade. The total linear velocity at the same point depends on several factors (e.g., the linear velocity at the rotor apex, the angular velocity of the low-speed shaft, and linear velocity at the blade node due to bi-axial bending), which has the following form

$$\mathbf{v_{b_1}(p)} = \mathbf{v_{ap}} + \boldsymbol{\omega_{ls}} \times \mathbf{r_{b_1}(p)} + \mathbf{v_{L,b_1}(p)} \tag{2.47}$$

Each component on the right-hand side of the above equation is known except $\mathbf{v_{L,b_1}(p)}$, which is the total linear velocity in the local blade coordinate and can be obtained by differentiating $\mathbf{r_{b_1}(p)}$ in Eq. 2.43 with respect to time, i.e., $\mathbf{v_{L,b_1}(p)} = \frac{d}{dt}\mathbf{r_{b_1}(p)}$. Now, using the time derivative of the DOF as the generalized speed, similar to other components, and rearranging them provide partial angular and linear velocities of the blade, which are expressed as

$$\boldsymbol{\omega_{i,b_1}(p)} = \boldsymbol{\omega_{i,ls}} + \begin{cases} -[\frac{d\phi_1(p)}{dp}.\theta_t(p) + \frac{d\varphi_1(p)}{dp}].\hat{h}_{1,1} + [\frac{d\phi_1(p)}{dp} - \frac{d\varphi_1(p)}{dp}.\theta_t(p)].\hat{h}_{1,2} & \text{for } i = 11 \\ -[\frac{d\phi_3(p)}{dp}.\theta_t(p) + \frac{d\varphi_3(p)}{dp}].\hat{h}_{1,1} + [\frac{d\phi_3(p)}{dp} - \frac{d\varphi_3(p)}{dp}.\theta_t(p)].\hat{h}_{1,2} & \text{for } i = 12 \\ -[\frac{d\phi_2(p)}{dp}.\theta_t(p) + \frac{d\varphi_2(p)}{dp}].\hat{h}_{1,1} + [\frac{d\phi_2(p)}{dp} - \frac{d\varphi_2(p)}{dp}.\theta_t(p)].\hat{h}_{1,2} & \text{for } i = 13 \\ \gamma_1^T(p).\hat{h}_{1,3} & \text{for } i = 14 \end{cases} \tag{2.48a}$$

$$\boldsymbol{v_{i,b_1}(p)} = \boldsymbol{v_{i,ap}} + \begin{cases} \boldsymbol{\omega_{i,ls}} \times \boldsymbol{r_{b_1}(p)} & \text{for } i = 1...10 \\ [\phi_1(p) - \varphi_1(p).\theta_t(p)].\hat{h}_{1,1} + [\phi_1(p).\theta_t(p) + \varphi_1(p)].\hat{h}_{1,2} & \\ -[S_{1,1}(p).u_{11} + S_{1,2}(p).u_{13} + S_{1,3}(p).u_{12}].\hat{h}_{1,3} & \text{for } i = 11 \\ [\phi_3(p) - \varphi_3(p).\theta_t(p)].\hat{h}_{1,1} + [\phi_3(p).\theta_t(p) + \varphi_3(p)].\hat{h}_{1,2} & \\ -[S_{3,3}(p).u_{12} + S_{2,3}(p).u_{13} + S_{1,3}(p).u_{11}].\hat{h}_{1,3} & \text{for } i = 12 \\ [\phi_2(p) - \varphi_2(p).\theta_t(p)].\hat{h}_{1,1} + [\phi_2(p).\theta_t(p) + \varphi_2(p)].\hat{h}_{1,2} & \\ -[S_{2,2}(p).u_{13} + S_{2,3}(p).u_{12} + S_{1,2}(p).u_{11}].\hat{h}_{1,3} & \text{for } i = 13 \end{cases} \tag{2.48b}$$

Here, it may be noted that the secondary subscript b_1 is removed on the right-hand side of Eq. 2.48 to avoid clutter. Using time differentiation of the above two equations, the expressions for the partial angular and linear accelerations can be obtained, i.e., $\alpha_{\mathbf{i,b_1}}\mathbf{(p)} = \frac{d}{dt}\omega_{\mathbf{i,b_1}}\mathbf{(p)}$ and $\mathbf{a_{i,b_1}(p)} = \frac{d}{dt}\mathbf{v_{i,b_1}(p)}$. Thus, the expression for the generalized inertia forces associated with the blade is given by

$$\begin{aligned} \mathbf{F^*_{i,b_1}} = & \int_0^{R_{b_1}} \mu_{b_1}(p).\mathbf{v_{i,b_1}(p).a_{b_1}(p)}.dp + \int_0^{R_{b_1}} \omega_{\mathbf{i,b_1}}\mathbf{(p)}.\mathbf{\bar{I}_{b_1}(p)}.\alpha_{\mathbf{b_1}}\mathbf{(p)}.dp \\ & + \int_0^{R_{b_1}} \omega_{\mathbf{i,b_1}}\mathbf{(p)}.\left\{\omega_{\mathbf{b_1}}\mathbf{(p)} \times \mathbf{\bar{I}_{b_1}(p)}.\omega_{\mathbf{b_1}}\mathbf{(p)}\right\}.dp \end{aligned} \tag{2.49}$$

where R_{b_1} is the blade length while $\mu_{b_1}(p)$ and $\mathbf{\bar{I}_{b_1}(p)}$ are the distributed mass and inertia dyadic of the blade, respectively. The terms $\mathbf{a_{b_1}(p)}$ and $\alpha_{\mathbf{b_1}}\mathbf{(p)}$ denote the nodal linear and angular accelerations of the blade. The distributed inertia dyadic of the blade has the following form

$$\boldsymbol{\bar{I}_{b_1}(p)} = I^F_{b_1}(p).\hat{i}_{1,1}.\hat{i}_{1,1} + I^E_{b_1}(p).\hat{i}_{1,2}.\hat{i}_{1,2} + \{\rho_{b_1}(p).I^p_{b_1}(p) + \mu_{b_1}(p).l^2_{cg,b_1}(p)\}.\hat{i}_{1,3}.\hat{i}_{1,3} \tag{2.50}$$

In the above equation, $I^F_{b_1}(p)$, $I^E_{b_1}(p)$ and $I^p_{b_1}(p)$ denote flapwise, edgewise, and rotational inertia of the blade, respectively. At the same time, $\mu_{b_1}(p)$ and $l_{cg,b_1}(p)$ are the mass density and offset of the centre of gravity of individual airfoil from the global centroidal axis, respectively, at a location p. Here, it may be noted that the individual section has non-zero $l_{cg,b_1}(p)$, which are used to obtain the global centroidal axis. Using these expressions of the blade velocities and accelerations along with its mass and inertial properties, Eq. 2.49 can be rearranged in the form of system matrices, where the mass matrix and remaining part of the generalized inertia force are given by

$$\boldsymbol{M_{i,j;b_1}(u,t)} = \int_0^{R_{b_1}} \mu_{b_1}(p).\boldsymbol{v_{i,b_1}(p).v_{j,b_1}(p)}.dp + \int_0^{R_{b_1}} \boldsymbol{\omega_{i,b_1}(p).\bar{I}_{b_1}(p).\omega_{j,b_1}(p)}.dp \quad \text{for } i,j = 1...14 \tag{2.51a}$$

$$\bar{\boldsymbol{F}}^{*}_{\boldsymbol{i,b_1}}(\boldsymbol{\dot{u},u,t}) = \int_0^{R_{b_1}} \mu_{b_1}(p).\boldsymbol{v_{i,b_1}(p)}.\left(\sum_{i=1}^{14}\frac{d}{dt}\{\boldsymbol{v_{i,b_1}(p)}\}.\dot{u}_i\right).dp$$
$$+\int_0^{R_{b_1}} \boldsymbol{\omega_{i,b_1}(p)}.\left[\bar{\boldsymbol{I}}_{\boldsymbol{b_1}}\boldsymbol{(p)}.\left\{\sum_{i=1}^{14}\frac{d}{dt}\{\boldsymbol{\omega_{i,b_1}(p)}\}.\dot{u}_i\right\}+\boldsymbol{\omega_{b_1}(p)}\times\bar{\boldsymbol{I}}_{\boldsymbol{b_1}}\boldsymbol{(p)}.\boldsymbol{\omega_{b_1}(p)}\right].dp \quad (2.51b)$$
$$\text{for } i = 1...14$$

The elastic forces in the blade arise from the strain energy stored due to deformation. As elastic coupling between the bending and torsional modes are considered here, the expressions for the generalized elastic forces obtained from the strain energy are

$$\boldsymbol{F_{i,b_1,el}(\dot{u},u,t)} = \begin{cases} -k^F_{1,1;b_1}.u_{11} - k^F_{1,2;b_1}.u_{13} - k^{FE}_{1,1;b_1}.u_{12} - k^{FT}_{1,1;b_1}.u_{14} & \text{for } \ i = 11 \\ -k^E_{1,1;b_1}.u_{12} - k^{FE}_{1,1;b_1}.u_{11} - k^{FE}_{2,1;b_1}.u_{13} - k^{ET}_{1,1;b_1}.u_{14} & \text{for } \ i = 12 \\ -k^F_{1,2;b_1}.u_{11} - k^F_{2,2;b_1}.u_{13} - k^{FE}_{2,1;b_1}.u_{12} - k^{FT}_{2,1;b_1}.u_{14} & \text{for } \ i = 13 \\ -k^T_{1;b_1}.u_{14} - k^{FT}_{1,1;b_1}.u_{11} - k^{FT}_{2,1;b_1}.u_{13} - k^{ET}_{1,1;b_1}.u_{12} & \text{for } \ i = 14 \end{cases} \quad (2.52)$$

where $k^F_{i,j;b_1}$ and $k^E_{i,j;b_1}$ are the generalized stiffness of the blade in its local flapwise and edgewise directions, respectively, without considering the de-stiffening effect of gravity and centrifugal force, which can be expressed as

$$k^F_{i,j} = \int_0^{R_{b_1}} EI^F_{b_1}(p)\left(\frac{d^2\gamma^F_i(p)}{dp^2}\right)\left(\frac{d^2\gamma^F_j(p)}{dp^2}\right)dp \quad \text{for } \ i,j = 1...2 \quad (2.53a)$$

$$k^E_{i,j} = \int_0^{R_{b_1}} EI^E_{b_1}(p)\left(\frac{d^2\gamma^E_i(p)}{dp^2}\right)\left(\frac{d^2\gamma^E_j(p)}{dp^2}\right)dp \quad \text{for } \ i,j = 1 \quad (2.53b)$$

$$k^{FE}_{i,j} = \int_0^{R_{b_1}} s^{FE}_{b_1}(p)\left(\frac{d^2\gamma^F_i(p)}{dp^2}\right)\left(\frac{d^2\gamma^E_j(p)}{dp^2}\right)dp \quad \text{for } \ i,j = 1...2 \quad (2.53c)$$

In this notation, $EI^F_{b_1}(p)$ and $EI^E_{b_1}(p)$ are the distributed stiffness properties of the blade in its flapwise and edgewise directions, respectively. The term $k^{FE}_{i,j;b_1}$ in Eq. 2.52 represents the coupled bending stiffness between i^{th} flapwise and j^{th} edgewise mode. Here, $s^{FE}_{b_1}$ represents the coupled flap-lag stiffness of the blade section obtained from PreComp [221], which utilizes classical laminate theory to determine the values of coupled stiffnesses. On the other hand, $k^T_{1;b_1}$ represents the generalized stiffness of the blade in its 1^{st} torsional mode, i.e., $k^T_{i;b_1} = \int_0^{R_{b_1}} GJ_{b_1}(p)\left(\frac{d\gamma^T_i(p)}{dp}\right)\left(\frac{d\gamma^T_i(p)}{dp}\right)dp$ for $i = 1$. The coupling between bending and torsional modes can arise from different sources. Inertia coupling effects are often result of the offsets of the centre of gravity. In contrast, elastic coupling can occur due to the offset of the elastic axis, unbalanced structural laminates of the airfoil, and change in ply angle or materials of the blade skin or spar, resulting in the interaction between bending and torsional modes. Lobitz and Laino [39] expressed these cross-stiffness terms with the help of normalized bending-torsion coupling coefficients $\lambda^{FT}_{b_1}$ and $\lambda^{ET}_{b_1}$, which are defined as

$$\lambda^{FT}_{b_1} = g^{FT}_{b_1}\Big/\sqrt{EI^F_{b_1}.GJ_{b_1}} \quad \text{where} -1 < \lambda^{FT}_{b_1} < 1 \quad (2.54a)$$

$$\lambda^{ET}_{b_1} = -g^{ET}_{b_1}\Big/\sqrt{EI^E_{b_1}.GJ_{b_1}} \quad \text{where} -1 < \lambda^{ET}_{b_1} < 1 \quad (2.54b)$$

Here, $\lambda^{FT}_{b_1}$ and $\lambda^{ET}_{b_1}$ denote the flap-twist and edge-twist coupling coefficients, whereas $g^{FT}_{b_1}$ and $g^{ET}_{b_1}$ refer to coupled flap-torsional and edge-torsional stiffness of the blade section, respectively. Although the values of $\lambda^{FT}_{b_1}$ and $\lambda^{ET}_{b_1}$ can theoretically vary from -1 to $+1$, generally, values of 0.2 to 0.4 are achievable in the case of turbine blades [222, 223]. Positive values of these coefficients denote flap-twist-to-feather (decreasing the angle of attack) and edge-twist-to-feather couplings between bending and torsional deformation for flapwise and edgewise deflections toward the suction side and leading edge, respectively. Hence, the generalized coupled stiffness between the i^{th} flapwise and j^{th} torsional mode is denoted by $k^{FT}_{i,j;b_1}$, i.e., $k^{FT}_{i,j;b_1} = \int_0^{R_{b_1}} g^{FT}_{b_1}(p)\left(\frac{d^2\gamma^F_i(p)}{dp^2}\right)\left(\frac{d\gamma^T_j(p)}{dp}\right)dp$ for $i,j = 1...2$, while the generalized coupled stiffness between i^{th} edgewise and j^{th} torsional mode is denoted by $k^{ET}_{i,j;b_1}$ i.e., $k^{ET}_{i,j;b_1} = \int_0^{R_{b_1}} g^{ET}_{b_1}(p)\left(\frac{d^2\gamma^E_i(p)}{dp^2}\right)\left(\frac{d\gamma^T_j(p)}{dp}\right)dp$ for $i,j = 1$. In the current formulation, flapwise offsets of the elastic axis are neglected as they are tiny, but the effects of edgewise offsets are considered. In this formulation, $l_{ea,b_1}(p)$ is the chordwise offsets of the elastic blade axis measured from its centroidal axis and positive towards the trailing edge.

The structural damping of the blade using Rayleigh's model can be expressed as

$$\boldsymbol{F_{i,b_1,d}(\dot{u},u,t)} = \begin{cases} -\frac{\xi^F_{1,b_1}.k^F_{1,1;b_1}}{\pi.f^F_{1,b_1}}.\dot{u}_{11} - \frac{\xi^F_{2,b_1}.k^F_{1,2;b_1}}{\pi.f^F_{2,b_1}}.\dot{u}_{13} & \text{for } i = 11 \\ -\frac{\xi^E_{1,b_1}.k^E_{1,1;b_1}}{\pi.f^E_{1,b_1}}.\dot{u}_{12} & \text{for } i = 12 \\ -\frac{\xi^F_{1,b_1}.k^F_{1,2;b_1}}{\pi.f^F_{1,b_1}}.\dot{u}_{11} - \frac{\xi^F_{2,b_1}.k^F_{2,2;b_1}}{\pi.f^F_{2,b_1}}.\dot{u}_{13} & \text{for } i = 13 \\ -\frac{\xi^T_{1,b_1}.k^T_{1,b_1}}{\pi.f^T_{1,b_1}}.\dot{u}_{14} & \text{for } i = 14 \end{cases} \tag{2.55}$$

where ξ^F_{i,b_1}, ξ^E_{i,b_1} and ξ^T_{i,b_1} denote the structural damping ratio in the i^{th} flapwise, edgewise and torsional mode of vibration, respectively. Similarly, f^F_{i,b_1}, f^E_{i,b_1} and f^T_{i,b_1} are the natural frequencies of a blade in its i^{th} mode of vibration along the aforesaid directions, respectively.

The primary source of excitation for a Horizontal Axis Wind Turbine (HAWT) is the aerodynamic forces due to wind. The element of the system matrices due to the aerodynamic forces on the blade are given by

$$\mathbf{F_{i,b_1,ae}(\dot{u},u,t)} = \int_0^{R_{b_1}} [\mathbf{v_{i,b_1}(p)}.\mathbf{F_{b_1,ae}(p)} + \omega_{\mathbf{i,b_1}}\mathbf{(p)}.\mathbf{M_{b_1,ae}(p)}].dp \quad \text{for } i = 11...13 \tag{2.56}$$

In the above expression, R_{b_1} is the blade length, $\mathbf{F_{b_1,ae}(p)}$ and $\mathbf{M_{b_1,ae}(p)}$ represent the aerodynamic forces and moments per unit length, respectively. Finally, the generalized active force due to gravity is given by

$$\mathbf{F_{i,b_1,gv}(\dot{u},u,t)} = -\int_0^{R_{b_1}} \mathbf{v_{i,b_1}(p)}.\mu_{b_1}(p).g.\hat{x}_2.dp \quad \text{for } i = 11...13 \tag{2.57}$$

The modeling of the other two blades follows the same procedure. Also, the aeroelastic and gravitational forces acting on them can be derived similarly.

2.2.5 Aerodynamic Load

Onshore wind turbines are exposed to different loads, e.g., aerodynamic, gravitational and seismic. Aerodynamic force on the rotor acts as a torque on the low-speed shaft, which is transferred to the generator through the drive-train to produce electricity. Thus, accurate aerodynamic load estimation is critical for wind turbine analysis and design, which is described below.

2.2.5.1 Rotationally Sampled Spectrum

The aerodynamic load acting on the rotor varies periodically. Thus, the wind field can be modeled from a stationary Rotationally Sampled Spectrum (RSS). It is based on Gust-Slicing by each airfoil, which affects the flow variance related to the rotational frequency and its harmonics. The RSS is determined from the homogeneous and isotropic 1D flow spectrum (e.g., Kaimal or von-Karman). The power spectrum of wind approaching a point on the rotating blade is defined by the following Fourier transform pairs [9, 157], i.e.,

$$S_u(f) = 2\int_0^{\infty} \kappa_u(\tau)\cos 2\pi f\tau d\tau \tag{2.58a}$$

$$\kappa_u(\tau) = \int_0^{\infty} S_u(f)\cos 2\pi f\tau df \tag{2.58b}$$

where f is the frequency in Hz, S_u and κ_u are the single-sided power spectrum and autocorrelation function of the wind speed fluctuations, respectively. The autocorrelation function κ_u is derived for a fixed point in space for the longitudinal component of turbulent wind from the input power spectrum, and then the relative autocorrelation functions for a rotating blade at different radial distances are determined. Finally, Eq. 2.58a is used to obtain the RSS.

In general, the Kaimal or von-Karman spectrum is used to derive the input power spectrum for the longitudinal component of turbulence. The energy in the Kaimal spectrum, compared to the von-Karman spectrum, is distributed over a frequency range with a lower peak, which is given by

$$S_u(f) = \frac{4\sigma_v^2 L/\bar{v}}{(1+6fL/\bar{v})^{5/3}} \tag{2.59}$$

where L is the integral length scale of turbulence, while $\bar{v}$ and σ_v are the mean and standard deviation of the wind speed, respectively. The Kaimal spectrum performs better in field conditions, while the von-Karman spectrum is more accurate for wind tunnel test data, which has the following expression

$$S_u(f) = \frac{4\sigma_v^2 L/\bar{v}}{\left[1+70.8\,(fL/\bar{v})^2\right]^{5/6}} \tag{2.60}$$

However, RSS is not directly used in this study to model the incoming wind. Instead of RSS, a freely available software package TurbSim [85], provided by NREL, is used here to simulate the 3D wind field using horizontal and vertical wind shear as well as spatial coherence. Once the wind field time-history is generated, rotational sampling is performed followed by the solution of the Blade Element Momentum (BEM) equations to evaluate the aerodynamic load adopting Ning's algorithm [99].

2.2.5.2 Blade Element Momentum Theory

BEM theory is the most popular tool for predicting aerodynamic forces on a rotating blade due to its computational efficiency compared to other options, e.g., computational fluid dynamics (CFD). It uses the geometric and aerodynamic properties of an airfoil. The blade is a collection of 2D airfoils (i.e., blade element) along its longitudinal dimension, with the flow passing over each airfoil being modeled by balancing the momentum on both sides of the rotor plane. As a result, it combines blade element and momentum theories. The aerodynamic force on a blade element is assumed to be independent (no interaction between the elements) and entirely reliant on the lift, drag, and pitching moment coefficients of that airfoil. Momentum theory (also known as disc actuator theory) is based on fluid dynamics conservation rules. In this approach, different BEM equations are used to evaluate the optimal inflow angle Φ_{opt}, which depends on the blade pitch angle (θ_p), structural twist (θ_s), and torsional twist (θ_t). The chord length (c) and rotational speed (Ω) also affect the aerodynamic forces operating at different locations along the blade length. The blade is discretized into several elements to evaluate the aerodynamic force on each of them, which, on integration along the length, provides the total load. This approach uses two different theories to create a set of equations that are solved iteratively.

The wake flow has two velocity components, one in the axial direction (i.e., V_x) and the other in the tangential direction (i.e., V_y). Hence, the velocity induced on the rotor plane has two orthogonal components, as shown in Fig. 2.3. From this figure, the relative flow velocity v_{rel} can be obtained as

$$v_{rel}(p,t) = \left[((1-a')V_x)^2 + ((1+a'')V_y)^2\right]^{1/2} \tag{2.61}$$

The relative velocity acts at an optimal inflow angle Φ_{opt} with the rotor plane, which can be expressed as

$$\Phi_{opt} = \tan^{-1}\left[\frac{V_x(1-a')}{V_y(1+a'')}\right] \tag{2.62}$$

where a' and a'' are the axial and tangential induction factors, respectively. As indicated in Fig. 2.3, the lift

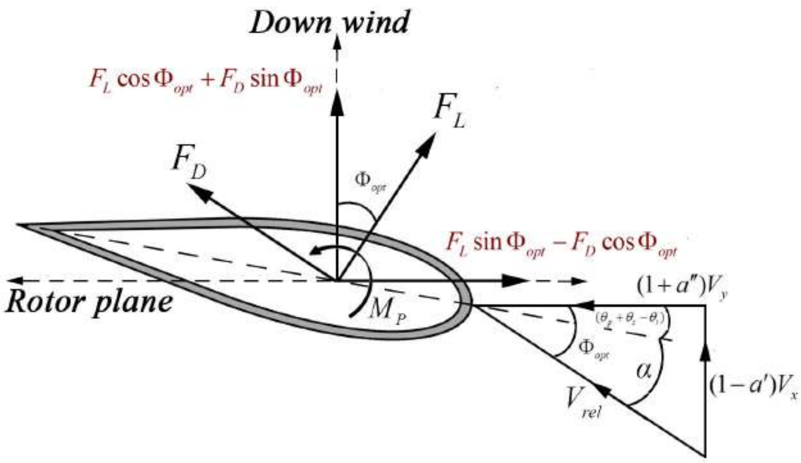

Figure 2.3: Schematic diagram of a 2D airfoil with the velocity and force components.

and drag forces acting on the blade element are perpendicular and parallel to the direction of the incoming flow. These forces on the radial length δp are given by

$$\delta F_L = \frac{1}{2}\rho_a v_{rel}^2 c(p) C_L(\alpha)\delta p \tag{2.63a}$$

$$\delta F_D = \frac{1}{2}\rho_a v_{rel}^2 c(p) C_D(\alpha)\delta p \tag{2.63b}$$

$$\delta M_p = \frac{1}{2}\rho_a V_{rel}^2 . c(p)^2 . C_M(\alpha)\delta p \tag{2.63c}$$

In the above expression, ρ_a is the density of air, and $c(p)$ is the chord length at a radial distance p from the center of rotation. In Eq. 2.63, C_L, C_D and C_M are lift, drag, and pitching moment coefficients of the 2D airfoil that depend on its angle of attack (α). The pitching moment coefficients are measured along the blade pitch axis, i.e., the quarter chord location of the airfoil from its leading edge [5]. The cambered airfoils used in wind turbine blades normally have an aerodynamic centre towards the leading edge of the airfoil from its pitch axis. So, the direction of the pitching moment is such that it tries to de-twist the blade sections (i.e., the moment acts against the structural twisting (θ_s) of the blade). The normal and tangential forces on the blade element can be determined by taking the components of lift and drag forces in the respective directions. Therefore, the normal and tangential forces acting on δp are given by

$$\delta F_N = \delta F_L \cos\Phi_{opt} + \delta F_D \sin\Phi_{opt} \tag{2.64a}$$

$$\delta F_T = \delta F_L \sin\Phi_{opt} - \delta F_D \cos\Phi_{opt} \tag{2.64b}$$

Total normal and tangential force and pitching moment acting on the blade are obtained by summing up the elemental forces along the length of the blade. Here, it may be noted that the tower has a circular cross-section; hence, it can only experience drag forces generated by the inflowing wind. The BEM theory generally ignores the influence of vortex shedding at the blade tip into the wake. As a result, corrections are required to account for various limitations in BEM theory, which are discussed in the following section.

2.2.5.3 Corrections

For a large axial induction factor, the inflow angle in Fig. 2.3 becomes very small, and the contribution of lift force in the tangential direction decreases. This is reflected in lower power output due to reduced torque, which occurs most commonly near the blade tip, referred to as tip-loss. Thus, the axial induction factor must be varied to account for this loss.

Using the wake-disc model, Prandtl [224] studied the behavior of particles downstream and provided an approximate solution that accounts for tip-loss, which is given by

$$f_{\text{loss}}^{\text{tip}}(p) = \frac{2}{\pi}\cos^{-1}\left[exp\left\{-\frac{N_b(R_{b_1}-p)}{2p\sin\Phi_{opt}}\right\}\right] \tag{2.65}$$

Similar to tip-loss correction, hub-loss (or root-loss) correction can be modeled in the following form [9]

$$f_{\text{loss}}^{\text{hub}}(p) = \frac{2}{\pi}\cos^{-1}\left[exp\left\{-\frac{N_b(p-r_{hub})}{2p\sin\Phi_{opt}}\right\}\right] \tag{2.66}$$

where r_{hub} is the hub radius, and N_b represents the number of blades. Thus, the combined tip and hub loss factor is $f_{loss} = f_{\text{loss}}^{\text{tip}} \cdot f_{\text{loss}}^{\text{hub}}$. The normal and tangential forces are modified using the loss factor in the following form

$$\delta F_N = f_{loss}.\delta F_N \tag{2.67a}$$

$$\delta F_T = f_{loss}.\delta F_T \tag{2.67b}$$

Therefore, the flow induction factors are evaluated as

$$a' = \frac{\sigma_p C_N(\alpha,\Phi_{opt})}{\sigma_p C_N(\alpha,\Phi_{opt}) + 4F_L\sin^2\Phi_{opt}} \tag{2.68a}$$

$$a'' = \frac{\sigma_p C_T(\alpha,\Phi_{opt})}{4F_L\sin\Phi_{opt}\cos\Phi_{opt} - \sigma_p C_T(\alpha,\Phi_{opt})} \tag{2.68b}$$

In the above equation, σ_p is the local solidity.

Glauert provided an empirical relationship for the thrust coefficient C_t based on experimental results when the axial induction factor is greater than 0.4, which has the following form

$$C_T = \begin{cases} 4a'(1-a') & \text{if} \quad a' \le a_c \\ 4(a_c^2 + (1-2a_c)a') & \text{if} \quad a' > a_c \end{cases} \tag{2.69}$$

In the above equation, the flow induction factor (for $a_c \simeq 0.2$) using Glauert's correction can be evaluated as

$$a = \begin{cases} \frac{1}{1+K} & \text{if} \quad a' \le a_c \\ \frac{1}{2}\left[2 + K(1-2a_c) - \sqrt{(K(1-2a_c)+2)^2 + 4\left(Ka_c^2 - 1\right)}\right] & \text{if} \quad a' > a_c \end{cases} \tag{2.70}$$

where $K = \frac{4\sin^2\Phi_{opt}}{\sigma_p C_N(\alpha,\Phi_{opt})}$.

Other researchers have also developed empirical curves to fit the experimental data, similar to Glauert's empirical relationship [225,226]. However, these empirical curves do not account for tip and hub losses. A few authors also suggested multiplying the loss factor by the axial induction factor to solve the equations, which creates a mathematical discontinuity. In this context, Buhl [96] suggested a modified version of Glauert's empirical curve to account for tip and hub loss corrections for axial induction factor greater than 0.4, which is given by

$$C_t = \frac{8}{9} + \left(4f_{loss} - \frac{40}{9}\right)a' - \left(4f_{loss} - \frac{50}{9}\right)a'^2 \tag{2.71}$$

2.2.5.4 Ning's Model

Though simple in concept, solving BEM equations with high precision, accuracy, and efficiency can be difficult. Several solution strategies are available in the literature for numerical convergence of axial and tangential induction factors [227,228]. These algorithms require a significant amount of computational time to achieve convergence and often experience numerical instability. In this regard, Ning [99] proposed a solution technique that ensures convergence. The solution of the BEM equation is segmented into three regions (i.e., momentum, empirical, and propeller break) in this proposal to determine the ideal flow angle θ, instead of the traditional approach for optimal induction factors. As a result, the number of equations to be optimized is decreased from two to one to enhance convergence. The local thrust coefficient for an annular ring of the rotor disc is given by blade element theory as follows

$$C_T = \left(\frac{1-a'}{\sin\Phi_{opt}}\right)^2 C_N(\alpha, \Phi_{opt})\sigma_r \tag{2.72}$$

Equating preceding equations (i.e., Eq. 2.71 and Eq. 2.72) offers an axial induction factor with Buhl's correction, which, after simplification, reaches the following form

$$a' = \frac{\gamma_1 - \sqrt{\gamma_2}}{\gamma_3} \tag{2.73}$$

where

$$\gamma_1 = \frac{2f_{loss}}{K} - \left(\frac{10}{9} - f_{loss}\right) \tag{2.74a}$$

$$\gamma_2 = \frac{2f_{loss}}{K} - f_{loss}\left(\frac{4}{3} - f_{loss}\right) \tag{2.74b}$$

$$\gamma_3 = \frac{2f_{loss}}{K} - \left(\frac{25}{9} - 2f_{loss}\right) \tag{2.74c}$$

In the above equation, $K = \frac{4f_{loss}\sin^2\Phi_{opt}}{\sigma_p C_N(\alpha,\Phi_{opt})}$, which is valid for the axial induction factor between 0.4 and 1. For $a' > 1$, the coefficient of thrust can be evaluated from the following expression

$$C_t = 4a'(a'-1)f_{loss} \tag{2.75}$$

Therefore, simplifying and equating the above equation with Eq. 2.72 produces

$$a' = \frac{1}{1-K} \tag{2.76}$$

Similarly, the torque coefficient from the blade element and momentum theories can be equated to determine the tangential induction factor a'', which is given by

$$a'' = \frac{1}{K'-1} \tag{2.77}$$

where K' is defined as

$$K' = \frac{4f_{loss}\sin\Phi_{opt}\cos\Phi_{opt}}{\sigma_p C_T(\alpha, \Phi_{opt})} \tag{2.78}$$

After obtaining the induction factors, the variables can be related to one another to form a residue function proposed by Ning, which results in a reliable and convergent solution, i.e.,

$$f(\Phi_{opt}) = \frac{\sin\Phi_{opt}}{(1-a')} - \frac{V_x}{V_y}\frac{\cos\Phi_{opt}}{(1+a'')} \tag{2.79}$$

As a result, the BEM solution has been reduced from a two-dimensional fixed-point algorithm to a one-dimensional root-finding algorithm. Thus, the steps for solving the BEM equation in this approach are given in Algorithm. 2.1.

2.2.6 Seismic Load

Seismic loads can applied in this model by considering the first three translational DOFs located at the tower base i.e., $i = 1..3$. The seismic forces are adopted using the lateral time histories of ground motion at the base. As a result, a damped oscillator is modeled at the base [122] to provide the required force. Therefore,

Algorithm 2.1: Modified BEM algorithm [99]

1. Consider local inflow angle, Φ.
2. Evaluate the local angle of attack, $\alpha = \Phi - (\theta_p + \theta_s - \theta_t)$.
3. Compute the lift and drag coefficients, i.e., $C_L(\alpha)$ and $C_D(\alpha)$.
4. Estimate normal and tangential coefficients, i.e., $C_N(\alpha, \Phi_{opt})$ and $C_T(\alpha, \Phi_{opt})$.
5. Determine the flow induction factors a' and a'' using Eq. 2.68.
6. Check the residual error from Eq. 2.79.
7. Assume a different local inflow angle until the residual error is zero.

the seismic force at each time step is derived using the base motion, which can be expressed as

$$F_{i,eq} = K_p.(u_{Ri}) + C_{d_p}.(\dot{u}_{Ri}) \quad \text{for} \ \ i = 1..3 \tag{2.80}$$

In the above equation, K_p and C_{d_p} represent the stiffness and damping coefficient of the oscillator, and the terms u_R (where $u_R = x_g - u_i$) and $\dot{u}_R$ are the relative displacement and velocity at the tower base. In the absence of a seismic event, the relative displacement and velocity at the tower base can be considered as zero. This capability of incorporating seismic forces in the mathematical model is utilized in the later chapters to design tower vibration control strategies. In this chapter, the numerical simulation presented further is conducted without considering any seismic loads.

2.3 Numerical Simulation

In this section, a numerical simulation of the response of a wind turbine is presented considering aerodynamic pitching moment and bending-torsion coupling. The dynamic response of the combined system in a multi-body framework is investigated for different operating conditions. For this purpose, properties of NREL-5MW onshore wind turbine with 61.5m blades have been used. The primary composite structural layup of this blade was first designed by Sandia National Laboratory (SNL) [229], which met the design criterion set by International Electrotechnical Commission (IEC) standards [87] and National Renewable Energy Laboratory (NREL) [5]. A typical composite layup of the baseline blade section is shown in Fig. 2.4. The materials used in this blade model are ELT-5500 (Uni Directional (UD)), SNL-Triax, Sartex, Carbon (UD), Foam and Gelcoat, whose details may be found in the Sandia report [229]. In the baseline model, different material stacks and layup sequences are used in different sections of the blade, such as spar cap, leading and trailing edge panels, the trailing edge reinforcements, root reinforcements, and shear webs. Only common layers marked yellow in Fig. 2.4 (i.e., blade skin) are made of SNL-Triax, which runs uniformly from root to tip of the blade. The blade skin is also subdivided into two layers (top and bottom), and all other materials are sandwiched in between, except Gelcoat, which forms the outermost layer for protection. All these layups are provided anti-symmetrically in the baseline model to avoid coupling between bending and torsion, i.e., without bending-torsion coupling (WBTC).

Structural properties of the blade, e.g., mass per unit length, stiffness, and elastic axis offsets, are evaluated from PreComp [221]. The skewness of the principal material direction of the laminae with respect to the blade axis is shown in Fig. 2.4. The mode shapes of the blade are determined using these properties in BModes [230] and are shown in Fig. 2.5. The response of the combined system is solved using these mode shapes in Kane's approach as described in §2.2. The response simulation is repeated for two cases, i.e., with and without coupling. Different response quantities (e.g., U_{B1_OOP}, U_{B1_IP}, U_{B1_T}, U_{TFA}, U_{TSS}) are considered in this analysis for comparison. Here, it may be noted that subscripts $B1\_OOP$, $B1\_IP$ and $B1\_T$ represent the out-of-plane, in-plane and torsional response of the 1^{st} blade, respectively, whereas subscripts TFA and TSS denote the fore-aft and side-to-side motions at the tower top. The beneficial and adverse effects of bending-torsion coupling are also demonstrated using these response quantities. Finally, a multi-objective optimization problem is solved to determine the optimal fibre orientation in the skin of the blade.

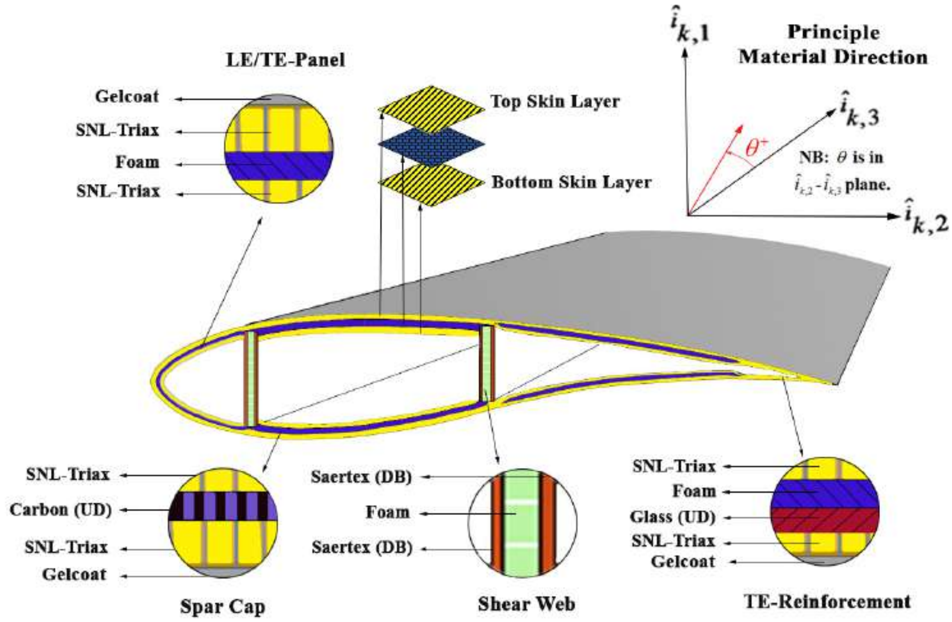

Figure 2.4: Cross-sectional layout of the composite blade (NB: θ shows positive fibre angle.)

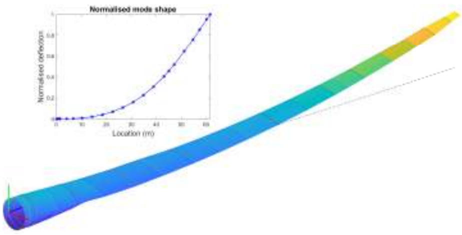

(a)

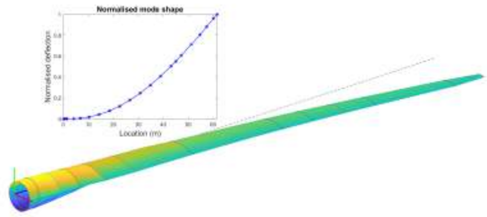

(b)

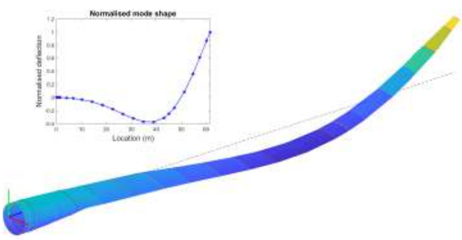

(c)

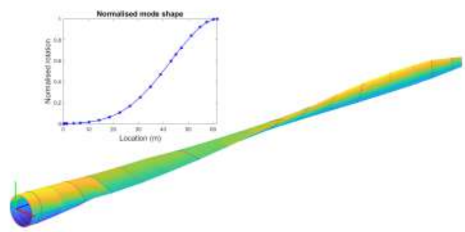

(d)

Figure 2.5: : Blade Mode Shapes; (a) 1^{st} Flapwise, (b) 1^{st} Edgewise, (c) 2^{nd} Flapwise & (d) 1^{st} Torsion (N.B.: Normalised shape is shown in inset)

2.3.1 Properties of Onshore Wind Turbine and Operational Conditions

The basic properties of the benchmark NREL 5MW wind turbine are presented in Table 2.3, where the subscripts ci, r and co represent the cut-in, rated, and cut-out values, respectively. The blades are composed of 8 different airfoils along their length, whose properties like structural-twist, lift, and drag coefficients may be found in NREL report [5]. The drive train has a gearbox ratio of 97 with torsional stiffness and generator inertia are 867637kN-m/rad and 534kg-m^2, respectively. In this numerical simulation, the generator is assumed to be operating with 100% efficiency without loss of generality and may be reduced if necessary. The properties of the baseline controllers and other parameters are also taken from the NREL report [5]. The steady and turbulent wind fields for different mean values corresponding to cut-in, below-rated, rated,

Table 2.3: NREL 5-MW Turbine Data [5].

Basic Descriptions		Blade (SNL-61.5m)		Tower	
Max. Power	5000 kW	Length	61.5 m	Height	87.6 m
No. of blades	3	Mass	17740 kg	Mass	347460 kg
Rotor dia.	126 m	f^F_{1,b_k}, f^F_{2,b_k}	0.826, 2.62 Hz	$f^{FA}_{1,tw}$	0.324Hz
Hub-height	90 m	f^E_{1,b_k}, f^E_{2,b_k}	1.00, 3.86 Hz	$f^{SS}_{1,tw}$	0.312Hz
V_{ci}, V_r, V_{co}	3 m/s, 11.4 m/s, 25 m/s	f^T_{1,b_k}	6.65 Hz	ξ^{FA}_{tw}, ξ^{SS}_{tw}	1%, 1%
Ω_{ci}, Ω_r	6.9 rpm, 12.1 rpm	$\xi^F_{b_k}$, $\xi^E_{b_k}$, $\xi^T_{b_k}$	0.47%, 0.47%, 1%		

above-rated and cut-out speeds at 90m hub height are simulated using TurbSim [85]. The onshore power-law exponent of 0.2 for steady wind and 15% turbulence with IEC Kaimal spectra have been used for wind field simulation. Fig. 2.6 shows the simulated wind field in this study corresponding to rated speed with 15% turbulence. The response of the multi-body system is obtained using these inputs and other structural properties for performance evaluation. However, before investigating the effect of bending-torsion coupling and its impact on optimal fibre orientation, the baseline control systems implemented on the turbine are discussed in the next subsection, and after that, the mathematical model is validated with benchmark responses.

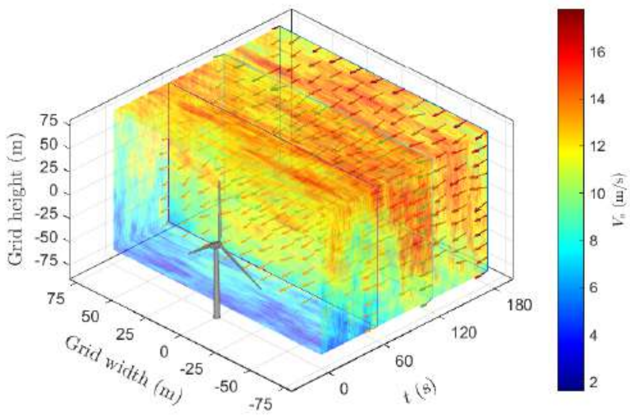

Figure 2.6: Simulated wind field for rated speed and 15% turbulence (N.B.: Turbine diagram is not to scale)

2.3.2 Baseline Control Systems

The traditional approach for power regulation in a horizontal axis wind turbine follows two distinct control strategies: generator-torque control and full-span rotor-collective blade-pitch control. The first option of these two strategies is set to operate below the rated wind speed, while the second option is configured above it. Thus, the generator-torque controller, in principle, maximizes power output, while the blade-pitch controller acts to maintain generator speed. The properties of these baseline controllers and other parameters for the benchmark NREL 5MW turbine are discussed in the following sub-sections.

2.3.2.1 Generator Torque Control

As stated earlier, the generator-torque controller primarily aims to maximize power output below the rated speed. Both generator-torque and blade-pitch controller use the generator speed as a primary feedback. A recursive, single-pole low-pass filter with exponential smoothing is normally used to filter the feedback for both torque and pitch controllers to mitigate any high-frequency excitation [231].

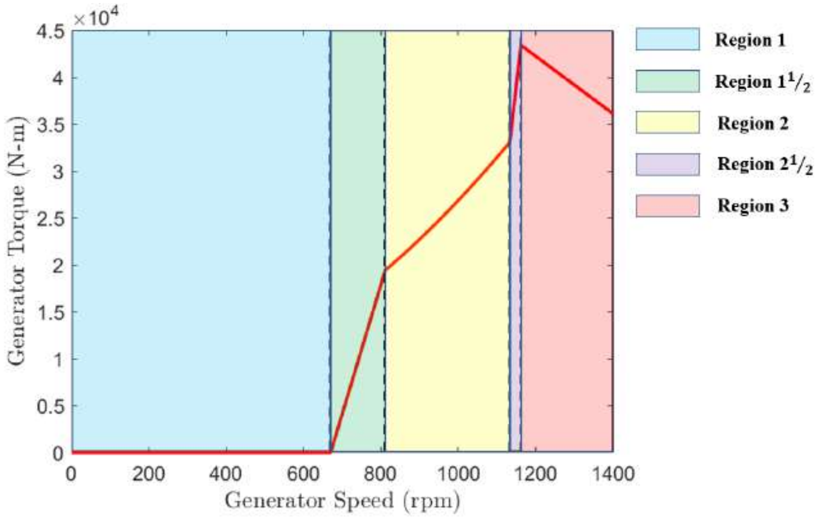

Figure 2.7: Generator torque in different control regions

The generator torque is evaluated in five different control zones, as shown in Fig. 2.7. Before the cut-in wind speed, i.e., Region 1, the generator torque is zero, and no electricity is extracted from the wind; instead, the airflow is used to initiate rotation, i.e., start-up. The next region with optimized power output is Region 2 (i.e., cut-in to rated condition). In this region, the generator torque is proportional to the square of the filtered feedback to maintain a constant (i.e., optimal) tip-speed ratio. Finally, the generator power is retained constant in Region 3 (i.e., rated to cut-out condition) so that the generator torque is inversely proportional to the filtered generator speed. Following the NREL report[5], two more transitions (i.e., Region 1½ and Region 2½) are employed to set the limit on the generator speed and tip speed ratio, as shown in Fig. 2.7. The transition speeds from one region to another (i.e., Region 1 to Region 1½, Region 1½ to Region 2, and Region 2½ to Region 3) are taken as 670 rpm, 871 rpm, and 1161.96 rpm, respectively. The torque and its rate (in absolute terms) in the generator torque controller are saturated to avoid excessive overloading. Table. 2.4 lists the essential parameters of the generator torque controller.

2.3.2.2 Collective Pitch Control

The blade-pitch controller maintains the generator speed above the rated flow. A full-span blade pitch controller is a single-variable device that changes the blade pitch angle to reduce generator speed fluctuation. The generator torque is inversely proportional to its speed to keep the power output constant above the rated wind, i.e.,

$$T_{gn} = \frac{P_0}{G_{br}.\Omega} \tag{2.81}$$

Here, G_{br} is the gearbox ratio, and Ω represents the rotor speed, which is obtained from the azimuth of the low-speed shaft (i.e., $\Omega{=}\dot{u}_9$). The term P_0 refers to the rated power of the turbine. The first-order Taylor series expansion of Eq. 2.81 has the following form

$$T_{gn} \approx \frac{P_0}{G_{br}.\Omega_0} - \frac{P_0}{G_{br}.\Omega_0^2}.\Delta\Omega \tag{2.82}$$

In the above equation, Ω_0 is the rated generator speed of the turbine. The aerodynamic torque exerted on the drive-shaft is a function of collective pitch angles (θ_p) of the rotor, i.e.,

$$T_{aero}(\theta_p) = \frac{P(\theta_p)}{\Omega_0} \tag{2.83}$$

In the above expression, θ_p represents the pitch angle at the rotor hub, and P denotes the power produced by the turbine at a particular time instant. Using first-order Taylor series expansion, i.e., similar to Eq. 2.82, Eq. 2.83 can be expressed as

$$T_{aero} \approx \frac{P_0}{\Omega_0} + \frac{1}{\Omega_0}.\left(\frac{\partial P}{\partial \theta_p}\right).\Delta\theta_p \tag{2.84}$$

In this expression, the perturbation of the pitch angle around its operating point is denoted by $\Delta\theta_p$, which is correlated to the rotor speed variation (i.e., $\Delta\Omega$) through the following expression [5]

$$\Delta\theta_p = K_P.G_{br}.\Delta\Omega + K_I\int_0^t G_{br}.\Delta\Omega.dt + K_D.G_{br}.\Delta\dot{\Omega} \tag{2.85}$$

In this format, the centralized controller has proportional, integral, and derivative gains for the pitch angle, which are denoted by K_P, K_I, and K_D, respectively. Thus, the dynamics of the drive-train can be modelled by the following expression

$$T_{aero} - G_{br}.T_{gn} = I_{DT}.\Delta\dot{\Omega} \tag{2.86}$$

Parameter I_{DT} in the above equation is the inertia of the drive-train. Substituting Eq. 2.82, Eq. 2.84 and Eq. 2.85 into Eq. 2.86 and rearranging them lead to the following second-order equation of motion for the rotor-speed fluctuation

$$\begin{aligned}&\left[I_{DT} - \tfrac{G_{br}}{\Omega_0}\left\{\tfrac{\partial P}{\partial\theta_p}.K_D\right\}\right].\ddot{\phi} + \left[-\tfrac{G_{br}}{\Omega_0}\left\{\tfrac{\partial P}{\partial\theta_p}.K_P +\right\} - \tfrac{P_0}{\Omega_0^2}\right].\dot{\phi}\\ &+\left[-\tfrac{G_{br}}{\Omega_0}\left\{\tfrac{\partial P}{\partial\theta_p}.K_I\right\}\right].\phi = 0\end{aligned} \tag{2.87}$$

The term $\dot{\phi}$ in this formulation is used as a substitute for $\Delta\Omega$ for simplification purposes only. As shown in Eq. 2.87, the idealized PID-controlled rotor-speed fluctuation behaves as a second-order system with the natural frequency ω_ϕ and the critical damping ratio η_ϕ, i.e.,

$$\omega_\phi = \sqrt{\frac{\left[-\tfrac{G_{br}}{\Omega_0}\left\{\tfrac{\partial P}{\partial\theta_p}.K_I\right\}\right]}{\left[I_{DT} - \tfrac{G_{br}}{\Omega_0}\left\{\tfrac{\partial P}{\partial\theta_p}.K_D\right\}\right]}} \tag{2.88a}$$

$$\eta_\phi = \frac{\left[-\tfrac{G_{br}}{\Omega_0}\left\{\tfrac{\partial P}{\partial\theta_p}.K_P\right\} - \tfrac{P_0}{\Omega_0^2}\right]}{2.\left[I_{DT} - \tfrac{G_{br}}{\Omega_0}\left\{\tfrac{\partial P}{\partial\theta_p}.K_D\right\}\right].\omega_\phi} \tag{2.88b}$$

The derivative term increases the effective inertia of the drive-train. At the same time, the proportional term introduces damping while the integral term provides restoring force with positive control gains. Also, since the generator torque decreases as the speed increases (i.e., to maintain constant power) above its rated value, the generator-torque controller incorporates negative damping in Eq. 2.87, as indicated by the term $\frac{P_0}{\Omega_0^2}$. The proportional term in the blade-pitch controller must compensate for this negative damping. As the drive-train inertia is significantly high, the derivative term in this control algorithm offers insignificant performance enhancement of the overall system. For all practical purposes, NREL recommends ignoring the negative damping and derivative term in Eq. 2.87 [5]. It also recommends $\omega_\phi = 0.6$ rad/s and $\eta_\phi = 0.7$ for the smooth operation of the 5MW benchmark turbine used in this simulation. The unknowns, i.e., K_P and K_I in Eq. 2.88 need to be determined for optimal performance of the pitch controller. The solutions to these equations are simple for a full-span rotor with a collective pitch controller. Moreover, if the blade-pitch sensitivity ($\frac{\partial P}{\partial\theta_p}$) is known, the optimal values of K_P and K_I can be determined directly. The linear relationship between the pitch sensitivity and blade-pitch angle provides proportional and integral gains, which are given by

$$K_P(\theta_p) = \frac{2I_{DT}\Omega_0\omega_\phi\eta_\phi}{G_{br}.\frac{-\partial P}{\partial y}(\theta_p = 0)}.G_K(\theta_p) \tag{2.89a}$$

$$K_P(\theta_p) = \frac{I_{DT}\Omega_0\omega_\phi^2}{G_{br}.\frac{-\partial P}{\partial y}(\theta_p = 0)}.G_K(\theta_p) \tag{2.89b}$$

G_k is the gain correction factor in the above equation depending on the pitch angle θ_p, which can be represented as $G_K(\theta_p) = 1 + {\theta_K}^{-1}\theta_p$. Here, it may be noted that the term θ_K is the blade pitch angle at

Table 2.4: Details of control system

Torque Controller		**Pitch Controller**	
Torque Constant in Region 2	0.02558 N-m/rpm^2	Min. Pitch	0^o
Rated Torque	43.0936 kN-m	Max. Pitch	90^o
Max. Torque	47.403 kN-m	Max. Pitch Rate	8^o/s
Max. Torque Rate	15 kN-m/s	Peak Power Coefficient	0.482
Min. Pitch for Region 3 torque	1^o	Pitch at Peak Power Coefficient	0^o

which pitch sensitivity is doubled from its value at the rated condition.

Following the procedure explained above for the benchmark turbine, NREL recommends the gains as, $K_P(\theta_p = 0) = 0.01882681s$, $K_I(\theta_p = 0) = 0.008068634$, and $K_D = 0$, corresponding to $\theta_K = 6.30234^o$ [5]. The essential parameters and saturation limits of the collective blade pitch controller employed in this numerical simulation are listed in Table. 2.4.

2.3.3 Model Validation

In this section, the proposed model for the wind turbine is validated extensively. The validation exercise is carried out in three different stages- (i) the load-deformation behavior of a composite beam under static loading along with bending torsion coupling, (ii) the dynamic response of the multi-body system without bending torsion coupling, and (iii) the combined dynamic response of the multi-body system with bending torsion coupling for the whole operating range with a finite element based benchmark software HAWC2 [213]. The details of this three-stage validation are explained below

- In the first case, the static response of a composite double-box cantilever beam is analyzed using the present code and compared with the published data by De Goejj et al.[1]. This exercise is carried out to demonstrate the accuracy of the bending-torsion coupling modeled in the MATLAB [232] code developed for this study. As the prime focus is on validating combined behavior with available experimental data, the static analysis is chosen to maintain uniformity with the published results. It is achieved by arresting all other DOFs except the blade. Also, the inertia module in Kane's formulation is not utilized in this validation. The structural layup of the beam is kept the same as proposed by De Goejj et al.[1]. The schematic diagram of the beam and the sectional details are shown in the inset of Fig. 2.8. This figure also shows the tip twist of the beam when exposed to a vertical point load at the free end. The torsional rotation at the tip obtained from different analyses (i.e., present MATLAB code, experimental and numerical results from De Goejj et al.[1]) are compared. It is observed that the MATLAB code developed in this study closely matches the other two results. The difference between these results is well within 5%. As the load increases, the experimental results slightly overpredict the response compared to the other two. However, even under this load condition, the MATLAB code developed in this study performs better than the other numerical result published in De Goejj et al.[1]. However, the slight difference in the response obtained from the different models is insignificant for all practical purposes. Therefore, it may be concluded that the present model can perform satisfactorily in computing the coupled response of a beam with sufficient accuracy.

- Once the model for bending-torsion coupling is validated, the combined multi-body dynamic code is verified next. For this purpose, the complete onshore wind turbine is developed using Kane's approach, and the coupled differential equations are solved using the 4^{th} order Ranga-Kutta integration scheme with a sufficiently small time step (i.e., $\delta_t = 0.0125s$) to retain the accuracy. The model is validated with the response obtained from FAST [76] without bending-torsion coupling, i.e., the DOFs corresponding to torsion are turned off. The aerodynamic loads in the normal and tangential direction of the rotor and the pitching moments are evaluated using two different codes, i.e., FAST and the present model, which is shown in Fig. 2.9. This figure shows a close match between the aerodynamic loads and pitching moments obtained from two different sources. The amplitude and frequency distribution of the aerodynamic loads obtained from these two sources are consistent, and the deviation between them is insignificant and, hence, not reported separately. Once the aerodynamic loads are validated, the multi-body dynamic system is solved and the responses (i.e., u_{B1_OOP}, u_{B1_IP}, u_{B1_T}, u_{TFA},

u_{TSS}) are compared (with baseline control) in Fig. 2.10, where their corresponding Fourier amplitudes are given in the inset. The deflected shape of the turbine, corresponding to the time of peak normal stress in the blade, is displayed in Fig. 2.12a, where the bi-directional bending of the blades and tower can be observed. The findings from these two codes are identical in magnitude and frequency content. It is explored further over the entire operating range, and the peak blade responses from these two codes are compared. Fig. 2.11 shows these results in the out-of-plane and in-plane directions for different wind flow conditions where the deviation between them is well within 5%. It demonstrates the modeling accuracy over the complete operating range, which implies the validity of the MATLAB code developed using the formulation presented in the previous sections. The states evaluated from this analysis can be further used to derive other structural responses, e.g., stress and strains developed in different components. Fig. 2.12b shows the stress contour of the deflected blade at the same time instant, i.e., 280.85s. It may be noted that the maximum stress concentration occurs at a distance of 34.85m from its root.

- Further, the multi-body model with bending-torsion coupling is validated with a Finite Element Method (FEM)-based benchmarked software HAWC2 [213] developed by the National Laboratory Denmark. The HAWC2 code is designed to model wind turbine responses in the time domain. Its structural analysis is based on a multi-body formulation, where each body is modeled as an assembly of Timoshenko beam elements. This general formulation allows for handling complex structures and accommodates arbitrarily large rotations of the bodies. This software represents the turbine by an assembly of bodies connected through constraint equations, including rigid couplings, bearings, prescribed fixed bearing angles, and more. The aerodynamic component of the HAWC2 code relies on blade element momentum theory, but it is extended beyond the classic approach to account for dynamic inflow, dynamic stall, skew inflow, shear effects on induction, and the impact of large deflections [213]. Hence, it is evident that HAWC2 is a more high-fidelity coupled model for horizontal-axis wind turbines.

  The results obtained from these two codes are compared in two steps. At first, the time history responses of different turbine DOFs are compared for rated wind and 10% Mann's turbulence [86] intensity, available in HAWC2. In this context, it should be noted that the turbulence box used in HAWC2 is imported into the MATLAB code for comparing the responses. The time histories of the concerned turbine DOFs ((i.e., u_{B1_OOP}, u_{B1_IP}, u_{B1_T}, $\dot{u}_{Ge\_Az}$, u_{TFA}, and u_{TSS})) obtained from these two models are compared in Fig. 2.13, where their corresponding Fourier amplitudes are given in the inset. The findings from these two codes are in good agreement regarding magnitude and frequency content. The maximum difference in the peak blade pout-of-plane response is found to be 6.6%, whereas it was 9.9% in the case of in-plane response. The tower response varied more ,with a maximum difference of 14.9% in the peak value. It should be noted that the present model is linear and cannot capture the effects of large deflections/rotations or geometric non-linearity. Also, the aerodynamic load simulation in HAWC2 is more detailed than in the present model. Therefore, the discrepancies in the responses can be attributed to the significantly fewer DOFs used in the present model compared to HAWC2. The goal of developing the current model is to achieve reasonable solutions with manageable computational costs, which has been successfully achieved in the simulations.

  In the second step of the validation, the complete operating range of the turbine is investigated. The peak responses of the DOFs mentioned earlier under steady wind flow are compared in Fig. 2.14, showing good consistency and agreement between these two codes. The maximum error of 8% is observed in the peak blade in-plane response at the cut-out speed. This discrepancy may be due to the fact that only a few modes are considered in the present model, whereas HAWC2 accounts for the complete FEM stiffness and mass matrices. The peak tower fore-aft response also differed by approximately 10% at the cut-out speed. The higher drag forces in the high wind speed regime, resulting from the inclusion of nacelle and hub as aero-drag elements in the HAWC2 model, contribute to the slightly higher errors in this DOF above the rated wind speed range. It is also important to note that the tower response in the fore-aft direction is around 0.14m at 25 m/s wind speed, which is significantly lower than the peak response at the rated condition. As a result, the errors in this case should not impact the design and analysis of actual industrial turbines. Errors in other DOFs are also negligible at this wind speed for the same reason. Therefore, based on the validations presented here, it may be concluded that the present model can perform satisfactorily in computing the bending-torsionally coupled aero-servo elastic response of a horizontal axis wind turbine.

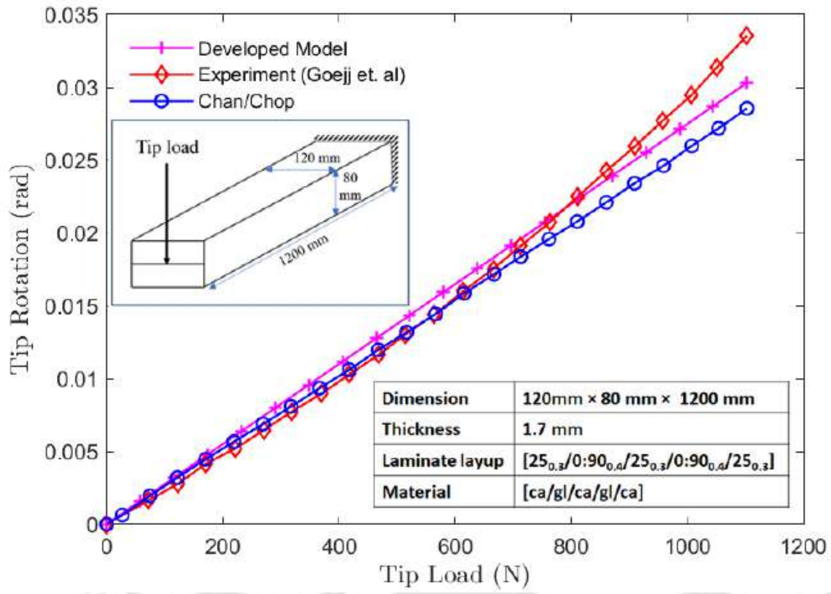

Figure 2.8: Response validation with De Goejj et al. [1] (Case 1)

2.3.4 Response Analysis: Dynamic Coupling

Once the model is validated, it is further used to study the effect of bending-torsion coupling (BTC) on the dynamic response of different structural components of the turbine under different operational scenarios. First, the dynamic coupling is considered without any elastic coupling. The offset of the blade aerodynamic centre (l_{ae,b_k}) from its pitch axis generates a pitching moment along the same axis, which in turn affects the torsional and bending response of the blade. The chordwise offsets (measured from the quarter chord location of the airfoil, i.e., pitch axis) of different airfoils are shown in Fig. 2.15a, and subsequently, a few nodal time histories of pitching moments are displayed in Fig. 2.15b. The flapwise offsets of these centres are insignificant, and hence they are not considered in this study. Thus, the aerodynamic response is simulated using the model described in §2.2, and the sample time histories corresponding to different response quantities selected earlier are shown in Fig. 2.16 for 17m/s mean wind speed and 15% turbulence. This value of wind speed is higher than its rated value and is selected without loss of generality to show the effects of dynamic coupling. However, if the bending-torsion coupling is zero (i.e., WBTC case), the blades experience an insignificant torsion as it is sufficiently stiffer in this DOF. Hence, the torsional DOF is not solved for the WBTC case in this simulation.

Fig. 2.16 shows that responses at the blade tip and nacelle increase due to dynamic bending-torsion coupling. Table 2.5 summarises the absolute values of the peak, mean and peak-to-peak (P2P), i.e., the range of these response quantities. It can be observed that the percentage increase in these quantities due to dynamic bending-torsion coupling are significant. The mean response of the blade is found to increase 32.55% in the out-of-plane direction, while its change in the orthogonal direction (i.e., in-plane) is 11.43%. The displacement at the top of the tower in its fore-aft direction increases by 11.97% due to dynamic coupling. However, the response at the tower top in its side-to-side direction does not vary much. It indicates that the dynamic bending torsion-coupling has no impact along this degree of freedom, where the torsional rigidity of the drive-train is very high.

Further, the study continues to investigate the impact of coupling at different wind speeds over the complete operating range of the turbine. The mean blade tip aerodynamic load variations due to dynamic coupling are shown in Fig. 2.17a for different wind speeds. These results show that the normal and tangential loads acting at the blade tip increase due to dynamic coupling beyond the rated speed. The variation in the dynamic responses also follows the same principle. Five different response quantities mentioned earlier are simulated for wind speeds corresponding to cut-in, rated and cut-out. Once the response time histories are simulated, the absolute values of the peak, mean and range of these responses with and without coupling are evaluated, which are summarised in Table 2.5. These result signify the importance of dynamic bending-torsion coupling for horizontal axis wind turbines. As evident, the effect of dynamic coupling is not prominent for cut-in wind speed, but the difference gradually increases with the increase of wind speed, reaching its

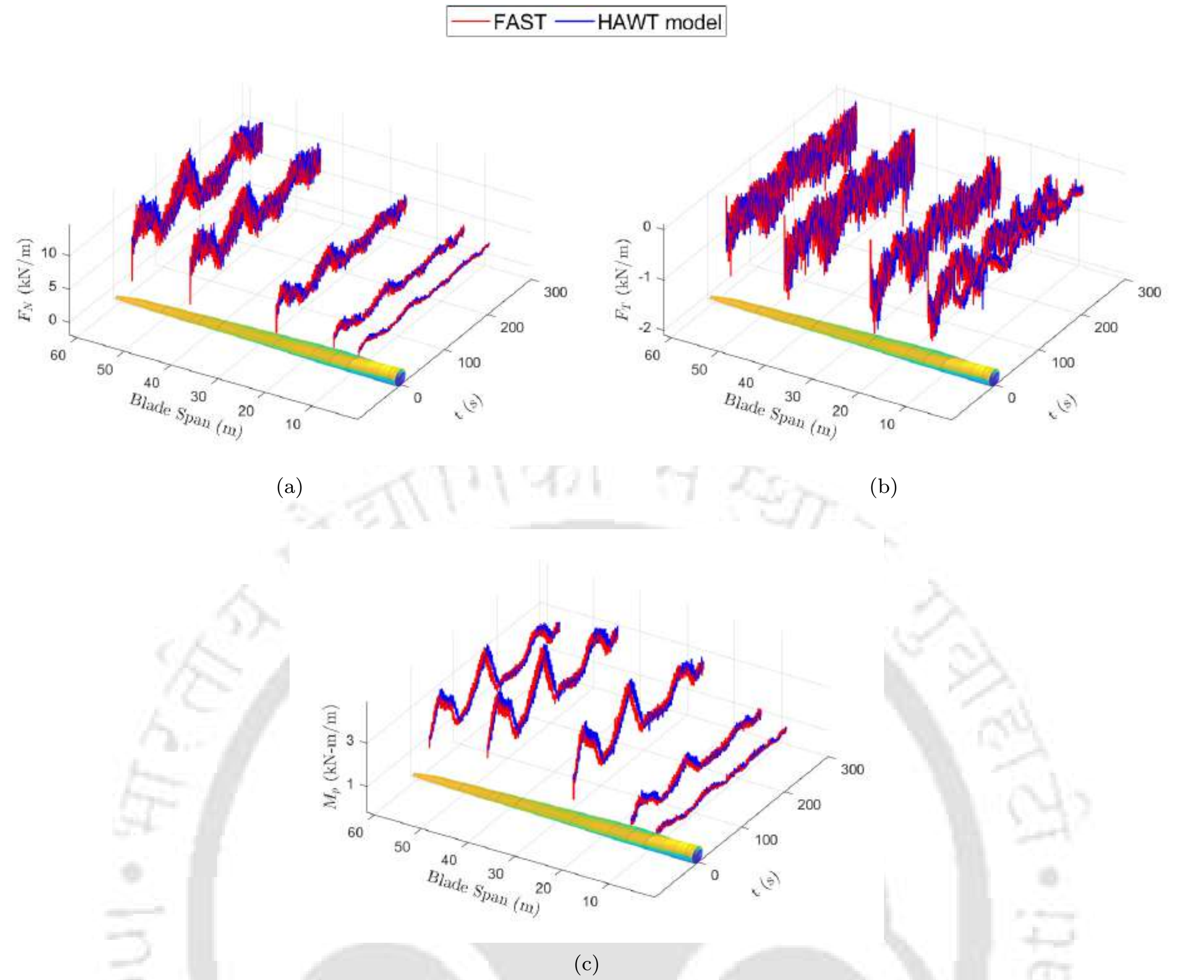

Figure 2.9: : Load validation (Case 2); (a) Normal force, (b) Tangential force & (c) Pitching moment at blade nodes for rated wind with 15% turbulence (N.B.: Blade diagram is used for representation purpose, it is not to scale)

maximum at cut-out. The percentage change in the mean(μ) responses due to dynamic coupling are further summarised in Fig. 2.17b. Here, it should be noted that the pitch angle of the blade is zero between the cut-in to rated speed. However, a fixed-pitch angle is applied beyond the rated value as recommended by NREL to maintain the rotor *rpm*. Together these results prove that dynamic coupling between bending deformation and torsion has a significant impact on the response of the turbine blade. Hence, it is necessary for accurate assessment of stresses developed in the blades, affecting their design and operational life.

2.3.5 Response Analysis: Elasto-Dynamic Coupling

Once the effect of dynamic bending-torsion coupling arising from the offset of the aerodynamic centre from the centroidal axis has been analyzed, the study continued to investigate the impact of elastodynamic coupling. Here, additional elastic coupling parameters are introduced in the model, as discussed in Eq. 2.54a. This coupled elastic stiffness can arise from non anti-symmetric composite layups, where the fibre orientation and laminate properties can be controlled to induce cross-coupled stiffness between bending and torsional modes. As mentioned in §2.2.4, the elastic coupling parameters can vary to ± 0.2 [222, 223]. Hence, the range of $\lambda_{b_k}^{FT}$ is selected to be ± 0.1 in this study, which falls well within the achievable limits. Here it should be noted that the blade is elasto-dynamically coupled between two orthogonal bending directions (i.e., flapwise and edgewise) because of the structural twisting, which is taken into account with the help of twisted mode shapes as mentioned earlier. Elastic flap-edge coupling originating from unbalance in composite layups is not considered in this simulation to focus on the impact of bending-torsional coupling only. A sensitivity analysis is carried out for different wind flow conditions keeping the above-mentioned parameters the same

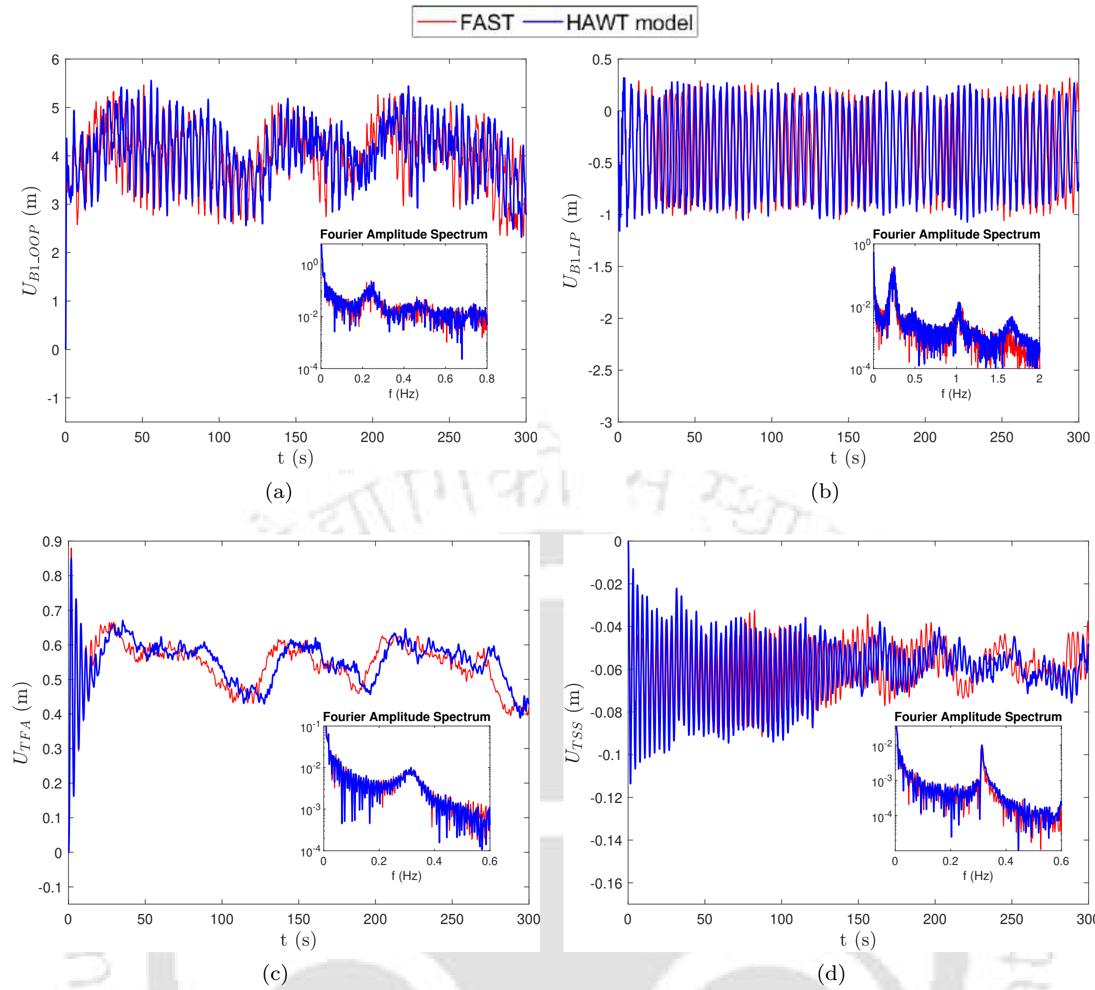

Figure 2.10: Response validation (Case 2); (a) blade out-of-plane, (b) blade in-plane, (c) tower top in fore-aft & (d) tower top in side-to-side for rated wind with 15% turbulence

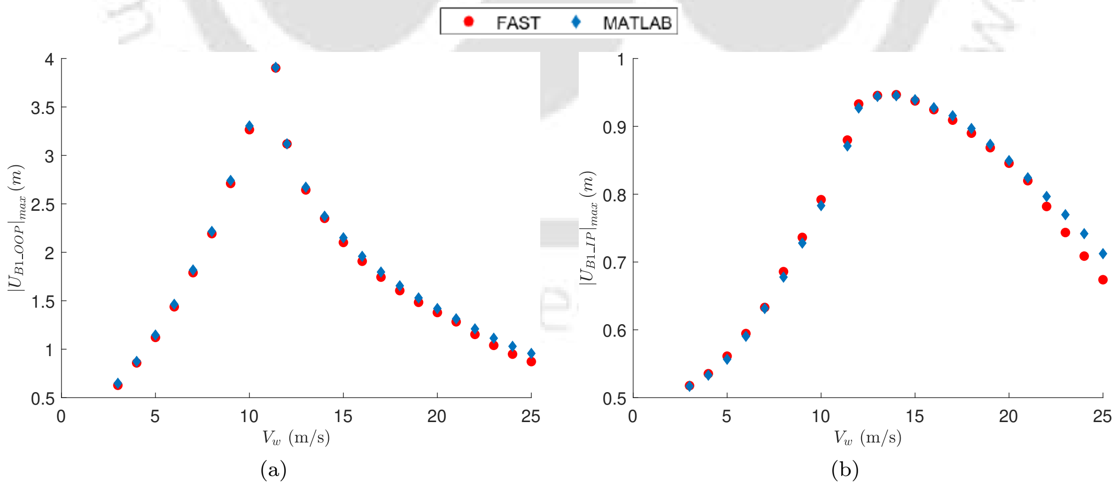

Figure 2.11: Peak response validation (Case 2); (a) blade out-of-plane, (b) blade in-plane

throughout the blade section. Fig. 2.18 shows the mean response of different DOFs due to different steady wind speeds and $\lambda_{b_k}^{FT}$, where predefined blade pitch angles are used, as suggested by NREL. These results show that as $\lambda_{b_k}^{FT}$ increases (i.e., twist-to-feather) the mean value of blade response quantities (e.g., in the out-of-plane direction, blade tip torsional twist) decrease over the complete range of flow conditions as shown in Fig. 2.18a and Fig. 2.18e, respectively. Since the angle-of-attack decreases with the increase of $\lambda_{b_k}^{FT}$, the

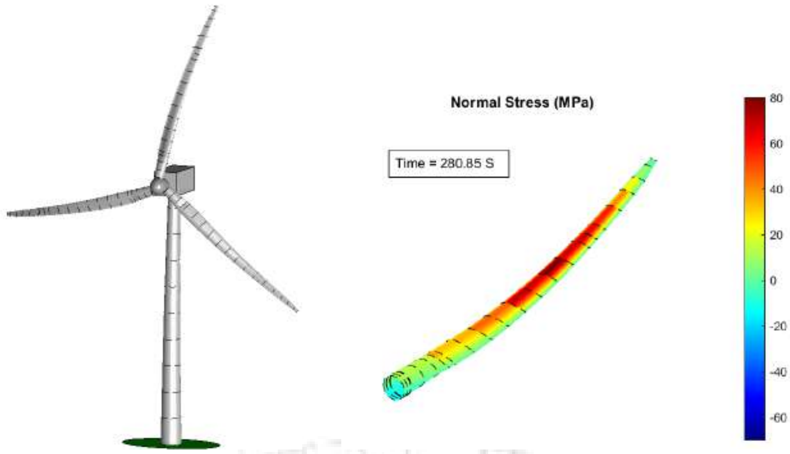

(a) (b)

Figure 2.12: Simulation results; (a) the deflected shape of the turbine at the time instant of peak normal stress of blade, for rated condition (N.B.: The actual deflected shape is exaggerated by a factor of 3 for better representation) & (b) blade stress contour

Table 2.5: Effect of dynamic bending-torsion coupling on absolute responses at cut-in, rated, above rated and cut-out speed

	DOFs	**Without BTC**			**With BTC**		
		Peak	**Mean**	**P2P**	**Peak**	**Mean**	**P2P**
Cut-in	$u_{B1\_OOP}(m)$	0.82	0.59	0.45	0.84	0.61	0.48
	$u_{B1\_IP}(m)$	0.56	0.02	1.09	0.56	0.02	1.08
	$u_{TFA}(m)$	0.06	0.03	0.06	0.06	0.03	0.06
	$u_{TSS}(m)$	0.05	0.00	0.10	0.05	0.00	0.10
	$u_{B1\_T}(rad)$	-	-	-	0.06	0.03	0.04
Rated	$u_{B1\_OOP}(m)$	5.91	3.67	4.15	5.95	3.89	4.02
	$u_{B1\_IP}(m)$	1.14	0.35	1.52	1.10	0.28	1.52
	$u_{TFA}(m)$	0.76	0.49	0.50	0.76	0.51	0.48
	$u_{TSS}(m)$	0.08	0.06	0.06	0.09	0.06	0.07
	$u_{B1\_T}(rad)$	-	-	-	0.06	0.03	0.04
17 m/s	$u_{B1\_OOP}(m)$	3.14	1.27	3.72	4.23	1.68	4.71
	$u_{B1\_IP}(m)$	1.36	0.35	2.02	1.39	0.39	2.01
	$u_{TFA}(m)$	0.36	0.24	0.24	0.42	0.27	0.28
	$u_{TSS}(m)$	0.07	0.14	0.13	0.07	0.12	0.14
	$u_{B1\_T}(rad)$	-	-	-	0.08	0.04	0.06
Cut-out	$u_{B1\_OOP}(m)$	2.84	0.22	5.26	3.21	0.44	5.97
	$u_{B1\_IP}(m)$	1.63	0.08	2.98	1.76	0.15	3.26
	$u_{TFA}(m)$	0.34	0.19	0.33	0.44	0.20	0.41
	$u_{TSS}(m)$	0.24	0.08	0.30	0.22	0.08	0.26
	$u_{B1\_T}(rad)$	-	-	-	0.03	0.03	0.002

N.B.: P2P refers to the peak-to-peak value of the response.

aerodynamic load in the out-of-plane direction and pitching moment decrease, ultimately affecting the mean tower response in the fore-aft direction (refer to Fig. 2.18c). This is an important positive aspect of elastic bending-torsion coupling, which helps in mitigating responses using torsion in the twist-to-feather direction. Fig. 2.18b shows the variation of mean in-plane blade response, which also exhibits similar behavior (i.e.,

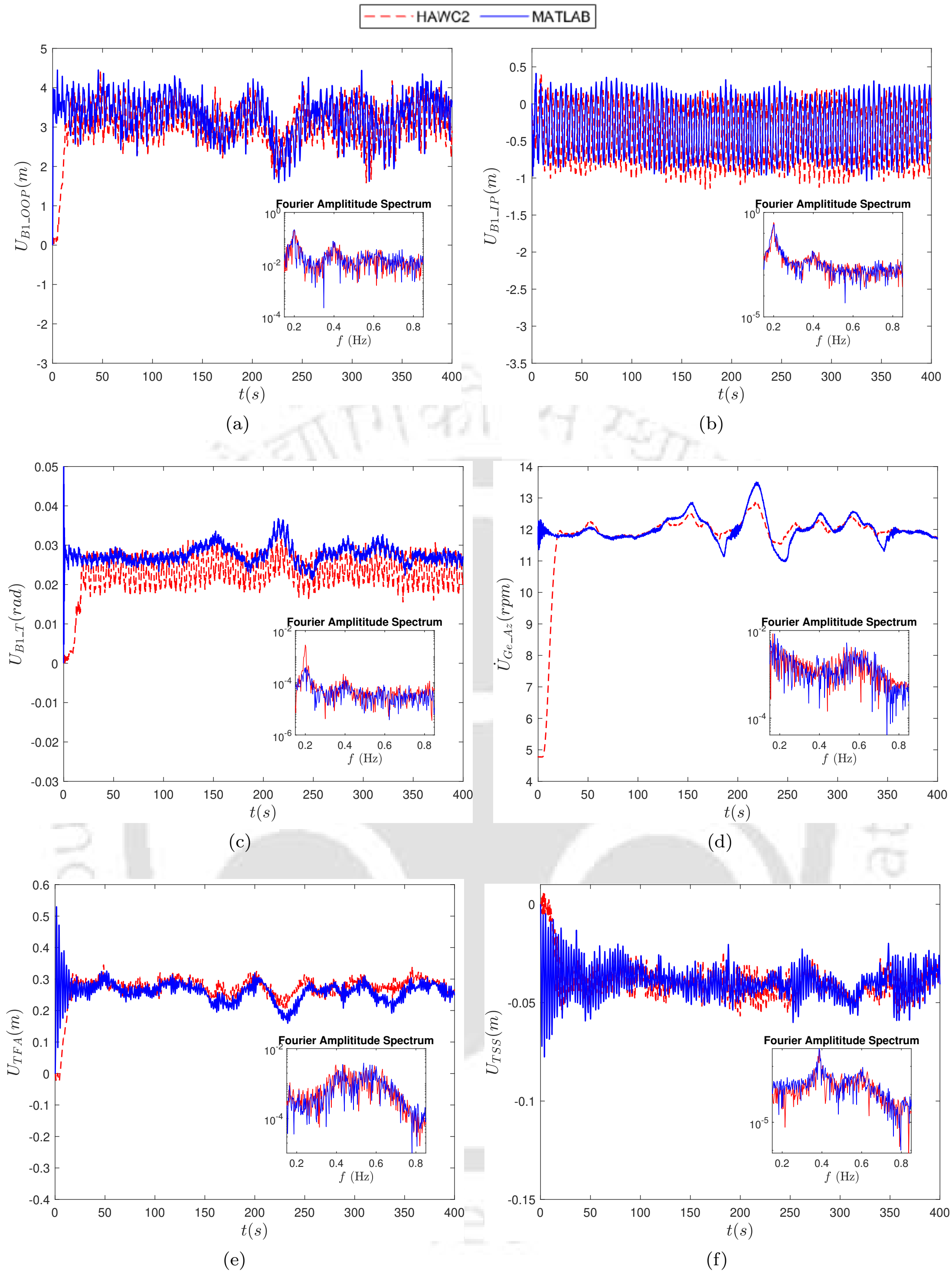

Figure 2.13: Response validation considering BTC for rated wind with 10% Mann's turbulence (Case 3); (a) blade out-of-plane, (b) blade in-plane, (c) blade tip-twist, (d) rotor speed, (e) tower top in fore-aft & (f) tower top in side-to-side

when $\lambda_{b_k}^{FT}$ is increased toward +0.1, the absolute value of the mean response decreases in this DOF). However, the change is more significant for higher wind speeds where the pitch angle is more. Tower top side-to-side mean response also exhibits the same phenomenon as shown in Fig. 2.18d; however, the change in mean response is not significant in this DOF due to the aforesaid reasons. All these features are summarised in Table 2.6 for different wind speeds.

From this table, it can be observed that positive $\lambda_{b_k}^{FT}$ (i.e., coupling in the twist-to-feather direction) can significantly affect the dynamic responses in the out-of-plane direction, e.g., 36.73% and 28.22% variation in

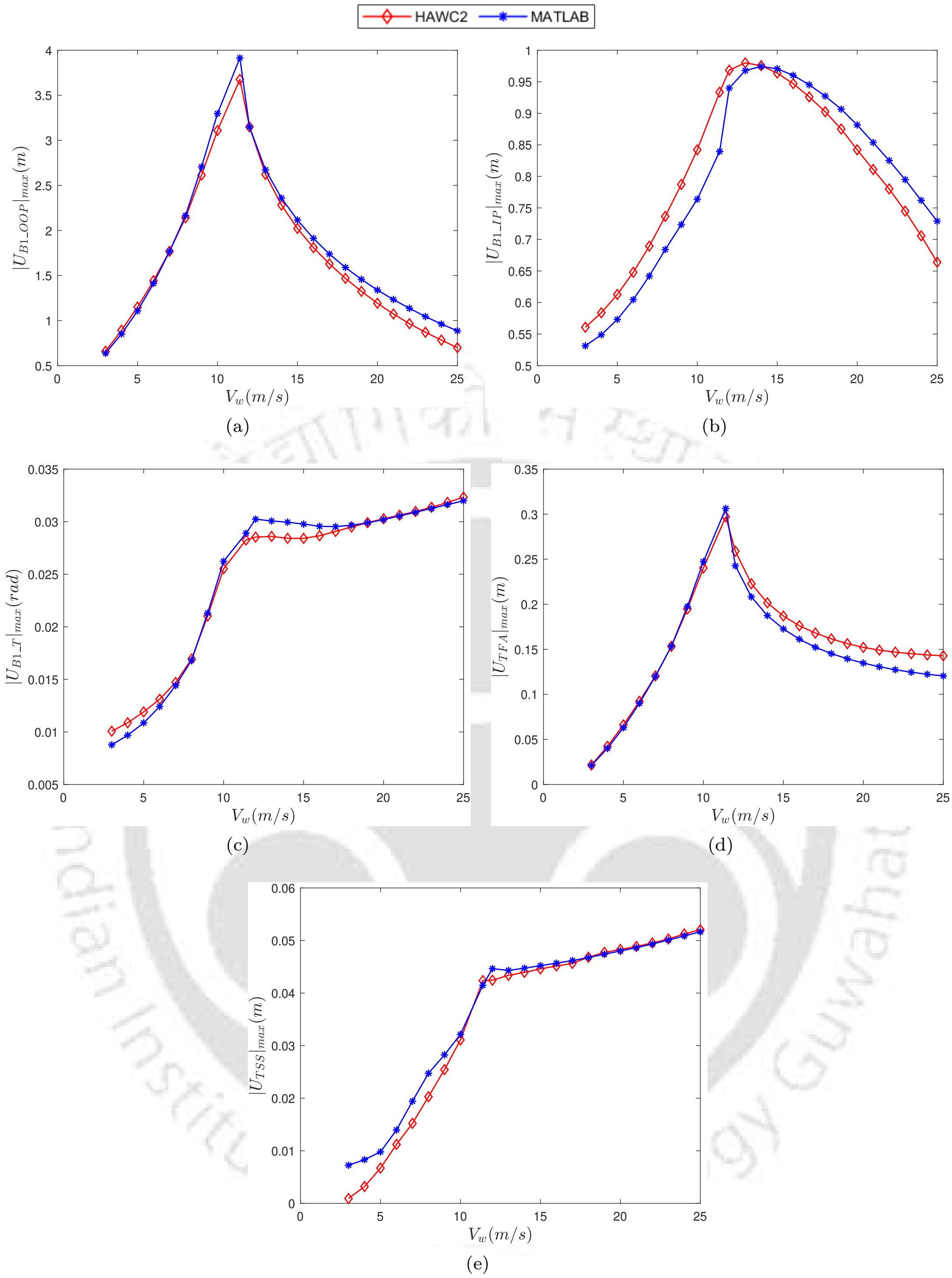

Figure 2.14: Peak response validation considering BTC (Case 3); (a) blade out-of-plane, (b) blade in-plane, (c) blade tip-twist, (d) tower top in fore-aft & (e) tower top in side-to-side

mean blade out-of-plane response corresponding to rated and cut-out speed, respectively. The mean blade in-plane response tends to increase by 10.83% due to twist-to-feather coupling at the rated wind speed. However, it is further reduced by 36.24% due to the action of the collective pitch angle beyond the rated value. This phenomenon is observed for all wind speeds beyond the rated value. Besides blade in-plane and out-of-plane responses, torsional response is also affected, where 89.83% and 41.17% variation are reported corresponding to rated and cut-out conditions, respectively. Here, it may be noted that the aerodynamic load acting on the blade decreases in its out-of-plane direction as elastic coupling increases. Due to this reason, the combined load acting on the tower top is also reduced, which ultimately affects the tower response. Thus,

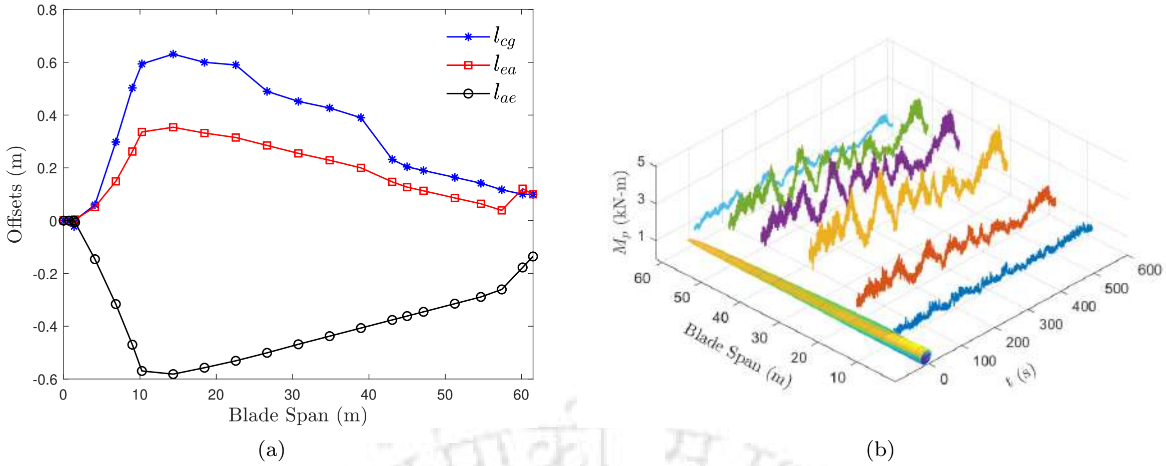

Figure 2.15: (a) Different offsets, (b) Pitching moment (N.B.: Blade diagram is not to scale

Table 2.6: Effect of elastodynamic bending-torsion coupling on absolute mean responses at rated and cut-out speed

	DOFs	**Abs. Mean** ($\lvert\mu_u\rvert$) $\lambda_{b_k}^{FT}=-1$	$\lambda_{b_k}^{FT}=+1$	**Percentage variation (%)**
Rated	$u_{B1\_OOP}(m)$	4.09	2.59	36.73
	$u_{B1\_IP}(m)$	0.34	0.37	-10.83
	$u_{TFA}(m)$	0.49	0.35	28.39
	$u_{TSS}(m)$	0.06	0.06	-1.81
	$u_{B1\_T}(rad)$	0.09	0.01	89.83
Cut-out	$u_{B1\_OOP}(m)$	0.65	0.47	28.22
	$u_{B1\_IP}(m)$	0.26	0.16	39.24
	$u_{TFA}(m)$	0.22	0.20	9.21
	$u_{TSS}(m)$	0.09	0.08	9.89
	$u_{B1\_T}(rad)$	0.04	0.02	41.17

tower fore-aft displacement is reduced by 28.39% and 9.21% corresponding to rated and cut-out conditions. However, the effect of elastodynamic coupling is not significant in the side-to-side motion of the tower.

Once the overall behavior of the turbine is investigated for different $\lambda_{b_k}^{FT}$, it is further generalized for different airfoils to replicate an actual blade. This, in turn, advocates for the solution of a multi-objective optimization problem, which is described in the following section. In the case of elastodynamic coupling, the blades are significantly stiffer in its edgewise direction and undergo small deformation compared to its flapwise response. Also, the shear centre has very small offset perpendicular to the chord. Hence, it is evident that flapwise bending mainly contributes to the bending-torsion coupling, so the term $\lambda_{b_k}^{ET}$ is assumed to be zero in this analysis.

2.3.6 Optimal Design of Fibre Orientation

In this section, the optimal design of fibre orientation is demonstrated for the rated wind flow condition. The blade layup at different sections can be adequately designed to impart appropriate elastic bending-torsion coupling for beneficial purposes. Thus, the asymmetric layup is preferred in design by controlling thickness, material properties and principal fibre orientation of the laminae. But variations of thickness and material properties in a blade can have a significant impact on its flapwise, edgewise and torsional stiffness, which, in turn, affect the overall dynamics of the system. Hence, only fibre orientation is used in this study to introduce elastic-bending torsion coupling for a given blade (i.e., thickness and material properties of the

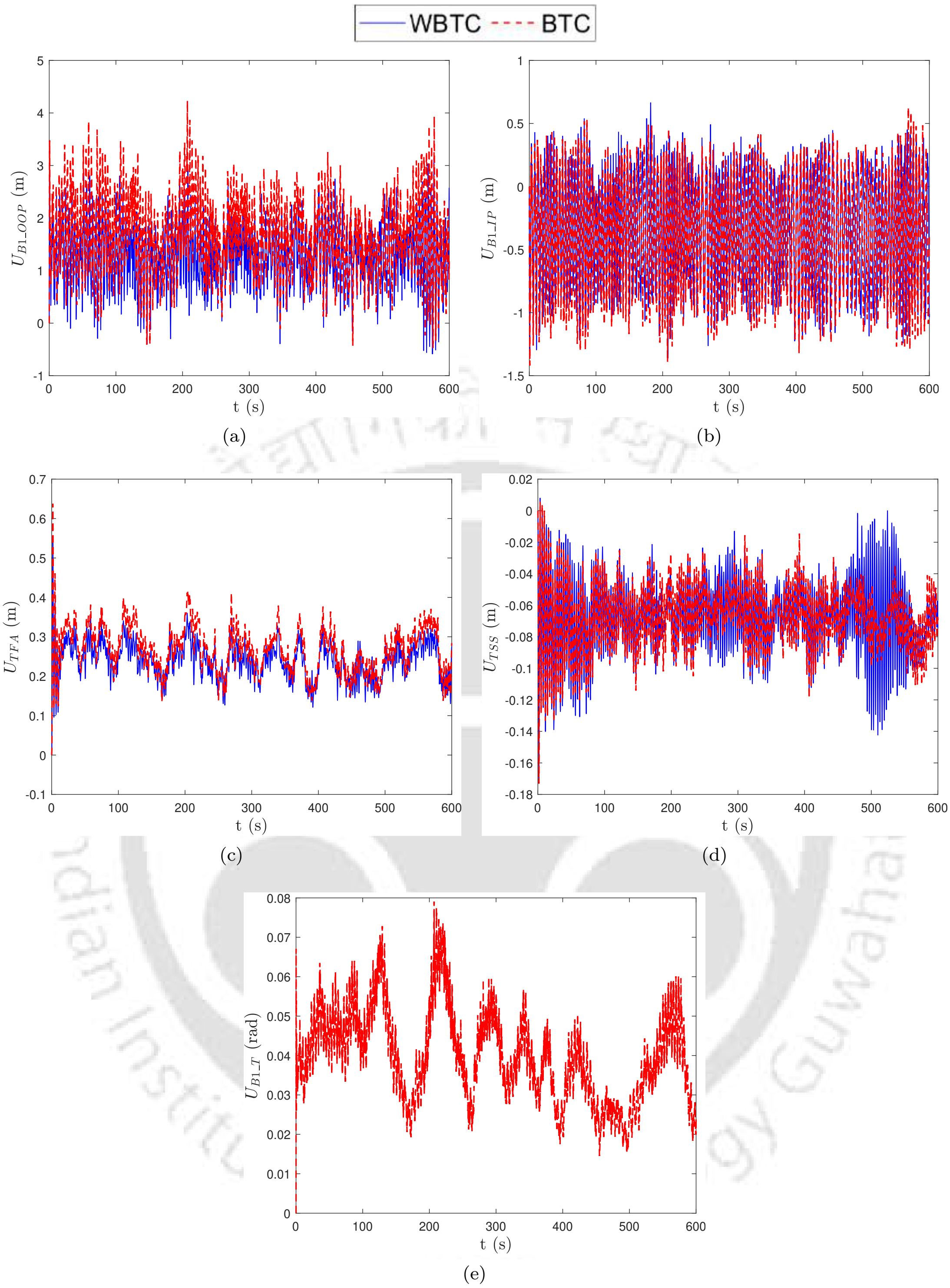

Figure 2.16: Response of turbine DOFs at 17m/s wind speed with 15% turbulence; (a) blade out-of-plane, (b) blade in-plane, (c) tower top fore-aft, (d) tower top side-to-side, (e) blade tip torsional twist. (N.B. Torsional DOF is not solved for WBTC case.)

laminae are fixed). Theoretically, the fibre orientation in the laminae can vary up to $\pm 90^o$. However, extreme fibre orientation (i.e., $\pm 90^o$) is not recommended as it reduces the overall stiffness of the blade in its flapwise direction.

Hence, for all practical purposes, the fibre orientation in the top and bottom skin layup have been varied within $\pm 75^o$ in this study. The blade sectional properties (mainly $\lambda_{b_k}^{FT}$) are obtained from PreComp [221] using different fibre orientations. These parameters are used in the modeling to evaluate the stiffness

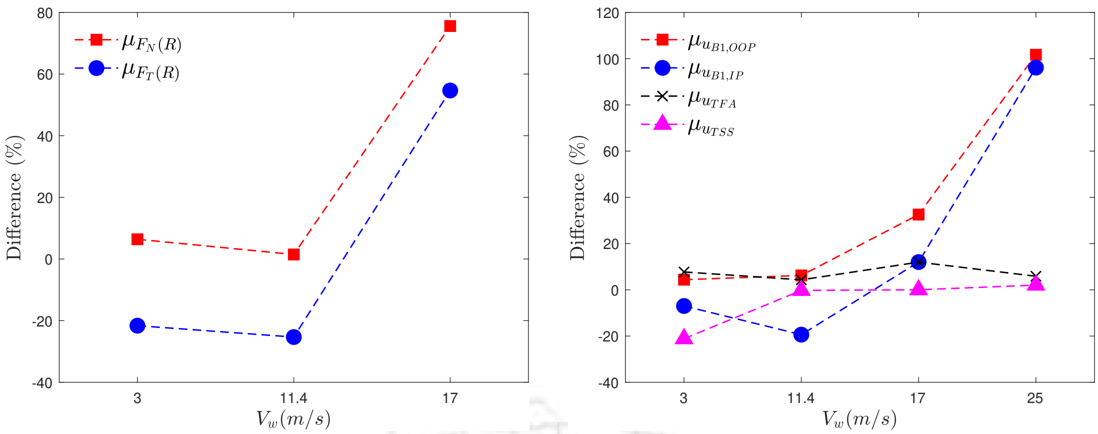

(a) (b)

Figure 2.17: Percentage changes due to dynamic BTC with 15% turbulent wind; (a) mean blade tip loads, (b) mean responses

as described in §2.2.4. The variations of the blade structural stiffness parameters due to changes in its principal material directions of the top and bottom skin layup (i.e., θ_{1,b_k} and θ_{2,b_k}, respectively) are shown in Fig. 2.19. As shown in Fig. 2.19a, the maximum value of flapwise stiffness is $2.85 \times 10^4 N/m$, and it occurs when both the skin layers have 0^o fibre angles due to obvious reasons. However, Fig. 2.19c shows that the coupling effect is maximum when both top and bottom skin layups of the blade have positive fibre angles. The torsional stiffness in that region is also maximum, as shown in Fig. 2.19b. Maximum flap-torsional coupled stiffness is observed to be $49.10 N/m$ when both θ_{1,b_k} and θ_{2,b_k} are at 30^o. On the other hand, the torsional stiffness of the blade reaches its maximum (i.e., $1.41 \times 10^6 Nm/rad$) when the fibre angles are set to $\pm 40^o$. The SNL-5MW blade structural parameters corresponding to both θ_{1,b_k} and θ_{2,b_k} at 30^o are given in Table. 2.7. Similar datasets have been produced for all the different combinations of the skin fibre angles using NuMad [233] and PreComp [221], and the subsequent analysis is carried out.

The numerical results presented above reveal that each stiffness parameter has global maxima at different locations within the analysis domain. These contradictory phenomena cause difficulties in finding an optimal design orientation for the skin layup of the blade. Hence, a multi-objective optimization problem is formulated for the efficient use of bending-torsion coupling on the overall response of the blade and tower. For this purpose, the peak response of the blade in its out-of-plane, in-plane, and torsional DOF and tower fore-aft direction are considered individually. The main aim of this study is to simultaneously minimize these response quantities by optimal fibre orientation. In this formulation, the tower side-to-side is not included, as the impact of fibre orientation along this DOF is negligible. Thus, the multi-objective optimization problem is formulated as follows

$$Obj.(\vec{\theta}) = \min\left(\left| u_{B1\_OOP}(\vec{\theta}) \right|_{\max}, \left| u_{B1\_IP}(\vec{\theta}) \right|_{\max}, \left| u_{B1\_T}(\vec{\theta}) \right|_{\max}, \left| u_{TFA}(\vec{\theta}) \right|_{\max} \right) \tag{2.90}$$

$$s.t. \quad \vec{\theta} \in \{-75^o \leq \theta_{i,b_1} \leq 75^o\} \quad \text{for} \quad i = 1, 2$$

In the above equation, $\vec{\theta}$ is the vector of fibre angles for different layers of blade skin. In this analysis, the blade has only top and bottom layers, i.e., variable $\vec{\theta}$ has two components θ_{1,b_k} and θ_{2,b_k}. Fig. 2.20 shows the variation of individual objective functions for different fibre orientations (i.e. θ_{1,b_k} and θ_{2,b_k}). It clearly shows the conflicting nature of different objective functions, which demand Pareto front analysis. Thus, the multi-objective optimization problem described in Eq. 2.90 is solved using pattern search and Genetic Algorithm (GA) in MATLAB for comparison.

The pattern search algorithm generates quasi-random samples satisfying the bounds and converges to the points near the actual Pareto front [234–236]. Whereas the genetic algorithm for multi-objective optimization uses a controlled, elitist GA [237], which always favors samples with better fitness value or the samples that can help increase the size of the population [238, 239]. The details of these algorithms are well documented in the literature cited above and hence, are not repeated here. A total of 961 sample points are used in the optimization process. The pattern search algorithm terminated after ten iterations with a total function

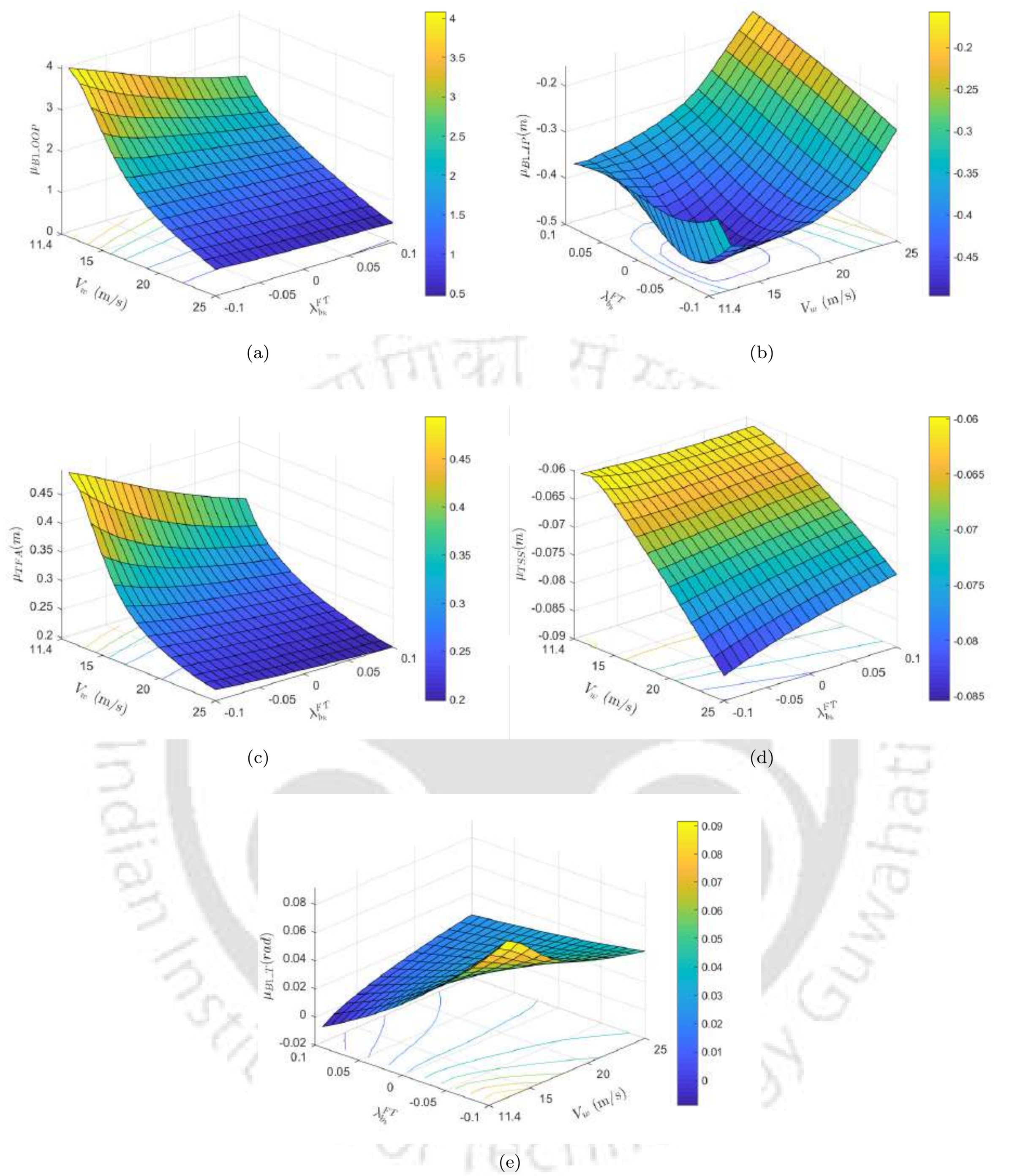

Figure 2.18: Mean response of turbine DOFs with variations of wind speeds and $\lambda_{b_k}^{FT}$; (a) blade out-of-plane, (b) blade in-plane, (c) tower top fore-aft, (d) tower top side-to-side, (e) blade tip torsional twist.

evaluation of 1630. Optimization is accomplished because the relative change in the distance of the Pareto set is smaller than 1e-4. On the other hand, the genetic algorithm identifies the Pareto optimal set after 104 generations with a final population of 50. In this process, 5200 function evaluations are used for convergence, i.e., tolerance is 1e-4. The optimization is terminated as the relative spread of the Pareto solution satisfies the convergence criteria.

The non-dominated Pareto optimal design points for the rated wind speed of the turbine are displayed in Fig. 2.21a and their corresponding objective function values are shown in Fig. 2.21b and Fig. 2.21c. These results show that the optimal design of fibre orientation is in between 0^o and 40^o for the rated condition. It is also the region where the coupled flap-torsional stiffness of the blade is maximum. The GA and Pattern

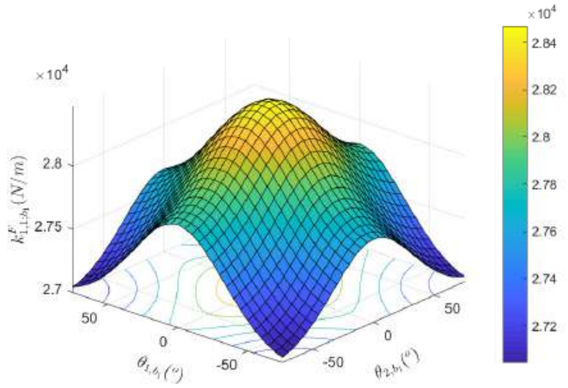

(a)

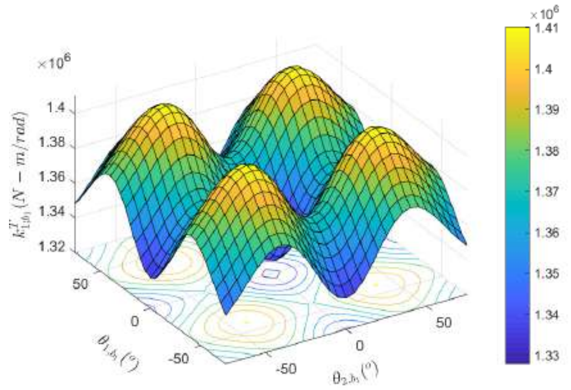

(b)

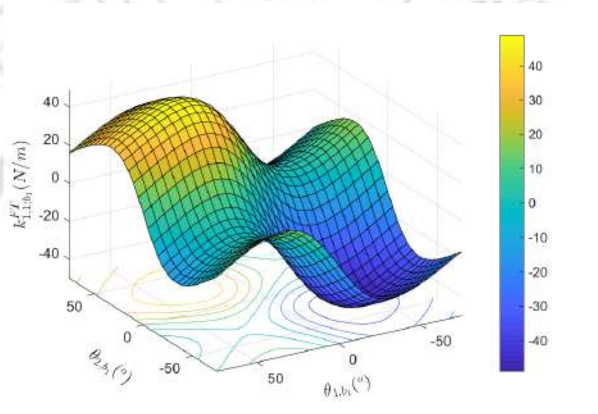

(c)

Figure 2.19: Blade stiffness variations with the fibre angle orientation of skin layup; (a) blade first flapwise stiffness, (b) blade torsional stiffness, (c) coupled first flapwise-torsional stiffness of blade.

search algorithm are consistent with each other; hence convergence of the optimization process is ensured. Quantitative analysis of the Pareto-front reveals that peak blade out-of-plane and in-plane responses can be reduced by 5.04% and 17.56%, respectively, whereas tip torsional twist can have a maximum reduction of 6.64% due to optimal skin fibre orientation. Although the tower fore-aft response tends to reduce with the reduction of blade out-of-plane response, the reduction in tower response is not significant in this case. Pareto optimization reveals that these results can not be achieved simultaneously and hence, the optimal design points should be chosen according to design requirements. A similar analysis is carried out for different wind speeds beyond the rated value. But the Pareto optima follows the same pattern for other values of mean wind speed and hence, they are not presented here to avoid repetition.

The objective of the optimization algorithm presented in this study is selected as the peak dynamic response mitigation of different components. Although it is true that the reduction of peak response does not always guarantee the reduction of stresses at critical locations, however, twist-to-feather coupling reduces the aerodynamic loads on the blade section. Hence, the overall force and moment at the critical locations (e.g., blade root, nacelle/drive-train, and the tower base) are expected to reduce as a natural consequence. Therefore, it can be justified that imparting bending-torsional coupling in the blade modeling and designing it optimally can have a significant beneficial effect on the overall dynamic response of the turbine.

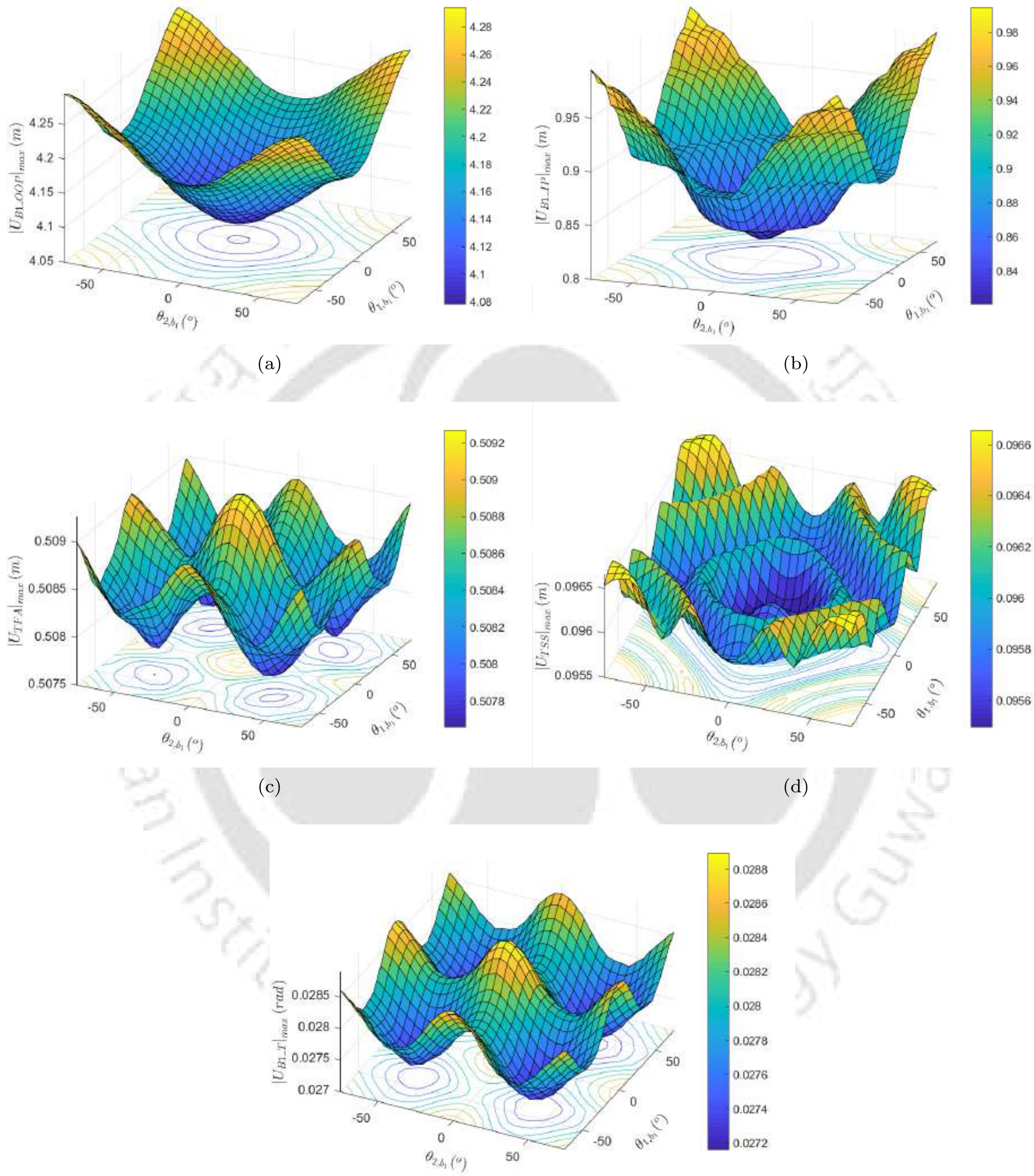

(e)

Figure 2.20: Peak responses of turbine DOFs with variations of fibre angle orientations of skin layup for rated wind speed; (a) blade out-of-plane, (a) blade in-plane, (c) tower top fore-aft, (d) tower top side-to-side, (e) blade tip torsional twist.

Table 2.7: SNL-5MW blade structural data corresponding to θ_{1,b_1} and θ_{2,b_1} at $+30^o$

BlNodes (m)	θ_s (^{o})	μ_{b_1} (kg/m)	$EI^F_{b_1}$ (Nm^2)	$EI^E_{b_1}$ (Nm^2)	GJ_{b_1} (Nm^2)	EA (N)	$\lambda^{FT}_{b_1}$ (-)
0.00	1.331E+01	1.127E+03	2.30E+10	2.28E+10	1.22E+10	1.66E+10	0.000E+00
0.70	1.331E+01	1.127E+03	2.30E+10	2.28E+10	1.22E+10	1.66E+10	0.000E+00
1.37	1.331E+01	8.709E+02	1.59E+10	1.54E+10	8.28E+09	1.15E+10	0.000E+00
1.50	1.331E+01	8.912E+02	1.61E+10	1.57E+10	8.30E+09	1.16E+10	0.000E+00
4.10	1.331E+01	9.818E+02	2.16E+10	2.09E+10	1.11E+10	1.28E+10	0.000E+00
6.83	1.331E+01	5.480E+02	1.31E+10	8.49E+09	2.64E+09	1.07E+10	-1.730E-04
9.00	1.331E+01	3.460E+02	6.78E+09	3.94E+09	7.07E+08	7.91E+09	-1.514E-03
10.25	1.331E+01	3.328E+02	4.34E+09	4.10E+09	4.66E+08	7.93E+09	-2.323E-03
14.35	1.148E+01	3.257E+02	3.31E+09	4.17E+09	3.69E+08	7.85E+09	-2.694E-03
18.45	1.016E+01	3.147E+02	3.03E+09	3.73E+09	3.25E+08	7.78E+09	-2.688E-03
22.55	9.010E+00	2.915E+02	1.83E+09	3.19E+09	1.92E+08	7.65E+09	-3.566E-03
26.65	7.800E+00	2.441E+02	1.16E+09	2.54E+09	1.24E+08	7.06E+09	-1.197E-03
30.75	6.540E+00	2.321E+02	1.01E+09	2.15E+09	1.02E+08	6.97E+09	-1.222E-03
34.85	5.360E+00	2.150E+02	6.26E+08	1.79E+09	6.14E+07	6.83E+09	2.944E-03
38.95	4.190E+00	2.039E+02	5.35E+08	1.51E+09	4.96E+07	6.75E+09	2.840E-03
43.05	3.130E+00	1.427E+02	2.53E+08	8.53E+08	3.04E+07	4.75E+09	7.425E-03
45.00	2.660E+00	1.323E+02	2.13E+08	6.96E+08	2.68E+07	4.29E+09	7.669E-03
47.15	2.140E+00	1.277E+02	1.92E+08	6.22E+08	2.34E+07	4.25E+09	7.547E-03
51.25	1.530E+00	1.189E+02	1.56E+08	4.99E+08	1.78E+07	4.18E+09	7.282E-03
54.67	8.600E-01	1.115E+02	1.29E+08	4.14E+08	1.39E+07	4.11E+09	7.023E-03
57.40	3.700E-01	1.034E+02	1.01E+08	3.34E+08	1.02E+07	4.05E+09	6.685E-03
60.13	1.100E-01	3.734E+01	2.93E+06	6.83E+07	2.85E+06	4.03E+08	0.000E+00
61.50	0.000E+00	2.334E+01	1.25E+06	2.91E+07	1.25E+06	2.87E+08	0.000E+00

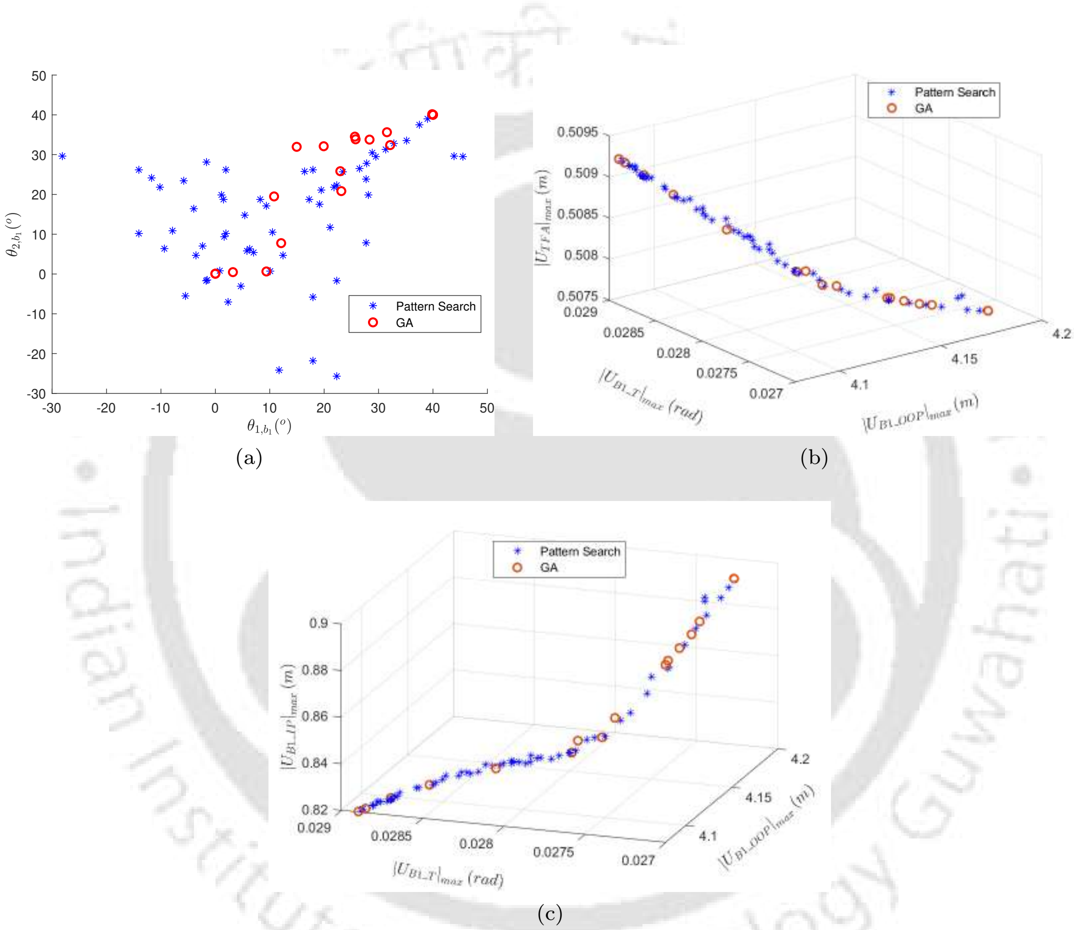

Figure 2.21: (a) Pareto optimal design points of blade skin layup orientation and (b) & (c) Objective function values at design points for rated wind.

2.4 Summary

In this chapter, a complete aero-servo-elastic multi-body model of a horizontal axis wind turbine considering the coupling effect between bi-axial bending and torsion of the blade is developed using Kane's approach. The detailed model does not impose any restriction on the modeling of sub-systems and their integration into the global framework. In this process, different types of coupling, i.e., dynamic and elastic, are modeled where the impact of composite layer orientation is investigated over the operating range of the turbine. The proposed modeling technique addresses several key challenges identified in the literature. It provides a comprehensive dynamic analysis of the complete system through a vector approach with fewer DOFs. However, further work is needed to incorporate non-linear effects such as the edge-twist coupling resulting from geometric non-linearity or torsional response resulting from large flapwise bending. The effect of the aforementioned coupling on the structural response of a benchmark turbine is studied under different flow regimes (i.e., from cut-in to cut-out with and without turbulence). The multi-objective optimization of fibre orientation of the composite blade skin layup is demonstrated. The significant findings from this study are mentioned below.

- The fore-aft response of the tower and blade response in two orthogonal directions (i.e., out-of-plane and in-plane) are mostly affected by the dynamic bending-torsion coupling and aerodynamic pitching moment. It can induce a significant vibration, particularly at higher wind speeds. Thus, neglecting these effects can lead to inaccurate estimation of the strains and subsequent stresses in different structural components.

- Elastic bending-torsion coupling in blades can have both adverse and beneficial effects on the dynamic response of the turbine depending upon its orientation (i.e., twist-to-feather or twist-to-stall). Among them, twist-to-feather coupling offers a beneficial effect as the angle-of-attack is reduced during this phenomenon, which is ultimately reflected in lower aerodynamic loads on the blade. Hence, this phenomenon can be utilized for the efficient design of airfoils.

- Positive fibre angle (refer to Fig. 2.4) in the blade skin induces positive coupling in flap-torsional stiffness and generates structural bending-torsion coupling in the twist-to-feather direction. The Pareto optimal solution of the principal material orientation in blade skin also lies in the same region. Thus, optimally inducing bending-torsion coupling in a blade can have a notable advantage in the dynamic response of a wind turbine.

Overall, the proposed modeling and optimal tuning of composite fibre orientation help to utilize its beneficial effects in load mitigation and subsequent response reduction of a horizontal axis wind turbine.

Chapter 3

Multi-Body Dynamic Model of a Monopile-Supported Offshore Wind Turbine Considering Soil-Structure Interaction

3.1 Introduction

Offshore wind farms have gained popularity in the recent past due to their various advantages, e.g., steady wind flow over an extended period and vast space in the marine environment. Many of these turbines in shallow water (depth around 30$\sim$50 m) are supported by monopiles, whose dimensions depend on the size and power rating of the turbines, besides other environmental factors. The design of these structures is challenging and requires a high-fidelity model of the complete multi-body rotating system, where Soil-Structure Interaction (SSI) plays a vital role. Developing a mathematical multi-body dynamic model of a monopile-supported offshore wind turbine and using it for the fatigue design of the monopile is the theme of this chapter. For this purpose, a benchmark turbine is modeled in Kane's approach, considering soil-structure interaction for a site at the North Sea. Each soil layer is modeled using the p-y curve, and the dynamic response of the combined system is simulated using aero-hydro-servo-elastic analysis. The fatigue life is estimated following International Electrotechnical Commission (IEC) 61400-3 guidelines. The numerical analysis presented in this chapter shows stress-based fatigue analysis using a rainflow algorithm in light of soil-structure interaction for short-term damage accumulation. Besides short-term effects, the study also investigates serviceability criteria over the lifespan of the structure, i.e., long-term effects. Finally, design curves are developed for a given power rating. Overall, the study highlights the importance of soil-structure interaction and its impact on the fatigue life of offshore wind turbines.

3.2 Mathematical Model

This section presents the modeling of a three-bladed horizontal axis offshore wind turbine, as shown in Fig. 3.1 supported over a monopile foundation.

3.2.1 Wind Turbine Model

In this section, Kane's approach [12] is adopted to model a monopile-supported turbine in a multi-body dynamic framework, which has significant advantages in accuracy and computational efficiency. The complete turbine is modeled as a 16 degrees of freedom (DOFs) system, including two flapwise and one edgewise modes for each blade and two modes in fore-aft and side-to-side directions for the monopile tower. However, this

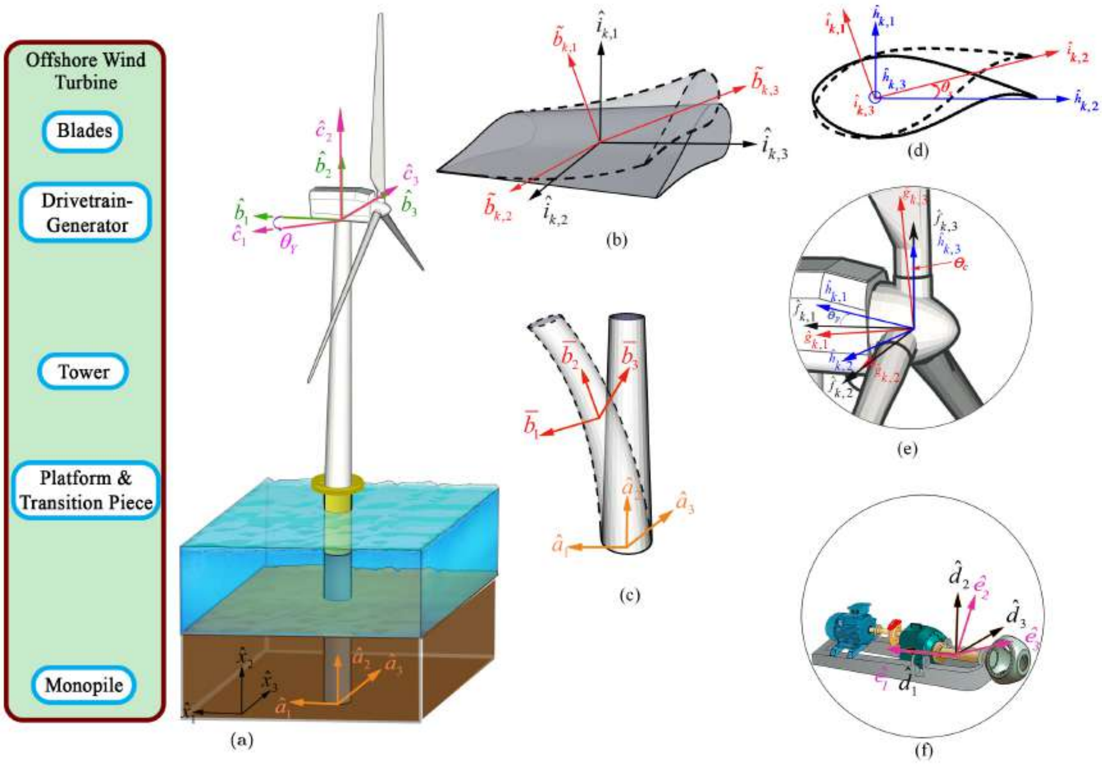

Figure 3.1: Schematic diagram of monopile supported offshore HAWT and coordinate systems: (a) wind turbine, (b) blade element, (c) monopile-tower element, (d) airfoil, (e) hub & (f) drivetrain.

formulation is general and can include as many modes as required for a particular case. The details of these DOFs are given in Table 3.1, which takes the following vector form.

$$\mathbf{u} = [\underbrace{u_1, ...u_4,}_{Monopile-Tower}\ \underbrace{u_5,}_{Nacelle}\ \underbrace{u_6, u_7,}_{Drive-train}\ \underbrace{u_8, ...u_{16}}_{Blades}]^T \tag{3.1}$$

Fig. 3.1 shows the global inertial reference frame marked by $\hat{x}$ along with all local coordinates, whose details are given in Table 3.1. In this context, each coordinate system has three orthogonal components, which are marked by subscripts j =1, 2, and 3 in Fig. 3.1. The blade coordinate systems have additional subscript k (e.g. $\hat{g}_{c,j}$), which denotes the blade number, i.e. k =1, 2, 3. The coordinate system $\hat{a}_{e,k,j}$ in Table 3.1 is used for aero-elastic load estimation. Appropriate transformation matrices are used to establish the relationships between each coordinate system [12].

Consequently, the governing equations of motion for n DOF system (here n = 16) are derived from Newton's law for holonomic multi-body system as

$$\mathbf{F_i} - \mathbf{F_i^*} = 0 \quad for \quad i = 1, 2, ..., n \tag{3.2}$$

In the above equation, $\mathbf{F_i}$ and $\mathbf{F_i^*}$ are the generalized active and inertia forces for i^{th} DOF, respectively. These forces can be derived from the displacement, velocity, and acceleration of each component, as discussed in §2.2 of chapter 2. Finally, the governing equation of motion can be derived in the global reference frame, which is described as

$$\mathbf{F_i^*} = \mathbf{F_{i,tw}^*} + \mathbf{F_{i,na}^*} + \mathbf{F_{i,hu}^*} + \mathbf{F_{i,gn}^*} + \sum_{k=1}^{3} \mathbf{F_{i,b_k}^*} \tag{3.3}$$

In the above equation, the first subscript i correspond to the DOF, while second subscripts tw, na, hu, gn and b_k represent monopile-tower, nacelle, hub, generator and k^{th} blade, respectively. Each component of external conservative and non-conservative forces, as well as the forces arising from the interaction of the multi-body systems and their constrained relations, contribute to the generalized active force, which can be

Table 3.1: Details of DOFs

Multibody Names	Components	DOFs	Local Coordinate	Remarks
Monopile-Tower	1^{st} Fore-aft mode	u_1	$\hat{a}$	Tower global
	1^{st} Side-to-side mode	u_2	$\hat{b}$	Tower top
	2^{nd} Fore-aft mode	u_3	$\bar{b}$	Tower element fixed system
	2^{nd} Side-to-side mode	u_4		
Nacelle	Nacelle yaw	u_5	$\hat{c}$	Yaw
Drive-train	Generator azimuth	u_6	$\hat{d}$	Slow speed shaft tilt and skew
	Shaft torsional DOF	u_7	$\hat{e}$	Rotating slow speed shaft
Blade 1	1^{st} Flap mode	u_8	$\hat{f}_1$	Global
	1^{st} Edge mode	u_9	$\hat{g}_1,\hat{h}_1,\hat{i}_1$	Cone, Centroidal, Twist
	2^{nd} Flap mode	u_{10}	$\tilde{b}_1$, $\hat{a}_{e1}$	Element fixed system
Blade 2	1^{st} Flap mode	u_{11}	$\hat{f}_2$	Global
	1^{st} Edge mode	u_{12}	$\hat{g}_2,\hat{h}_2,\hat{i}_2$	Cone, Centroidal, Twist
	2^{nd} Flap mode	u_{13}	$\tilde{b}_2$, $\hat{a}_{e2}$	Element fixed system
Blade 3	1^{st} Flap mode	u_{14}	$\hat{f}_3$	Global
	1^{st} Edge mode	u_{15}	$\hat{g}_3,\hat{h}_3,\hat{i}_3$	Cone, Centroidal, Twist
	2^{nd} Flap mode	u_{16}	$\tilde{b}_3$, $\hat{a}_{e3}$	Element fixed system

expressed as

$$\begin{aligned}\mathbf{F_i} = \mathbf{F_{i,tw,hy}} + \mathbf{F_{i,tw,ae}} + \sum_{k=1}^{3}\mathbf{F_{i,b_k,ae}} + \mathbf{F_{i,tw,gv}} + \mathbf{F_{i,na,gv}} + \mathbf{F_{i,hu,gv}} + \sum_{k=1}^{3}\mathbf{F_{i,b_k,gv}} + \mathbf{F_{i,gn}} \\ + \mathbf{F_{i,br}} + \mathbf{F_{i,tw,el}} + \sum_{k=1}^{3}\mathbf{F_{i,b_k,el}} + \mathbf{F_{i,ls,el}} + \mathbf{F_{i,yb,el}} + \mathbf{F_{i,tw,d}} + \sum_{k=1}^{3}\mathbf{F_{i,b_k,d}} + \mathbf{F_{i,ls,d}} + \mathbf{F_{i,yb,d}}\end{aligned} \tag{3.4}$$

The generalized active forces acting on the wind turbine include the monopile-tower (tw), nacelle (na), generator (gn), low-speed shaft (ls), hub (hu), yaw bearing (yb), and three blades (b_k). Hence, in the above equations, the subscripts $tw, na, hu, gn, ls, yb, b_k$ signify the center of gravity for these subsystems. The secondary subscripts hy, ae, gv, br, el, and d represent the hydrodynamic, aerodynamic, gravitational, brake, elastic, and damping forces of these components, respectively. Substituting Eq. 3.3 and Eq. 3.4 into Eq. 3.2 and rearranging them in matrix form leads to the following governing equation of motion

$$[\mathbf{M}(\mathbf{u}, \mathbf{t})] . \{\ddot{\mathbf{u}}\} + \{\bar{\mathbf{F}}(\dot{\mathbf{u}}, \mathbf{u}, \mathbf{t})\} = 0 \tag{3.5}$$

Eq. 3.5 reveals that $[\mathbf{M}(\mathbf{u}, \mathbf{t})]$ is the time-dependent system matrix and $\{\bar{\mathbf{F}}(\dot{\mathbf{u}}, \mathbf{u}, \mathbf{t})\}$ contains stiffness and damping forces besides other externally applied loads. The external force vectors depend on wind, wave velocities, and gravitational acceleration. The complete derivation of the matrices in Eq. 3.5 for monopile-tower assembly is similar to §2.2.1 presented in chapter 2 and hence, are omitted in this chapter to avoid repetition.

3.2.2 Soil-Monopile Model

In this study, the monopile foundation is modeled using finite elements, where Winkler's approach models the soil layers. For this purpose, two noded Euler-Bernoulli beam elements [240] and soil springs [241] are used to quantify the monopile deformation for equivalent stiffness in multi-body dynamic analysis. Thus, the combined soil-monopile element stiffness matrix can be expressed as follows

$$K_{n_e}^e = \underbrace{\frac{E_p I_p}{l_e^3} \begin{bmatrix} 12 & -6l_e & -12 & -6l_e \\ -6l_e & 4l_e^2 & 6l_e & 2l_e^2 \\ -12 & 6l_e & 12 & 6l_e \\ -6l_e & 2l_e^2 & 6l_e & 4l_e^2 \end{bmatrix}}_{\text{Monopile stiffness}} + \underbrace{\frac{E_s l_e}{420} \begin{bmatrix} 156 & -22l_e & 54 & 13l_e \\ -22l_e & 4l_e^2 & -13l_e & -3l_e^2 \\ 54 & -13l_e & 156 & 22l_e \\ 13l_e & -3l_e^2 & 22l_e & 4l_e^2 \end{bmatrix}}_{\text{Soil stiffness}} \tag{3.6}$$

where l_e is the element length, and the subscript n_e is the element number. E_p and I_p are Young's modulus and the second moment of area of the monopile element, while E_s is the soil modulus based on the p-y curve. The lateral characteristic of sandy soil is modeled as recommended in the American Petroleum Institute (API) guideline [242], i.e.

$$p = A_L p_u \tanh\left(\frac{k_{in} H_{so}}{A_L p_u} y\right) \tag{3.7}$$

where A_L is the factor for accounting different loading cases, i.e. $A_L = (3 - 0.8 H_{so} D_p^{-1}) \geq 0.9$ for static loading and $A_L = 0.9$ for cyclic loading. The parameter k_{in} denotes the initial modulus of the subgrade reaction, and y is the lateral deformation of the monopile. The angle of internal friction (ϕ) of the sand dictates the initial modulus of the subgrade reaction. The parameter p_u in Eq. 3.7 is the ultimate bearing capacity of soil at a depth H_{so}, which is estimated from the failure mechanism of soil, i.e., wedge failure and/or flow failure. The minimum of ultimate bearing capacity of the soil is evaluated, which is given by

$$p_u = \begin{cases} (C_1 H_{so} + C_2 D_p)\, \gamma_s H_{so} & \text{wedge failure} \\ C_3 D_p \gamma_s H_{so} & \text{flow failure} \end{cases} \tag{3.8}$$

In these equations, D_p and H_{so} denote the diameter of the monopile and height of the soil strata, while γ_s represents the effective soil weight. The coefficients C_1, C_2 and C_3 are the functions of internal friction of soil (ϕ), which are evaluated using the following expressions [243]

$$C_1 = C_0 C_a^{-1/2} \tan\phi \sin\beta_s \cos^{-1}\alpha_s + C_a^{-1/2} \tan^2\beta_s \tan\alpha_s + C_0 \tan\beta_s \left[\tan\phi \sin\beta_s - \tan\alpha_s\right] \tag{3.9a}$$

$$C_2 = C_a^{-1/2} \tan\beta_s - C_a \tag{3.9b}$$

$$C_3 = 0.4 \tan\phi \tan^4\beta_s + C_a \left(\tan^8\beta_s - 1\right) \tag{3.9c}$$

where $\alpha_s = 0.5\phi$ and $\beta_s = 45^o + \alpha_s$. C_0 is the coefficient of earth pressure at rest, which is constant ($C_0 = 0.4$), whereas C_a is the coefficient of active earth pressure [$C_a = \tan^2(45° - \alpha_s)$]. Similarly, the soil resistance against the axial deformation due to skin friction and soil end bearing is modeled using t-z and Q-z springs [242], respectively. The soil stiffness is evaluated by computing the slope of the line between the two consecutive points on the p-y curve. For the non-linear region, the stiffness is obtained from the deformation after the convergence analysis using a modified Newton–Raphson technique at every time instant [244]. The equivalent monopile properties are estimated by considering $Kx^* = K_{eq}x^*$, which is used for the multi-body dynamic analysis, as shown in Fig. 3.2. The modulus of the subgrade reaction for the next iteration is evaluated from this soil stiffness and is fed back to the finite element model at every time step.

Here, it is worth mentioning that the p-y curve in the API [242] is also recommended by Det Norske Veritas (DNV) [245], and it has gained popularity over the past decades among the designers. However, the use of API p-y curve for the offshore wind turbine has been questioned by many researchers. The reason behind the critics of API p-y curve is due to its formulation-based cyclic load test on a smaller diameter pile ($D_p < 1$ m) in the controlled environment of the laboratory, which differs from the actual field condition [3]. Several experiments using centrifuge models have been proposed in the literature [246, 247] to model this issue. Lee et al. [3] conducted centrifuge model tests on monopiles in dry, dense sand and proposed a cyclic p-y backbone curve.

$$p = y\left(\frac{1}{k_{in}} + \frac{y}{p_u}\right)^{-1} \tag{3.10}$$

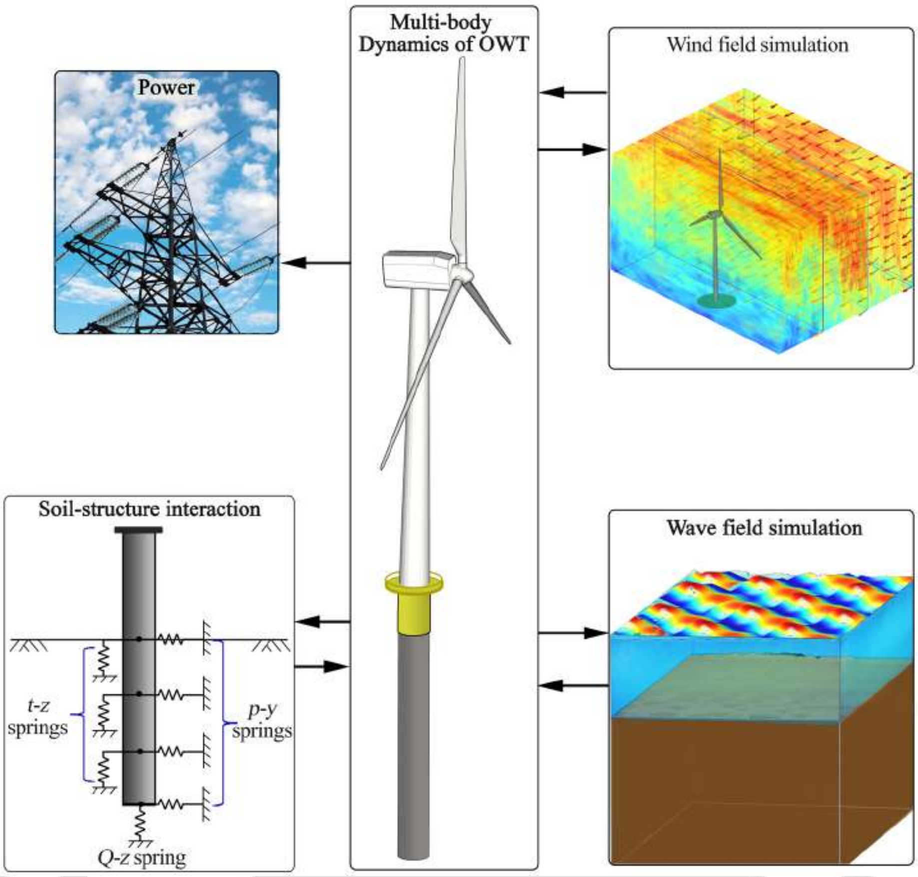

Figure 3.2: Flowchart of MBD-SSI model.

where p_u is the ultimate soil resistance, which is defined as

$$p_u = A_r K_{ps} \gamma_s {H_{so}}^{n_r} D_p \tag{3.11}$$

In the above equation, A_r and n_r are the constants obtained from regression analysis, whereas K_{ps} is the Rankine's passive earth pressure coefficient.

3.3 Forces Acting on Offshore Wind Turbine

Offshore wind turbines are exposed to aerodynamic and hydrodynamic loads in addition to the gravitational field, as shown in Fig. 3.1. IEC 61400-3 [87] recommends different wind flow conditions, including operating and non-operating regions for fatigue analysis with six simulated time-histories of ten minutes each or a single one-hour response time-history. The details of these loads are briefly described with only the relevant formulations in the following subsections.

3.3.1 Aerodynamic Load

The wind load acting on a blade has a mean and a fluctuating component depending upon the position and orientation. The fluctuating part is modeled using rotationally sampled spectrum (RSS), which is derived from the 1D power spectral density of the wind flow (e.g., Kaimal or von-Karman) [248, 249]. In this study, the turbulence is generated using the Kaimal spectrum in TurbSim [85]. The detailed description of the aerodynamic loads used for modeling and analysis in this study is given in §2.2.5 of chapter 2, hence it is not reiterated here.

3.3.2 Hydrodynamic Load

Besides aerodynamic loads, wind turbines in the offshore environment are also exposed to hydrodynamic loads. Ocean wave profiles are generated from the Joint-North-Sea-Wave-Project (JONSWAP) spectrum [101] using critical wave parameters, i.e., effective depth, fetch length. The details of these spectra are not discussed here as they are available in the literature. Using the directional spectrum, i.e. $S(f_i, \theta_j)$, the wave time-history can be evaluated by linear superposition of sinusoids [250], which is given by

$$H_w(x,y,t) = \sum_{j=1}^{\infty}\sum_{k=1}^{\infty}\sqrt{2S(f_j,\theta_k)\Delta f_j \Delta\theta_k}.\cos[k_j x\cos(\theta_k) + k_j y \sin(\theta_k) - f_j t - \epsilon_{j,k}] \tag{3.12}$$

$H_w(x,y,t)$ is the wave amplitude time-history at a location (x, y) on the surface in $\hat{x}$ coordinate, where $\epsilon_{j,k}$ is the uniformly distributed phase angle between 0 to 2π. Here, the distance x and y are measured along $\hat{x}_1$ and $\hat{x}_3$, respectively. In the above equation, the parameter k_j represents the wave number corresponding to the frequency f_j while θ_k denotes the direction of wave propagation. Once the wave is simulated, Morisson's equation [87] is used for finding the force acting on the monopile, which is expressed by the following equation.

$$\begin{aligned}\mathbf{dF_{i,tw,hy}(x,t)} = &\overbrace{-C_A\left(\frac{\pi D_p(x)^2}{4}\right)\rho\ddot{u}_i(x,t)dx}^{\text{Added Mass}} + \overbrace{C_{Mf}\left(\frac{\pi D_p(x)^2}{4}\right)\rho a_i^f(x,t)dx}^{\text{Fluid Inertia}} \quad \text{for } i = 1...4 \\ &+ \overbrace{\frac{1}{2}C_{Dr}\left(v_i^f(x,t) - v_{i,tw}(x,t)\right)\rho D_p(x)\left|v_i^f(x,t) - v_{i,tw}(x,t)\right| dz}^{\text{Viscous Drag}}\end{aligned} \tag{3.13}$$

In the above equation, the first term denotes the added mass associated with the motion of the pile, while the second and third terms imply fluid inertia force and viscous drag force, respectively. Added mass, also known as virtual mass, refers to the additional inertia that a system experiences when an object accelerates or decelerates within a fluid. This occurs because, as the object moves, it must push or redirect some portion of the surrounding fluid, which also gains motion. Since the object and the fluid cannot coexist in the same space, the fluid's movement adds to the overall inertia of the system. The effect can be simplified by considering a specific volume of fluid moving with the object. Here, ρ is the water density, and C_A, C_{Mf}, and C_{Dr} are the coefficients for added mass, fluid inertia, and viscous drag force, respectively. The dimensionless added mass coefficient C_A is the added mass divided by the displaced fluid mass. $D_p(x)$ represents the diameter of the monopile at a depth x along $\hat{x}_2$. In Eq. 3.13, $v_i^f(x,t)$ and $a_i^f(x,t)$ are the instantaneous fluid velocity and acceleration along i^{th} DOF at a depth x, which are evaluated from the surface velocity (i.e. $\dot{H}_w$) and acceleration (i.e. $\ddot{H}_w$) using linear wave theory, while $v_{i,tw}(x,t)$ is the velocity of the monopile-tower at depth x and dx is the differential height objecting the flow. The fluid diffraction and radiation-damping forces obtained from the potential flow theory are nominal for the current scenario as the monopile is a slender cylindrical object undergoing very small rotations. The diameter of the monopile is less compared to the wavelength of deep-sea waves, and hence the fluid diffraction and radiation-damping forces are not included in this mathematical modeling.

3.3.3 Gravitational Load

The gravitational force on a blade changes with its rotation, which can be resolved into two components. Thus, the in-plane bending moment due to gravity changes with its position and reaches its maximum when the blade is horizontal. The gravitational load acts vertically downward for different structural components (i.e., nacelle, hub, generator, and monopile-tower system). For the case of monopile-tower, the generalized active force arising from gravity is discussed in Eq. 2.24 of chapter 2. Here, it should be noted that only the DOF numbering in all the equations of Section 2.2.1 is changed in the present chapter according to the current DOF string.

3.4 Fatigue Analysis of Monopile

Fatigue damage due to cyclic loading often starts at the surface (i.e., extreme fibre) and eventually grows to failure. It may occur even when the stresses are below the yield strength of the material. Thus, fatigue damage assessment is essential while designing the structures that are subjected to load reversal. In this study, the fatigue life of monopile is estimated using stress at the extreme fibre. Fig. 3.3 shows the axial force and bending moment acting on a monopile, where the total axial stress at any point on the cross-section can be evaluated as follows

$$\sigma_{\mathrm{L}} = \frac{V_{fz}}{A_{cr}} + \frac{M_x x_c}{I_y} - \frac{M_y y_c}{I_x} \tag{3.14}$$

In the above expression, V_{fz} is the axial force in the z-direction, and A_{cr} is the cross-sectional area. Simultaneously, M_x and M_y are the bending moments in the x and y directions, respectively, where the second moment of areas are I_x and I_y. The total shear stress is evaluated using the following expression

$$\tau = \frac{2\sqrt{V_{fx}^2 + V_{fy}^2}\sin\beta_\tau}{A_{cr}} + \frac{M_z D_p}{2J} \tag{3.15}$$

where V_{fx} and V_{fy} are the shear forces in two orthogonal directions, β_τ is the angle between the point at which the internal stress is estimated and the total internal shear vector. M_z is the torsional moment, D_p is the pile diameter, and J is the polar moment of inertia of the cross-section. Once the component stresses are evaluated, von Mises stress can be estimated [60] for failure analysis.

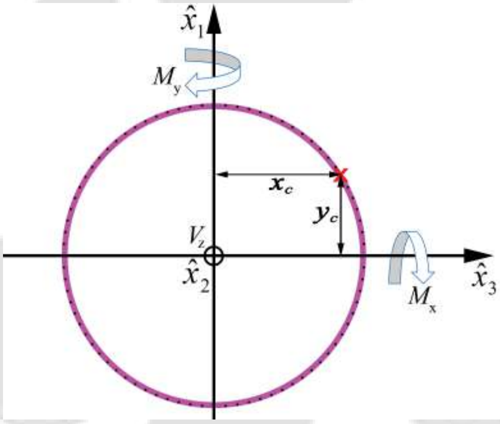

Figure 3.3: Bending moment and axial force of monopile for stress calculation.

Fatigue life estimation of a structure involves accurate counting of stress reversals and corresponding accumulated damage for a given stress time history. The finite number of stress reversals is estimated using the rainflow algorithm proposed by Downing and Socie [251]. Once the number of cycles is estimated from the response time history, the allowable number of cycles for the monopile material is estimated from the S-N curve using equivalent alternating stress obtained from the Goodman relation. Usually, the Goodman corrected fatigue life decreases with the increase of the mean of the applied alternating load. Therefore, Goodman relation [252] and the S-N curve must be used to find the maximum number of alternating stress cycles that a material can undergo until its fatigue failure. Goodman line is a linear relationship between the mean stress and alternating stress to estimate the equivalent alternating stress (σ_{ji}^{ae}), which can be expressed as

$$\sigma_{ji}^{ae} = \frac{\sigma_{ji}^{a}\left(|\sigma^{mf}| - \sigma^{u}\right)}{|\sigma_{ji}^{m}| - \sigma^{u}} \tag{3.16}$$

where σ_{ji}^{m} and σ_{ji}^{a} are the mean stress and alternating stress of the i^{th} cycle in the j^{th} time-history. Parameter σ^{mf} is the fixed mean stress, while σ^{u} is the ultimate stress of the material.

The S-N curve for steel is selected based on DNV-OS-J101 [253] guideline, and the damage accumulation is evaluated using Palmgren-Miner summation, which was first proposed by Palmgren [254] and popularized by Miner [255]. According to their model, the damage accumulated in each cycle is equal to $1/N$, when the material fails after N number of constant stress cycles. Therefore, the damage accumulated from the j^{th}

stress time-history (i.e., short-term damage) is evaluated as

$$D_j^{ST} = \sum_i \frac{n_{ji}}{N_{ji}} \tag{3.17}$$

where n_{ji} is the rainflow cycle count and N_{ji} is the allowable number of load cycles corresponding to the i^{th} stress reversal.

The lifetime damage is estimated using the probability of occurrence and the availability factor during its design life. In general, the hourly mean wind speed for a year is modeled by Weibull distribution [9], while the availability factor indicates its effective duration. Therefore, the damage accumulation during the lifetime is estimated as

$$D^L = \sum_j f_{av} f_j^L D_j^{ST} \tag{3.18}$$

where f_{av} is the availability factor of the wind turbine, and f_j^L is the scaling factor for the j^{th} time series to account for the probability of occurrence. The material fails when the damage index D^L reaches 1. The fatigue life can be obtained using the damage accumulation over the flow duration (i.e., the time duration multiplied by the inverse of the damage accumulation).

Further, the short-term and lifetime Damage-equivalent Load (DEL) need to be investigated for safe design. The DEL is defined as the fatigue load with constant mean and amplitude occurring at a fixed frequency, which induces the same damage resulting from variable spectrum load. In this study, Damage-equivalent Stress (DES) is evaluated instead of DEL. Thus, the short-term DES is computed as [256]

$$\sigma_{DE_j}^{ST} = \left[\frac{\sum_i n_{ji} \left(\sigma_{ji}^{ae}\right)^m}{f^{eq} T_j} \right]^{\frac{1}{m}} \tag{3.19}$$

where f^{eq} and T_j are the frequency of DES and the total time duration of the j^{th} time-history. The parameter m denotes the slope of the S-N curve. The lifetime damage-equivalent stress is evaluated from different load cases using the following expression

$$\sigma_{DE}^{L} = \left[\frac{\sum_j \sum_i f_j^L n_{ji} \left(\sigma_{ji}^{ae}\right)^m}{\sum_j f_j^L f^{eq} T_j} \right]^{\frac{1}{m}} \tag{3.20}$$

Once the damage-equivalent stress is estimated, the long-term performance of the monopile can be analyzed to ensure its serviceability.

3.5 Long-Term Performance

Long-term offshore wind turbine behavior is designed by satisfying the Serviceability Limit State (SLS) as per DNV guideline [245]. In general, the accumulation of rotation (or tilt) and the deflection (or strain) at the seabed must be within the allowable limits (i.e., serviceability). The long-term strain accumulation is investigated from the lifetime stress-based damage-equivalent load. In this context, different methods are often prescribed in the literature for finding the accumulated strain after N cycles from the strain in the first load cycle, which are described below.

3.5.1 Power-Law

Power-law is based on the pressuremeter test on monopiles in sandy soil under lateral cyclic loading [257]. The lateral deformation after the N cycle is evaluated as

$$y_N = y_1 N^{\alpha_c} \tag{3.21}$$

In the above equation, y_1 is the static displacement corresponding to the first cycle, and α_c is the cyclic degradation parameter depending on the soil and monopile properties, installation method, and loading characteristics. Therefore, the strain accumulation in a typical monopile foundation after N cycles can be expressed as

$$\epsilon_{N}^{PL} = \epsilon_1 N^{\alpha_c} \tag{3.22}$$

where ϵ_1 is the strain in the first cycle of loading. However, this law does not account for the degradation of stiffness. Hence, it is applicable only for piles that undergo little or no flexural stiffness degradation during their lifetime.

3.5.2 Logarithmic Method

The power-law expression is further modified to incorporate the degradation factor, which depends on the soil properties, types of pile installation/loading, pile penetration length, and the ratio of pile/soil relative stiffnesses based on the experimental results [258]. In this method, a logarithmic relation for the accumulated strain is used

$$\epsilon_{N}^{LL} = \epsilon_1 \left[1 + \beta_d \ln(N)\right] \tag{3.23}$$

Here, β_d is the degradation factor, which is evaluated using the following expression

$$\beta_d = 0.032\lambda_p F_d F_i F_l \tag{3.24}$$

Parameter λ_p in the above equation is the ratio of the length of monopile (L_p) to its characteristic length (L_c), which depends on the properties of monopile and soil, i.e. $L_c = (E_p I_p/n_h)^{\frac{1}{5}}$, and n_h is the coefficient of subgrade reaction. Factors F_d, F_i, and F_l account for soil density, monopile installation method, and cyclic load ratio, respectively. For a driven monopile in medium-dense soil with one-way loading, these factors are $F_d = 1.125$, $F_i = 1.0$, and $F_l = 1.0$. However, this method is developed using small-scale pile tests in the laboratory, and hence, its prediction for an actual monopile is doubtful.

3.5.3 Stiffness Degradation Method

This method for estimating accumulated strain (using stiffness degradation based on drained cyclic triaxial tests combined with finite element analysis) was developed by Achmus et al. [259]. The plastic strain in each cycle is inversely proportional to the secant stiffness of the soil. Therefore, the accumulated strain after the N cycle is obtained as

$$\epsilon_{_{PN}} = \epsilon_{_{P1}} \frac{E_{_{S1}}}{E_{_{SN}}} \tag{3.25}$$

where $\epsilon_{_{PN}}$ and $E_{_{SN}}$ are the plastic strain and Young modulus of soil at the N^{th} load cycle. Achmus et al. [259] proposed an empirical form of the above equation based on cyclic stress ratio, i.e.

$$\epsilon_{N}^{SD} = \epsilon_{_{P1}} N^{b_1 X_c^{b_2}} \tag{3.26}$$

In the above expression, b_1 and b_2 are the model parameters, while X_c is the characteristic cyclic stress ratio that varies from 0 to 1. This method is useful for large monopiles in the marine environment.

Various other methods are also proposed in the literature [48], which are not described here for brevity. The procedures mentioned above are used to investigate the long-term behavior using the multi-body dynamic soil-structure interaction model in the following section.

3.6 Numerical Results and Discussion

In this study, a benchmark National Renewable Energy Laboratory (NREL) 5MW OC3 Phase II [2] wind turbine on a monopile foundation is considered for numerical analysis. It has three blades of length 61.5 m, connected to a hub of diameter 3 m. The nacelle of this turbine is placed at the height of 87.6 m from the mean sea level. The blades are made of 8 different airfoils, whose lift and drag coefficients, mass distribution, bending stiffness, and aero-twist are given in the NREL report [2]. It operates within the wind speeds of 3 m/s to 25 m/s (i.e., cut-in and cut-out), while the rated speed for optimal performance is 11.4 m/s (i.e., 12.1 rpm). The pitch angle up to the rated speed is kept zero while it is adjusted above the rated speed to keep the rpm unaltered. The complete system is mounted over a steel monopile with a depth of 36 m from the mudline. The total length is 76 m, whose height above the mean sea level is 10 m. The properties of soil and monopile are selected from the NREL report [2]. The Young's modulus and shear modulus of the steel monopile are 210 GPa and 80.8 GPa, respectively, whose material density is 8,500 kg/m^3. The response time histories are evaluated for fatigue design of the monopile using these details of the benchmark turbine. However, before fatigue analysis, the model is validated with FAST [76] in the following subsection.

3.6.1 Validation

The validation of the proposed model with FAST is carried out at the rated speed with 10% turbulence considering 1.634 m wave height with 5.838 s peak spectral period. The responses are simulated without considering SSI to maintain the uniformity between these models. Under these conditions, the blade and tower responses are evaluated for comparison, as shown in Fig. 3.4. In this figure, U denotes the total deformation, while the subscripts $B1\_OOP$, $B1\_IP$, TFA, and TSS denote the blade out-of-plane, blade in-plane, tower top fore-aft, and tower top side-to-side directions, respectively. These results show that the responses simulated from the two codes (i.e., the proposed model and FAST) are consistent in amplitude and frequency content. Small variations are observed due to the difference in the numerical solvers of these codes. However, these small differences are negligible for all practical purposes. Other turbine parameters such as drivetrain torsional rotation (U_{DrTr}), nacelle yaw motion (U_{NacYaw}), and rotor speed ($\dot{U}_{GeAz}$) are also compared with FAST, which is given in Fig. 3.5. The bending moments acting at the mudline of the monopile are critical for determining its fatigue life. Fig. 3.6 shows the bending moments obtained from FAST and the code developed in this study, where the superscript m denotes the mudline and the subscripts fa and ss denote the fore-aft and side-to-side directions respectively. All the comparisons made in this study are plotted after removing the initial transience (about the first 300 s), and the results are compared for a significantly longer duration (700 s). These results show consistency and are in good agreement with each other. Therefore, it proves the accuracy of the mathematical model developed in this study. Hence, it can be used further for fatigue life estimation and long-term performance analysis of the monopile foundation.

3.6.2 Response Analysis

The monopile turbine system with soil-structure interaction is modeled, as discussed in §3.2 using the soil characteristics given in Fig. 3.7. The model is further used for response time-history analysis to study its fatigue life and long-term behavior. For this purpose, the combined system is solved for different wind flow conditions covering the operational range as prescribed in IEC 61400-3 [87]. Thus, 17 load cases are selected in this study as per data provided for the K13 site in the Dutch North Sea [260], which are given in Table 3.2. For each load case, there can be a misalignment between the wind and wave loading as in the present analysis (i.e., seven different misalignments between 0^o to 90^o @ 15^o interval). For a given misalignment in a particular load case, six simulated time-histories of 10 minutes duration are prescribed for fatigue analysis in the aforementioned standard. Therefore, 714 (= $17 \times 7 \times 6$) tune-histories, each having 600s duration, have been used in this study. V and $Turb.$ are the mean wind speed and turbulence intensity at the hub height in this table. Parameters H_w and T_p are the wave height and corresponding period. Six load cases in Table 3.2 (i.e., LC1 and LC13-LC17) are in the non-operating range. For LC17, the mean wind speed is set to 38 m/s [61]. The wind fields for all 17 load cases are simulated using TurbSim. The corresponding wave fields are generated as described in §3.3.2, which are further used to solve the multi-body dynamic system in MATLAB using ode45 solver [232].

In this subsection, the results are presented for the monopile of diameter 7 m and thickness 0.07 m, subjected to the 6$^{\text{th}}$ load case (i.e., LC6). The wind-wave misalignment is assumed to be 0°, as the fatigue failure is most prone to this angle between wind and wave. Fig. 3.8a shows the wind speed at the hub height and wave elevation for LC6, where Fig. 3.8b shows the Fourier amplitude spectrum for the same. The wave elevation reaches its peak at 0.17 Hz, as shown in Fig. 3.8b. The aerodynamic and hydrodynamic loads acting on the blade and monopile are demonstrated in Fig. 3.9. Fig. 3.10a illustrates the p-y curve of the sand layers used in this study for soil-structure interaction. Similarly, the axial resistance due to soil skin friction and soil end bearing are modeled using t-z and Q-z curves, as shown in Fig. 3.10c and Fig. 3.10d, respectively. The soil-pile finite element model is developed using these soil spring properties. The equivalent stiffness of the soil-monopile system obtained from the finite element analysis is used for multi-body dynamic analysis. The process is repeated at every time step to ensure the numerical convergence of the complete

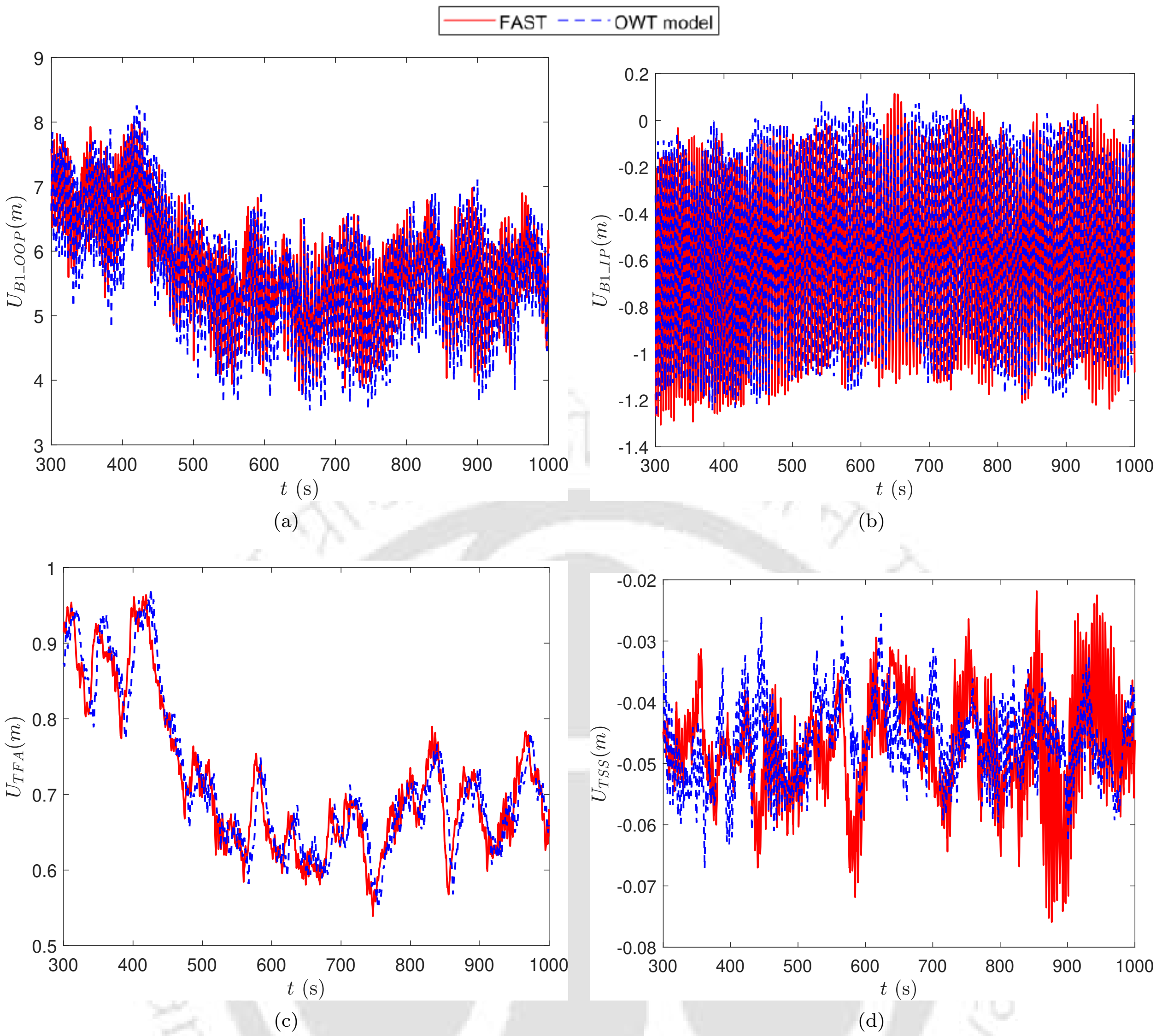

Figure 3.4: Blade and tower displacement time-history for 10% turbulent wind speed of 11.4 m/s; (a) blade tip out-of-plane, (b) blade tip in-plane, (c) tower-top out-of-plane & (d) tower-top in-plane.

system. Fig. 3.10b shows the monopile trajectory at the mudline, whose maximum value in the fore-aft direction is 4.755 mm. This figure indicates that the soil nonlinearity in fore-aft and side-to-side directions is not fully mobilized. The response is also evaluated using the p-y curve proposed by Lee et al. [3]. Fig. 3.11a and Fig. 3.11b show this p-y curve and monopile trajectory at the mudline, respectively. This p-y curve offers less soil stiffness compared to the API curve. It is reflected in the little increase of mudline deformation (refer to the difference in Fig. 3.10b and Fig. 3.11b). However, as the DNV guideline [245] refers API curve, it is used further in this analysis.

The platform motion in the fore-aft and side-to-side directions are shown in Fig. 3.12 along with their Fourier amplitude spectrum, where superscript p denotes platform. Fig. 3.12 also indicates that the first natural frequency lies in between the rotational frequency (i.e. 1P) and the blade passing frequency (i.e., 3P). Thus, the design of the monopile comes under the soft-stiff category, which is generally preferred. The response around 0.17 Hz in Fig. 3.12b corresponds to the spectral frequency of the hydrodynamic load.

Further, deformations of the combined system at different locations are obtained using the soil-structure interaction model (i.e., model-I) and compared with the fixed bottom case (i.e., model-II), shown in Table 3.3. This table indicates that model-II always underestimates the response, which can be as high as 100%. Therefore, these results advocate for a detailed multi-body dynamic analysis considering SSI. Fig. 3.13 shows the variation of peak displacement at the mudline, platform, and nacelle in the fore-aft and side-to-side directions over the complete operational window of the turbine (i.e., cut-in to cut-out).

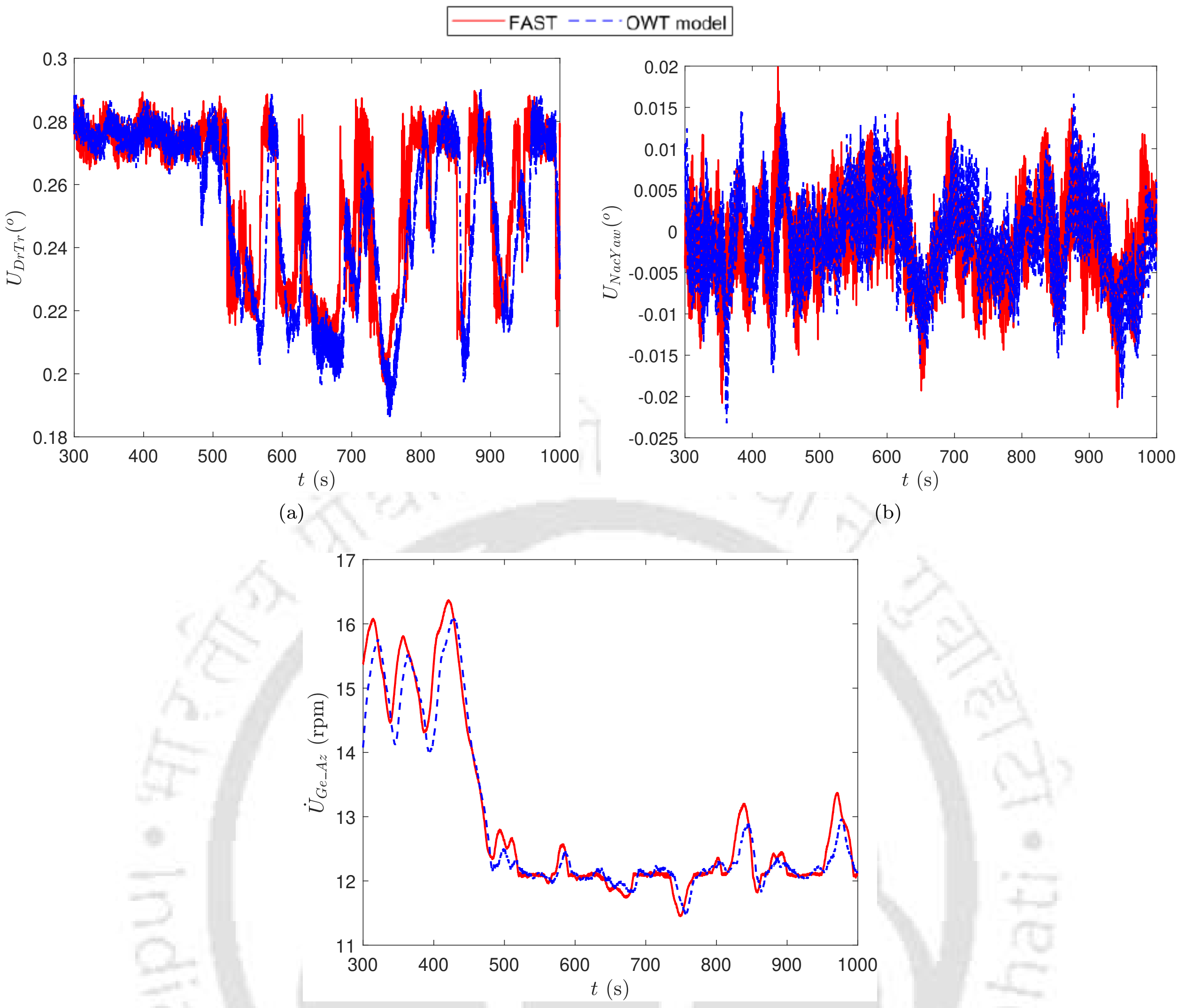

Figure 3.5: Response time-history of rotor and nacelle at rated wind speed with 10% turbulence; (a) drive-train torsion, (b) yaw motion of nacelle & (c) rotor speed

Besides displacement, rotation/tilt of the structure is equally important from the serviceability point of view. Fig. 3.14a and Fig. 3.14b show the fore-aft and side-to-side rotation of the platform, where the peak, mean and Root Mean Square (RMS) values are included within the figure. The allowable tilt at the mudline is limited to 0.5°, including the tolerance of 0.25° for tower installation [245]. These deformations at the mudline for the benchmark turbine are found to be within the allowable limits of rotation, i.e. the peak fore-aft and side-to-side rotation at this location are 0.0074° and 0.0046°, respectively. The response of the wind turbine is also affected by the wind-wave misalignment in the marine environment. Thus, the response of the turbine is simulated for various misalignment cases from 0° to 90°, which are summarised in Table 3.4. These data show that the magnitudes of the internal forces (i.e., shear force and bending moment) in the fore-aft direction are significantly higher than in the side-to-side direction. This is because the aerodynamic force is more in this direction. The results in Table 3.4 also highlight that the wind-wave misalignment has more impact on the side-to-side response. The response in the side-to-side direction experiences a 45∼70% change in magnitude compared to 5∼10% in the fore-aft direction due to wind-wave misalignment. The shear force in the fore-aft direction reaches its peak at 60° wind-wave misalignment, whose impact on the fatigue damage is presented in the following subsection. The bending stresses at the mudline are evaluated for 100 points over the cross-section, where the mean and peak stresses due to the fore-aft moment are 27.495 MPa and 56.347 MPa, respectively. In contrast, the same parameters due to the side-to-side bending moment are 1.987 MPa and 8.454 MPa, respectively. In addition to bi-axial bending stresses, the stress due to axial force is also evaluated, whose mean and peak values are 5.511 MPa and 9.416 MPa, respectively. The total

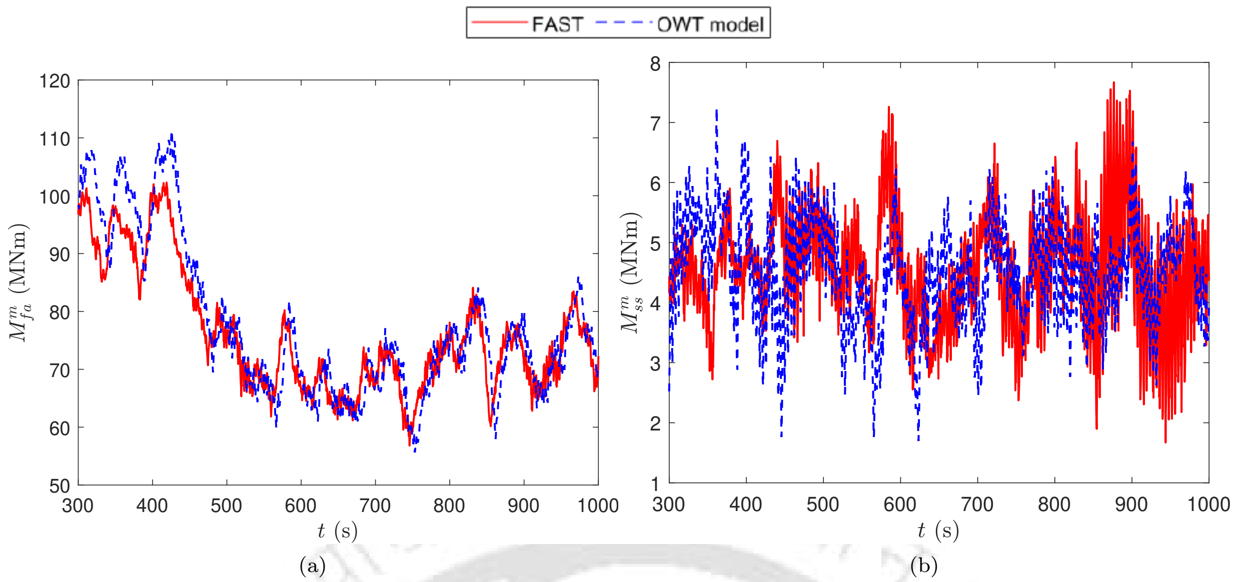

Figure 3.6: Bending moment time-history at mudline for 10% turbulent rated wind speed; (a) fore-aft & (b) side-to-side.

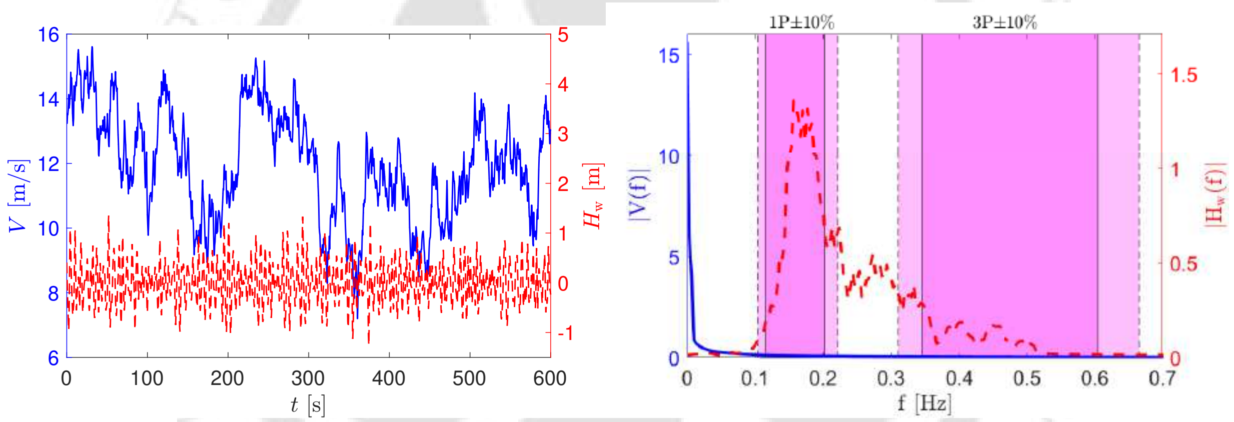

Figure 3.8: Load case 6; horizontal wind velocity at hub height and wave elevation (a) time history & (b) Fourier amplitude.

longitudinal stress distribution is estimated using Eq. 3.14, which is dominated by the fore-aft moment. The critical location for maximum stress over the cross-section is at x_c = -0.2198 m, y_c = 3.4931 m, as shown in the inset of Fig. 3.15a. The shear stress due to torsion is also evaluated, and the mean and peak values are obtained as 8.063 kPa and 598.942 kPa, respectively. Thus, the mean and peak of the shear stress time history are estimated as 0.788 MPa and 2.411 MPa, respectively, which are less in this case than other stresses. The von Mises stress time history is obtained from the different stress components, whose mean and peak values are 33.080 MPa and 62.108 MPa, respectively.

The mean and peak values of strains at the critical location are 157.51E-6 and 295.75E-6, respectively, and are well within the allowable limit (i.e. 1262E-6 [261]). However, the turbine undergoes a large number of cyclic loading during its lifetime in the marine environment. Therefore, fatigue life and long-term performance are investigated further for the design of the monopile foundation.

3.6.3 Fatigue Life Estimation

The fatigue life is evaluated using the S-N curve recommended in the DNV guideline [4] for steel structures in the marine environment (refer to Fig. 3.15b), whose ultimate strength is 440 MPa. The availability factor is assumed to be 1, i.e., the turbine offers full power generation within its operational window. Besides material properties and availability factor, lifetime fatigue design requires the probability distribution of

Table 3.2: Wind and wave parameters.

LC No.	V_w [m/s]	$Turb.$ [%]	H_w [m]	T_p [s]
1	2	29.2	1.07	6.03
2	4	20.4	1.10	5.88
3	6	17.5	1.18	5.76
4	8	16.0	1.31	5.67
5	10	15.2	1.48	5.74
6	12	14.6	1.70	5.88
7	14	14.2	1.91	6.07
8	16	13.9	2.19	6.37
9	18	13.6	2.47	6.71
10	20	13.4	2.76	6.99
11	22	13.3	3.09	7.40
12	24	13.1	3.42	7.80
13	26	12.0	3.76	8.14
14	28	11.9	4.17	8.49
15	30	11.8	4.46	8.86
16	32	11.8	4.79	9.12
17	34-42	11.7	4.90	9.43

NB: LC stands for load case.

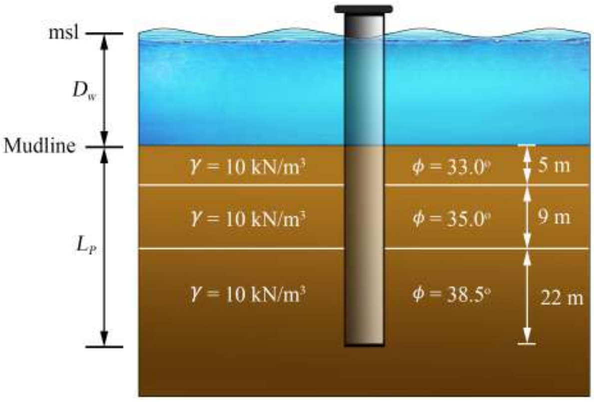

Figure 3.7: Soil profile for OC3 Phase II [2].

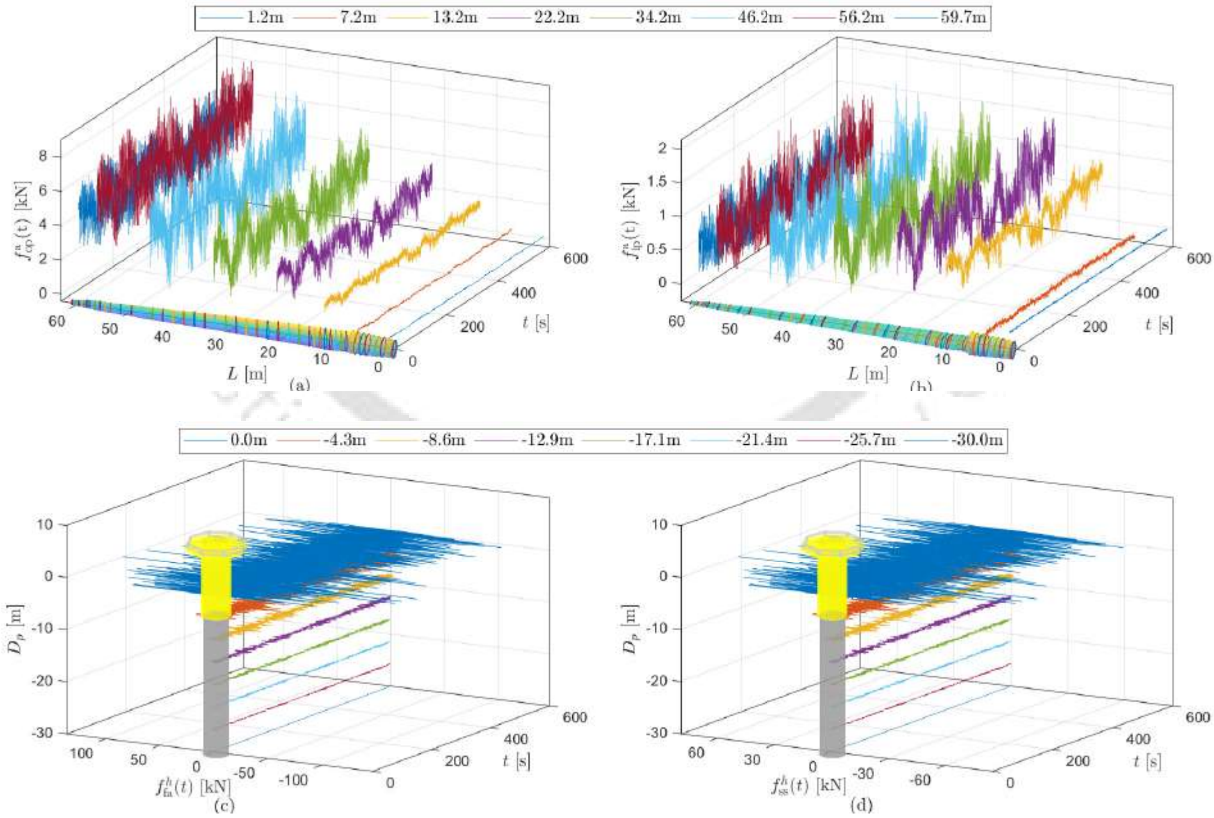

Figure 3.9: Aerodynamic and hydrodynamic load with 30° wind-wave misalignment for LC6; (a) aerodynamic load on blade out-of-plane direction (b) aerodynamic load on blade in-plane direction, (c) hydrodynamic load in fore-aft direction & (d) hydrodynamic load in side-to-side direction.

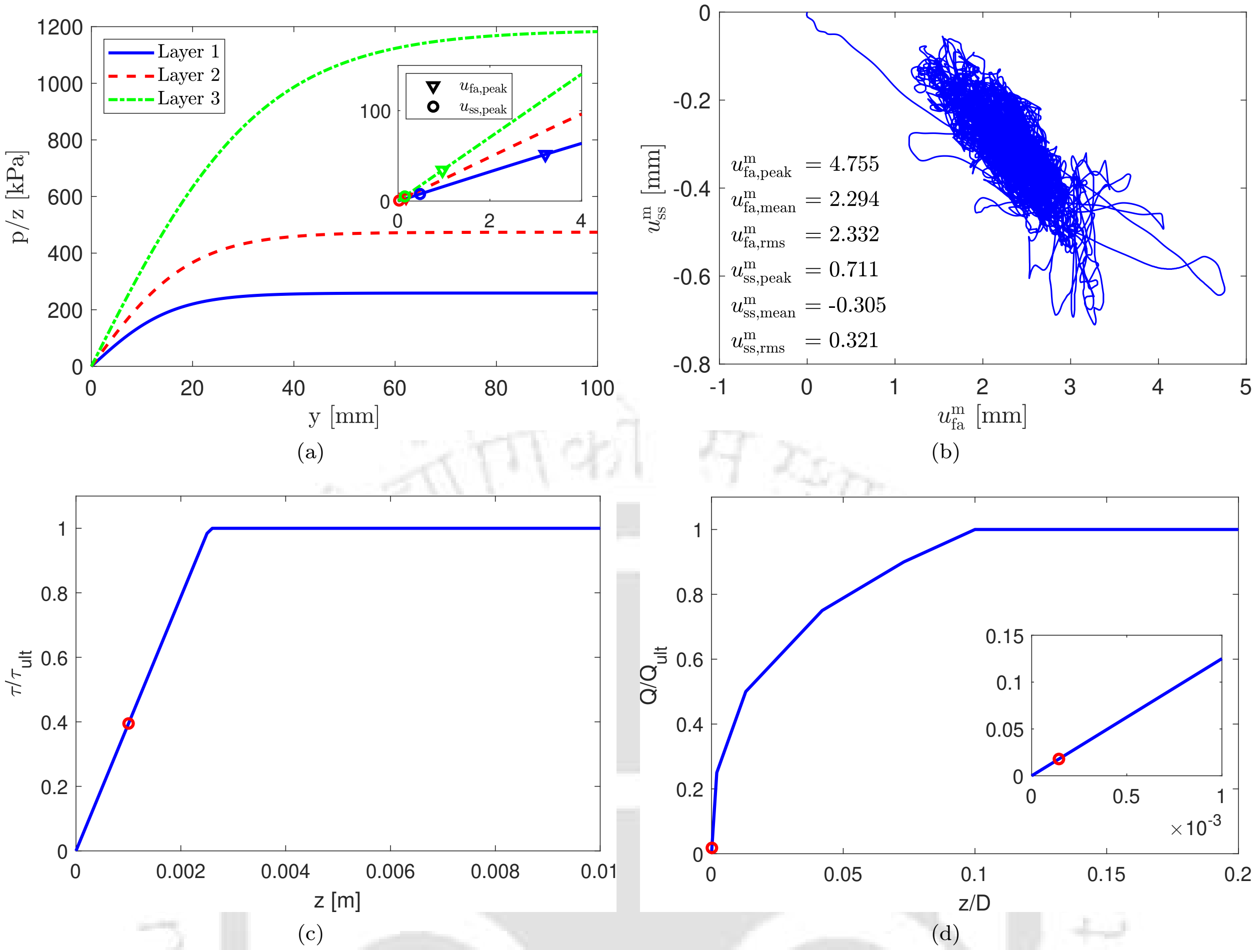

Figure 3.10: (a) API p-y curve for different soil layers, (b) monopile trajectory at mudline for LC6, (c) t-z curve & (d) Q-z curve

.

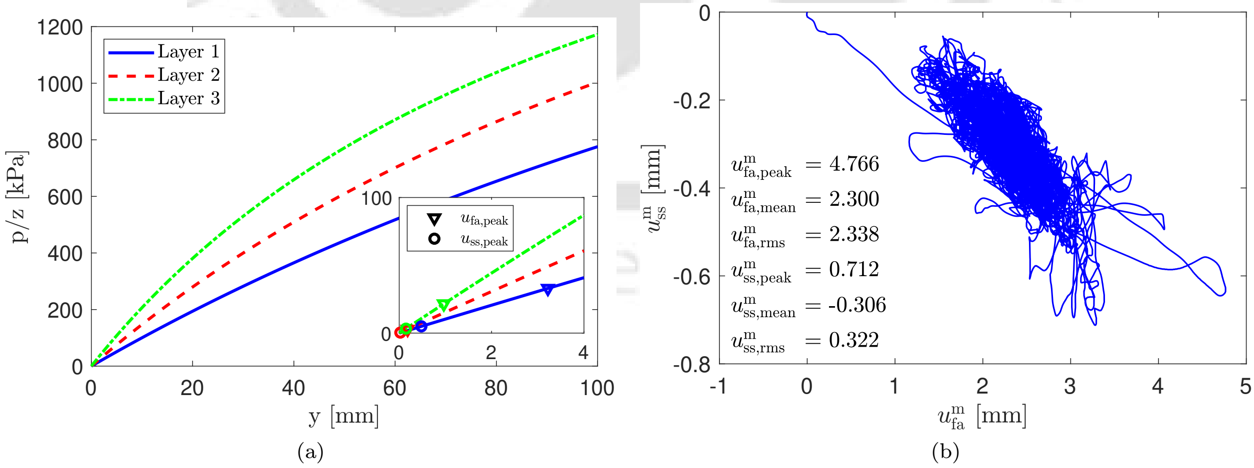

Figure 3.11: (a) p-y curve for different soil layers as per Lee et al. [3] & (b) monopile trajectory at mudline for LC6.

environmental loads at the site, modeled as Weibull distribution for each load case given in Table 3.2. The parameters of this probability density function are $c = 11.31$ m/s (i.e. scaling parameter) and $k = 1.97$ (i.e. shape parameter) [260]. The fatigue life is estimated separately from the fore-aft moment and stress as 29.87

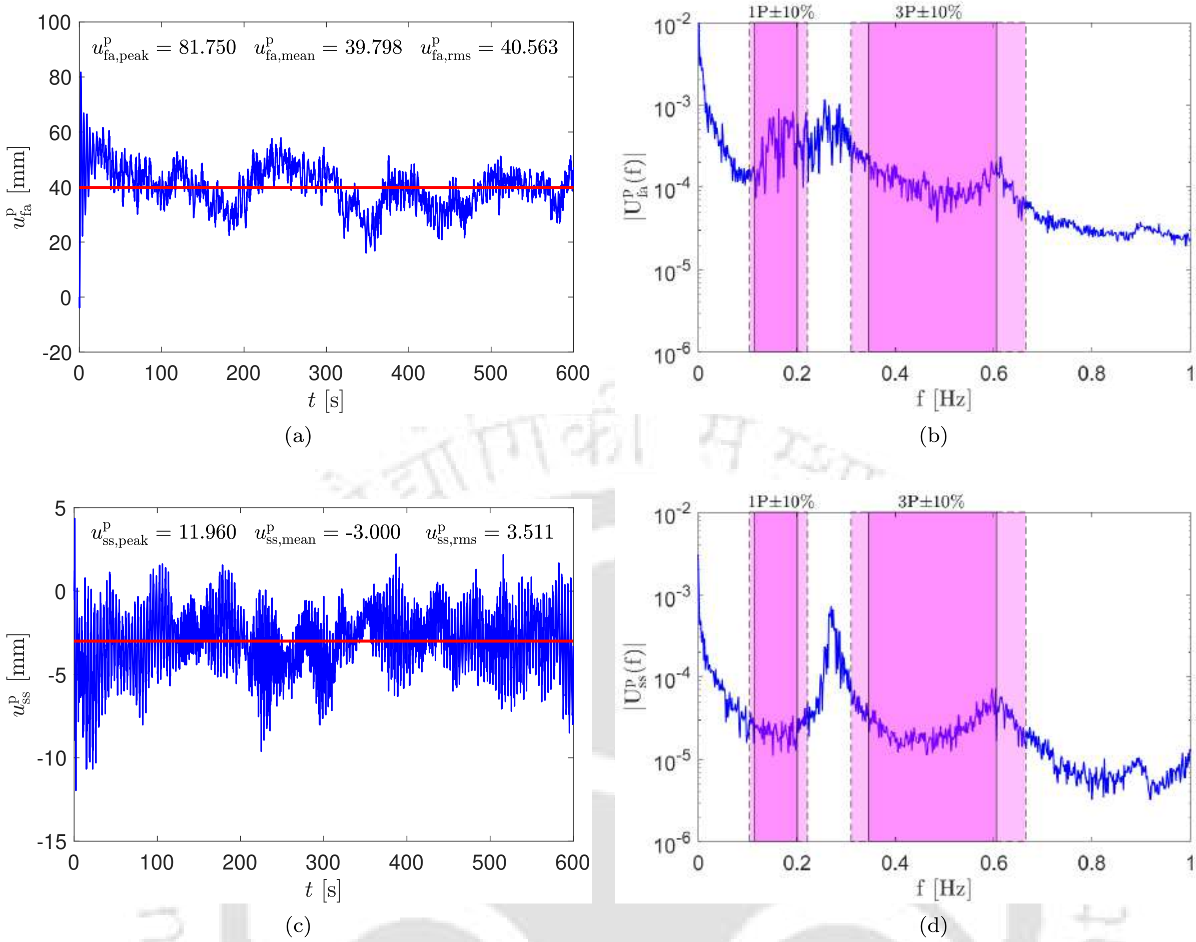

Figure 3.12: Platform deformation with monopile diameter 7 m and thickness 0.07 m for LC6; (a) fore-aft, (b) Fourier amplitude spectrum of fore-aft deformation, (c) side-to-side & (d) Fourier amplitude spectrum of side-to-side deformation.

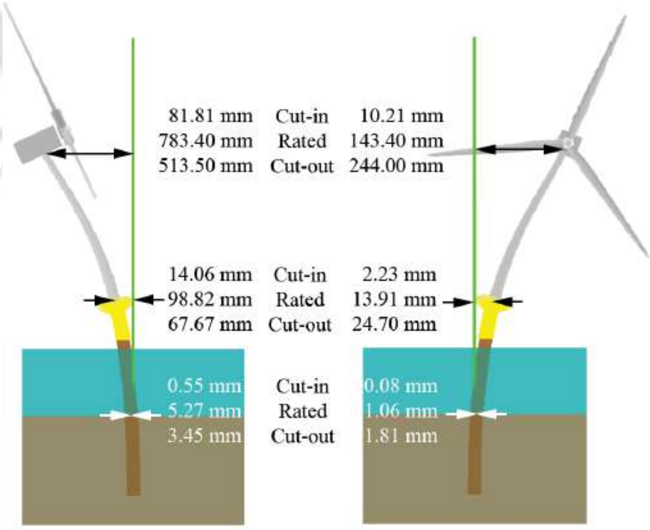

Figure 3.13: Peak deformations of an offshore wind turbine in fore-aft and side-to-side directions. [N.B.: figures are not in scale].

years and 26.92 years, respectively. Fore-aft moment-based calculation overestimates the fatigue life by 11%, mainly due to two reasons - (i) change in critical location and (ii) the additional stress due to the axial force.

Table 3.3: Deformation of the wind turbine, NB: Model-I is using SSI, Model-II is using the fixed bottom method.

Location	**Model**	**Fore-aft** [mm]			**Side-to-Side** [mm]		
		peak	**mean**	**rms**	**peak**	**mean**	**rms**
Mudline	I	4.755	2.294	2.332	0.711	-0.305	0.321
	II	0.000	0.000	0.000	0.000	0.000	0.000
Platform	I	81.750	39.798	40.563	11.960	-3.000	3.511
	II	57.890	26.762	27.262	8.842	-2.092	2.645
Tower-top	I	650.000	314.362	319.575	124.600	-53.578	56.504
	II	337.700	161.676	164.407	74.590	-29.416	31.559

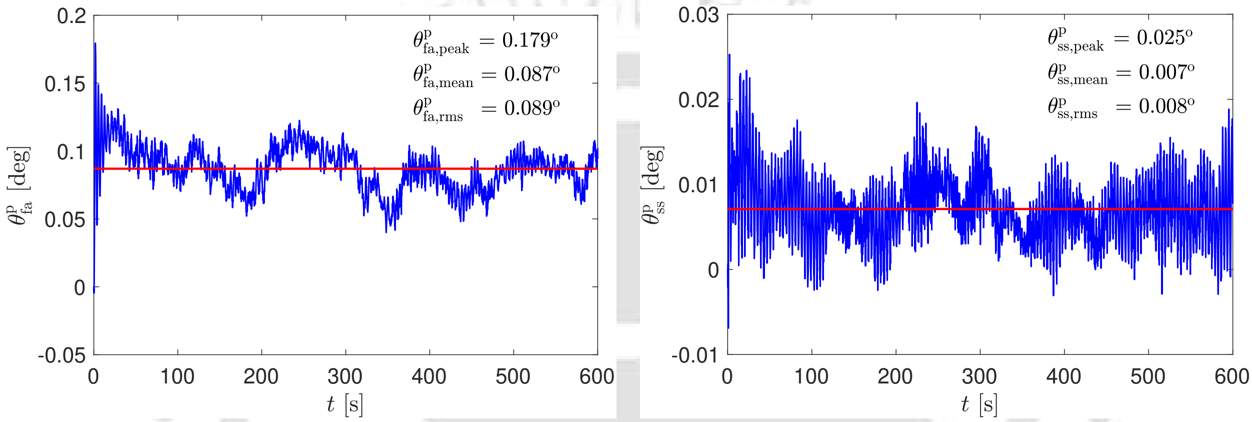

(a) (b)

Figure 3.14: Rotation of wind turbine at platform level with monopile diameter 7 m and thickness 0.07 m for LC6; (a) fore-aft & (b) side-to-side.

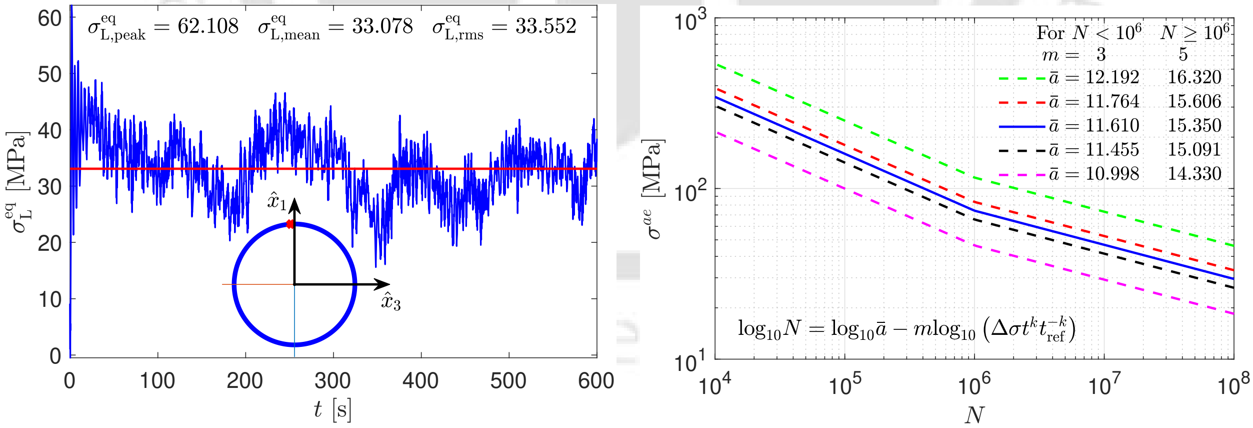

(a) (b)

Figure 3.15: (a) Longitudinal stress of monopile at the critical point & (b) S-N curve for offshore steel material [4].

The fatigue lives without Goodman correction in these cases are 38.05 years and 36.15 years, respectively.

Further, the impact of wind-wave misalignment on monopile fatigue damage is investigated (refer to Fig. 3.16). The critical location is changed to x_c = -0.4387 m, y_c = 3.4724 m for higher wind-wave misalignment, i.e. $\theta_{ma} \geq 30°$. It is observed that the maximum short-term damage occurs during the 12$^{\text{th}}$ load case, which corresponds to the maximum wind speed within the operational window. However, the 12$^{\text{th}}$ load case has less probability of occurrence than load case 6. Due to this reason, the 6$^{\text{th}}$ load case contributes most to

Table 3.4: Shear force and bending moment of monopile at mudline for various wind-wave misalignment cases.

Reactions	Wind-wave misalignment	Fore-aft			Side-to-Side		
		peak	mean	rms	peak	mean	rms
Shear Force [kN]	0°	1525.000	592.600	650.421	287.200	-6.433	60.005
	15°	1497.000	592.623	647.584	343.500	-6.647	90.910
	30°	1416.000	592.687	639.898	517.800	-6.843	140.015
	45°	1286.000	592.787	629.303	698.900	-7.008	185.848
	60°	1299.000	592.917	618.597	838.200	-7.129	221.452
	75°	1322.000	593.068	610.753	924.600	-7.200	243.348
	90°	1367.000	593.229	608.062	952.000	-7.215	249.706
Bending Moment [kNm]	0°	147.300	71.876	73.349	22.100	5.194	6.199
	15°	147.500	71.877	73.329	22.170	5.205	7.382
	30°	148.200	71.879	73.276	29.090	5.214	9.078
	45°	149.300	71.882	73.205	34.560	5.222	10.687
	60°	150.800	71.885	73.137	38.130	5.227	11.873
	75°	152.700	71.889	73.092	40.400	5.230	12.465
	90°	154.900	71.894	73.084	40.350	5.230	12.391

lifetime damage accumulation. Fig. 3.16c shows the lifetime damage for various wind-wave misalignments. This figure also indicates that the maximum lifetime damage occurs when the wind and wave loads are coincident. The minimum damage occurs when θ_{ma} is 60° due to the change in the fore-aft shear force.

Once the fatigue life is estimated, both short-term and lifetime damage-equivalent stresses are evaluated to study the serviceability criteria. As discussed earlier, the maximum short-term DES corresponding to the 12$^{\text{th}}$ load case has a mean value of 23.00 MPa with an amplitude of 9.99 MPa. Thus, the strain during this cycle is 157.10E-6, which is well within the design limit. The lifetime DES is obtained as 6.94 MPa corresponding to 580848302.6 equivalent cycles of load with a mean 23.00 MPa at 1 Hz, which is further used in the following subsection to study the long-term performance.

3.6.4 Long-Term Deformation Estimation

The long-term performance of monopile is usually estimated to check the serviceability limit. In this study, the long-term performance is evaluated in terms of strain using lifetime damage-equivalent stress obtained from the fatigue analysis. The maximum absolute stress in the first cycle of damage-equivalent stress for diameter 7 m and thickness 0.07 m in 30 m water depth is 29.94 MPa. Therefore, the corresponding strain in the first cycle is 142.57E-6. The long-term performance of the monopile is evaluated by three different methods, as discussed in §3.6.4. Fig. 3.17 shows the variation of strain vs the number of cycles, where the soil condition is considered to be medium-dense sand. This figure also reveals that the overall dimensions of the monopile satisfy its serviceability limit.

3.6.5 Sensitivity Analysis

The aquatic profile in the marine environment varies with its spatial extent. The hydrodynamic load increases with the water depth, which ultimately affects the fatigue life of the foundation. Thus, a sensitivity analysis is conducted for various water depths, which is presented in Table 3.5. A comparison of fatigue life using fore-aft moment and longitudinal stress is also presented in this table, which clearly shows that fatigue life is overestimated using the fore-aft moment-based approach. The results in this table highlight the impact of diameter and thickness, i.e., as diameter increases, the required thickness decreases and vice versa. However, for specific water depth, a minimum thickness corresponding to a particular diameter is recommended by API [242] guidelines to avoid local buckling. This issue is discussed further in the following subsection.

Besides buckling, different monopile parameters (i.e., diameter, thickness, and water depth) also affect the short-term DES. Fig. 3.18 shows this analysis for different load cases that offer fatigue life above its

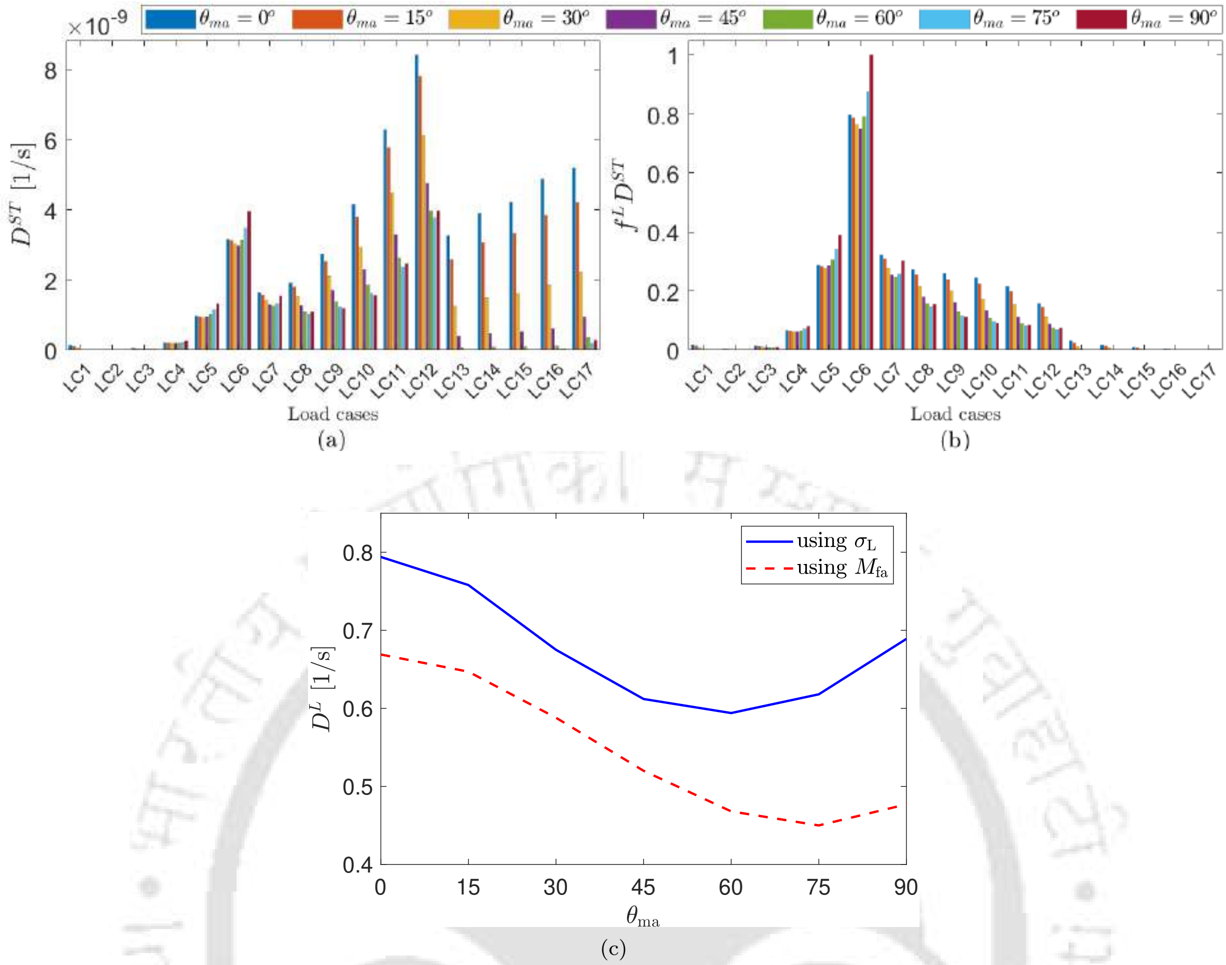

Figure 3.16: Damage of monopile for different load cases with various wind-wave misalignment; (a) short-term damage, (b) weighted damage with the probability of occurrence & (c) lifetime damage.

design value, i.e. 20 yrs. The general trend of the short-term DES (i.e., refer to Fig. 3.18) follows the damage accumulation pattern (i.e., refer to Fig. 3.16) for different wind-wave misalignments. It indicates that the short-term DES increases with the load case number, and it is maximum at the cut-out wind speed. However, due to more probability of occurrence, rated speed (i.e., load case 6) contributes more damage accumulation during the lifetime, as shown in Fig. 3.18b.

3.6.6 Site-Specific Design Curve

The sensitivity analysis presented in the above subsection clearly shows the impact of water depth on fatigue life. It motivates to development of the design curve for a given power rating at a particular site. As stated earlier, the minimum thickness for a given diameter is recommended by API guidelines [i.e., $t_p^{min} = 0.01D_p + 0.00635$] to avoid local buckling. Fig. 3.19a shows the variation of diameter and thickness for different water depth and power ratings, i.e., 5 MW. Here, it is worth mentioning that the fatigue life for each case is more than its design value, i.e., 20 years. The outer diameter of a monopile depends on the size of the tower and transition piece. Fig. 3.19b shows the effect of wall thickness for a given diameter of the monopile. The dotted line in this figure corresponding to 7 m diameter indicates the region vulnerable to local buckling. Table 3.6 shows the variation of first natural frequency in two orthogonal directions, fatigue life, and corresponding strain levels for the design curve in Fig. 3.19b. The first natural frequency in two orthogonal directions (i.e., fore-aft and side-to-side) lies between 1P and 3P, as shown in Fig. 3.20. Hence, the monopile design using the dimensions obtained from these curves (i.e., Fig. 3.19) does not suffer resonance due to blade rotation. Table 3.6 also highlights the strains in different cycles using techniques discussed in § 3.6.4. These results indicate that soil stiffness degradation significantly affects the performance of the monopile. However, the data in Table 3.6 shows that the long-term performance (i.e., strain in the

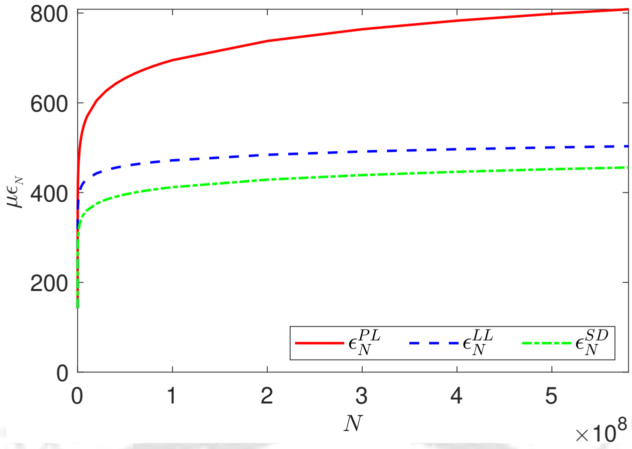

Figure 3.17: Variation of strain with respect to the number of cycles.

Table 3.5: Fatigue life of OC3 monopile wind turbine.

D_p[m]	t_p[m]	**Fatigue life [years]**									
		using fore-aft moment					**using longitudinal stress**				
		D_w **[m]**					D_w **[m]**				
		10.00	**20.00**	**30.00**	**40.00**	**50.00**	**10.00**	**20.00**	**30.00**	**40.00**	**50.00**
6.00	0.05	4.50	-	-	-	-	3.36	-	-	-	-
6.00	0.06	11.54	6.02	-	-	-	8.78	4.95	-	-	-
6.00	0.07	25.53	13.41	-	-	-	19.63	11.10	-	-	-
6.00	0.08	49.47	26.22	11.32	-	-	38.37	21.85	10.53	-	-
6.00	0.09	87.84	46.30	20.96	-	-	68.81	39.00	19.63	-	-
6.00	0.10	-	-	36.15	12.81	5.90	-	-	31.20	11.29	5.23
6.00	0.11	-	-	-	20.55	10.21	-	-	-	18.07	9.04
7.00	0.06	57.71	30.35	14.14	-	-	41.86	23.85	12.68	-	-
7.00	0.07	124.94	66.91	29.87	12.46	-	90.69	52.64	26.92	11.29	-
7.00	0.08	240.99	130.33	57.39	26.51	10.62	175.67	103.06	52.00	24.00	9.93
7.00	0.09	428.08	234.65	100.20	48.52	17.95	313.61	186.14	91.32	44.08	16.87
7.00	0.10	-	-	-	-	29.71	-	-	-	-	26.07
8.00	0.08	-	-	261.92	103.37	27.87	-	-	226.09	91.01	25.84
8.00	0.09	-	-	475.65	184.87	48.83	-	-	409.06	162.99	45.35
8.00	0.10	-	-	799.09	304.73	87.84	-	-	684.93	269.85	82.13

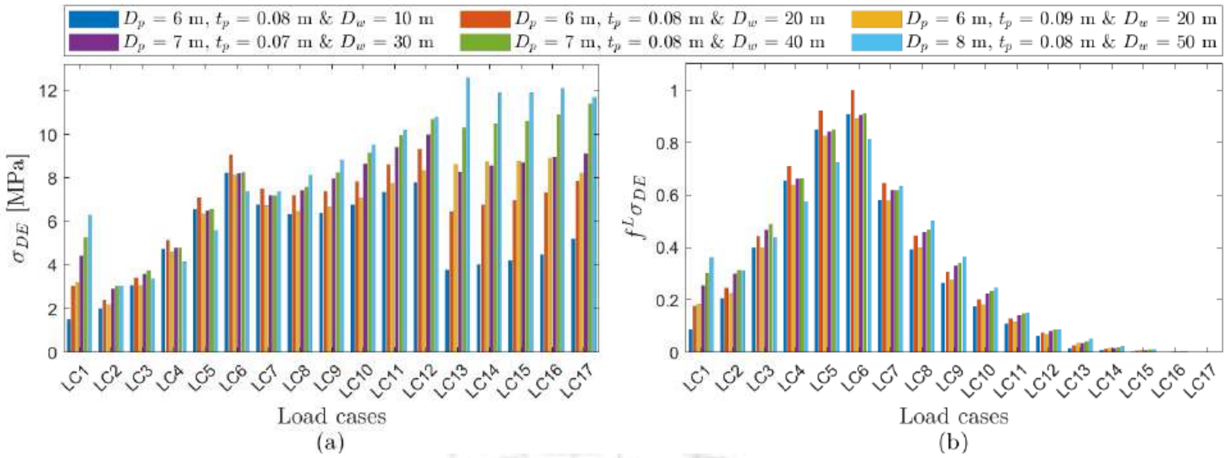

Figure 3.18: Short-term DES of various monopile model for different load cases; (a) short-term DES & (b) relative short-term DES weighted with the probability of occurrence.

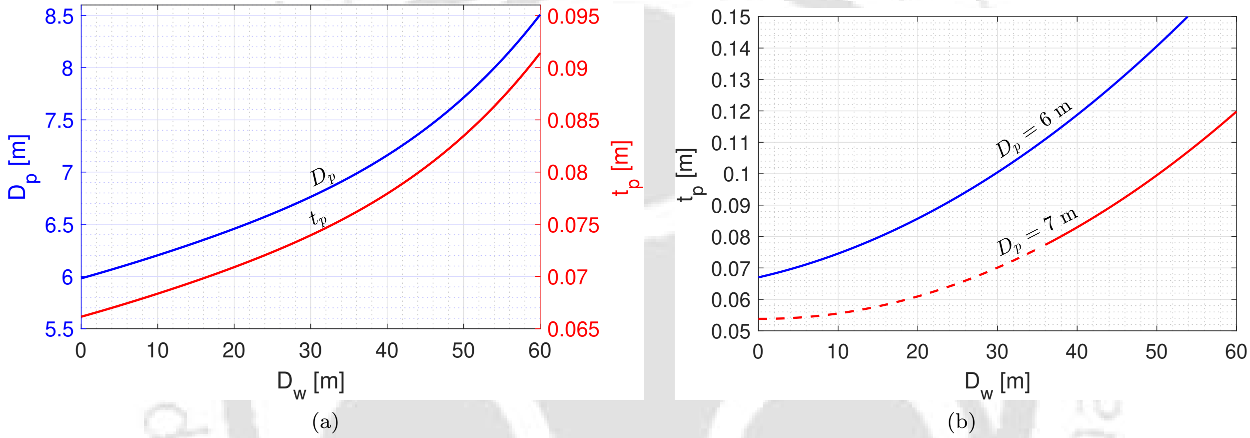

Figure 3.19: Design curve for NREL 5MW offshore wind turbine monopile dimensions with the depth of water; (a) for varying diameter & (b) for fixed diameter.

N^{th} cycle) is satisfactory (i.e., within the allowable limit).

Finally, the variation of fatigue life due to changes in wind speed distribution is investigated. Fig. 3.21a shows the variation of wind distribution for different scale and shape parameters (i.e. c & κ) and Fig. 3.21b illustrates the impact of these parameters on the fatigue life. The minimum fatigue life from this analysis is obtained as 23.97 years corresponding to $c = 13$ m/s and $\kappa = 3$, i.e., at the maximum value of scale and shape parameter. Thus, the curves in Fig. 3.19 can be used to design monopiles for similar turbines in dense sandy soil.

3.7 Summary

The work presented in this chapter develops a multi-body dynamic soil-structure interaction model of an offshore wind turbine for fatigue design and long-term performance evaluation. The study demonstrates stress-based fatigue analysis considering various monopile parameters, water depth, and operational conditions. The significant contributions of this study are as follows -

- The combined system is modeled in Kane's approach using equivalent monopile properties obtained from a detailed substructure analysis. It uses Winkler's beam theory to model the soil layers defined by their respective p-y curves. The model is validated using the properties of a benchmark turbine for turbulent wind. The proposed model offers good agreement with FAST. It is further used to model soil-structure interaction in the marine environment.

Table 3.6: Fatigue life and long-term strain of monopile with 6 m and 7 m diameter for various water depth.

D_p	D_w	t_p	f_{fa}	f_{ss}	Fatigue Life	Strain in 1st cycle	Strian in N^{th} cycle		
[m]	[m]	[m]	[Hz]	[Hz]	[Years]	$\mu\epsilon_1$	$\mu\epsilon_N^{PL}$	$\mu\epsilon_N^{LL}$	$\mu\epsilon_N^{SD}$
6.00	10.00	0.075	0.2967	0.2883	26.22	160.48	910.16	600.43	541.54
	20.00	0.085	0.2567	0.2783	27.56	160.00	907.46	588.24	539.19
	30.00	0.100	0.2567	0.2617	31.20	140.48	796.73	504.98	446.44
	40.00	0.120	0.2567	0.2567	28.30	137.62	780.53	482.62	433.45
	50.00	0.140	0.2567	0.2483	29.20	136.67	775.13	469.55	429.15
7.00	10.00	0.055	0.2967	0.2950	25.80	162.38	920.97	593.00	550.97
	20.00	0.062	0.2967	0.2817	27.99	161.43	915.57	579.64	546.24
	30.00	0.070	0.2567	0.2650	30.23	142.57	808.62	503.32	456.07
	40.00	0.082	0.2567	0.2617	26.72	140.95	799.43	486.85	448.62
	50.00	0.100	0.2567	0.2567	26.07	137.14	777.83	461.10	431.30

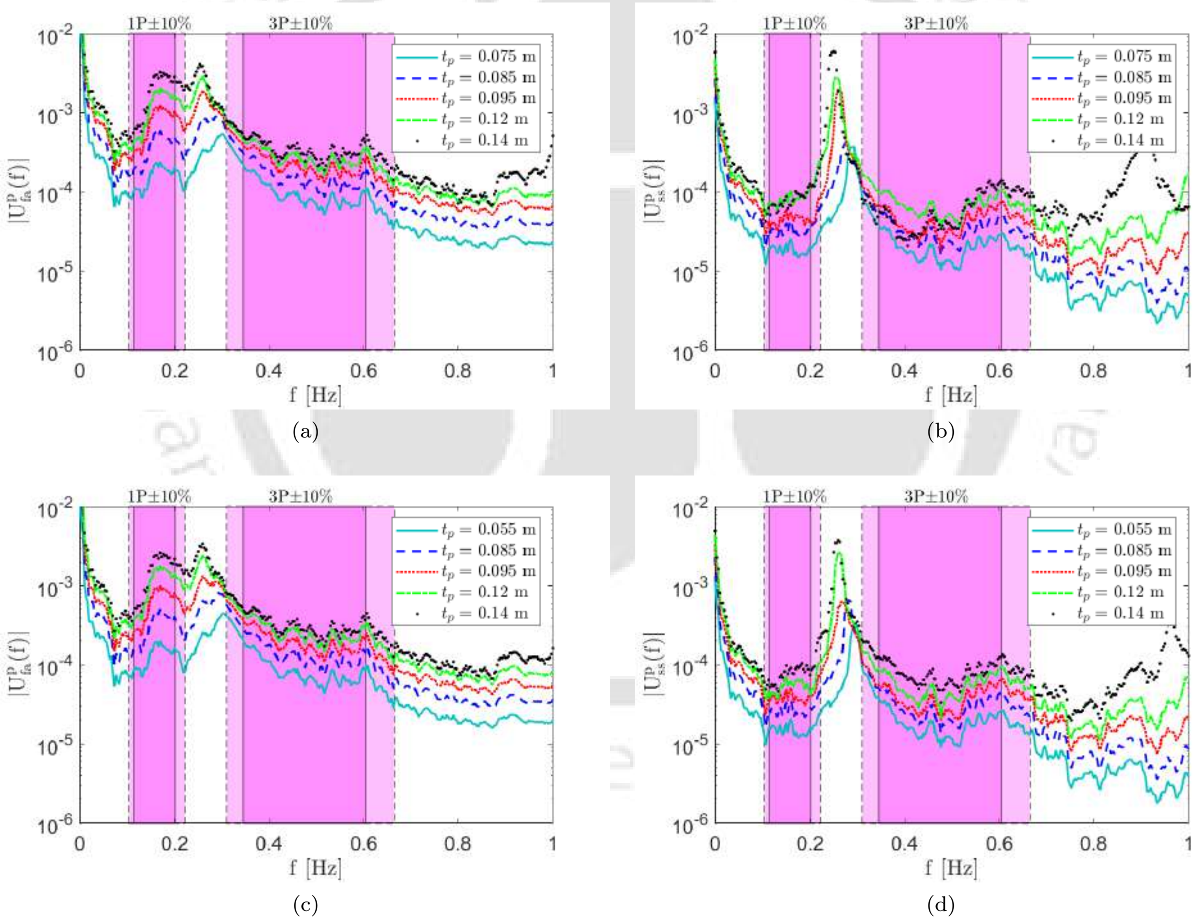

Figure 3.20: Fourier amplitude spectrum of platform deformation with monopile dimensions as per design curve for LC6; (a) $D_p = 6m$, fore-aft, (b) $D_p = 6m$, side-to-side, (c) $D_p = 7m$, fore-aft & (d) $D_p = 7m$, side-to-side.

- The numerical results demonstrate fatigue design of monopile foundation considering different load cases prescribed in IEC guidelines [87]. These results highlight the significance of stress-based modeling using soil-structure interaction for long-term performance evaluation.

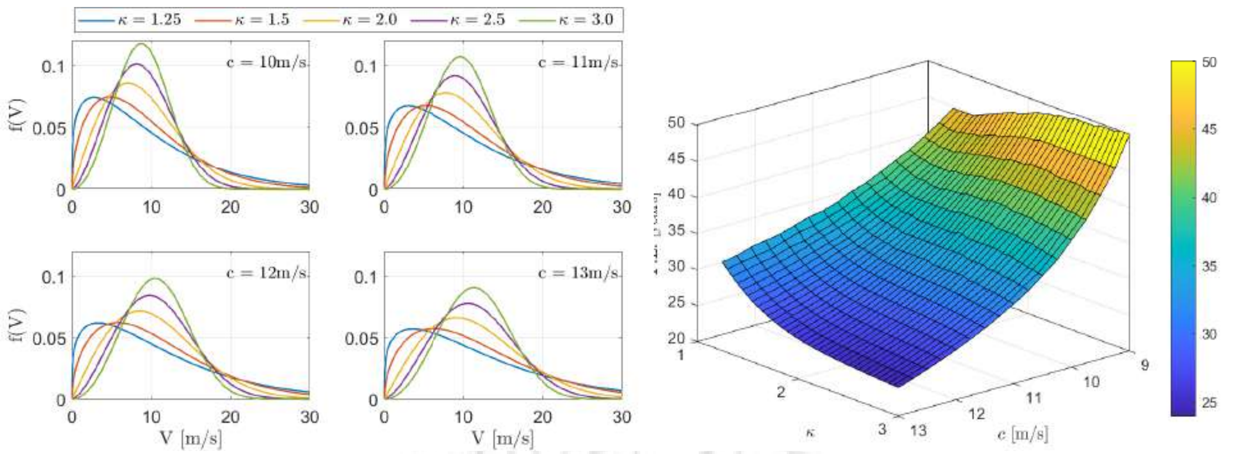

(a) (b)

Figure 3.21: (a) Weibull distribution of wind speed for different scaling and shape parameters & (b) Fatigue life variation for various Weibull parameters.

- As evident, the maximum damage occurs when the aerodynamic and hydrodynamic forces coincide, and their effect is minimal when the misalignment is sixty degrees. The maximum short-term damage occurs at the cut-out speed, while the rated wind speed mostly contributes to the lifetime damage. Therefore, long-term damage due to fatigue load is governed by the rated speed as the turbine witnesses maximum exposure to this operational condition.
- The work also investigates the long-term behavior and the parameters that influence damage-equivalent stress to meet the stringent serviceability criteria. The results demonstrate the impact of stiffness degradation on monopiles' long-term performance in the marine environment.
- Finally, the study offers the design curves for a given power rating of the turbine. These design curves mostly highlight the interrelation between three key parameters, i.e. diameter, thickness, and depth of water. The dimensions obtained using these design curves are satisfactory in terms of fatigue life and serviceability criteria. Thus, these curves can be helpful for the design of similar structures and for project planning that resembles the same marine environment.

Chapter 4

Multi-Body Dynamic Model of Floating Spar-Type Offshore Wind Turbine

4.1 Introduction

In the present chapter, a comprehensive mathematical multi-body model for the floating spar-type offshore wind turbine is developed using Kane's approach with proper aero-elastic and hydrodynamic simulation. For this purpose, 3D wind fields are generated in TurbSim as discussed in the previous chapter, and the waves are simulated from the Pierson-Moskovitch spectrum considering wind-wave correlation and misalignment. Aerodynamic loads are computed using modified Blade Element Momentum theory, while hydrodynamic loads are generated using Morison's equation. The mathematical model is then validated by comparing its response time histories with FAST[76].

4.2 Dynamics of Spar-Type Floating Wind Turbine

In this section, the dynamics of a spar-type offshore wind turbine is formulated using Kane's approach [12]. It is based on the vector representation of forces for solving a multi-body dynamic problem, which provides significant computational advantages. In this approach, the offshore floating wind turbine is modeled by 25 degrees of freedom (DOFs) whose details are given in Table 4.1. Since the complete system floats on water as a rigid body and is free to rotate, the complete DOFs of the spar-type floating wind turbine are defined by the following vector

$$\mathbf{u} = [\underbrace{u_1, ...u_6,}_{Spar}\underbrace{u_7, ...u_{10},}_{Tower}\underbrace{u_{11},}_{Nacelle}\underbrace{u_{12}, u_{13},}_{Drive-train}\underbrace{u_{14}, ...u_{25}}_{Blades}]^T \tag{4.1}$$

The rotation at the tower base is considered here, as the turbine modeled here is supported on a floating spar. As a result, the DOFs 1,2,3 in Eq. 4.1 indicate translational (surge, sway, and heave) motions, and the DOFs 4,5,6 in Eq. 4.1 refer to the rigid body rotation (roll, pitch, and yaw) of the tower base. The tower vibration is represented by the first two modes in its fore-aft and side-to-side directions, i.e., the following four DOFs. The nacelle yaw, drive-train torsion, and generator azimuth (i.e., slow-speed shaft) are modeled by a single degree of freedom for each of them. Finally, two flapwise, one edgewise, and one torsional mode are considered to simulate each blade. However, the formulation is general and can incorporate as many modes as necessary for a particular application. The details of these DOFs for different components are shown in Table 4.1. Besides DOFs, the formulation of the multi-body system also demands different coordinates for the global system as well as individual components as described in Tab. 4.1. The details of these coordinate systems are also marked in Fig. 4.1. The global inertial reference frame is defined by $\hat{x}$. The local coordinates used in this multi-body system are for spar/tower base ($\hat{a}$), tower top ($\hat{b}$), nacelle ($\hat{c}$), low-speed shaft ($\hat{d}$), generator azimuth ($\hat{e}$) and blades ($\hat{f}_k$). In addition to these coordinates, there are separate coordinate systems used for blade coning ($\hat{g_k}$), pitch ($\hat{h_k}$), local structural twist ($\hat{i_k}$) and blade elements ($\tilde{b_k}$). Blade also has two more local coordinates for its deformed elements ($\bar{b}_k$) and aerodynamic loads ($\hat{a}_{ek}$). In this context, it may

Table 4.1: Details of DOFs and Coordinate Systems

Multibody Names	**Components**	**DOFs**	**Local Coordinate**	**Remarks**
Spar	Surge	u_1		
	Sway	u_2		
	Heave	u_3	$\hat{a}$	For rigid body translation and rotation
	Roll	u_4		
	Pitch	u_5		
	Yaw	u_6		
Tower	1^{st} Fore-aft mode	u_7	$\hat{a}$	Tower global
	1^{st} Side-to-side mode	u_8	$\hat{b}$	Tower top
	2^{nd} Fore-aft mode	u_9	$\bar{b}$	Tower element fixed system
	2^{nd} Side-to-side mode	u_{10}		
Nacelle	Nacelle yaw	u_{11}	$\hat{c}$	Yaw
Drive Train	Shaft azimuth	u_{12}	$\hat{d}$	Slow speed shaft tilt and skew
	Shaft torsional DOF	u_{13}	$\hat{e}$	Rotating with slow speed shaft
Blade 1	1^{st} Flap mode	u_{14}	$\hat{f}_1$	Global
	1^{st} Edge mode	u_{15}	$\hat{g}_1$,$\hat{h}_1$,$\hat{i}_1$	Cone, Centroidal, Twist
	2^{nd} Flap mode	u_{16}	$\tilde{b}_1$, $\hat{a}_{e1}$	Element fixed system
	1^{st} Torsional mode	u_{17}		
Blade 2	1^{st} Flap mode	u_{18}	$\hat{f}_2$	Global
	1^{st} Edge mode	u_{19}	$\hat{g}_2$,$\hat{h}_2$,$\hat{i}_2$	Cone, Centroidal, Twist
	2^{nd} Flap mode	u_{20}	$\tilde{b}_2$, $\hat{a}_{e2}$	Element fixed system
	1^{st} Torsional mode	u_{21}		
Blade 3	1^{st} Flap mode	u_{22}	$\hat{f}_3$	Global
	1^{st} Edge mode	u_{23}	$\hat{g}_3$,$\hat{h}_3$,$\hat{i}_3$	Cone, Centroidal, Twist
	2^{nd} Flap mode	u_{24}	$\tilde{b}_3$, $\hat{a}_{e3}$	Element fixed system
	1^{st} Torsional mode	u_{25}		

be noted that each coordinate systems have three components along with three orthogonal directions which are marked by appropriate subscripts, e.g., $\hat{a}_1$, $\hat{a}_2$ and $\hat{a}_3$ for the spar. In the case of coordinate systems having k as subscripts, it refers to blade number, e.g. $\hat{g}_k$ for $k = 1, 2, 3$ for three blades with another three secondary subscripts for three directions for a particular blade. The detailed descriptions and origins of these coordinate systems are given in Table. 4.2. As the spar, blades, and tower can rotate about more than one axis simultaneously, the use of traditional transformation matrices is restricted, henceforth small-angle approximation [12] is used to form Euler 1-2-3 Rotation matrices to establish transformation relation between these coordinate systems, which makes the formulation of the matrices independent of the sequence of rotation.

Once the DOFs and coordinate systems are defined, the governing equation of motion can be formulated using Kane's approach. Derived from Newton's law of motion, Kane's equation for a holonomic multi-body system can be expressed as a set of scalar equations [12]

$$\mathbf{F_i} - \mathbf{F_i^*} = 0 \quad for \quad i = 1, 2, ..., n \tag{4.2}$$

where n is the total number of degrees of freedom in the system (i.e., $n = 25$ in this case). $\mathbf{F_i}$ and $\mathbf{F_i^*}$ represent the generalized active and inertia forces, respectively. These forces for each multibody component can be determined by the expressions presented in Eq.2.3 to Eq. 2.6 of the previous chapter, hence they are not repeated here.

Components	Coordinate Systems	Representation	Origin	Remarks
Tower	Tower base	$\hat{a}$	Intersection of centre of tower base and platform support	Translates and rotates with platform
	Tower top	$\hat{b}$	On yaw axis at top of tower	Moves with the tower but does not yaw
	Tower element	$\bar{b}$	On each tower nodes	Moves with the deformed tower elements
Nacelle	Yaw	$\hat{c}$	Same as $\hat{b}$	Moves with the tower and yaw of nacelle
Drive-train	Slow-speed Shaft	$\hat{d}$	Intersection of rotor axis and $\hat{c}_2$-$\hat{c}_3$ plane of nacelle coordinate system	Skews and tilts with the shaft but does not spin with rotor
	Azimuth	$\hat{e}$	Same as shaft coordinate system	Spins with rotor
Blade	Global	$\hat{f}_k$	At blade roots	Spins with rotor
	Coned	$\hat{g}_k$	Same as $\hat{f}_k$	Cones with blade
	Pitched	$\hat{h}_k$	Same as $\hat{f}_k$	Pitches with blade
	Twisted	$\hat{h}_k$	On each blade nodes	Twisted with blade's structural twist
	Blade-element	$\hat{i}_k$	Same as $\hat{h}_k$	Moves with the deformation of blade elements
	Aerodynamic	$\hat{a}_{ek}$	Same as $\hat{h}_k$	Used to calculate aeroelastic forces on the blades (normal and tangential to the rotor plane)

Table 4.2: Coordinate systems of different components

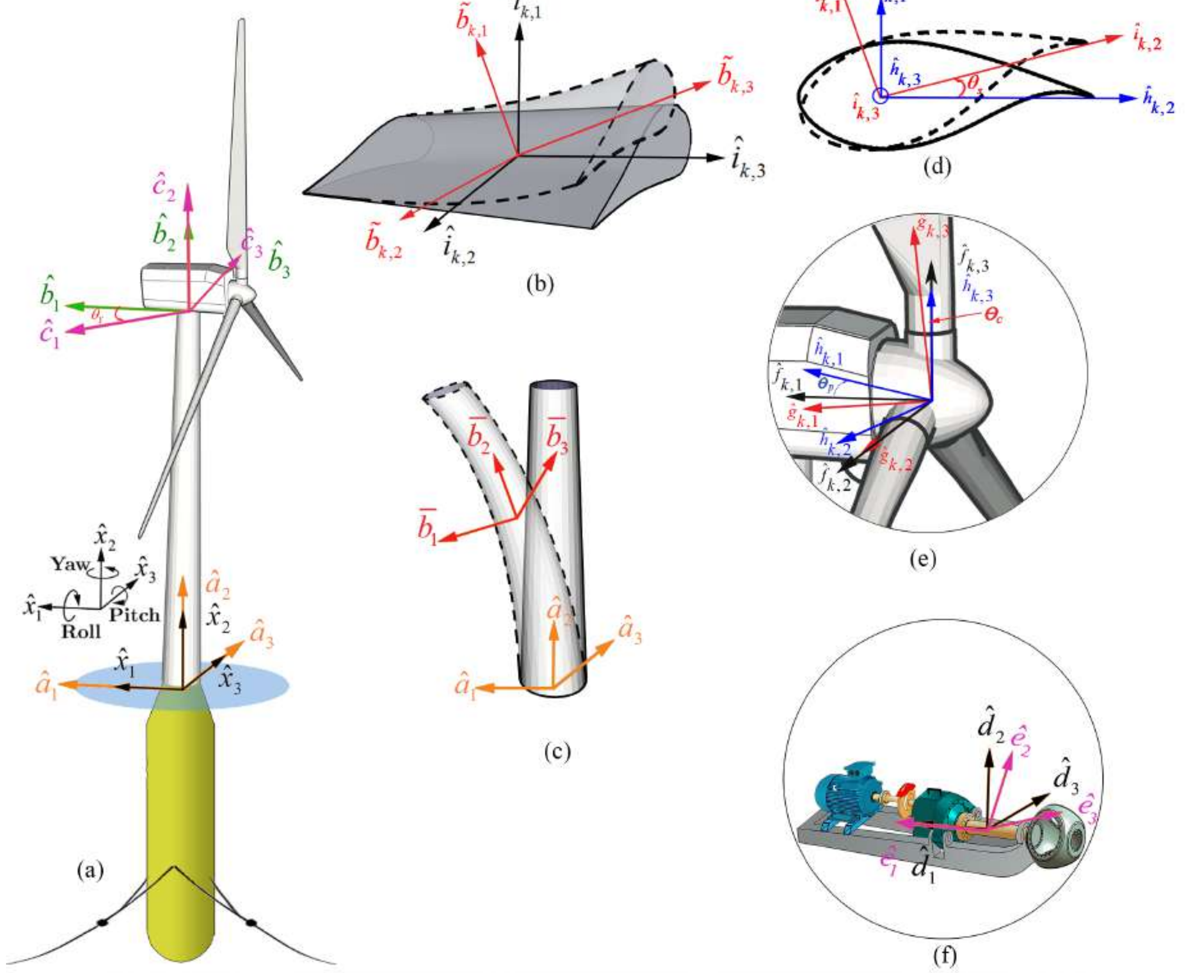

Figure 4.1: Schematic diagram of spar-type floating Horizontal Axis Wind Turbine (HAWT) and associated coordinates; (a) combined multi-body system, (b) deformed blade element, (c) deformed tower, (d) local twist of blade, (e) cone and pitch & (f) drive-train

The governing equation of motion for the complete multi-body system in its global reference frame can be determined from the generalized inertia and active forces of each component. In this scenario, the complete structure of the wind turbine comprises the floating spar (s), tower (tw), nacelle (na), generator (gn), low-speed shaft (ls), hub (hu), yaw bearing (yb), and three blades (b_k). Thus, $c_k = \{s, tw, na, hu, gn, ls, yb, b_1, b_2, b_3\}$ denotes the two-letter acronym representing the center of gravity of these subsystems. Except for the low-speed shaft and yaw bearing, which exhibit slow movement, each element contributes to the generalized inertia force. Consequently, the total generalized inertia force can be articulated using the subsequent equation

$$\begin{aligned} \mathbf{F_i^*} = & \mathbf{F^*_{i,s}} + \mathbf{F^*_{i,tw}} + \mathbf{F^*_{i,na}} + \mathbf{F^*_{i,hu}} + \mathbf{F^*_{i,gn}} \\ & + \cancelto{0}{F^*_{i,ls}} + \cancelto{0}{F^*_{i,yb}} + \mathbf{F^*_{i,b_1}} + \mathbf{F^*_{i,b_2}} + \mathbf{F^*_{i,b_3}} \end{aligned} \tag{4.3}$$

The generalized active force, which includes both internal and external conservative and non-conservative forces, acts on each sub-system in addition to the generalized inertia force in Eq. 4.3. The floating turbine experiences hydrostatic and hydrodynamic loads arising from buoyancy and irregular ocean waves rather than seismic forces as in the onshore case. Additionally, the spar is also subjected to mooring loads resulting from the mooring cables used to anchor the entire structure to the ocean floor. Thus, elastic (el), damping (d), aeroelastic (ae), gravitational (gv), generator (gn), brake (br), hydrostatic and dynamic (hy), and mooring (mr) forces acting on the turbine can be modeled as

$$\begin{aligned}
&\mathbf{F_i} = \mathbf{F_{i,tw,el}} + \mathbf{F_{i,b_1,el}} + \mathbf{F_{i,b_2,el}} + \mathbf{F_{i,b_3,el}} + \mathbf{F_{i,ls,el}} + \mathbf{F_{i,yb,el}} + \mathbf{F_{i,tw,d}} + \mathbf{F_{i,b_1,d}} + \mathbf{F_{i,b_2,d}} \\
&+\mathbf{F_{i,b_3,d}} + \mathbf{F_{i,ls,d}} + \mathbf{F_{i,yb,d}} + \mathbf{F_{i,tw,ae}} + \mathbf{F_{i,b_1,ae}} + \mathbf{F_{i,b_2,ae}} + \mathbf{F_{i,b_3,ae}} + \mathbf{F_{i,tw,gv}} + \mathbf{F_{i,s,gv}} \\
&+\mathbf{F_{i,na,gv}} + \mathbf{F_{i,hu,gv}} + \mathbf{F_{i,b_1,gv}} + \mathbf{F_{i,b_2,gv}} + \mathbf{F_{i,b_3,gv}} + \mathbf{F_{i,gn}} + \mathbf{F_{i,br}} + \mathbf{F_{i,s,hy}} + \mathbf{F_{i,s,mr}}
\end{aligned} \tag{4.4}$$

Ultimately, the equation of motion governing the system can be derived by inserting Eq.4.3 and Eq.4.4 into Eq. 4.2 and reorganizing them in matrix form. This process results in the subsequent equation:

$$[\mathbf{M(u,t)}] . \{\mathbf{\ddot{u}}\} + \left\{\mathbf{\bar{F}(\dot{u},u,t)}\right\} = 0 \tag{4.5}$$

The mass matrix $[\mathbf{M(u,t)}]$ is constituted by the inertial components in the equation presented above. The remaining portion denoted as $\left\{\mathbf{\bar{F}(\dot{u},u,t)}\right\}$, encompasses stiffness and damping in addition to externally applied forces. The complete derivation of each component in Eq. 4.5 for various subsystems is presented in §2.2 of chapter 2, except for the floating spar. Hence, here the derivation of the terms in Eq. 4.5 for the floating spar is presented in the following subsection.

4.2.1 Spar

In this sub-section, the governing equation of motion for the spar using Kane's approach is demonstrated step by step, which is assumed to be a rigid body. The rationale behind this assumption is that the diameter of the spar is significantly more than the tower, which makes it relatively stiffer. The motion of the spar is derived from the tower base. Thus, the position vector of the tower base t_b with respect to reference frame $\hat{x}$ is given by

$$\mathbf{r_{t_b}} = u_1.\hat{x}_1 - u_2.\hat{x}_3 + u_3.\hat{x}_2 \tag{4.6}$$

where r_{t_b} is the position vector of the tower base, which is used to locate the position of the spar. Now, the linear velocity of the reference point t_b can be expressed as

$$\mathbf{v_{t_b}} = \dot{u}_1.\hat{x}_1 - \dot{u}_2.\hat{x}_3 + \dot{u}_3.\hat{x}_2 \tag{4.7}$$

As mentioned earlier the tower base can undergo rigid body rotation as it is supported by a floating spar, hence, the angular velocity at the same point is given by

$$\omega_{\mathbf{t_b}} = \dot{u}_4.\hat{x}_1 - \dot{u}_5.\hat{x}_3 + \dot{u}_6.\hat{x}_2 \tag{4.8}$$

Now, the position vector r_s of the center of gravity of spar (i.e. s) from the tower base is given by

$$\mathbf{r_s} = h_s.\hat{a}_2 \tag{4.9}$$

where h_s is the vertical distance from the tower base. Using Eq. (4.7) to Eq. (4.9), the linear velocity at the center of mass of the spar (s) is given by

$$\mathbf{v_s} = \mathbf{v_{t_b}} + \omega_{\mathbf{t_b}} \times \mathbf{r_s} \tag{4.10}$$

In this formulation, time derivatives of the displacement field along the generalized coordinate are termed as the generalized speed (i.e. $q_i = \dot{u}_i$). Using this expression of q_i and rearranging Eq. (4.7) in the format of Eq. (2.5a) reveals that the terms that do not follow linear superimposition are zero, i.e. $v_{t,t_b} = 0$ and the remaining components are given by

$$\mathbf{v_{i,t_b}} = \begin{cases} \hat{x}_1 & \text{for } i = 1 \\ -\hat{x}_3 & \text{for } i = 2 \\ \hat{x}_2 & \text{for } i = 3 \end{cases} \tag{4.11}$$

Similarly, using Eq. (4.8) in the format of Eq. (2.5b) indicates that $\omega_{t,t_b} = 0$ and the remaining components are expressed as follows

$$\omega_{\mathbf{i},\mathbf{t_b}} = \begin{cases} \hat{x}_1 & \text{for } \ i = 4 \\ -\hat{x}_3 & \text{for } \ i = 5 \\ \hat{x}_2 & \text{for } \ i = 6 \end{cases} \tag{4.12}$$

Using above two expressions for partial linear and angular velocities (i.e. $\mathbf{v_{i,t_b}}$ and $\omega_{\mathbf{i,t_b}}$) in their respective total velocities and substituting them in Eq. (4.10), it can be concluded that the components of the total linear velocity at the center of mass of the spar (s) that do not follow linear superimposition are zero ($v_{t,s} = 0$), while the other components are given by

$$\mathbf{v_{i,s}} = \mathbf{v_{i,t_b}} + \omega_{\mathbf{i,t_b}} \times \mathbf{r_s} \qquad \text{for } \ i = 1...6 \tag{4.13}$$

Now using the above expression, partial linear acceleration can be derived. Thus, differentiating Eq. (4.13) with respect to time leads to the following expression

$$\frac{d}{dt}(\mathbf{v_{i,s}}) = \omega_{\mathbf{i,t_b}} \times (\omega_{\mathbf{t_b}} \times \mathbf{r_s}) \qquad \text{for } \ i = 4...6 \tag{4.14}$$

Moreover, as $v_{t,s} = 0$, its time derivative is also zero i.e. $\frac{d}{dt}(v_{t,s}) = 0$. Once the components of linear accelerations are derived, each term of the angular acceleration can also be derived similarly. In this context, Eq. (2.6b) for total angular acceleration at the tower base demands differential of Eq. (4.12) with respect to time, which are zero in this case i.e., $\frac{d}{dt}(\omega_{\mathbf{i,t_b}}) = 0$ for $i = 4...6$ and $\frac{d}{dt}(\omega_{\mathbf{t,t_b}}) = 0$. As mentioned earlier, the spar is acting as a rigid body attached to the tower base. Hence, all linear velocities and accelerations are calculated with respect to the spar center of mass, but the rotational velocities and acceleration of the spar are calculated with respect to the tower base. Using all appropriate expressions of linear and angular velocities and accelerations in Eq. (2.4), the generalized inertia force on spar can be expressed as

$$\begin{aligned} \mathbf{F^*_{i,s}} &= [\mathbf{v_{i,s}}.(m_s.\mathbf{a_s}) + \omega_{\mathbf{i,t_b}}.(\mathbf{\bar{I}_s}.\alpha_{\mathbf{t_b}} + \omega_{\mathbf{t_b}} \times \mathbf{\bar{I}_s}.\omega_{\mathbf{t_b}})] \\ &= \mathbf{v_{i,s}}.\left[m_s\left\{\left(\sum_{i=1}^{6}\mathbf{v_{i,s}}.\mathbf{\ddot{u}_i}\right) + \left(\sum_{i=4}^{6}\frac{d}{dt}(\mathbf{v_{i,s}}).\dot{u}_i\right)\right\}\right] \\ &\quad + \omega_{\mathbf{i,t_b}}.\left[\mathbf{\bar{I}_s}.\left(\sum_{i=4}^{6}\omega_{\mathbf{i,t_b}}.\mathbf{\ddot{u}_i}\right) + \omega_{\mathbf{t_b}} \times \mathbf{\bar{I}_s}.\omega_{\mathbf{t_b}}\right] \end{aligned} \tag{4.15}$$

where $\mathbf{\bar{I}_s}$ is the moment of inertia dyadic for spar, which can be obtained from its three orthogonal components along roll, yaw, and pitch axis (i.e., subscripts r, y, and p) in the following expression

$$\mathbf{\bar{I}_s} = I_{s_r}.\hat{a}_1.\hat{a}_1 + I_{s_y}.\hat{a}_2.\hat{a}_2 + I_{s_p}.\hat{a}_3.\hat{a}_3 \tag{4.16}$$

Once the generalized inertia force of spar is derived, the components of the system matrices can be obtained by rearranging Eq. (4.15), which leads to the following expressions

$$\mathbf{M_{i,j;s}(u,t)} = m_s.\mathbf{v_{i,s}}.\mathbf{v_{j,s}} + \omega_{\mathbf{i,t_b}}.\mathbf{\bar{I}_s}.\omega_{\mathbf{j,t_b}} \quad \text{for } \ i,j = 1...6 \tag{4.17a}$$

$$\mathbf{\bar{F}^*_{i,s}} = m_s.\mathbf{v_{i,s}}.\left[\left(\sum_{i=4}^{6}\frac{d}{dt}(\mathbf{v_{i,s}}).\dot{u}_i\right)\right] + \omega_{\mathbf{i,t_b}}.\left[\omega_{\mathbf{t_b}} \times \mathbf{\bar{I}_s}.\omega_{\mathbf{t_b}}\right] \quad \text{for } \ i = 1...6 \tag{4.17b}$$

Finally, generalized active forces acting on the spar are derived for the complete equation of motion. So, the contribution of wave forces and moments acting on the spar is given by

$$\mathbf{F_{i,s,hy}} = \mathbf{v_{i,s}}.F_{s,hy} + \omega_{\mathbf{i,t_b}}.M_{t_b,hy} \qquad \text{for } \ i = 1...6 \tag{4.18}$$

In the above expression, $F_{s,hy}$ and $M_{t_b,hy}$ represent the hydrodynamic forces and moments acting at the tower base, respectively, which depend on wave and motion of the spar. These are expressed as follows

$$F_{s,hy} = \left(\sum_{i=1}^{6} F_{s,hy_i}.\ddot{u}_i \right) + F_{s,hy_t} \tag{4.19a}$$

$$M_{t_b,hy} = \left(\sum_{i=4}^{6} M_{t_b,hy_i}.\ddot{u}_i \right) + M_{t_b,hy_t} \tag{4.19b}$$

where F_{s,hy_t} and M_{t_b,hy_t} are the hydrostatic and hydrodynamic forces and moments, respectively that do not depend on the inertia of the spar. Finally, the system matrices due to wave (i.e. both static and dynamic) acting on the spar are given by

$$\mathbf{M_{i,j;s,hy}}(\mathbf{u}, \mathbf{t}) = [-\mathbf{v_{i,s}}.F_{s,hy_j} - \omega_{\mathbf{i,t_b}}.M_{t_b,hy_j}] \quad \text{for} \quad i,j = 1...6 \tag{4.20a}$$

$$\mathbf{F_{i,s,hy}}(\dot{\mathbf{u}}, \mathbf{u}, \mathbf{t}) = [\mathbf{v_{i,s}}.F_{s,hy_t} + \omega_{\mathbf{i,t_b}}.M_{t_b,hy_t}] \quad \text{for} \quad i = 1...6 \tag{4.20b}$$

Generalized active forces due to gravity on the spar are given by

$$\mathbf{F_{i,s,gv}}(\dot{\mathbf{u}}, \mathbf{u}, \mathbf{t}) = \mathbf{v_{i,s}}.(-m_s.g.\hat{x}_2) \qquad \text{for} \quad i = 1...6 \tag{4.21}$$

where g is the acceleration due to gravity. Applying a similar methodology to that used for the spar, the equation of motion for every other component can be obtained within the global reference frame, as discussed in §2.2 of the previous chapter. Subsequently, these individual equations are assembled to formulate the comprehensive model of the offshore turbine system. The subsequent sections delve into a discussion of the external loads acting on the turbine.

4.3 External Loads on Floating Wind Turbine

Different external loads act on a floating wind turbine: aerodynamic load on the blades and the tower, hydrodynamic load on the spar, and mooring forces arising from the anchoring cables. A detailed description of the aerodynamic loads is already presented in §2.2.5 of chapter 2. Hence, only the necessary equations for modeling the other loads in offshore turbines are discussed in detail below.

- **Hydrodynamic Load:** Generally, a zero mean Gaussian stationary power spectrum is used to simulate the sea states. In this chapter, the ocean wave profile is simulated using the Pearson-Moskowitch (PM) spectrum [101], which represents a developed sea state. The water velocities and acceleration time histories at different depths are estimated for a given significant wave height H_s and the peak period T_p. The PM spectrum is given by

$$S_{PM}(f) = 0.3125 H_s^2 f_p^4 f^{-5} \exp\left\{ -1.25 \left(\frac{f_p}{f} \right)^4 \right\} \tag{4.22}$$

where f_p is the peak frequency. Finally, Morison's equation is used to estimate the linear wave inertia forces and non-linear viscous drag forces acting on the spar and torus. It assumes viscous drag forces dominate the total drag force, and the damping due to radiation is negligible. As the spar is cylindrical in shape and undergoes small rotations, these assumptions are valid in this case. The elemental force acting on a strip dx of the spar in the surge or sway degrees of freedom is obtained from

$$\mathbf{dF_{i,s,hy}}(\mathbf{x}, \mathbf{t}) = \overbrace{-C_A \left(\frac{\pi D_s(x)^2}{4} \right) \rho \ddot{u}_i(x,t) dx}^{\text{Added Mass}} + \overbrace{C_{Mf} \left(\frac{\pi D_s(x)^2}{4} \right) \rho a_i^f(x,t) dx}^{\text{Fluid Inertia}} \qquad \text{for } i = 1,2 \tag{4.23}$$
$$+ \overbrace{\frac{1}{2} C_{Dr} \left(v_i^f(x,t) - v_{i,s}(x,t) \right) \rho D_s(x) \left| v_i^f(x,t) - v_{i,s}(x,t) \right| dz}^{\text{Viscous Drag}}$$

In the above equation, the first term denotes added mass associated with the motion of the spar or torus while the second and third terms imply fluid inertial forces and viscous drag forces, respectively. Here, ρ is the water density, and C_A, C_{Mf}, and C_{Dr} are the coefficients for added mass, fluid inertia, and viscous drag forces, respectively. $D_s(x)$ is the diameter of the spar at depth x. In (4.23), v_i^f and a_i^f are the instantaneous fluid velocities and acceleration, and $v_{i,s}$ is the velocity of the spar. The roll and pitch moments acting on the spar can be expressed as

$$\mathbf{dM_{i,t_b,hy}(x,t)} = \begin{cases} dF_{2,s,hy}(x,t).x & \text{for } i = 4 \\ -dF_{1,s,hy}(x,t).x & \text{for } i = 5 \end{cases} \tag{4.24}$$

where the total forces and moments acting on the spar can be obtained by integrating elemental forces and moments along their depths. In this study, the yaw moment and heave force are assumed to be zero as the spar is symmetrical about the vertical axis. Equation (4.23) does not include the added mass associated with spar heave motion hence it is added separately.

- **Mooring Loads:** The mooring dynamic loads acting in the spar are computed by an open-source mooring line simulation program, MoorDyn [262]. It utilizes a lumped-mass mooring cable model accounting for the forces due to internal axial stiffness and damping, weight, buoyancy, hydrodynamic forces from Morison's equation, and vertical spring-damper forces arising from the contact with the seabed. As shown in Fig. 4.2, the cable is divided into N_c number of line segments with (N_c+1) nodes, having identical properties of density, unstretched length, diameter, and Young's modulus. Each node is defined by its corresponding position vector r_i for $i = 0...N_c$. The wave kinematics on the mooring cables are neglected because the fairleads of the spar-type Floating Wind Turbine (FWT) are deep below the water surface. Readers may refer to literature [263, 264] for further details on this topic. The MoorDyn module is coupled with the model of FWT and the instantaneous mooring loads are evaluated using this coupled model.

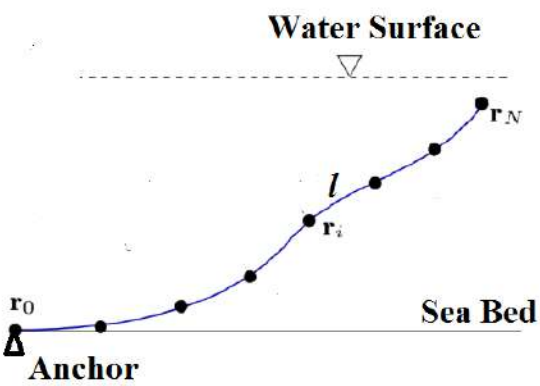

Figure 4.2: Schematic diagram of mooring cable

4.4 Numerical Results and Discussion

This section presents the numerical analysis of the proposed model of the spar-type FWT to verify its response with the available open-source software FAST. Aerodynamic and hydrodynamic loads are simulated, considering wind-wave correlation and misalignment. For mathematical modeling of Spar-type FWT, the benchmark properties of National Renewable Energy Laboratory (NREL) 5MW wind turbine on the OC3-Hywind spar [6] is used here. Six different time histories [spar surge (U_{s_Su}) and sway (U_{s_Sw}), spar roll (U_{s_R}) and pitch (U_{s_P}), tower top fore-aft (U_{TFA}) and side-to-side (U_{TSS}) motions] are analyzed and presented below to demonstrate the performance of the developed model.

4.4.1 Properties of Spar-type FWT and other Environmental Parameters

The basic properties of the benchmark turbine are shown in Table 4.3. The blades are composed of 8 different airfoils along their length, whose properties like chord length, aero-twist, lift and drag coefficients and blade structural properties like mass per unit length and stiffness are taken from the NREL report [5]. The drivetrain has a gear tooth ratio of 97 with torsional stiffness, and generator inertia are 867637kN-m/rad and 534kg-m^2, respectively. The OC3-Hywind spar is 120m deep with 3 mooring lines, whose fundamental properties are given in Table 4.4 along with the properties of mooring cable.

Table 4.3: NREL 5-MW Turbine Data [5].

Basic Descriptions		Blade (LM61.5 P2)		Tower	
Max. Power	5000 kW	Length	61.5 m	Height	87.6 m
No. of blades	3	Mass	17740 kg	Mass	347460 kg
Rotor dia.	126 m	f^F_{1,b_k}, f^F_{2,b_k}	0.66, 2.07 Hz	$f^{FA}_{1,tw}$	0.324Hz
Hub-height	90 m	f^E_{1,b_k}, f^E_{2,b_k}	1.08, 4.05Hz	$f^{SS}_{1,tw}$	0.312Hz
V_{ci}, V_r, V_{co}	3 m/s, 11.4 m/s, 25 m/s	$\xi^F_{b_k}$, $\xi^E_{b_k}$	0.47%, 0.47%	ξ^{FA}_{tw}, ξ^{SS}_{tw}	1%, 1%
Ω_{ci}, Ω_r	6.9 rpm, 12.1 rpm				

Table 4.4: Details of spar & mooring cables [6].

OC3-HyWind spar		Mooring cables	
Draft	120m	Depth to anchors	320m
Depth to taper top	4m	Depth of fairleads	70 m
Depth to taper bottom	12 m	Radius to anchors	853.87 m
Dia. above taper	6.5 m	Radius to fairleads	5.2 m
Dia. below taper	9.4 m	Unstretched length	902.2 m
Mass	7.47e6 kg	Cable dia	0.09 m
CM below SWL	90 m	Eq. mass density	77.71 kg/m
Roll inertia about CM	4.23e9 kg-m^2	Eq. extensional stiffness	384,243 kN/m
Pitch inertia about CM	4.23e9 kg-m^2		
Yaw inertia about CM	1.64e8 kg-m^2		

The steady and turbulent wind fields for mean velocity (11.4m/s) corresponding to rated speed at 90m hub height are simulated in TurbSim. As the marine environment has less turbulence compared to onshore [14], the power-law exponent of 0.2 for steady wind and 10% turbulence with IEC Kaimal spectra have been used for wind field simulation. The joint probability distribution of mean wind speed at 10m height along with significant height and peak period of the wave as presented by Johannessen et al.[265], are considered here. Using these parameters, wave acceleration and velocities at different depths are generated from the Pierson-Moskowitch spectrum, as mentioned in §4.3. Using these inputs and other structural properties, the responses of the mathematical model are validated with the benchmark response.

4.4.2 Model Validation

The mathematical model of the floating turbine described in §4.2 is developed in MATLAB [232]. The fourth-order Ranga-Kutta integration scheme is used here to solve the coupled differential equations of motion numerically. A sufficiently small time step of 0.0125s has been used to retain the accuracy of the numerical integration. The validation exercise is carried out in two stages- (i) under steady wind and sinusoidal waves and (ii) under corresponding random waves generated from the Pierson-Moskowitch spectrum. Below, the explanation for this two-stage validation process is provided.

- In the first case, the sea state is assumed to generate 3.1m high sinusoidal waves having a period of 11s for steady wind at the rated speed with 30^o wave-wind misalignment. Using these conditions, which make the two models (i.e. the code developed in this study and FAST) identical and the inputs uniform, the multi-body dynamic systems are solved, and the response corresponding to the six performance parameters mentioned earlier are demonstrated in Fig. 4.3. Here, it is worth noting that Morison's equation is used in the present analysis to estimate the hydrodynamic load while FAST uses potential flow theory.

  The diameter of the spar and the ocean wavelength in this validation exercise reveal that their ratio is well below the threshold of 0.2, and hence, the small body assumption is valid. This, in turn, ensures that Morison's equation can be applicable in this case [266]. The key response parameters in Fig. 4.3 reveal that the two codes are in agreement with each other, where a close match is observed between them except for a few discrete locations at the initial transient stage. However, these occasional differences at the initial stage are small for all practical purposes. Thus, the results in Fig. 4.3 prove the accuracy of the code developed in MATLAB, where the fluid diffraction and radiation damping are neglected. These components of the hydrodynamic damping are modeled using potential flow theory in FAST. However, the results in Fig. 4.3 establish the fact that their effects are small. Thus, the use of Morison's equation is also justified in this case.

- After validating the model under steady wind and sinusoidal waves, the wind field is generated by TurbSim corresponding to rated speed, and the corresponding wave acceleration and velocities at different depths are generated from the Pierson-Moskowitch spectrum as mentioned in §4.3. The response of the spar-type FWT is generated at rated speed with 30^o wave-wind misalignment. The simulated results of the aforesaid 6 performance parameters using FAST and the model developed in this study are presented in Fig. 4.4, with their corresponding Fourier amplitudes shown in the inset. Results obtained from these two codes are in agreement with each other in terms of the range and frequency content of the response, which, in turn, proves the accuracy of the code developed in MATLAB. In this context, it may be noted that exact point-by-point matching is difficult, if not impossible, cause the random wave profile generated by the HydroDyn module in FAST is not exactly the same as that used in the current model due to different random seeds for simulation. However, the response magnitude and frequency contents from both these models remain the same, which is important for this analysis and also implies the validity of the proposed mathematical model used in this study.

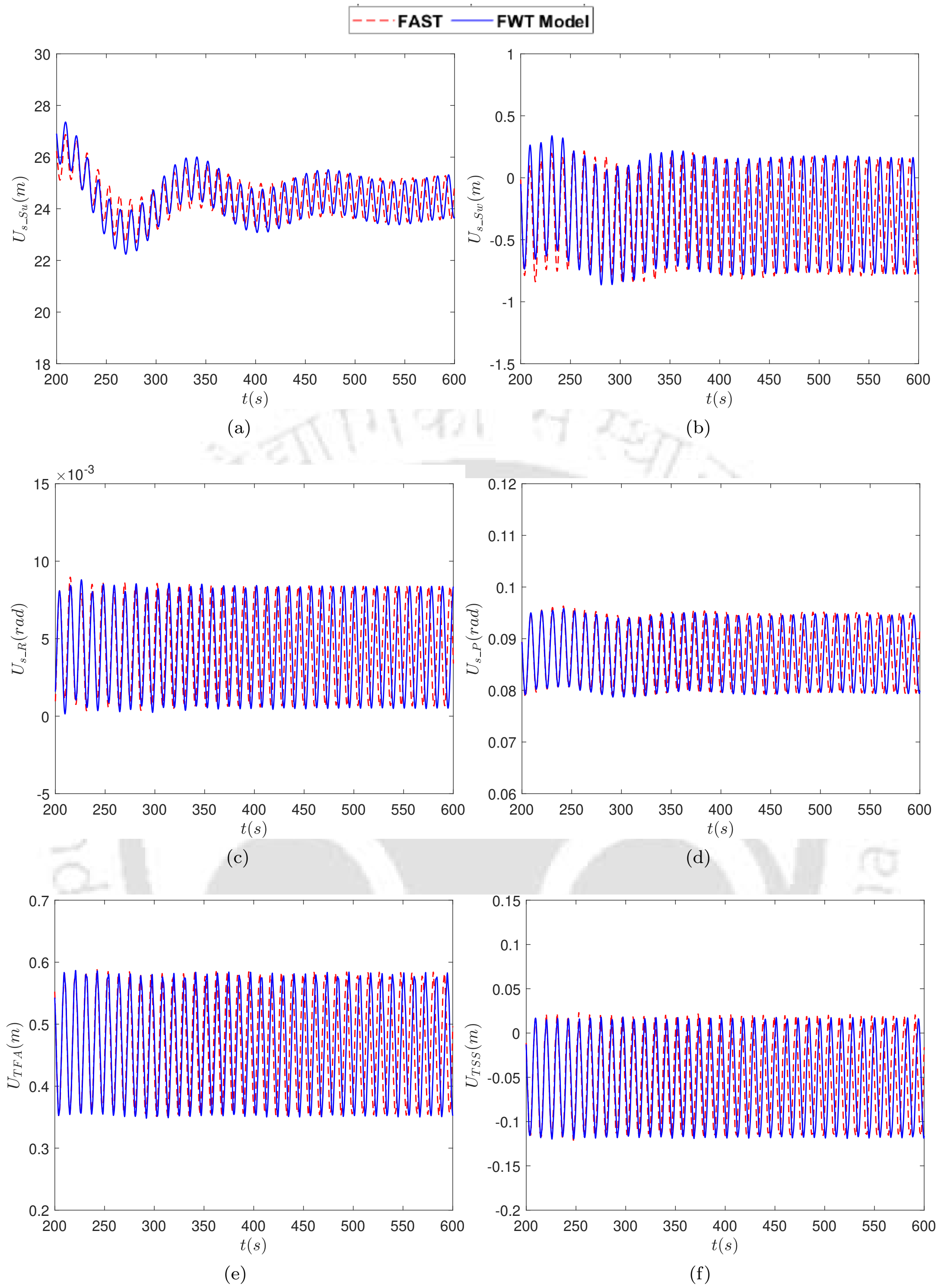

Figure 4.3: Response validation (Case 1); (a) spar in surge, (b) spar in sway, (c) spar in roll, (d) spar in pitch, (e) tower top in fore-aft & (f) tower top in side-to-side

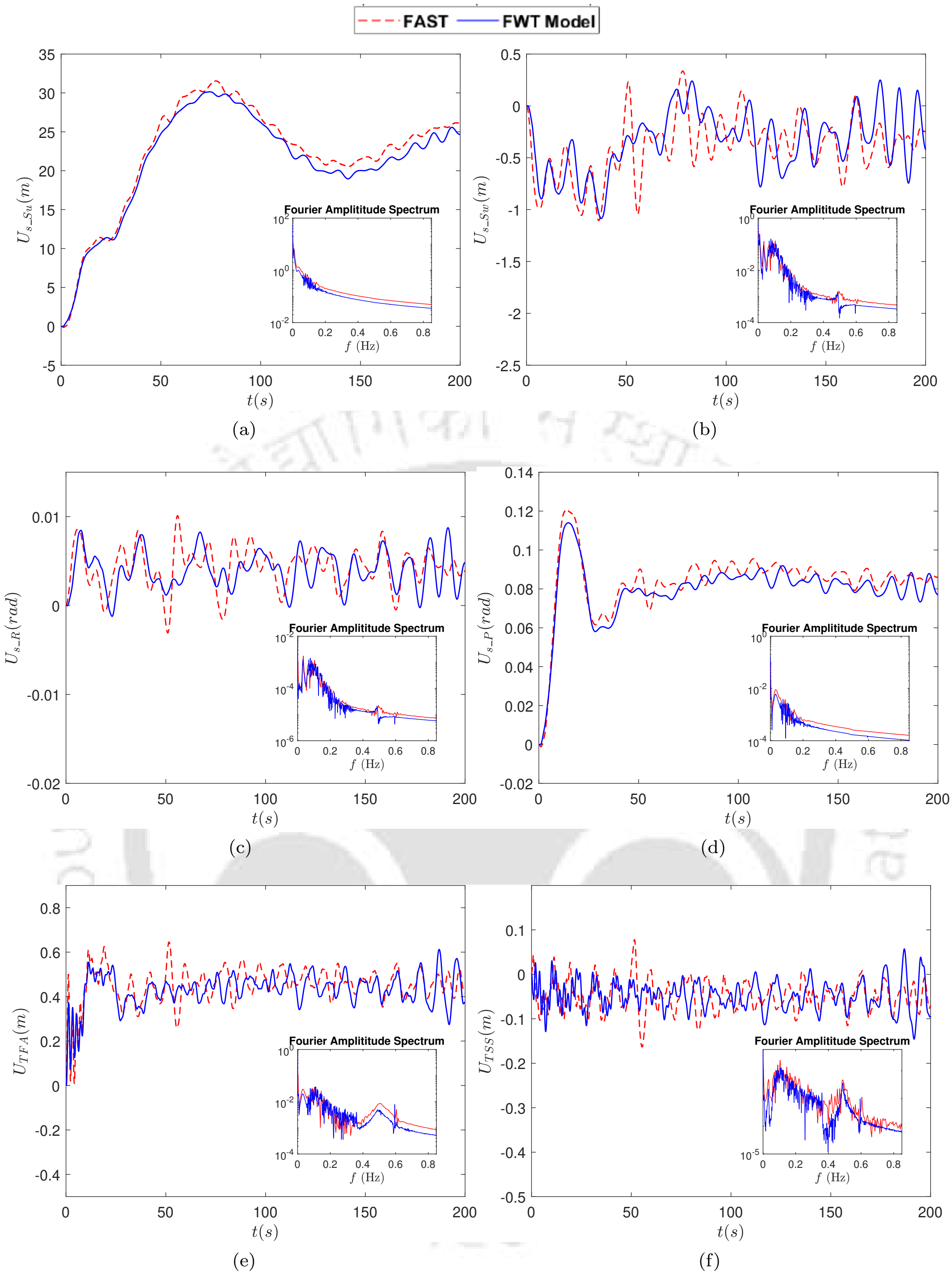

Figure 4.4: : Response validation (Case 2); (a) spar in surge, (b) spar in sway, (c) spar in roll, (d) spar in pitch, (e) tower top in fore-aft & (f) tower top in side-to-side

4.5 Summary

This chapter details the development and analysis of spar-type floating offshore horizontal axis wind turbines through mathematical modeling, focusing on:

- The development of a comprehensive aero-servo-elastic model within a multi-body framework using Kane's approach, which accounts for various coupling effects among the structural components.

- The consideration of external loads, including aerodynamic, hydrodynamic, and gravitational forces, to simulate different environmental conditions an offshore turbine might face throughout its service life. The model simulates state time histories for structural components, validated with a benchmark turbine's parameters.

- The model has the ability to incorporate complex control systems for predicting performance across diverse environmental and operational scenarios. Although not discussed in this work, other relevant design parameters, (e.g., stress distribution, fatigue life, and reliability [15, 161, 267]) can be evaluated using the state time histories and material properties as a natural consequence. The MATLAB code developed is highlighted for its efficiency and adaptability to integrate additional control laws and design guidelines into the multi-body dynamic analysis framework.

Chapter 5

Tower Vibration Control of Onshore Turbine with Bi-Directional Tuned Mass Damper

5.1 Introduction

Global wind power generation has experienced rapid growth in the recent past due to the ever-increasing demand for carbon-free renewable energy. As the power production of a Horizontal Axis Wind Turbine (HAWT) depends on its rotor area, modern multi-megawatt turbines are taller to accommodate ultra-large blades. These slender towers undergo severe vibration when exposed to in-flowing wind and seismic excitations. Thus, tower vibration control is an essential component for safe and sustained operation. It helps to provide a stable platform at the tower top, which is a primary requirement for housing the generator, drive-train, and rotor assembly. With this in mind, this chapter delves into the tower vibration control with the help of a bi-directional Tuned Mass Damper (TMD) installed in the nacelle. At first, the performance of the passive TMD is evaluated. For this purpose, the tuned mass damper is combined with an aero-servo-elastic turbine model in the multi-body framework. The combined system is exposed to turbulent wind and seismic ground motion to investigate the controller performance in extreme operating conditions. Then to further improve the controller's performance, an active wavelet-based strategy is introduced for fore-aft vibration control of onshore horizontal axis wind turbine towers. The optimal tuning is achieved by frequency-dependent gain scheduling via wavelet transform. Analytic Morse wavelet is used as a basis function for transforming the input and feedback to recast the classical Linear Quadratic Regulator (LQR) in the time-frequency domain over a finite time horizon. The scale-dependent differential Riccati equations are solved for optimal gains, which are used to estimate the optimal control force. Numerical studies presented in this paper demonstrate the advantage of the proposed gain scheduling over classical LQR. The efficiency of the proposed algorithm is verified using different flow conditions and seismic input, where the performance is compared with benchmark results.

5.2 Mathematical Model of the Onshore HAWT with Bi-Directional Tuned Mass Damper

In this work, the multi-body dynamics of a wind turbine is modeled using Kane's approach [12]. The model of the complete onshore turbine is already presented in §2.2 of chapter 2. The schematic diagram of the onshore HAWT with bi-directional TMD housed inside the nacelle is presented in Fig. 5.1f along with their associated coordinate systems. The dynamics of the bi-directional TMD are modeled by two additional DOFs, i.e., u_{23} and u_{24}, which are used to describe the translation of TMD in the fore-aft (TMD_{FA}) and side-to-side (TMD_{SS}) direction, respectively. Therefore, the DOFs for the complete system can be expressed as

$$u = \{\underbrace{u_1, ...u_3,}_{Base} \underbrace{u_4, ...u_7,}_{Tower} \underbrace{u_8,}_{Nacelle} \underbrace{u_9, u_{10},}_{Drive-Train} \underbrace{u_{11}, ...u_{22},}_{Blades} \underbrace{u_{23},}_{TMD_{FA}} \underbrace{u_{24}}_{TMD_{SS}}\}^T \tag{5.1}$$

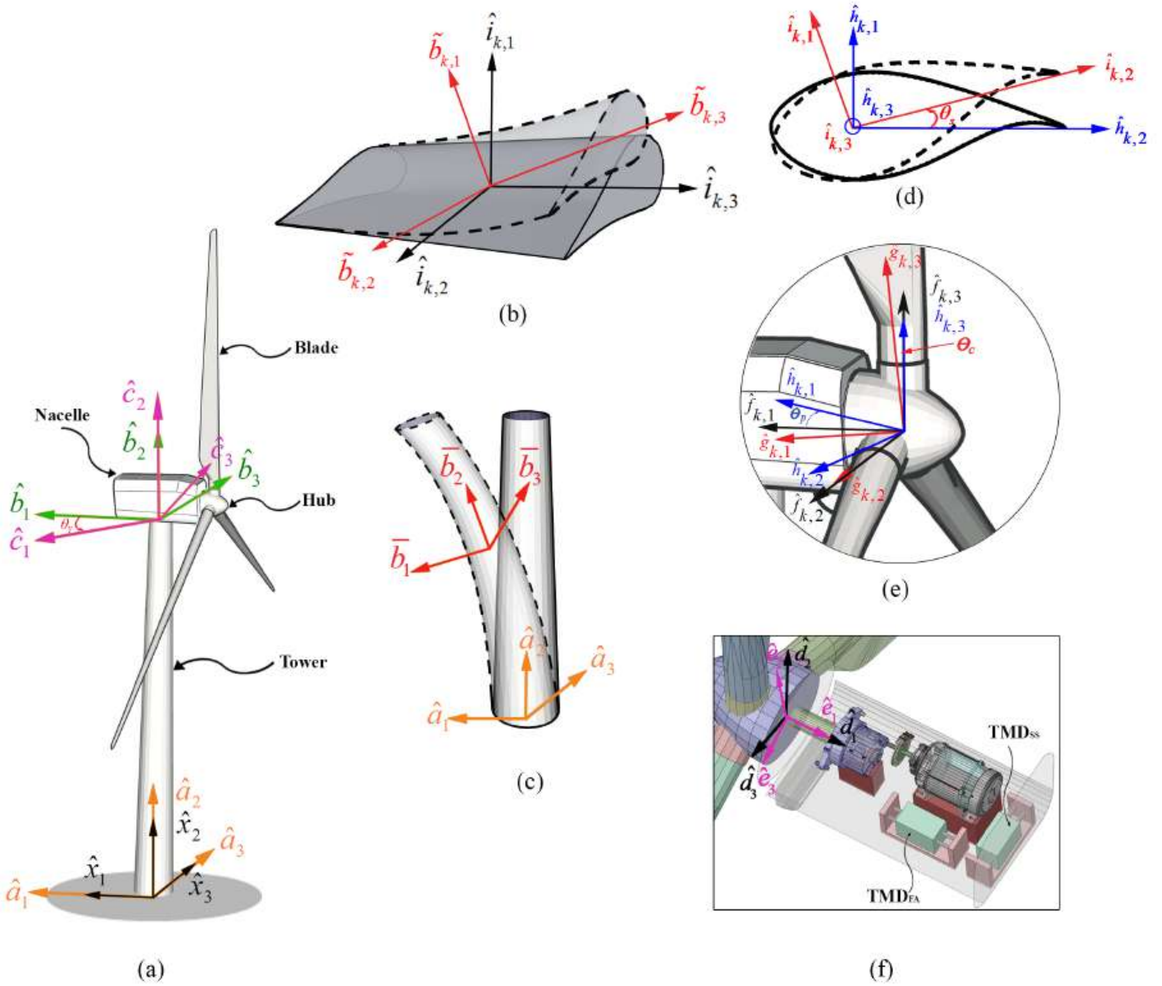

Figure 5.1: Schematic diagram of HAWT with TMD and associated coordinates; (a) combined multi-body system, (b) deformed blade element, (c) deformed tower, (d) local twist of blade, (e) cone and pitch & (f) drive-train and TMD

Using this approach, the force-equilibrium equation of an n DOF multi-body system (i.e., $n = 24$ in this case) is given by

$$\mathbf{F_i} - \mathbf{F_i^*} = 0 \quad for \quad i = 1, 2, ..., n \tag{5.2}$$

In the above equation, F_i and F_i^* are the generalized active forces and generalized inertia forces, respectively. The detailed equations of linear, angular velocities and the generalized forces may be found in §2.2 of chapter 2 and hence, they are not repeated here. Substituting the terms of Eq. 5.2, the equations of motion can then be written in the matrix form, i.e.

$$[\mathbf{M(u, t)}] . \{\ddot{\mathbf{u}}\} + \left\{\bar{\mathbf{F}}(\dot{\mathbf{u}}, \mathbf{u}, \mathbf{t})\right\} = 0 \tag{5.3}$$

In this equation, $\mathbf{M}$ is the mass matrix that depends on the states $\vec{u}$ and time t. The non-linear forcing function $\bar{\mathbf{F}}$ depends on the external forces, states, and control input. The complete derivation of each term in Eq. 5.3 for the TMD is presented in the following subsection. The derivation of the remaining components in Eq. 5.3 follows the same principle described in §2.2 and hence, is excluded here to avoid repetition.

5.2.1 Tuned Mass Damper Inside Nacelle

Two active tuned mass dampers (TMD) are used in this model for tower vibration control in its two orthogonal directions (refer to Fig. 5.1f). Thus, two additional DOFs, i.e., u_{23} and u_{24}, are used to describe the translation of TMD in the fore-aft and side-to-side direction, respectively. Following the same procedure described in the previous chapters, the kinetics of the bi-directional TMD can be developed. In this section, the equation of motion for the TMD in the fore-aft direction is derived. The governing equation for the TMD in the other direction (i.e., side-to-side) is similar; hence, it is not repeated here. The position vector of the TMD with respect to the origin (O) of the nacelle reference frame is given by

In this section, the equation of motion for the TMD in the fore-aft direction is derived. The governing equation for the TMD in the other direction (i.e., side-to-side) is similar; hence, it is not repeated here. The position vector of the TMD with respect to the origin (O) of the nacelle reference frame is given by

$$\mathbf{r_{tmd}} = u_{23}.\hat{c}_1 + h_{tmd}.\hat{c}_2 \tag{5.4}$$

where h_{tmd} is the vertical distance between the centre of mass of the TMD and the tower top. The total linear velocity at the centre of mass of the TMD can be obtained from Eq. 5.4, which is given by

$$\mathbf{v_{tmd}} = \mathbf{v_O} + \mathbf{v_{ln,tmd}} + \boldsymbol{\omega}_\mathbf{O} \times \mathbf{r_{tmd}} \tag{5.5}$$

where $\mathbf{v_O}$ and $\omega_\mathbf{O}$ is the linear and angular velocity at the tower top, given by $\mathbf{v_O} = \mathbf{v_{tw}}(\mathbf{H_{tw}})$ and $\omega_\mathbf{O} = \omega_\mathbf{tw}(\mathbf{H_{tw}})$ respectively. $\mathbf{v_{ln,tmd}}$ is the linear velocity of the TMD with respect to the nacelle coordinate system. The term $\mathbf{v_{ln}^{tmd}}$ can be derived from Eq. 5.4, which has the following form

$$\mathbf{v_{ln,tmd}} = \dot{u}_{23}.\hat{c}_1 \tag{5.6}$$

The total linear velocity in Eq. 5.5 can be expressed as a summation of the partial terms as in the earlier cases. Hence, using time derivatives of the degree of freedom as generalized speed, the partial linear velocity of the TMD can be expressed in the following form

$$\mathbf{v_{i,tmd}} = \mathbf{v_{i,O}} + \begin{cases} \omega_\mathbf{i,O} \times \mathbf{r_{tmd}} & \text{for } i = 1...8 \\ \hat{c}_1 & \text{for } i = 23 \end{cases} \tag{5.7}$$

where $\mathbf{v_{i,O}}$ and $\omega_\mathbf{i,O}$ are the partial linear and angular velocity at O, respectively. Partial linear acceleration can be obtained from the above equation. Therefore, differentiating Eq. 5.7 with respect to time yields the following expression

$$\frac{d}{dt}(\mathbf{v_{i,tmd}}) = \frac{d(\mathbf{v_{i,O}})}{dt} + \begin{cases} \frac{d(\omega_\mathbf{i,O})}{dt} \times \mathbf{r_{tmd}} + \omega_\mathbf{i,O} \times (\mathbf{v_{ln,tmd}} + \omega_\mathbf{O} \times \mathbf{r_{tmd}}) & \text{for } i = 1...8 \\ (\omega_\mathbf{O} \times \hat{c}_1) & \text{for } i = 23 \end{cases} \tag{5.8}$$

In this equation, the terms $\frac{d(\mathbf{v_{i,O}})}{dt}$ and $\frac{d(\omega_\mathbf{i,O})}{dt}$ are the partial linear and angular accelerations at O, respectively. Finally, the generalized inertia forces for the TMD are determined by the foregoing equations of linear velocities and accelerations, which can be expressed as

$$\mathbf{F^*_{i,tmd}} = \mathbf{v_{i,tmd}}.\left[m_{tmd}.\left\{\sum_{i=1}^{23}\mathbf{v_{i,tmd}}.\ddot{u}_i + \sum_{i=1}^{23}\frac{d(\mathbf{v_{i,tmd}})}{dt}.\dot{u}_i\right\}\right] \quad \text{for } i = 1...23 \tag{5.9}$$

The TMD system matrix can be derived from the generalized inertial forces by rearranging Eq. 5.9, i.e.,

$$\mathbf{M_{i,j:tmd}}(\mathbf{u},\mathbf{t}) = m_{tmd}.\mathbf{v_{i,tmd}}.\mathbf{v_{j,tmd}} \quad \text{for } i,j = 1...23 \tag{5.10a}$$

$$\mathbf{\bar{F}^*_{i,tmd}} = m_{tmd}.\mathbf{v_{i,tmd}}.\left[\sum_{i=1}^{23}\frac{d(\mathbf{v_{i,tmd}})}{dt}.\dot{u}_i\right] \quad \text{for } i = 1...23 \tag{5.10b}$$

where m_{tmd} is the mass of the controller. The generalized active forces on the TMD have gravitational, elastic, and damping components along with the actuator forces in two orthogonal directions. The generalized active force due to the gravitational field on the TMD is given by

$$\mathbf{F_{i,tmd,gv}} = -\mathbf{v_{i,tmd}}.(m_{tmd}.g.\hat{x}_2) \quad \text{for } \ i = 1...23 \tag{5.11}$$

Considering strain energy stored in the mass-spring system and Rayleigh's model, the generalized active forces due to elasticity and damping are given by

$$\mathbf{F_{i,tmd,el}} = -K_{tmd}.u_i \qquad \text{for } \ i = 23 \tag{5.12a}$$

$$\mathbf{F_{i,tmd,d}} = -\frac{\xi_{tmd}.K_{tmd}}{\pi.f_{tmd}}.\dot{u}_i \quad \text{for } \ i = 23 \tag{5.12b}$$

where K_{tmd}, ξ_{tmd}, and f_{tmd} are the stiffness, critical damping ratio, and frequency in Hz, respectively. The generalized active force on the TMD exerted by the actuator can be modeled as

$$\mathbf{F_{i,tmd,act}} = -\mathbf{f_{act,FA}}(\mathbf{\dot{u}}, \mathbf{u}, \mathbf{t}) \quad \text{for } \ i = 23 \tag{5.13}$$

where $\mathbf{f_{act,FA}}$ is the actuation force in the fore-aft direction, which can be taken zero in the passive case. The actuator force for the active controller is calculated using Eq. 5.34, which is later discussed in this work,

Eq. 2.7 and Eq. 2.8 in chapter 2 can be augmented with the above-mentioned generalized inertia and active forces due to TMD. Finally, the elements of the respective system matrices for different turbine components are assembled to form the complete multi-body system.

5.3 External Loads on Onshore Wind Turbine

An onshore wind turbine is exposed to different forces, which include aerodynamic forces on the blades and tower, as well as seismic excitations at the base, besides gravitational pull. The detailed description of these aerodynamic and seismic loads used for modeling and analysis in this study is given in §2.2.5 and §2.2.6 of chapter 2, hence they are not repeated here.

5.4 Proposed Wavelet-LQR for Active Tuning

A wavelet-based LQR controller is proposed in this study to mitigate tower vibration in its fore-aft direction. Wavelet transform can analyze signals in the time-frequency domain simultaneously. Therefore, a controller working in a seismic environment and tuned in real-time as per time-frequency variation is bound to be more efficient under seismic loading than a classical LQR-based controller operating in the time domain. On this basis, an actively tuned mass damper is developed, where the control force is computed depending on the frequency content of the input and feedback.

5.4.1 Active TMD Using LQR Algorithm

This section presents a brief overview of the traditional LQR control theory to explain the rationale behind the proposed wavelet-based strategy. The governing equations of motion and the corresponding observation/measurement equations of a linear time-varying system can be expressed in the following form

$$\dot{U}(t) = A_s(t).U(t) + B_c(t).F_c(t) + B_F(t).F(t) \tag{5.14a}$$

$$Y(t) = C_O.U(t) + D_c(t).F_c(t) + D_F(t).F(t) \tag{5.14b}$$

where $U(t)$, $F_c(t)$, and $F(t)$ are the state vector, control input, and external disturbance, respectively. In this representation, $A_s(t)$ consists of system matrices, i.e., mass, stiffness, and damping. In contrast, $B_c(t)$ and $B_F(t)$ are the matrices that correlate the control force and external force to the appropriate degrees of freedom. The multi-body dynamic system presented by Eq. 5.3 can be represented in the form of Eq. 5.14a to find the state matrices. The measurement vector is given by $Y(t)$, where coefficients C_O, D_c and D_F

correlate the state vector, control force, and external disturbances with the measurement vector, respectively. The quadratic cost function to be optimized in this approach can be defined as [268]

$$J = \frac{1}{2}\int_0^{t_f} \left[U^T.Q.U^T + {F_c}^T.R.F_c\right] dt + \frac{1}{2}\left[U(t_f)^T.S^f.U(t_f)\right] \tag{5.15}$$

where Q and R are the weight matrices for the states and control force, respectively. As the main objective is to reduce the vibration of the parent structure, the weights corresponding to the state (i.e., Q) are more than the control force (i.e., R). The cost function has a finite upper limit, and hence, the boundary conditions of the states are included to solve the optimal control gains. Thus, the second term in Eq. 5.15 represents the terminal penalty function, where S^f is the terminal weight matrix. To solve this optimization problem, the control Hamiltonian is developed, which is given by

$$\mathcal{H} = \frac{1}{2}\left[U^T.Q.U + {F_c}^T.R.F_c\right] + \lambda^T\left[A_s.U + B_c.F_c\right] \tag{5.16}$$

In this expression, λ is the co-state vector. The co-state equation for the optimal state vector, along with its stationarity, demands the control Hamiltonian to be minimum, which leads to the following set of equations

$$\left(\frac{\partial H}{\partial U}\right) = 0 \Rightarrow \dot{\lambda} = -\left(\frac{\partial H}{\partial U}\right) = -\left(Q.U + A_s^T.\lambda\right) \tag{5.17a}$$

$$\left(\frac{\partial H}{\partial F_c}\right) = 0 \Rightarrow F_c = -R^{-1}.{B_c}^T.\lambda \tag{5.17b}$$

The state and co-state vectors are related through the matrix P_{LQR} [i.e., $\lambda(t) = P_{LQR}(t).U(t)$; where P_{LQR} is a time-varying, symmetric, and positive definite matrix]. Hence, it leads to the following relation

$$\left[\dot{P}_{LQR} + P_{LQR}.A_s(t) + A_s(t)^T.P_{LQR} - P_{LQR}.B_c(t).R^{-1}.B_c(t)^T.P_{LQR} + Q\right].U = 0 \tag{5.18}$$

Setting the bracketed term in Eq. 5.18 to zero, the Differential Riccati Equation (DRE) of matrix P_{LQR} can be formed, i.e.

$$\dot{P}_{LQR} + P_{LQR}.A_s(t) + A_s(t)^T.P_{LQR} - P_{LQR}.B_c(t).R^{-1}.B_c(t)^T.P_{LQR} + Q = 0 \tag{5.19}$$

The system matrices A_s and B_c in the above equation are time-varying. Hence, the solution of the DRE can be carried out in backward time with the help of boundary condition $P_{LQR}(t_f) = S^f$. The positive-definite solution for $P_{LQR}(t)$ is stored and used to compute the control force in forwarding time. Hence, the optimal solution for the control force can be expressed in the following form

$$F_c(t) = -R^{-1}.{B_c}^T.P_{LQR}.U = -G_{LQR}(t).U(t) \tag{5.20}$$

In the above expression, G_{LQR} is the feedback gain matrix corresponding to Q, R, and the terminal penalty matrix S^f. Finally, the control force at any time step is obtained by multiplying gain with the state vector.

In this formulation, the non-stationary frequency content of the input, i.e., earthquake (and corresponding output), is ignored. Moreover, the previous works [119, 269] reported in the literature simplify the problem using average values of the time-dependent system matrices. In fact, the above-mentioned works solved an inverse problem using white noise excitation and identified time-invariant system matrices. This approximate representation of the actual aerodynamics of the wind turbine system has inherent error. Due to this reason, the control algorithm is bound to under-perform. To address this issue, wavelet-based time-frequency analysis is proposed by the authors where gain scheduling is based on the instantaneous time-frequency content of the signal, which is discussed below.

5.4.2 Continuous Wavelet Transform

The continuous wavelet transform, in principle, is the inner product of a finite energy signal with the scaled and translated versions of a basis function. It helps to extract instantaneous features of any signal and, therefore, has an inherent advantage compared to Fourier transformation. The basis function used in this transformation should have finite energy (i.e., $E = \int_{-\infty}^{+\infty} |\psi(t)|^2 dt < \infty$) with zero mean and must satisfy the following admissibility criteria [270]

$$C_\Psi = \int_0^{+\infty} \frac{|\Psi(\omega)|^2}{\omega} d\omega < \infty \tag{5.21}$$

Thus, the wavelet transform of $x(t) \in \mathscr{L}^2(\mathbb{R})$ using a basis function $\psi(t)$ is defined as

$$W_\psi x(a,b) = \frac{1}{\sqrt{|a|}} \int_{-\infty}^{+\infty} x(t)\psi^*\left(\frac{t-b}{a}\right) dt \qquad a \in \mathbb{R}^+; b \in \mathbb{R} \tag{5.22}$$

where $\psi^*(t)$ is the complex conjugate of the basis function $\psi(t)$, and a is the scale or dilation parameter in the above equation, and b is the translational or position parameter. The continuous wavelet transform of a discrete-time series x_n with N data points and dt time step can be expressed in the frequency domain as

$$W_\psi \hat{x}_k(a,n) = \sum_{k=0}^{N-1} \hat{x}_k \hat{\Psi}^*(a\omega_k) e^{i\omega_k n dt} \tag{5.23}$$

where $\hat{x}_k$ is the discrete Fourier transform of x_n. In order to get back the original signal, inverse wavelet transform is performed on the coefficients obtained in Eq. 5.22, i.e.,

$$x(t) = \frac{1}{2\pi C_\Psi} \int_{-\infty}^{+\infty} \int_0^{+\infty} \frac{1}{a^2} W_\psi x(a,b) \tilde{\psi}\left(\frac{t-b}{a}\right) dadb \tag{5.24}$$

where $\tilde{\psi}(t)$ represents the wavelet dual of the basis function. In this study, the analytic Morse wavelet is used, which is a complex-valued wavelet having only positive real Fourier transform [271]. It has the inherent advantage of representing signals having varying amplitude and frequency content over time [272,273]. The amplitude spectrum of this wavelet in the frequency domain is given by

$$\Psi_{\beta,\nu}(\omega) = \mathrm{H}(\omega) a_{\beta,\nu} \omega^\beta e^{-\omega^\nu} \tag{5.25}$$

In the above equation, $\mathrm{H}(\omega)$ is the Heaviside step function and $a_{\beta,\nu}$ is a normalising constant given by $a_{\beta,\nu} = 2\left(\frac{e\nu}{\beta}\right)^{\frac{\beta}{\nu}}$. The parameters β and ν signify the compactness and symmetry of the wavelet [274], respectively, which can be chosen according to the requirement of a signal to be analyzed. The time-bandwidth product of the resulting wavelet is given by $P_m^2 = \beta\nu$. Efficient algorithms developed by Lilly [275] for computing Morse wavelet coefficients are available in MATLAB [232], which are used in this study. In this context, it should be noted that the skewness of the Morse wavelet becomes zero when the symmetry parameter $\nu = 3$. Hence, default parameter values of $\nu = 3$ and $P_m^2 = 60$ are used in this study. Fig. 5.2 shows the Morse basis function in the time domain and its spread in the time-frequency domain.

5.4.3 Proposed Wavelet-LQR Control Strategy

This section presents the proposed wavelet-LQR based frequency-dependent gain scheduling of an active tuned mass damper for fore-aft vibration control of the wind turbine tower. The multi-body system developed in the earlier section is considered for this purpose. The state-space model of this time-varying system, as in Eq. 5.14a, is transformed into the wavelet domain to evaluate the optimal control force. Thus, wavelet transforming both sides Eq. 5.14a using basis function $\psi(t)$ with scale parameter a and translation parameter b gives the following expression

$$\frac{\partial}{\partial b} W_\psi U(a,b) = W_\psi \left[A_s(t).U(t)\right](a,b) + W_\psi \left[B_c(t).F_c(t)\right](a,b) + W_\psi \left[B_F(t).F(t)\right](a,b) \tag{5.26}$$

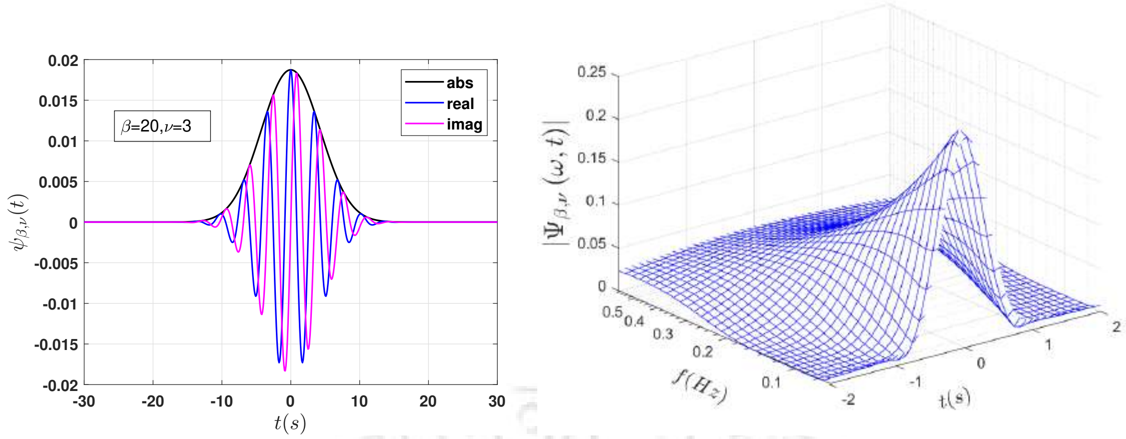

(a) (b)

Figure 5.2: Morse wavelet; (a) time domain representation and (b) amplitude spectrum in time-frequency domain

For a time interval of $[t_0, t]$, the wavelet transform of the first term on the right side of the above equation can be expressed with the help of Eq. 5.22 as

$$W_\psi[A_s(b).U(b)] = \frac{1}{\sqrt{|a|}} \int_b A_s(b).U(b).\psi^* \left(\frac{t-b}{a}\right) db \tag{5.27}$$

The translated and dilated function $\psi[(t-b)/s]$ decays at a faster rate around $t = b$, while $A_s(t)$ and $B_c(t)$ vary slowly. These two together lead to the following simplification

$$\begin{aligned} W_\psi\left[A_s(t).U(t)\right](a,b) &\approx A_s(b).W_\psi\left[U(t)\right](a,b) \\ W_\psi\left[B_c(t).F_c(t)\right](a,b) &\approx B_c(b).W_\psi\left[F_c(t)\right](a,b) \end{aligned} \tag{5.28}$$

where $A_s(b)$ and $B_c(b)$ are the state matrices localised at $t = b$. Using Eq. 5.28 in Eq. 5.26, the state-space equation of the combined system can be expressed as

$$\frac{\partial}{\partial b} W_\psi U(a,b) = A_s(b).W_\psi U(a,b) + B_c(b).W_\psi F_c(a,b) + B_F(b).W_\psi F(a,b) \tag{5.29}$$

This version of the governing equation is used to formulate the modified LQR problem in the wavelet domain, where the scale-dependent cost function J_a is used for optimal control force estimation. Hence, the modified cost function in the wavelet domain can be written as

$$\begin{aligned} J_a = \tfrac{1}{2}\int_0^{b_f} &\Big[\left[W_\psi U(a,b)\right]^T.Q_a.\left[W_\psi U(a,b)\right] + \left[W_\psi F_c(a,b)\right]^T.R_a.\left[W_\psi F_c(a,b)\right]\Big] db \\ &+\tfrac{1}{2}\Big[\left[W_\psi U(a,b_f)\right]^T.S_a^f.\left[W_\psi U(a,b_f)\right]\Big] \end{aligned} \tag{5.30}$$

where Q_a and R_a are the weight matrices that are dependent on the scale parameter. S_a^f is the terminal weight for scale a and localised at b_f. Similarly, the control Hamiltonian in the wavelet domain also depends on the scale parameter and localized system matrices, which is defined by the following form

$$\begin{aligned} \mathcal{H}_a = \tfrac{1}{2}&\Big[\left[W_\psi U(a,b)\right]^T.Q_a.\left[W_\psi U(a,b)\right] + \left[W_\psi F_c(a,b)\right]^T.R_a.\left[W_\psi F_c(a,b)\right]\Big] \\ &+\lambda_a^T\left[A_s(b).W_\psi U(a,b) + B_c(b).W_\psi F_c(a,b)\right] \end{aligned} \tag{5.31}$$

where λ_a^T is the scale-dependent co-state vector in the wavelet domain. Following the same procedure described in Sec. 5.4.1, the Differential Riccati Equation for solving optimal controller gain corresponding to scale a is given by

$$\frac{\partial P_a}{\partial b} + P_a.A_s(b) + A_s(b)^T.P_a - P_a.B_c(b).R_a^{-1}.B_c(b)^T.P_a + Q_a = 0 \tag{5.32}$$

The DRE can be solved backward in the translational parameter b with the help of boundary condition. Hence, the optimal solution for the control force in the wavelet domain can be expressed in the following expression

$$W_\psi F_c(a,b) = -R_a^{-1}.B_c{}^T.P_a.W_\psi U(a,b) = -G_a(b).W_\psi U(a,b) \tag{5.33}$$

It can be noted that the gain matrix G_a depends on the scale a, which is inversely related to the frequency. In this way, a frequency-dependent gain matrix can be obtained for different scales. Once the gain matrix is evaluated, the inverse wavelet transform of Eq. 5.33 can be invoked to derive the control force in the time domain, i.e.

$$F_c(t) = \frac{1}{2\pi C_\Psi} \int_a \int_b \frac{1}{a^2} \left[W_\psi F_c(a,b)\right].\tilde{\psi}\left(\frac{t-b}{a}\right) db.da \tag{5.34}$$

The weight matrices corresponding to frequency scales having the highest and lowest energy are chosen first to evaluate the frequency-dependent gain matrix. Then, the relative energy in each scale is computed using the decomposed signal in the wavelet domain. Finally, the gain matrix is interpolated between the maximum and minimum values to schedule it for individual scales based on the energy arrival of the input. The proposed control algorithm is shown in Fig. 5.3, where the estimated control force is saturated using actuator limits before sending it back to the plant.

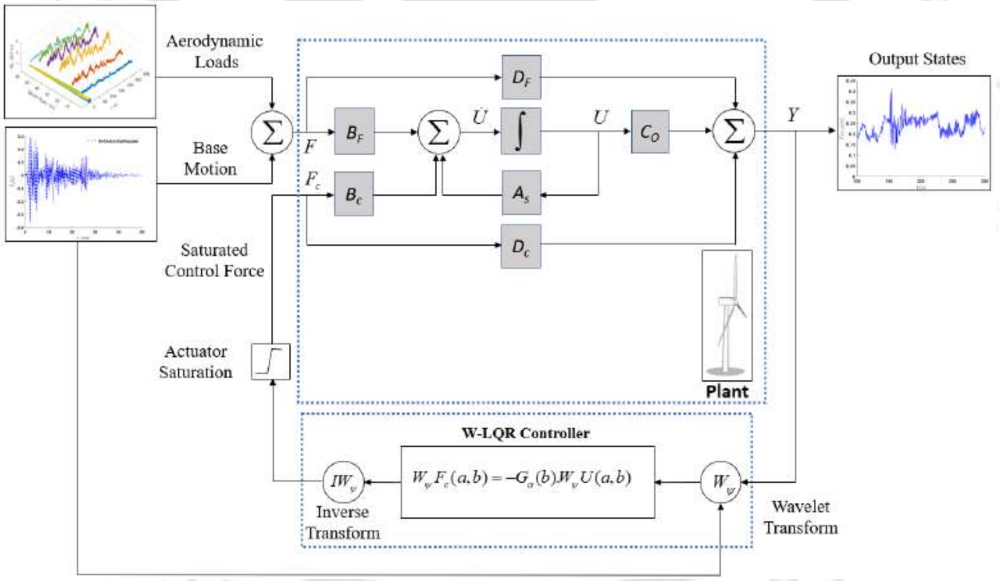

Figure 5.3: Block diagram of proposed controller

5.5 Numerical Results and Discussions

In this section, the performance of the proposed wavelet-based gain scheduling for active tuning of the mass damper is discussed in detail. It is compared with the classical LQR algorithm used in FAST-SC [276] to demonstrate its effectiveness. For this purpose, the NREL 5 MW onshore wind turbine [5] with an active TMD inside the nacelle is considered in this work. The wavelet-based controller is designed in MATLAB, which is combined with the multi-body model of the wind turbine to simulate its response when subjected to different wind and seismic loading.

Table 5.1 shows the essential properties of the benchmark turbine. The blades are made up of 8 different airfoils that are taken from the NREL report [5] along with other details, i.e., chord length, aero-twist, lift and drag coefficients, and blade structural parameters, including mass per unit length and stiffness. The drive-train has a torsional rigidity of 867637kN-m/rad, with the generator inertia and gearbox ratio of 534kg-m^2 and 97, respectively.

TurbSim [85] is used to simulate the turbulent wind field at 90m hub height with separate mean velocities corresponding to rated, cut-out, and parked conditions (i.e., 11.4, 25, and 30 m/s, respectively). The power-law exponent of 0.2 for steady wind and 15% turbulence with IEC Kaimal spectra are assumed for wind field simulation, as the in-flowing wind in the onshore environment generally has higher turbulence. The wind field generated by TurbSim corresponding to rated speed with 15% turbulence is shown in Fig. 5.4a. The subfigures 5.4b and 5.4c display the time histories and corresponding Fourier amplitude spectra of the normal aerodynamic loads at different blade sections, which are obtained using the modified BEM theory. The frequency characteristics of the loads in Fig. 5.4c show the peak amplitudes of the aerodynamic loads corresponding to the blade rotational frequency (i.e., 0.20 Hz) and its harmonics. Five different historical earthquakes are considered in this study, which are El-Centro (1940), Parkfield (1966), Loma Prieta (1989), Kobe (1995), and Chichi (1999).

Before evaluating the controller's performance, the multi-body dynamic model of the turbine with a passive TMD (i.e., actuator force is zero) inside the nacelle is validated using FAST [218]. The following section describes the details of the structural parameters and environmental conditions used for the validation purpose.

Table 5.1: NREL 5-MW Turbine Data [5].

Basic Descriptions		**Blade (LM61.5 P2)**		**Tower**	
Max. Power	5000 kW	Length	61.5 m	Height	87.6 m
No. of blades	3	Mass	17740 kg	Mass	347460 kg
Rotor dia.	126 m	f^F_{1,b_k}, f^F_{2,b_k}	0.66, 2.07 Hz	$f^{FA}_{1,tw}$	0.324Hz
Hub-height	90 m	f^E_{1,b_k}, f^E_{2,b_k}	1.08, 4.05 Hz	$f^{SS}_{1,tw}$	0.312Hz
V_{ci}, V_r, V_{co}	3 m/s, 11.4 m/s, 25 m/s	$\xi^F_{b_k}$, $\xi^E_{b_k}$	0.47%, 0.47%	ξ^{FA}_{tw}, ξ^{SS}_{tw}	1%, 1%
RPM_{ci}, RPM_r	6.9 rpm, 12.1 rpm			Hub mass	56780 kg
				Nacelle mass	240000 kg

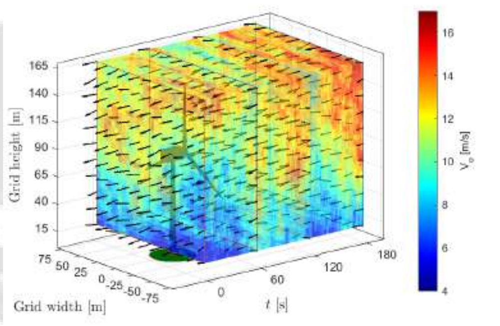

(a)

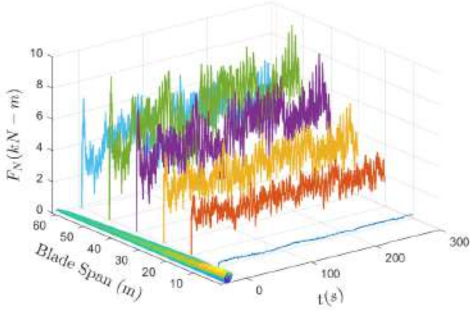

(b)

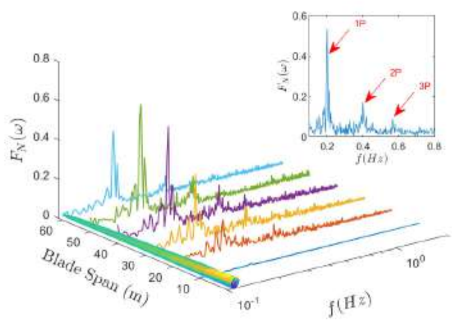

(c)

Figure 5.4: Aerodynamic load simulation corresponding to rated speed; (a) 3D wind field, (b) normal component of load and (c) Fourier amplitude spectrum (N.B.: normal load at 40.2m showing rotational frequencies and its harmonics in inset)

5.5.1 Validation Exercise

The coupled differential equations of motion for the multi-body system in §5.2 are numerically solved using the 4^{th} order Ranga-Kutta integration scheme. To maintain the precision of the numerical integration, a suitably small time step of 0.0125s is chosen after the convergence check, and the response is validated with FAST [218]. The time history responses are simulated corresponding to the rated wind speed with 5% turbulence for this exercise. The mass, stiffness, and damping parameters of the passive TMD are selected so that the mass ratio is 1%, while the stiffness and damping are 41.4kN/m and 2035.7N/m/s, respectively. The mass of the TMD, m_{TMD}, is 10000 kg. The value is chosen to achieve a mass ratio of 1% with respect to the mass of the whole tower and rotor. Standard practice in the literature uses the whole system mass to calculate the mass ratio rather than the contributing vibrational mass, as shown in the paper by Lackner and Rotea [108], and also used in NREL. Given the tower's near-symmetry, the TMD is tuned to both the fore-aft and side-to-side modes. Hence. The stiffness parameter $K_tmd = 41400$ N/m is chosen with a frequency ratio of 1. The damping ratio is selected after conducting a sensitivity analysis. For El-Centro and Kobe Earthquakes, the optimal damping ratio for the TMD ranged between 12% and 14% for peak response reduction. The variation of the performance function is insignificant in this range of damping ratio (e.g., 6.53% to 6.55% for the El-Centro earthquake). However, a value of 10% damping ratio is selected for the passive TMD as the nearest multiple of 10. Optimizing this damping parameter is a challenging task because of the non-stationarity of the earthquake input. The optimal parameters can vary depending on the type of seismic excitation and the operating condition. Hence, the primary focus of this study is the development of a wavelet-LQR-based active TMD to overcome the drawbacks of passive dampers. For the validation purpose, the time history response of the tower top in its fore-aft direction is compared with the passive TMD, as shown in Fig. 5.5a, which demonstrates the agreement between these two codes. The peak, mean, and RMS values of the time history obtained from FAST are 0.299m, 0.273m, and 0.274m, respectively, whereas the same parameters obtained from the present model are 0.293m, 0.267m, and 0.268m, respectively. The maximum difference between these two codes is $\sim 2\%$, which is insignificant for all practical purposes. For further verification, the response of the tower is simulated and compared with FAST using El-Centro ground motion with rated wind speed. Fig. 5.5b displays the time history response of the tower top simulated by the two codes when the earthquake is applied at 150s. This delay ensures the dying out of initial transients before the seismic ground motion is applied. The peak, mean, and RMS values of the time history obtained from FAST are 0.487m, 0.273m, and 0.274m, respectively, whereas the same parameters obtained from the model developed in this study are 0.483m, 0.272m, and 0.273m, respectively. In this case, less than 1% variation is observed between the two codes, and hence the MATLAB model is found to act satisfactorily. Finally, the peak tower response of the turbine in its complete operating range is compared, as shown in Fig. 5.5c by varying the wind speeds. The closeness of the peak tower responses at different mean wind flows also justifies the validity of the MATLAB model. Here, it should be noted that the multi-body dynamic model of the wind turbine without a passive TMD was also extensively validated in chapter 2, which is not repeated here. With these validation results in hand, the model is further utilized to study the performance of the proposed wavelet-based gain scheduling for active control of fore-aft tower vibration.

5.5.2 Seismic Response with Passive TMD

To evaluate the control performance of the TMD, the dynamic response of the turbine for a given seismic ground motion at the tower base is evaluated. El-Centro's (1940) ground motion is applied in the fore-aft direction to demonstrate it. The acceleration time history of this ground motion is presented in Fig. 5.8a. Fig. 5.6 displays the time history response at the tower top for rated and parked conditions simulated in MATLAB when the earthquake is applied at the 60s. This delay in applying earthquake ground motion ensures the dying out of initial transients. Here, a passive TMD is used to suppress the structural vibration. The mass, stiffness, and damping parameters of the passive TMD were selected in the same way as mentioned in the validation exercise. The mass damper is tuned to the fundamental tower frequency. The time history response at the tower top in its fore-aft direction is compared, as shown in Fig. 5.6, demonstrating the effectiveness of the passive TMD. These time histories reveal that the passive TMD can reduce the peak and RMS response of the tower by 0.85% and 0.2%, respectively, during the rated condition. The reason behind this low percentage reduction at rated speed is that the maximum aerodynamic damping occurs at this condition, which affects the tower response in the fore-aft direction. It should be noted that the side-to-side vibration is often more critical in earthquake scenarios due to the lack of aerodynamic damping, particularly when the turbine is operational. However, the performance of the TMD is better when the turbine is parked, offering a reduction of 8.28% and 48.08% of the peak and RMS value, respectively. In

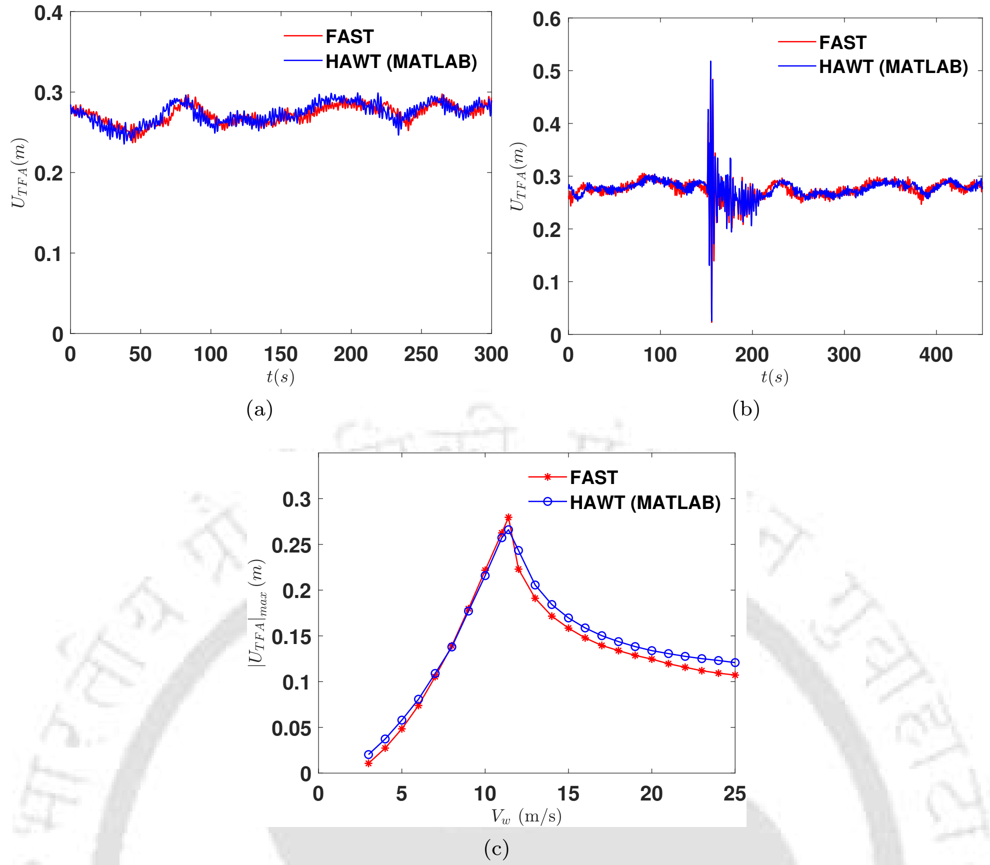

Figure 5.5: Tower fore-aft response; (a) at rated speed, (b) at rated speed with El-Centro ground motion and (c) peak response for different mean wind speeds at hub height

this case, the tower response is dominated by its fundamental frequency; hence, the passive TMD tuned to it absorbs a significant amount of energy due to resonance.

The study continued to investigate the performance of the bi-directional TMD under different ground motions. Five different historical earthquakes are considered for this purpose which are El-Centro (1940), Parkfield (1966), Loma Prieta (1989), Kobe (1995), and Chichi (1999). The north-south components of the aforesaid ground motions are applied in the fore-aft direction of the turbine, whereas the east-west components are applied in the perpendicular direction. The effectiveness of the passive TMDs in mitigating tower top vibration is also studied under different operating conditions (i.e., rated, cut-out, and parked), which are reported in Table. 5.2. This table shows that the percentage reduction grows with the mean wind speed. The rotor does not move when it is parked. Therefore, the aerodynamic damping is minimal, leaving only the structural damping in the governing equation of motion. Moreover, the response is dominated by the fundamental frequencies without any influence of the rotational frequency. Hence, a passive TMD successfully mitigates the structural load due to wind and earthquake during this condition, resulting in a more significant response reduction in the fore-aft direction. Here, it may be noted that the multi-body dynamic model discussed in this chapter can further enhance the controller performance by deploying actuator force (i.e., active TMD), which is a simple extension for further studies, continued in the following subsections.

5.5.3 Tuning Active TMD Parameters

In this analysis of active tuning, the mass and stiffness values of the TMD are kept the same as in §5.5.1. These parameters are chosen so that the frequency ratio ω_r is 1 for all cases. The choice of weight matrices is critical for active control, which for different cases are explained below

i. **LQR Control**: For classical LQR-based ATMD, the weighting matrix Q is chosen to give more importance to controlling tower vibration compared to other DOFs. Therefore, the diagonal elements

Table 5.2: Performance evaluation of the passive TMD under different earthquakes

Earthquake	Wind Speed	Uncontrolled						Passive TMD					
		fore-aft (m)			side-to-side (m)			fore-aft (m)			side-to-side (m)		
	(m/s)	Peak	RMS	P2P	Peak	RMS	P2P	Peak	RMS	P2P	Peak	RMS	P2P
El Centro	11.4	0.41	0.23	0.45	0.32	0.13	0.58	0.40 [0.85]	0.23 [0.20]	0.43 [3.62]	0.29 [9.36]	0.08 [42.27]	0.50 [13.62]
	25.0	0.34	0.12	0.52	0.28	0.10	0.46	0.31 [6.53]	0.12 [2.36]	0.48 [7.71]	0.29 [-1.93]	0.07 [24.17]	0.48 [-2.38]
	30.0	0.33	0.12	0.64	0.29	0.08	0.53	0.30 [8.28]	0.06 [48.08]	0.57 [11.11]	0.24 [17.32]	0.06 [30.67]	0.48 [10.05]
Parkfield	11.4	0.34	0.23	0.20	0.22	0.07	0.37	0.33 [1.94]	0.23 [-0.05]	0.19 [3.73]	0.21 [7.85]	0.05 [18.66]	0.32 [14.92]
	25.0	0.26	0.12	0.31	0.27	0.08	0.43	0.25 [4.52]	0.11 [0.63]	0.29 [4.55]	0.25 [9.07]	0.06 [22.36]	0.37 [13.96]
	30.0	0.11	0.03	0.23	0.15	0.04	0.30	0.10 [10.79]	0.03 [24.75]	0.20 [12.59]	0.13 [12.72]	0.03 [27.09]	0.25 [14.94]
Loma Prieta	11.4	0.49	0.23	0.64	0.17	0.06	0.26	0.49 [0.94]	0.23 [0.48]	0.62 [2.85]	0.15 [9.62]	0.05 [16.97]	0.23 [9.62]
	25.0	0.34	0.12	0.60	0.23	0.08	0.36	0.34 [0.31]	0.12 [1.24]	0.59 [1.76]	0.18 [24.58]	0.06 [25.72]	0.25 [31.44]
	30.0	0.43	0.17	0.79	0.15	0.04	0.26	0.41 [4.16]	0.09 [46.22]	0.74 [7.32]	0.13 [9.93]	0.03 [25.14]	0.24 [9.27]
Kobe	11.4	0.41	0.23	0.40	0.44	0.15	0.83	0.40 [2.66]	0.23 [0.39]	0.38 [4.63]	0.38 [13.70]	0.09 [39.31]	0.68 [17.46]
	25.0	0.30	0.12	0.37	0.45	0.15	0.81	0.30 [1.07]	0.12 [1.38]	0.36 [0.90]	0.41 [8.34]	0.10 [34.07]	0.69 [15.20]
	30.0	0.32	0.11	0.63	0.29	0.08	0.56	0.27 [14.21]	0.06 [42.24]	0.53 [15.83]	0.26 [8.47]	0.06 [26.33]	0.50 [11.26]
Chichi	11.4	0.33	0.24	0.26	0.30	0.08	0.53	0.33 [0.73]	0.24 [-0.08]	0.24 [6.56]	0.23 [23.07]	0.05 [35.88]	0.38 [27.75]
	25.0	0.25	0.12	0.29	0.32	0.09	0.55	0.25 [-0.56]	0.12 [0.41]	0.28 [1.61]	0.23 [26.23]	0.06 [28.02]	0.37 [32.67]
	30.0	0.18	0.03	0.31	0.22	0.04	0.41	0.15 [18.51]	0.02 [32.69]	0.26 [15.54]	0.17 [22.43]	0.03 [26.74]	0.32 [21.45]

N.B.: P2P and RMS refer to the peak-to-peak and root mean square value of the response, respectively.
The values in [.] refer to percentage reduction with respect to the uncontrolled response.

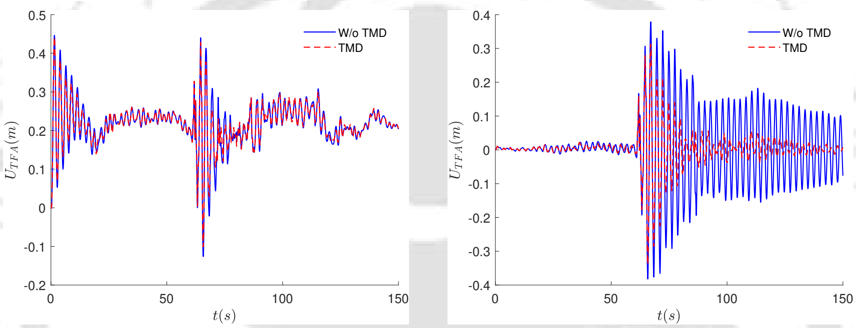

(a) (b)

Figure 5.6: Dynamic response at the tower top in fore-aft direction; (a) rated ($V_w = 11.4$ m/s) condition, & (b) parked ($V_w = 30$ m/s) condition

of Q is set to 10^8 for the states u_4 and $\dot{u}_4$ (i.e., tower fore-aft displacement and velocity, respectively), which is constant the complete analysis. The weight matrix R, which is the penalty on control effort, is kept as 1 to ensure lesser importance on the control effort than states. The LQR problem is solved using FAST-SC [108,119], where constant weight matrices (i.e., Q and R) are used to solve the algebraic Riccati equation to estimate the gain matrix. In this process, FAST-SC solves an inverse problem to get the equivalent time-invariant system matrices in Eq. 5.14a, i.e., A_{eq} and B_{eq} in place of time-varying $A_s(t)$ and $B_c(t)$ matrices. This is done by additionally solving the inverse problem using white noise excitation. This entire mathematical operation in FAST is aimed at avoiding time-dependent matrices and associated complexities in the LQR algorithm. This linearization introduces approximations that are bound to affect the controller performance. The computation of the gain matrix is done offline, and the steady-state solution of the gain matrix is stored, which is applied during the simulation. The control force is obtained from the constant gain matrix using Eq. 5.20 throughout the simulation.

ii. **Wavelet-based LQR control**: As mentioned in the previous section, the state feedback is transformed into the wavelet domain (i.e., in different scales). This transformation is performed using the analytic Morse wavelet (refer §5.4.2) as the basis function. The relative energy corresponding to each scale is obtained from the wavelet coefficients. The gain matrix is scheduled proportionally in each scale based on the energy levels. The weight $Q_{u_4} = 10^8$ is associated with the scale having the highest relative energy. On the other hand, the weight Q for the scale associated with the lowest energy is multiplied by 100 (i.e., $Q_{u_4} = 10^{10}$). Thus, the gain is scheduled based on the relative energy content of the different frequency levels. The resulting envelope of the gain matrix corresponding to maximum (marked in red) and minimum (marked in blue) energy levels are shown in Fig. 5.7a and Fig. 5.7b. Thus, the proposed gain scheduling ensures that the decomposed signal with the lowest energy receives a higher gain so that the control force at this scale does not become insignificant. Using this distribu-

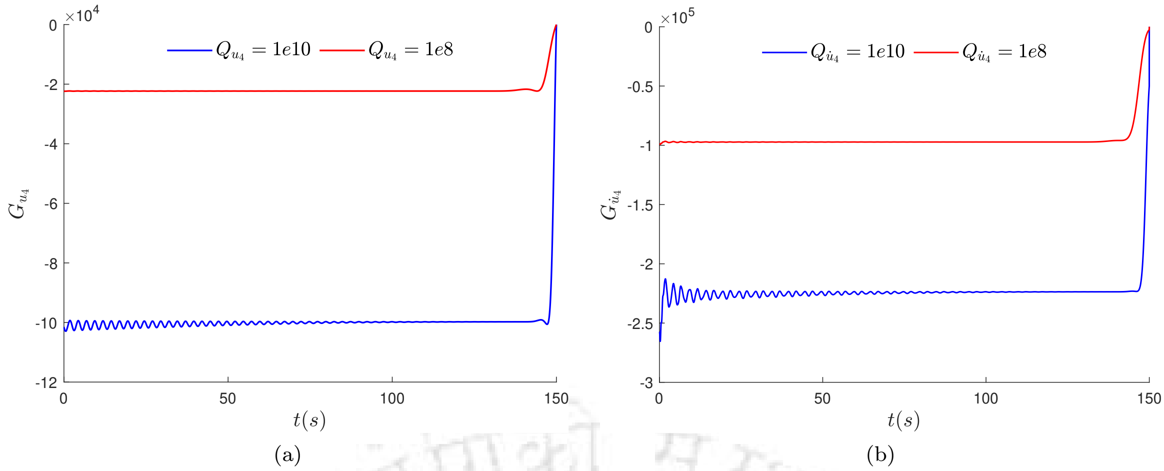

Figure 5.7: Solution of differential Riccati equation; (a) tower fore-aft displacement and (b) tower fore-aft velocity

tion, the complete frequency-dependent gain matrix is obtained and multiplied with the decomposed signal to get the control force in the wavelet domain, which is finally transformed back into the time domain before applying through the actuator in a close loop.

5.5.4 Seismic Response with Active TMD

The turbine response is simulated for different load cases to study the performance of the proposed control strategy. Three different wind speeds are considered for this purpose, i.e., rated (11.4m/s), cut-out (25.0m/s), and parked (30.0m/s) with 15% turbulence. Each simulation is run for 300s with earthquakes starting at the 150s.

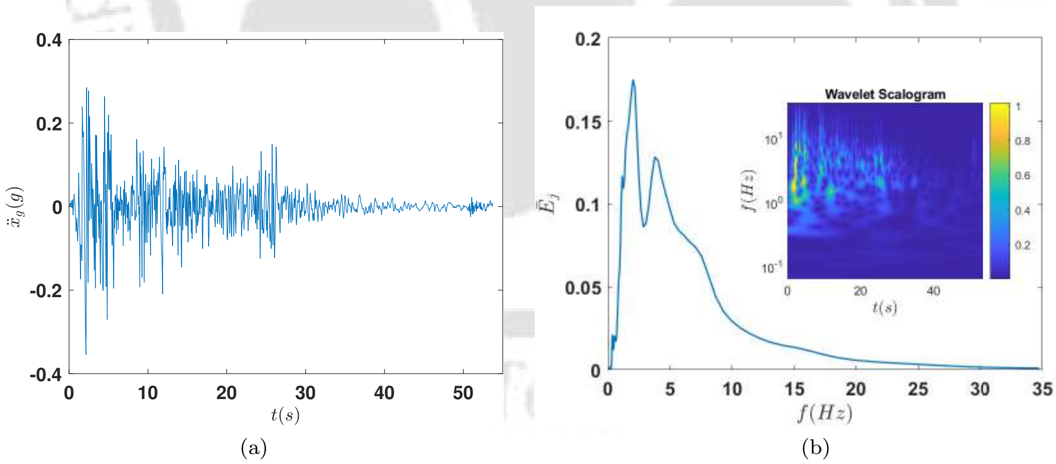

Figure 5.8: El-Centro ground motion; (a) acceleration time history and (b) normalized energy distribution

As mentioned in the earlier section, the energy associated with the strong motion is spread over a range of frequencies. To demonstrate it further, the accelerogram of the El-Centro earthquake is displayed in Fig. 5.8a, and the corresponding relative energy distribution in Fig. 5.8b. This figure, along with the wavelet scalogram presented in the inset of Fig. 5.8b shows the variation of energy in different scales or frequencies, where the higher wavelet amplitudes represent the higher energy arrival. This feature of the input also implies that the output is bound to exhibit different energy levels in the time-frequency domain. The relative energy distribution of tower fore-aft displacement and velocity corresponding to different wind conditions are shown in Fig. 5.9. The wavelet scalogram presented in the insets of these figures shows the energy variation under different wind conditions.

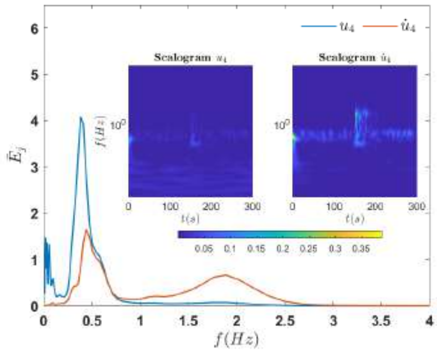

(a)

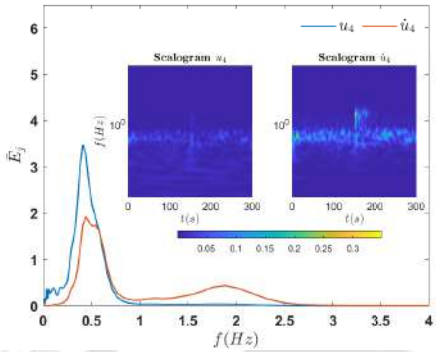

(b)

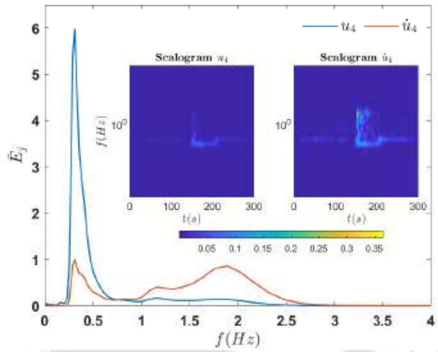

(c)

Figure 5.9: Energy distribution in tower fore-aft response; (a) at rated speed, (b) at cut-out speed and (c) parked condition (N.B.: scalograms for different states are shown in inset)

Once the energy distribution of the input is obtained over a finite interval, the proposed gain scheduling using wavelet-LQR mentioned in §5.5.3 is adopted to get the complete gain matrix in the time-frequency domain for each load case. Fig. 5.10 displays the elements of the gain matrix for the tower fore-aft displacement and velocity corresponding to El-Centro motion. It can be observed that the dominant frequencies with the highest energy are consistent with the strong motion, and the scheduled gain matrix is in compliance with Fig. 5.9. The tower response due to El-Centro ground motion is shown in Fig. 5.11. From this figure, it is clear that wavelet-based LQR performs better than classical LQR in FAST-SC in all three different wind cases. Since the weight matrices are varied proportionally based on the energy content of the earthquake in different scales, better reductions of the peak, peak-to-peak, and Root Mean Square (RMS) responses are observed. At the rated condition, the reduction of the peak, RMS, and peak-to-peak are 8.20%, 1.64%, and 25.70%, respectively, with classical LQR in FAST, while the same is 16.24%, 1.72%, and 46.22%, respectively in the case of the proposed wavelet-based LQR. The reductions follow a similar pattern at the cut-out wind speed, with the wavelet-based controller offering more reduction than classical LQR. The aerodynamic damping is negligible in the parked condition as the blades are stationary. Due to this reason, significant structural vibration is observed in the uncontrolled case as shown in Fig. 5.11e. The inset of sub-figures in Fig. 5.11 show the characteristics of the tower response with and without the controller during the initial few seconds of the earthquake when the energy is maximum. In the parked condition, the peak response is reduced by 38.97% in the case of an LQR-based controller, while wavelet-based LQR offers a reduction of 54.01%. A similar trend is observed for RMS reduction and peak-to-peak reduction, where the proposed gain scheduling offers superior performance.

Finally, different recorded ground motions are adopted to study the efficiency of the proposed controller. In this process, four additional earthquakes mentioned earlier are used, and the complete study is repeated for each of them. The results are reported in Table. 5.3, where each ground motion is applied for three different wind flow conditions. It can be observed from this table that the proposed wavelet-based gain scheduling outperforms classical LQR in all the cases. In general, the percentage reduction increased with the wind speed. As it reaches parked condition, the rotor does not move, and hence the aerodynamic damping drops, leaving the structural damping alone. During this extreme condition, the structural load due to wind and

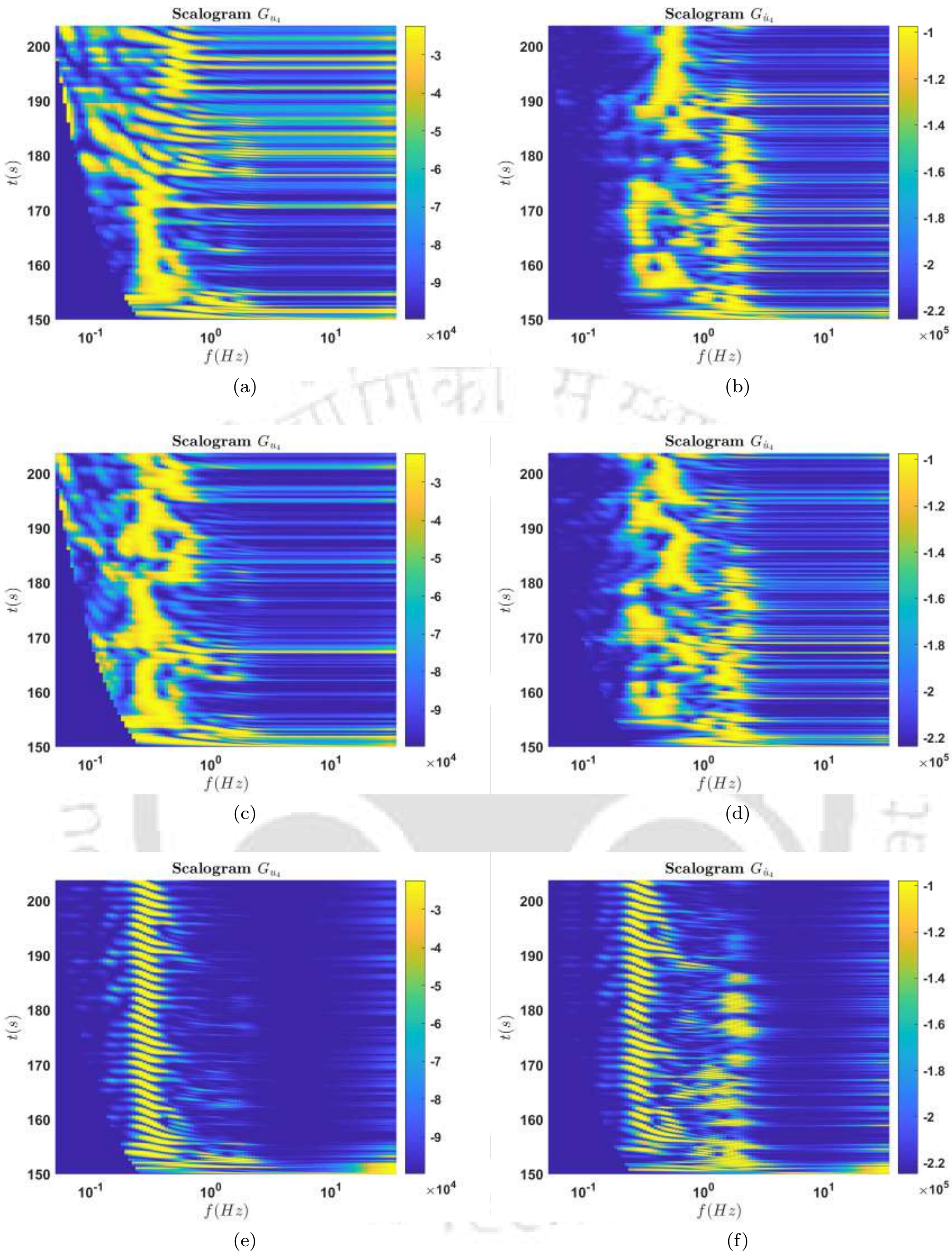

Figure 5.10: Time-frequency representation of controller gains for tower fore-aft response under El-Centro ground motion; (a) displacement at rated speed, (b) velocity at rated speed, (c) displacement at cut-out speed, (d) velocity at cut-out speed, (e) displacement at the parked condition and (f) velocity at parked condition

earthquake is successfully handled by the proposed control algorithm, which offers better response reduction. Overall, the full spectrum analysis is presented in Table. 5.3 demonstrates the superiority of the proposed control strategy where time-frequency analysis plays a vital role.

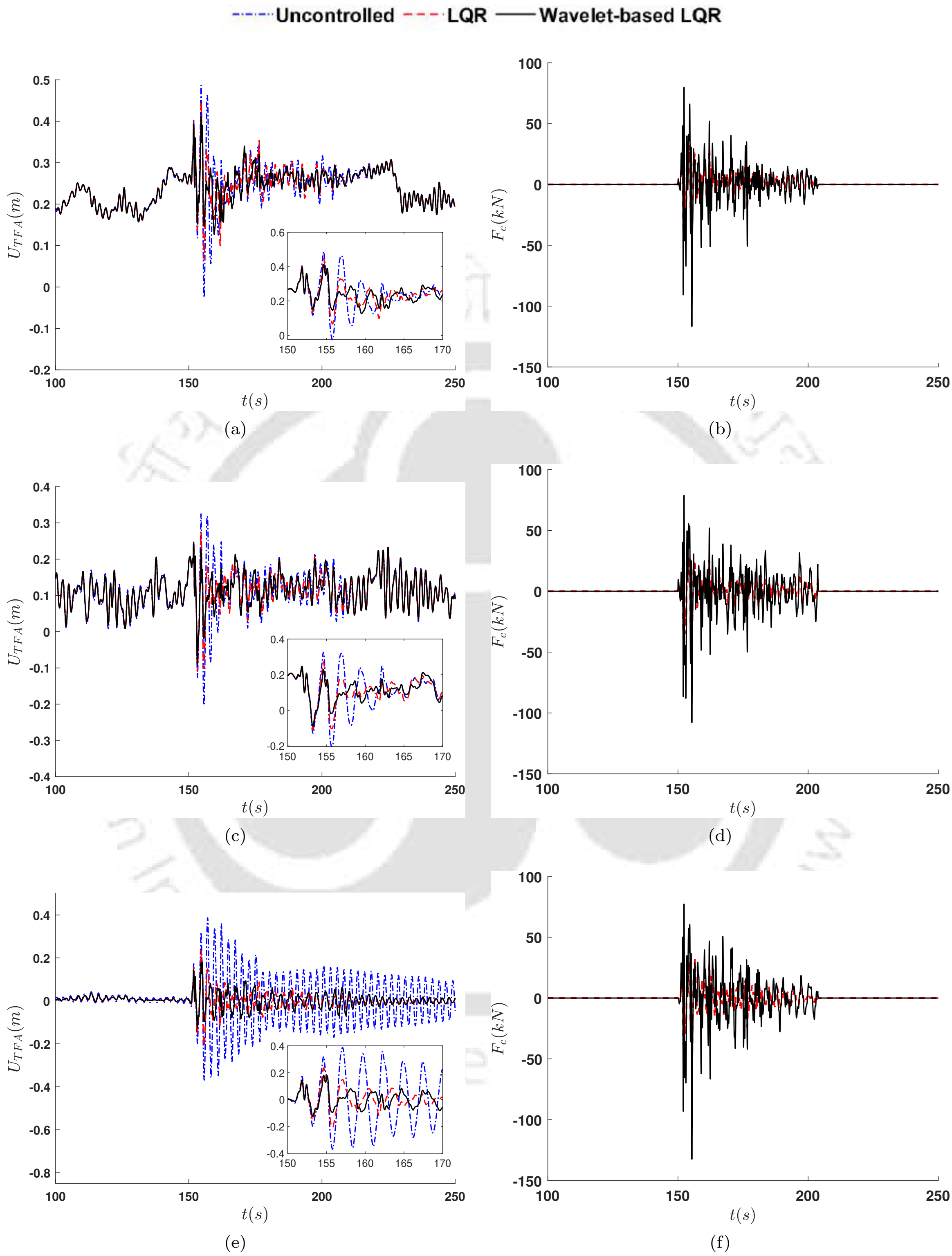

Figure 5.11: Fore-aft tower displacement and control force for El-Centro ground motion; (a) displacement at rated speed, (b) control force at rated speed, (c) displacement at cut-out speed, (d) control force at cut-out speed, (e) displacement at parked condition and (f) control force at parked condition

Table 5.3: Performance evaluation of the proposed controller under different earthquakes

Earthquake	Wind Speed (m/s)	Tower fore-aft response (m)								
		Uncontrolled			LQR			Wavelet-based LQR		
		Peak	RMS	P2P	Peak	RMS	P2P	Peak	RMS	P2P
El Centro	11.4	0.487	0.263	0.512	0.447 [8.20]	0.259 [1.64]	0.380 [25.70]	0.408 [16.24]	0.259 [1.72]	0.275 [46.22]
	25.0	0.325	0.140	0.528	0.275 [15.59]	0.131 [6.70]	0.385 [27.20]	0.251 [22.75]	0.124 [11.63]	0.360 [31.89]
	30.0	0.387	0.151	0.755	0.236 [38.97]	0.053 [65.23]	0.446 [40.99]	0.178 [54.01]	0.047 [69.23]	0.303 [59.90]
Parkfield	11.4	0.912	0.336	1.311	0.721 [21.02]	0.284 [15.45]	0.993 [24.27]	0.666 [26.96]	0.284 [15.46]	0.930 [29.10]
	25.0	0.799	0.234	1.306	0.590 [26.15]	0.174 [25.61]	0.975 [25.40]	0.524 [34.39]	0.172 [26.58]	0.891 [31.82]
	30.0	0.975	0.414	1.884	0.624 [36.02]	0.152 [63.21]	1.202 [36.22]	0.588 [39.75]	0.195 [52.81]	1.142 [39.38]
Loma Prieta	11.4	0.495	0.274	0.548	0.443 [10.65]	0.262 [4.51]	0.455 [16.88]	0.436 [11.92]	0.261 [4.78]	0.405] [26.10]
	25.0	0.368	0.175	0.576	0.363 [1.43]	0.156 [10.78]	0.528 [8.32]	0.331 [10.07]	0.138 [21.22]	0.437 [24.17]
	30.0	0.297	0.180	0.588	0.272 [8.44]	0.132 [26.26]	0.475 [19.22]	0.231 [22.32]	0.103 [42.57]	0.408 [30.68]
Kobe	11.4	0.674	0.275	0.806	0.551 [18.24]	0.258 [6.11]	0.515 [36.08]	0.482 [28.49]	0.258 [6.24]	0.386 [52.08]
	25.0	0.490	0.148	0.634	0.395 [19.46]	0.132 [10.90]	0.440 [30.57]	0.334 [31.77]	0.127 [14.16]	0.393 [38.01]
	30.0	0.586	0.294	1.079	0.420 [28.26]	0.081 [72.56]	0.624 [42.16]	0.307 [47.57]	0.085 [71.26]	0.467 [56.69]
Chichi	11.4	0.446	0.231	0.457	0.406 [8.97]	0.219 [5.42]	0.351 [23.16]	0.372 [16.66]	0.218 [5.71]	0.304 [33.43]
	25.0	0.225	0.132	0.355	0.211 [6.41]	0.125 [5.57]	0.303 [14.86]	0.203 [10.01]	0.116 [12.29]	0.266 [25.13]
	30.0	0.267	0.160	0.518	0.188 [29.38]	0.063 [60.83]	0.345 [33.46]	0.177 [33.61]	0.053 [67.15]	0.304 [41.38]

N.B.: P2P and RMS refer to the peak-to-peak and root mean square value of the response, respectively. The values in [.] refer to percentage reduction with respect to the uncontrolled response.

5.6 Summary

The study reported in this chapter demonstrates a novel strategy for vibration control of horizontal axis wind turbine towers exposed to turbulent wind and seismic ground motion. Under this condition, an active tuned mass damper is used, and the linear quadratic regulator algorithm is adopted in the time-frequency framework for optimal tuning of the actuator force. The major contributions of this work are summarized below –

- The mathematical model of the combined system (i.e., horizontal axis wind turbine and active TMD) is derived in a multi-body dynamic framework using Kane's approach. The system matrices (i.e., mass, stiffness, and damping) are state-dependent. This feature offers a serious challenge to adopt a conventional LQR algorithm, especially when the system is exposed to an input whose frequency content varies with time, e.g., earthquake. In order to address this issue, wavelet-based time-frequency analysis is proposed in this study, which helps recast the LQR control problem in the time-frequency format. In this proposal, the scale-dependent DRE is developed for appropriate gain scheduling, which is efficient for active tuning of the mass damper.

- The proposed formulation does not demand estimation of equivalent system matrices for active tuning of the mass damper as in Lackner and Rotea [108, 119] or FAST-SC [276]. An equivalent linearization proposed in these literature to bypass the time-dependent system matrices is inherently having modeling error. Moreover, the identification scheme adopted in the literature mentioned above applies additional white noise excitation to solve the inverse problem, which also has some modeling and estimation errors. Therefore, there are multiple levels of approximation in the current state-of-the-art for active tuning of mass-damper for wind turbine towers, which are bypassed in this work for more efficient tuning. In summary, the proposed methodology is more efficient and mathematically accurate, which is also reflected in its performance.

- The proposed scale-dependent gain scheduling in the time-frequency plane is based on the energy content of the feedback. This helps to properly estimate the control force, which ultimately reduces the vibration better than the same achieved by the classical LQR algorithm implemented in FAST-SC [276]. The numerical results presented in this chapter demonstrate the performance of the proposed control strategy over the complete operating spectrum of the turbine (i.e. from rated to parked condition) with different recorded earthquake ground motions. The percentage reductions of the peak, P2P, and RMS response of the tower in its fore-aft direction are significant. All these results together prove the superiority of the proposed wavelet-LQR-based gain scheduling for active tuning of the mass-damper for fore-aft vibration control of the onshore horizontal axis wind turbine tower.

Chapter 6

Tower Vibration Control of Offshore Turbine using Modified Spar-Torus Combination

6.1 Introduction

Spar-type floating wind turbines exposed to marine environments experience significant vibration, which is more prominent under wind-wave misalignment. This unavoidable vibration, particularly in the sway direction, affects overall performance and can induce significant damage to sensitive electro-mechanical components, leading to downtime for maintenance. With this in view, the present chapter aims to propose a modified spar-torus combination by introducing springs and dashpot in between so that it can work as an isolator. First, a comprehensive mathematical model for this multi-body system is developed using Kane's approach with proper aero-elastic and hydrodynamic simulation. For this purpose, 3D wind fields are generated in TurbSim, and the waves are simulated from the Pierson-Moskovitch spectrum, considering wind-wave correlation and misalignment. Aerodynamic loads are computed using modified Blade Element Momentum theory, while hydrodynamic loads are generated using Morison's equation. Using these inputs, the response of the modified spar-torus combination is solved, which demonstrates the efficiency and advantage of the proposed vibration isolation. Different sea states and wind conditions are simulated, replicating the actual scenario to investigate the performance envelope of the proposed controller for spar-type floating wind turbines.

6.2 Description of Modified Spar-Torus Combination

The spar-torus combination [277] has a light donut-shaped floating buoy (i.e., torus) as a wave energy converter. This combination is modified in this study, where the torus is used as a floater that isolates wave energy. As stated above, the modified spar-torus combination (MSTC) (refer Fig. 6.1) acts as a vibration absorber that primarily controls the response of a floating wind turbine in passive mode. Here, it may be noted that the magnitude of the hydrodynamic load is maximum near the surface and decreases with depth. Thus, the torus encircling the part of the spar near the sea surface effectively isolates the incident hydrodynamic loads. Fig. 6.1 shows the modified spar-torus combination, which consists of the following key elements

- A floating spar is used to support the wind turbine. The dimensions of the spar depend on the size of the turbine, its power rating, water depth, and wind profile at the site. The spar is moored with the help of a catenary, to support the turbine.
- A modified torus is a hollow cylindrical shaped floating buoy, encircling the spar up to a sufficient depth to effectively isolate wave loads. It can move in two orthogonal directions (i.e., surge and sway) relative to the spar.

- The ballast tanks inside the spar and torus bring their centre of gravity below their centre of buoyancy to provide sufficient stability to carry a heavy wind turbine on top of it.
- The bearing system along the outer periphery of the spar consists of a flexible spring and dashpot, as shown in Fig. 6.1 to connect the torus with the spar and allow it to have relative translations in surge and sway and no rotation.

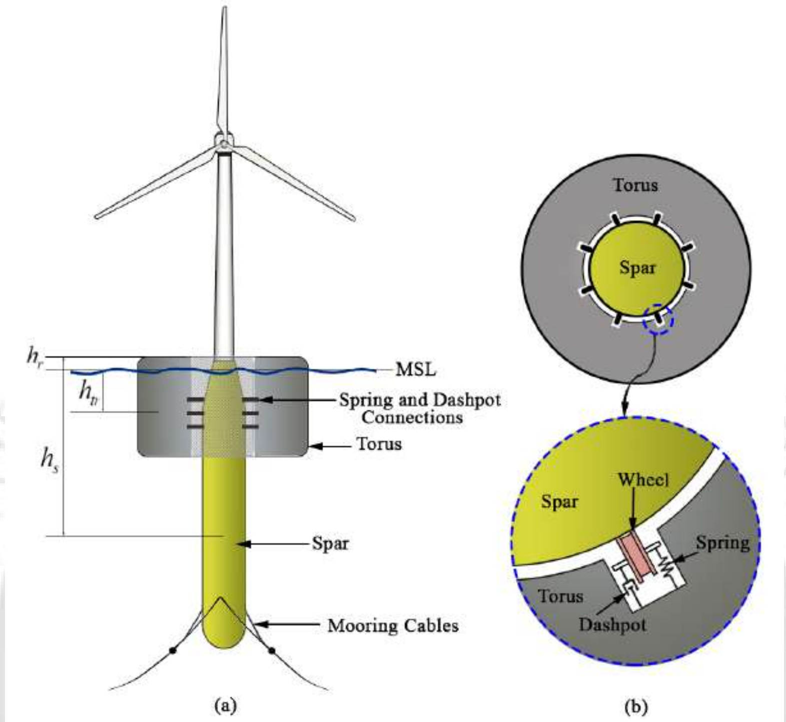

Figure 6.1: Schematic diagram of the modified spar-torus combination; (a) elevation & (b) plan

6.3 Mathematical Model of Spar-Type Floating Wind Turbine with Modified Torus System

The multi-body dynamics of the modified spar-type Floating Wind Turbine (FWT) is modeled using Kane's approach [12] in this section. The model of the complete spar-type FWT without the modified torus is already presented in §4.2 of chapter 4. Here, the schematic diagram of the spar-type FWT with the modified torus system attached to the spar is shown in Fig. 6.2 along with their associated coordinate systems. The proposed modified torus can move in the surge and sway directions with respect to the spar. Hence, 2 DOFs are considered to model this body., i.e., u_{26} and u_{27}, which are used to describe the translation of the torus in the surge (Tr_Su) and sway (Tr_Sw) direction, respectively. Thus, the complete DOFs of the modified spar-type floating wind turbine are defined by the following vector

$$u = \{\underbrace{u_1, ...u_6,}_{Spar}\underbrace{u_7, ...u_{10},}_{Tower}\ \underbrace{u_{11},}_{Nacelle}\ \underbrace{u_{12}, u_{13},}_{Drive-Train}\ \underbrace{u_{14}, ...u_{25},}_{Blades}\ \underbrace{u_{26},}_{Tr\_Su}\ \underbrace{u_{27}}_{Tr\_Sw}\ \}^T \tag{6.1}$$

Employing this method, the force-equilibrium equation for a multi-body system with n degrees of freedom (where $n = 27$ in this instance) is expressed as

$$\mathbf{F_i} - \mathbf{F_i^*} = 0 \quad for \quad i = 1, 2, ..., n \tag{6.2}$$

In the equation, $\mathbf{F_i}$ and $\mathbf{F_i^*}$ represent the generalized active forces and generalized inertia forces, respectively. The specific formulations for linear and angular velocities, as well as the generalized forces, can be referenced

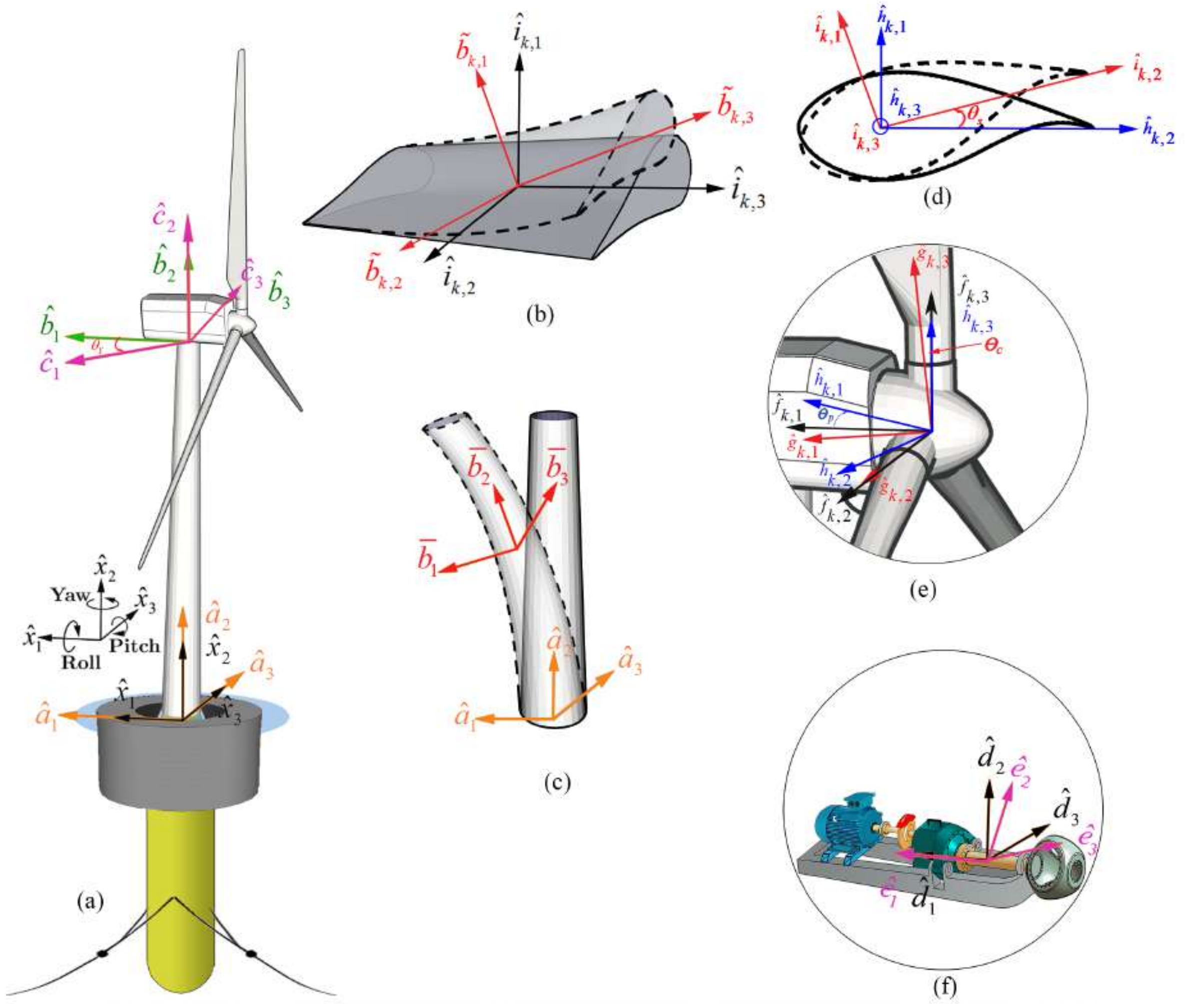

Figure 6.2: Schematic diagram of FWT with Modified Spar-Torus Combination (MSTC) and associated coordinates; (a) combined multi-body system, (b) deformed blade element, (c) deformed tower, (d) local twist of the blade, (e) cone and pitch & (f) drive-train

in §4.2 of chapter 4. Therefore, these details are not reiterated here. By substituting the terms from Eq. 6.2, the equations of motion can be expressed in matrix form, as follows

$$[\mathbf{M}(\mathbf{u},\mathbf{t})]\,.\,\{\ddot{\mathbf{u}}\} + \left\{\bar{\mathbf{F}}(\dot{\mathbf{u}},\mathbf{u},\mathbf{t})\right\} = 0 \tag{6.3}$$

where $\mathbf{M}$ denotes the mass matrix, which is contingent on both the states $\vec{u}$ and the time variable t. The non-linear forcing function $\bar{\mathbf{F}}$ is influenced by external forces, states, and control input. A comprehensive derivation of each term in Eq. 6.3 adheres to the same principles described in §4.2 for a spar-type FWT. Consequently, it is omitted here to prevent redundancy. Hence, here, only the complete derivation of each term in Eq. 6.3 for the modified torus system is presented in the following subsection.

6.3.1 Modified Torus System

The modified torus is attached to the spar of the wind turbine with springs and dashpot. The dynamics of the torus is modeled by two degrees of freedom in surge and sway, denoted by u_{26} and u_{27}, respectively. Only the translation of the torus in these two directions is considered. Following the same procedure, as described in chapter4 for the spar, the kinetics of the modified torus system can be derived.

The position vector of the point (s^*) on the spar where the torus is connected, with respect to tower base t_b, can be written as

$$\mathbf{r}_{\mathbf{s}^*} = -h_{tr}.\hat{a}_2 \tag{6.4}$$

As the translation of the modified system is described in the spar coordinate system ($\hat{a}$), the position vector of the center of mass of torus (tr) from the point (s^*) is given by

$$\mathbf{r_{tr}} = u_{26}.\hat{a}_1 - u_{27}.\hat{a}_3 \tag{6.5}$$

Using Eq. (6.4) and Eq. (6.5), the total linear velocity at the center of mass of the torus (tr) is given by

$$\mathbf{v_{tr}} = \mathbf{v_{s^*}} + \mathbf{v_{ln,tr}} + \omega_{\mathbf{t_b}} \times \mathbf{r_{tr}} \tag{6.6}$$

where $\mathbf{v_{s^*}}$ is the velocity at s^* and $\mathbf{v_{ln,tr}}$ is the linear velocity of the torus in the spar coordinate system. They can be derived using Eq. (6.4) and Eq. (6.5), which are given by the following expressions

$$\mathbf{v_{s^*}} = \mathbf{v_{t_b}} + \omega_{\mathbf{t_b}} \times \mathbf{r_{s^*}} \tag{6.7a}$$

$$\mathbf{v_{ln,tr}} = \dot{u}_{26}.\hat{a}_1 - \dot{u}_{27}.\hat{a}_3 \tag{6.7b}$$

As mentioned in chapter 4, assuming generalized speeds as the time derivatives of the degrees of freedom and rearranging Eq. (6.6) in the format of Eq. (2.5a) indicates $v_{t,tr} = 0$. Hence, the partial linear velocity of the torus given by

$$\mathbf{v_{i,tr}} = \mathbf{v_{i,s^*}} + \begin{cases} \omega_{\mathbf{i,t_b}} \times \mathbf{r_{tr}} & \text{for } i = 1...6 \\ \hat{a}_1 & \text{for } i = 26 \\ -\hat{a}_3 & \text{for } i = 27 \end{cases} \tag{6.8}$$

where $\mathbf{v_{i,s^*}}$ is the partial linear velocity at s^* and is given by

$$\mathbf{v_{i,s^*}} = \mathbf{v_{i,t_b}} + \omega_{\mathbf{i,t_b}} \times \mathbf{r_{s^*}} \quad \text{for } i = 4...6 \tag{6.9}$$

Following the same procedure as described for the spar, the partial linear acceleration terms for the torus are given by

$$\frac{d}{dt}(\mathbf{v_{i,tr}}) = \frac{d(\mathbf{v_{i,s^*}})}{dt} + \begin{cases} [\frac{d(\omega_{\mathbf{i,t_b}})}{dt} \times \mathbf{r_{tr}} & \\ +\omega_{\mathbf{i,t_b}} \times (\mathbf{v_{ln,tr}} + \omega_{\mathbf{t_b}} \times \mathbf{r_{tr}})] & \text{for } i = 1...6 \\ (\omega_{\mathbf{t_b}} \times \hat{a}_1) & \text{for } i = 26 \\ -(\omega_{\mathbf{t_b}} \times \hat{a}_3) & \text{for } i = 27 \end{cases} \tag{6.10}$$

Here, it should be noted that $\frac{d}{dt}(\mathbf{v_{t,tr}}) = 0$ as the term $\mathbf{v_{t,tr}} = 0$ in Eq. (6.10). In the above equation, $\frac{d(\mathbf{v_{i,s^*}})}{dt}$ is the partial linear acceleration at s^* and is derived by differentiating Eq. (6.9) with respect to time i.e.

$$\frac{d}{dt}(\mathbf{v_{i,s^*}}) = \omega_{\mathbf{i,t_b}} \times (\omega_{\mathbf{t_b}} \times \mathbf{r_{s^*}}) \quad \text{for } i = 4...6 \tag{6.11}$$

Using the above equations of linear and angular velocities and accelerations in Eq. (2.4), the generalized inertial forces for the modified torus are given by

$$\mathbf{F^*_{i,tr}} = \mathbf{v_{i,tr}}.[m_{tr}.\{(\sum_{i=1}^{27} \mathbf{v_{i,tr}}.\ddot{u}_i) + (\sum_{i=1}^{27} \frac{d(\mathbf{v_{i,tr}})}{dt}.\dot{u}_i)\}] \tag{6.12}$$

So, the system matrices of the torus can be obtained from the generalized inertial forces, by rearranging Eq. (6.12) i.e.

$$\mathbf{M_{i,j:tr}}(\mathbf{u}, \mathbf{t}) = m_{tr}.\mathbf{v_{i,tr}}.\mathbf{v_{j,tr}} \quad \text{for } i, j = 1...27 \tag{6.13a}$$

$$\bar{\mathbf{F}}^*_{i,tr} = m_{tr}.\mathbf{v_{i,tr}}.\left[\sum_{i=1}^{27} \frac{d(\mathbf{v_{i,tr}})}{dt}.\dot{u}_i\right] \qquad \text{for } i = 1...27 \tag{6.13b}$$

Similar to spar, the system matrices due to gravitational forces on the torus are given by

$$\mathbf{F_{i,tr,gv}} = \mathbf{v_{i,tr}}.(-m_{tr}.g.\hat{x}_2) \quad \text{for} \;\; i = 26, 27 \tag{6.14a}$$

Considering Rayleigh's damping for the modified spar-torus system, respective generalized active forces are given by

$$\mathbf{F(\dot{u}, u, t)_{i,tr,el}} = -K_{tr}.u_i \quad \text{for} \;\; i = 26, 27 \tag{6.15a}$$

$$\mathbf{F(\dot{u}, u, t)_{i,tr,d}} = -\frac{\xi_{tr}.K_{tr}}{\pi.f_{tr}}.\dot{u}_i \quad \text{for} \;\; i = 26, 27 \tag{6.15b}$$

where m_{tr}, K_{tr}, ξ_{tr}, f_{tr} are the mass, stiffness, damping ratio, and frequency in Hz, respectively, for the modified torus system. Similar to the spar, the hydrostatic and hydrodynamic forces also act on the torus. Thus, the generalized active forces on the modified torus system due to these loads are given by

$$\mathbf{F_{i,tr,hy}} = \mathbf{v_{i,tr}}.F_{tr,hy} \qquad \text{for} \;\; i = 1...27 \tag{6.16}$$

In the same way as in §4.2.1 in chapter 4, hydro-static and hydrodynamic forces acting on the torus ($F_{tr,hy}$) can be written using the following expressions

$$F_{tr,hy} = \left(\sum_{i=1}^{27} F_{{tr,hy}_i}.\ddot{u}_i \right) + F_{{tr,hy}_t} \tag{6.17}$$

where $F_{{tr,hy}_t}$ in Eq. (6.17) is the wave force that does not depend on the inertia of the torus, whereas the term $F_{{tr,hy}_i}$ contributes to the added mass of the system matrices. Therefore, the system matrices due to wave loads on the torus can be obtained as

$$\mathbf{M_{i,j;tr,hy}(u,t)} = -\mathbf{v_{i,tr}}.F_{{tr,hy}_j} \quad \text{for} \;\; i,j = 1...27 \tag{6.18a}$$

$$\mathbf{F_{i,tr,hy}(\dot{u}, u, t)} = \mathbf{v_{i,tr}}.F_{{tr,hy}_t} \quad \text{for} \;\; i = 1...27 \tag{6.18b}$$

Following the same procedure for the torus, the governing equation of motion for each component can be derived in the global reference frame. Finally, they are assembled to get the combined model of the modified spar-torus system. The aerodynamic and hydrodynamic loads are discussed in the following sections.

6.4 External Loads on Floating Offshore Wind Turbine

Spar-type floating offshore wind turbines with a modified torus system are subjected to different forces, which include aerodynamic forces on the blades and tower, hydrodynamic forces on the spar and torus, and mooring forces arising from anchoring cables, besides gravitational pull. The detailed description of these aerodynamic and hydrodynamic loads used for modeling and analysis in this study is given in §2.2.5 of chapter 2, and §4.3 of chapter 4, hence they are not included here to avoid repetition.

6.5 Numerical Results and Discussion

In this section, the numerical analysis of the proposed MSTC for mitigating the vibration of a spar-type FWT is introduced. The simulation incorporates aerodynamic and hydrodynamic loads, taking into account wind-wave correlation and misalignment. The mathematical model of the Spar-type FWT utilizes the benchmark properties of the NREL 5MW wind turbine on the OC3-Hywind spar as detailed in [6]. To assess the effectiveness of the proposed MSTC, six distinct time histories are examined and presented. These include spar surge (U_{s_Su}) and sway (U_{s_Sw}), spar roll (U_{s_R}) and pitch (U_{s_P}), as well as tower top fore-aft (U_{TFA}) and side-to-side (U_{TSS}) motions. The analysis encompasses various wind speeds and wind-wave misalignment angles, providing a comprehensive illustration of the MSTC's performance.

6.5.1 Properties of the Spar-type FWT with the Attached Torus and Other Environmental Parameters

The basic properties of the benchmark FWT used in this study are presented in §4.4.1 of chapter 4. The proposed MSTC is designed to ensure its compatibility with the spar. It is 30m deep with outer and inner diameters are 18m and 17m, respectively. The total mass of this system is 7.47e5kg having its center of mass at 15m below the sea level. The spring stiffness and damping constant of the MSTC are 144.43kN/m and 65.7kNs/m, respectively, which are kept the same for both surge and sway degrees of freedom. However, before investigating the efficiency of the proposed MSTC, the mathematical model is validated with the benchmark response, and the validation results are already shown in §4.4.2 of chapter 4, hence they are not repeated here.

TurbSim is used to simulate steady and turbulent wind fields for various mean velocities (3, 11.4, 25 m/s), corresponding to cut-in, rated, and cut-out speeds at a 90 m hub height. The wind field simulation utilizes a power-law exponent of 0.2 for steady wind and incorporates 10% turbulence with IEC Kaimal spectra. Environmental conditions, including the joint probability distribution of mean wind speed at 10 m height and significant height and peak period of the wave from Johannessen et al. [265], are considered (refer to Table 6.1).

Wave acceleration and velocities at different depths are generated using the Pierson-Moskowitz spectrum as detailed in Sec. 4.3, based on the specified parameters. To assess the impact of wind-wave misalignment under various marine states, five cases ranging from 0^o to 90^o are examined. Fig. 6.3a illustrates the wind field generated by TurbSim at the rated speed with 10% turbulence. Additionally, Fig. 6.3b presents time histories of simulated waves along the surge axis, corresponding to a significant wave height of 3.1 m at different depths without misalignment. Notably, the magnitude of wave velocity is maximum near the surface, which is aimed to be isolated from the floating spar. Utilizing these inputs, along with other structural properties, the responses of the combined system are obtained for performance evaluation.

Table 6.1: Wind and wave profile data

Wind profiles		**Sea state**	
Mean speed	3 m/s, 11.4 m/s, 25m/s	Significant height	1.6 m, 3.1 m, 5.9 m
Turbulence	0%, 10%	Peak period	10s, 11s, 13s
		Heading direction	0^o, 30^o, 45^o, 60^o, 90^o

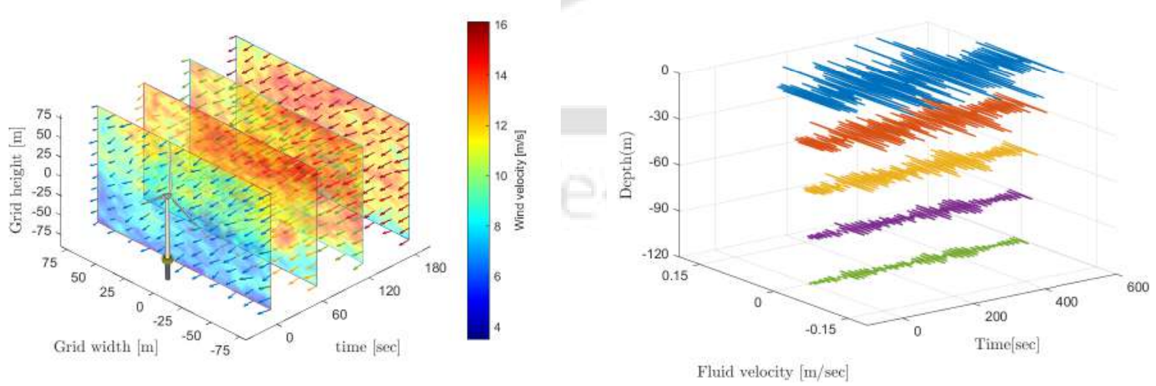

(a) (b)

Figure 6.3: Simulated wind and wave time histories (turbine model shown in the figure is not to scale); (a) Wind field & (b) Wave in surge

6.5.2 Vibration Control Using MSTC

Once the model is validated, it is further used for performance evaluation of the proposed modified spar-torus system. First, the rated speed of the turbine is considered to study the dynamics of the combined system under regular operation. Fig. 6.4 shows the response of spar due to steady wind and 30° wind-wave misalignment. This figure clearly shows the effect of MSTC on the sway (i.e. side-to-side) response of the spar. The percentage reduction of peak response along surge and sway DOFs are 1.09% and 49.8%, respectively. Here, it may be noted that the combined floating system acts as a rigid body, which is dragged along the wind, i.e., surge. It can be observed in Fig. 6.4a, which shows the response has a large mean displacement along with the fundamental period of the mooring load in that direction. The inset in this figure shows the transient mooring force, which has a fundamental frequency of 0.001Hz that dies out as time progresses, leaving the mean component of the force, which is also reflected in the surge response of the spar. Thus, the response in the surge is dominated by the mooring frequency, which is superimposed by the dynamic response of a very small amplitude caused by the sea waves. Due to this reason, the response reduction in the surge direction is low. On the other hand, rigid body motion is absent in the sway or side-to-side direction, and the wave motion fully governs the dynamics of the spar. Thus, MSTC offers better isolation of wave force, which is maximum near the surface, and hence, significant response reduction is achieved in this direction. Similarly, the peak response in the rolling and pitching motion of the spar is observed to be reduced by 19.9% and 2.33% for steady wind. These two DOFs also show identical phenomena as in the case of surge and sway responses of the spar. The rolling motion shows better reduction as compared to pitching due to the large mean component of the dominant mooring load that leads to rigid body motion.

As the spar acts like a rigid floating body that supports a tall tower, a small reduction in spar motion is bound to have an amplified effect at the top of the tower, i.e. nacelle. The displacement time histories at the top of the tower in fore-aft and side-to-side directions with and without MSTC are shown in Fig. 6.5 for steady wind and in Fig. 6.6 for 10% turbulence with 30^o misalignment. These figures show that the response at the top of the tower is significantly reduced by the MSTC system. The peak responses at the top of the tower in these two directions (i.e. fore-aft and side-to-side) are reduced by 16.68% and 41.68% for steady wind and 41.6% and 60.2% for turbulence, respectively. In this context, it may be noted that the fore-aft DOF at the top of the tower receives the highest amount of aerodynamic damping, which increases with the level of turbulence and ultimately affects the dynamic response. However, even under high aerodynamic damping and rigid body motion, the proposed MSTC offers significant vibration control at the top of the tower, which is the main objective of this study.

Table 6.2: Response reduction at rated speed

	Wind-wave misalignment angle	% reduction of peak response: Spar Surge	Spar Sway	Spar Roll	Spar Pitch	tower top Fore-aft	tower top Side-to-side
Steady Wind	0^o	0.03	1.07	-1.76	5.41	19.66	11.85
	30^o	1.09	49.80	19.89	2.34	16.68	41.68
	45^o	0.93	55.87	23.49	0.71	13.70	45.37
	60^o	0.75	58.35	26.10	-1.31	9.50	47.13
	90^o	0.34	59.73	28.46	-2.67	-2.08	48.30
10% Turb.	0^o	0.21	-10.57	24.42	0.19	12.88	10.32
	30^o	-0.01	41.66	25.48	0.18	11.32	60.21
	45^o	-0.27	55.25	28.88	0.13	9.07	62.77
	60^o	-0.63	61.37	31.12	0.17	5.40	62.75
	90^o	-0.76	66.06	31.73	0.44	-0.08	61.82

Once the performance of the proposed MSTC is demonstrated, a sensitivity analysis is carried out to investigate the performance under different wave-wind misalignment, which is shown in Table 6.2. This table shows the response reduction in all 6 DOFs for both steady and turbulent wind under different levels of misalignment. From this table, it can be observed that significant response reductions are obtained in the

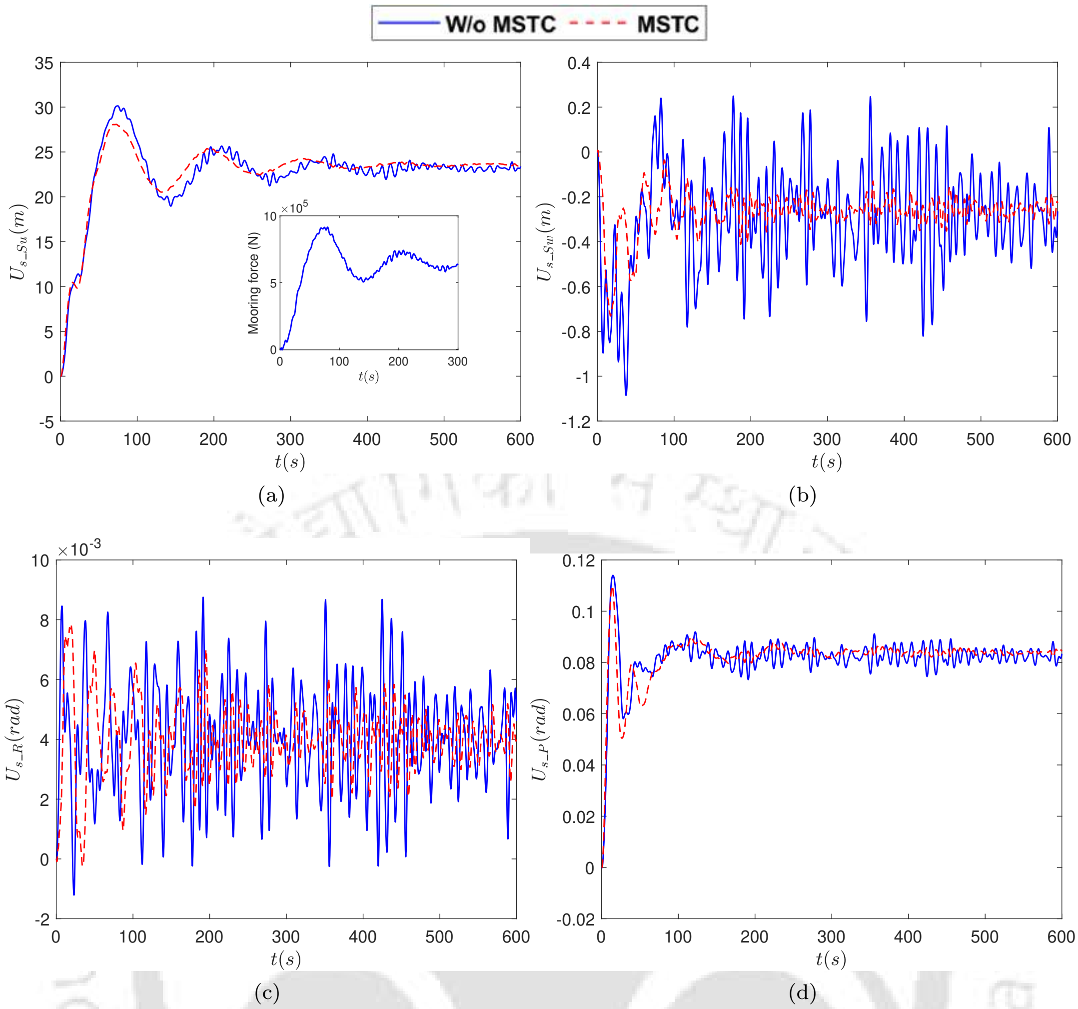

Figure 6.4: Response of spar at rated speed without turbulence; (a) surge, (b) sway, (c) roll & (d) pitch

sway and rolling motion of the spar, which ultimately affects the tower response in the side-to-side direction. Besides sway vibration control of the spar, the tower fore-aft is also reduced by 20% in the steady wind with zero misalignment. Moreover, the performance of the controller significantly increases with the wind-wave misalignment reaching more than 60% reduction for maximum misalignment. This justifies the efficiency of the proposed controller to improve the response of a spar-type floating wind turbine in sway motion.

Next, the performance envelope of the proposed controller, ranging from the cut-in to cut-out speeds corresponding to different misalignments, is evaluated. Fig. 6.7 and Fig. 6.8 show the complete performance envelope of MSTC in terms of key performance parameters under both steady and turbulent wind. From these figures, it can be observed that MSTC offers better performance between the cut-in and the rated speed (i.e. under regular operation) when the wave loads are dominant, and hence, MSTC is more effective. Considering the steady wind, the peak response reduction at the tower top in the fore-aft is observed to reach 52.4% at cut-in speed. The reduction percentage drops to 19.66% during rated operation and again increases to 48.17% at cut-out speed. The higher aerodynamic damping during rated operation, particularly in the fore-aft motion of the rotor, is indeed a factor in the observed performance pattern of the MSTC system. Here, it may be noted that the blade pitch remains unchanged during the cut-in to the rated speed regime. Pitch control is activated beyond the rated speed to maintain *rpm* and power output. This adjustment reduces aerodynamic load, and hence, the response in the fore-aft beyond the rated speed decreases gradually. The closed-loop mechanism of the pitch controller, which can induce negative damping due to the pitch controller's response to increased apparent wind speed, is an important consideration here. The baseline controller is designed in such a way that its closed-loop pole is below the frequency of the fore-aft vibrational modes of the rotor. The lower aerodynamic damping at cut-out conditions positively impacts the MSTC's performance in the fore-aft direction, as also observed in the numerical analysis.

Finally, the impacts of different depths of MSTC are studied, which are shown in Fig. 6.9a and 6.9b

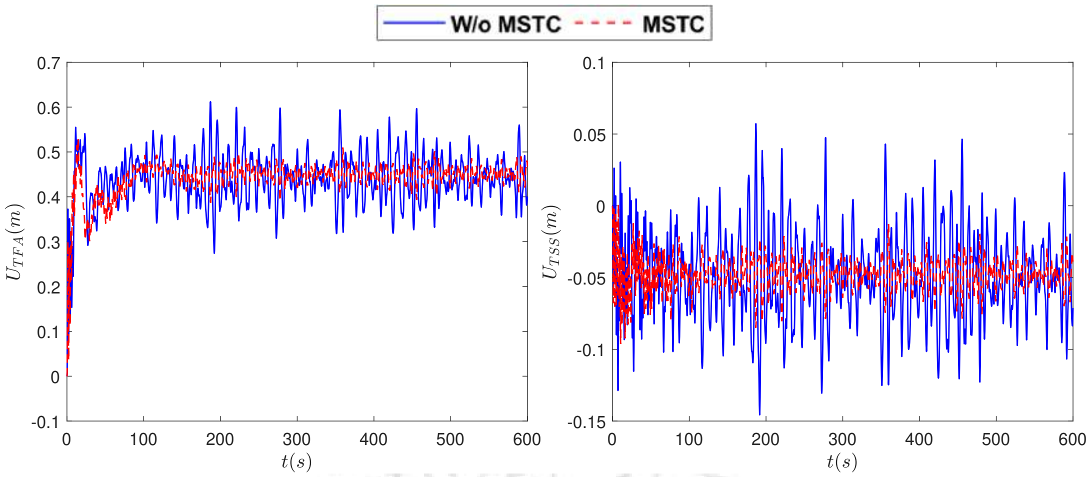

(a) (b)

Figure 6.5: Tower response at rated speed and no turbulence; (a) fore-aft & (b) side-to-side

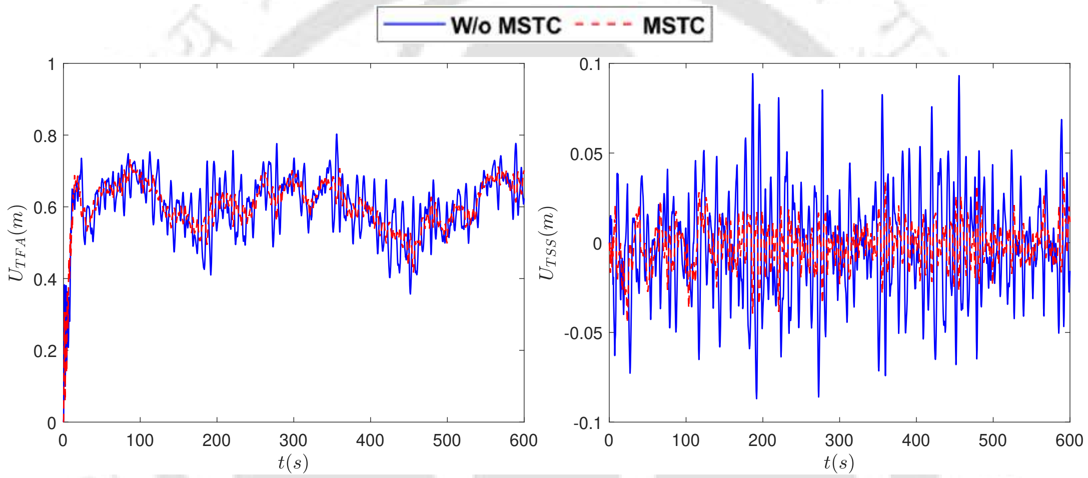

(a) (b)

Figure 6.6: Tower response at rated speed with 10% turbulence (a) fore-aft & (b) side-to-side

corresponding to the steady and turbulent wind. The magnitude of vibration control is observed to increase with depth as it can isolate more wave force. It is found to offer a maximum reduction of 30m and hence, is selected for this study. Beyond this value, the inertia force of the MSTC increases compared to the magnitude of the isolated wave force, and thus, the reduction decreases. Therefore, it reveals that the depth of MSTC should be such that it offers maximum isolation of wave force near the surface only.

6.6 Summary

A new concept for vibration control of a spar-type floating wind turbine using a modified torus is presented in this chapter. The proposed modification isolates wave energy, which ultimately affects the dynamics of the spar supporting the blade-tower assembly. An aero-servo-elastic multi-body dynamic model using Kane's approach is developed to study the performance of the proposed system. Different aerodynamic and hydrodynamic loading conditions ranging from cut-in to cut-out wind speed with corresponding wave heights considering wind-wave correlations and misalignment are simulated. The numerical results presented in this chapter demonstrate substantial improvement in the overall response of FWT; particularly in the sway direction. The significant observations from this numerical analysis are highlighted below

- The modified torus system can be installed in a spar-type FWT without affecting the main structure or adding any extra weight in the main structure to control wave-induced vibrations as in the case of a tuned mass damper. In this context, it is worth mentioning that housing a tuned mass damper within

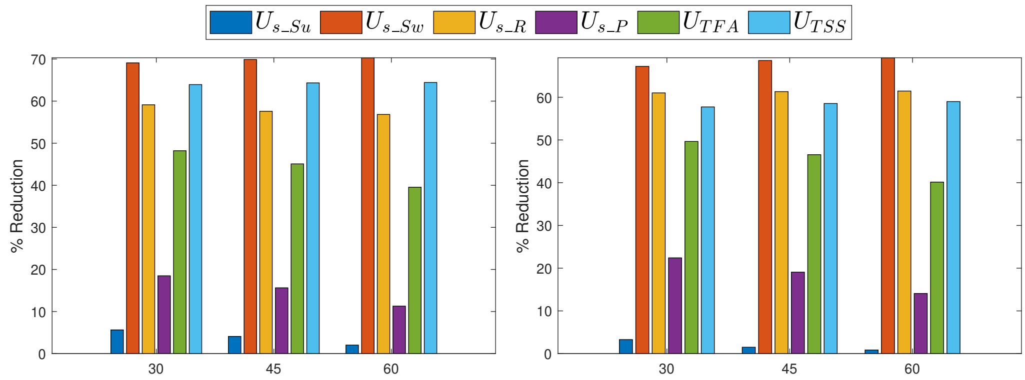

Figure 6.7: Percentage reduction of peak responses for cut-in speed (a) Steady wind & (b) With 10% turbulence

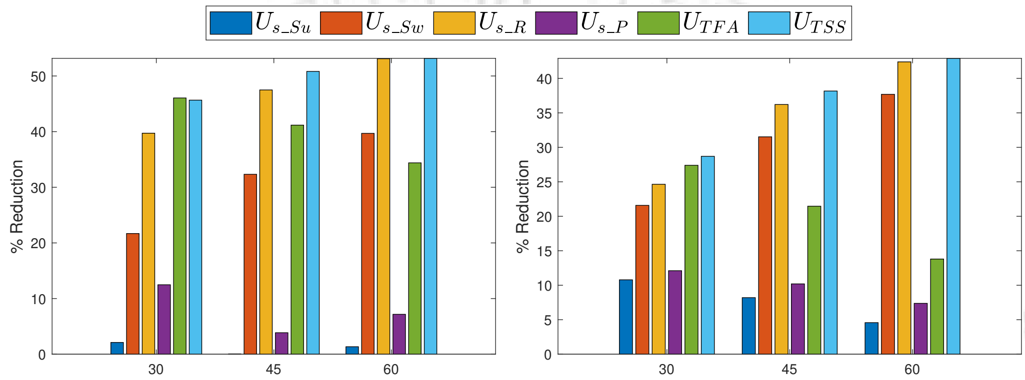

Figure 6.8: Percentage reduction of peak responses for cut-out speed (a) Steady wind & (b) 10% turbulence

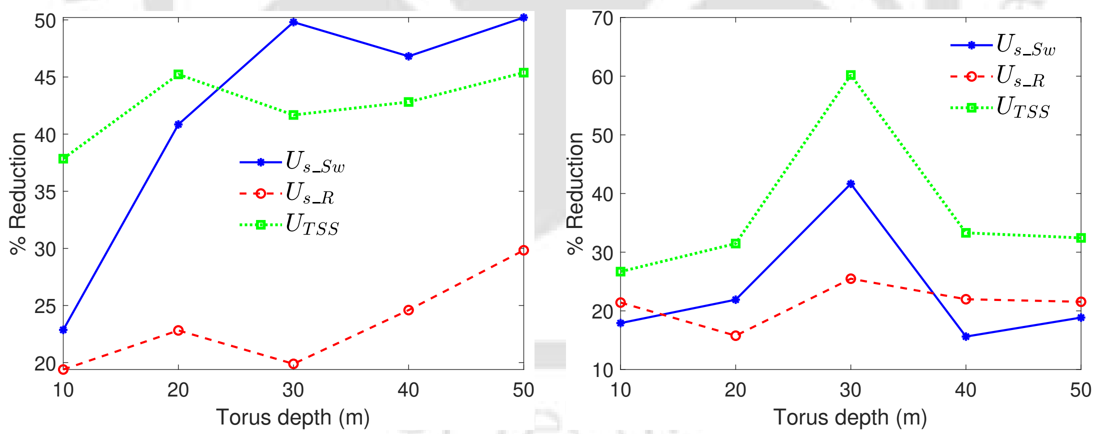

(a) (b)

Figure 6.9: Percentage reduction vs. torus depth at rated speed (a) steady wind & (b) 10% turbulence

the nacelle is a challenging task due to space constraints. The proposed MSTC, being a floating mass outside the main structure, has no such problem.

- The peak response reduction of spar and tower is found to be more than 60% depending upon the wind speed, turbulence, significant wave heights, and wind-wave misalignment. Being a passive system, the proposed controller does not need any power or real-time monitoring, which is an advantage in deep-sea operation.
- The increase in wind-wave misalignment angle results in better performance of the MSTC to control the sway response of the spar and side-to-side motion of the nacelle, which are the main objective

of this study as excessive motion in the sway or side-to-side direction is detrimental for the sensitive electro-mechanical components of the drivetrain.

Overall the proposed MSTC is found to be effective, particularly in controlling the sway or side-to-side motion of the spar-type floating wind turbine.

Chapter 7

Power Regulation and Vibration Control of Onshore Wind Turbine with Double-Pitched Rotor

7.1 Introduction

Power fluctuation and vibration control are the two most common features often encountered in any modern horizontal axis wind turbine due to their ultra-large size and lightweight rotor operating in turbulent wind. To address this issue, a double-pitched rotor (i.e., with two different pitch angles) is proposed in this chapter. The model is developed using Kane's approach, considering bending-torsion coupling with proper aero-elastic simulation. Firstly, a centralized Proportional Integral Derivative (PID) control algorithm is developed to tune two differential pitch angles of the rotor. The gain scheduling in this algorithm is carried out using a multi-objective optimization based on the rotor speed error and structural vibration. The benchmark data of a 5MW turbine is used to demonstrate the performance of this algorithm to highlight its superiority over a generalized full-blade single-pitch baseline control. Different flow conditions are simulated to replicate the actual operating conditions for assessing the performance envelope of the proposed controller. Secondly, a centralized Linear Quadratic Regulator (LQR) control algorithm with optimized control parameters for two different pitch angles is developed, and the performance of the proposed control strategy under different flow conditions is demonstrated. The optimized gains are estimated based on the standard deviation in rotor speed, which affects power fluctuation. The performance of the proposed control strategy highlights its superiority to a generalized full-blade single-pitch baseline control documented in the literature. The numerical results presented in this study also demonstrate the sensitivity of the proposed control strategy while meeting the key objectives, i.e., reducing structural vibrations, actuator demand, and rotor speed fluctuations.

7.2 Mathematical Model of Wind Turbine with a Double-Pitched Rotor

Double-pitched smart rotors have been developed in the recent past [200] where the blades are divided into two segements; an inboard section whose pitch angle is controlled at the root and an outboard section with a different pitch angle near the free end, i.e., (tip-controlled rotor). The power output can be tuned by regulating the pitch angle of the outboard section using a separate actuator. Tip-controlled rotor offers better start-up and shutdown abilities, faster control, lower weight, and more liberty in airfoil selection compared to a single-pitched rotor [201, 202]. The horizontal-axis wind turbine is modeled as a collection of multiple bodies experiencing mutual interactions. Here, Kane's formulation [12] is adopted to address this problem, where the complete system with a double-pitched rotor is modeled using 19 degrees of freedom (DOF) representing tower, nacelle, drive-train, and blades, i.e.

$$u = \{\underbrace{u_1, ...u_4,}_{Tower} \underbrace{u_5,}_{Nacelle} \underbrace{u_6, u_7,}_{DriveTrain} \underbrace{u_8, ...u_{19}}_{Blades}\}^T \tag{7.1}$$

In this model, the tower base is considered fixed, hence the first three DOFs described in Eq. 2.1 are omitted here. The fixed global reference frame $\hat{x}$ for the complete system is located at the base of the tower, as shown in Fig. 2.1 of chapter 2. The force equilibrium of the turbine in a holonomic multi-body dynamic framework has the following form

$$\boldsymbol{F_i} - \boldsymbol{F_i^*} = 0 \quad for \quad i = 1, 2, ..., n \tag{7.2}$$

In the above equation, n represents the total number of DOFs (i.e., $n = 19$ in this case). $\boldsymbol{F_i}$ and $\boldsymbol{F_i^*}$ represent the generalized active and inertia forces, respectively. The complete model of a stand-alone turbine with rotors having a single pitch angle is established with complete validation in chapter 2. However, only the modification of the rotor with two pitch angles under bending-torsion coupling is described here. Hence, the same is not repeated here. Following this formulation, the governing equation of motion is obtained from the components of $\boldsymbol{F_i}$ and $\boldsymbol{F_i^*}$ in Eq. 7.2 in the matrix form

$$[\boldsymbol{M(u,t)}] . \{\boldsymbol{\ddot{u}}\} + \left\{\boldsymbol{\bar{F}(\dot{u}, u, t)}\right\} = 0 \tag{7.3}$$

The vector $\left\{\boldsymbol{\bar{F}(\dot{u}, u, t)}\right\}$ in the above equation includes stiffness, damping, and externally applied forces. As stated in the objective, this work primarily focuses on the optimal tuning of the double-pitched rotor, which is the new component and main contribution of this work. The increase in mass due to the double-pitch mechanism was minimal, mainly because of the lighter blade tip (only about 3% of the total blade mass). The bending stiffness of this blade segment is a thousand times smaller than the stiffness near the blade root. Also, the edgewise stiffness of the blade is significantly higher than in the other direction. It was observed that the blade natural frequency and mode shapes remain virtually unchanged (change is observed only at the 4^{th} decimal place in the frequency) considering tip-actuator mass as 10% of the mass of this tip segment (i.e., 0.3% of the total blade mass). Also, the blade flapwise and edgewise time-history responses with this additional actuator mass match the responses points by point without considering the actuator mass. Hence, it is not reported separately here. However, the model is designed to accommodate additional mass at specific blade nodes, including gravitational loading effects, if required. Hence, only the modification (i.e. blade model with two different pitch angles) is discussed below. All other details (i.e., multi-body dynamics of tower, nacelle, drive-train, and hub along with aerodynamic and gravitational load) are provided in chapter 2.

7.2.1 Model of the Double-Pitched Blades Considering Bending-Torsion Coupling

The blade is assumed to be an elastic rotating beam of length R_{b_k} that vibrates in its flapwise, edgewise, and torsional directions and is rigidly connected to the hub. Together with the structural pre-twist angle θ_s, and collective pitch angle $\theta_{p,1}$ at the root (i.e., first part), defines the orientation of each blade element (i.e., along $\hat{i}_{k,i}(r)$ coordinates located at a distance r from its root, where $i = 1, 2, 3$ represent three orthogonal directions and k refers to the blade number). In the case of a double-pitched blade, an outboard pitch angle is introduced at r_{dp} from the blade root. Thus, the rotor elements beyond this length (i.e., $r > r_{dp}$) are pitched by an additional angle $\theta_{p,2}$, as shown in Fig. 7.1. The blade mode shapes are defined along its flapwise, edgewise, and torsional directions. Using these mode shapes and curvature, the deflection at any point along its length can be expressed in its local coordinate system, i.e., $\hat{h}_{k,i}(r)$ by double-integrating the curvature in $\hat{h}_{k,i}(r)$ coordinates, thereby introducing coupling between the two orthogonal bending directions. For example, a nodal position $[X_{b_1}(r), Y_{b_1}(r)]$ on the 1^{st} blade can be expressed as

$$X_{b_1}(r) = \phi_1(r).u_8 + \phi_2(r).u_{10} + \phi_3(r).u_9 \tag{7.4a}$$

$$Y_{b_1}(r) = \varphi_1(r).u_8 + \varphi_2(r).u_{10} + \varphi_3(r).u_9 \tag{7.4b}$$

In the above equations, ϕ_i and φ_i are the twisted bending modes originating from flapwise and edgewise bending modes [13], which have the following form

$$\phi_1(r) = \int_0^r \int_0^{\bar{\bar{r}}} \left[\frac{d^2\gamma_1^F(\bar{r})}{d\bar{r}^2} \cos\{\theta_s(\bar{r}) + \theta_{p,2}(\bar{r})\} \right] d\bar{r} d\bar{\bar{r}} \tag{7.5a}$$

$$\phi_2(r) = \int_0^r \int_0^{\bar{\bar{r}}} \left[\frac{d^2\gamma_2^F(\bar{r})}{d\bar{r}^2} \cos\{\theta_s(\bar{r}) + \theta_{p,2}(\bar{r})\} \right] d\bar{r} d\bar{\bar{r}} \tag{7.5b}$$

$$\phi_3(r) = \int_0^r \int_0^{\bar{\bar{r}}} \left[\frac{d^2\gamma_1^E(\bar{r})}{d\bar{r}^2} \sin\{\theta_s(\bar{r}) + \theta_{p,2}(\bar{r})\} \right] d\bar{r} d\bar{\bar{r}} \tag{7.5c}$$

$$\varphi_1(r) = -\int_0^r \int_0^{\bar{\bar{r}}} \left[\frac{d^2\gamma_1^F(\bar{r})}{d\bar{r}^2} \sin\{\theta_s(\bar{r}) + \theta_{p,2}(\bar{r})\} \right] d\bar{r} d\bar{\bar{r}} \tag{7.5d}$$

$$\varphi_2(r) = -\int_0^r \int_0^{\bar{\bar{r}}} \left[\frac{d^2\gamma_2^F(\bar{r})}{d\bar{r}^2} \sin\{\theta_s(\bar{r}) + \theta_{p,2}(\bar{r})\} \right] d\bar{r} d\bar{\bar{r}} \tag{7.5e}$$

$$\varphi_3(r) = \int_0^r \int_0^{\bar{\bar{r}}} \left[\frac{d^2\gamma_1^E(\bar{r})}{d\bar{r}^2} \cos\{\theta_s(\bar{r}) + \theta_{p,2}(\bar{r})\} \right] d\bar{r} d\bar{\bar{r}} \tag{7.5f}$$

In this format, $\bar{r}$ and $\bar{\bar{r}}$ are dummy variables, and the functions $\gamma_i^F(\bar{r})$ and $\gamma_i^E(\bar{r})$ denote the i^{th} flapwise and edgewise modes, respectively. The outboard pitch angle $\theta_{p,2}(\bar{r})$ in Eq. 7.5 is zero when $\bar{r} < r_{dp}$. These twisted modes determine the deformed shape of the blade with respect to its centroidal (i.e., reference) axis. The coupling between bending and torsional DOFs is primarily caused by twists and offsets of the aerodynamic and elastic centres of the cross-section from its centre of gravity. The offset of the aerodynamic centre from the pitch axis produces an aerodynamic pitching moment in addition to lift and drag forces, causing torsional vibration, which can interact significantly with the bending deformations. This, in turn, has inertial effects on the blade, which can be modeled using its position vector. The dynamic torsion is assumed to be positive in the opposite direction of the blade twist. As a result, the position vector of the 1^{st} blade at a distance $(r + r_{hu})$ from the rotor apex (ap) can be written as

$$\begin{aligned} \mathbf{l_{b_1}(r)} = &\{X_{b_1}(r) - Y_{b_1}(r).\theta_{t,b_1}(r)\}.\hat{h}_{1,1} + \{X_{b_1}(r).\theta_{t,b_1}(r) + Y_{b_1}(r)\}.\hat{h}_{1,2} \\ &+ [r + r_{hu} - 0.5\{S_{1,1}(r).u_8^2 + S_{2,2}(r).u_{10}^2 + S_{3,3}(r).u_9^2 + 2S_{1,2}(r).u_8.u_{10} \\ &+ 2S_{1,3}(r).u_8.u_9 + 2S_{2,3}(r).u_{10}.u_9\}].\hat{h}_{1,3} \end{aligned} \tag{7.6}$$

In this equation, $\theta_{t,b_1}(r) = \gamma_1^T(r).u_{11}$ is the twist of the blade node due to torsion, where, $\gamma_1^T(r)$ is its first torsional mode. The combined effect of bi-axial bending modes is represented by the scalar values $S_{i,j}$ in Eq. 2.43, which signifies axial shortening of the blade [13].

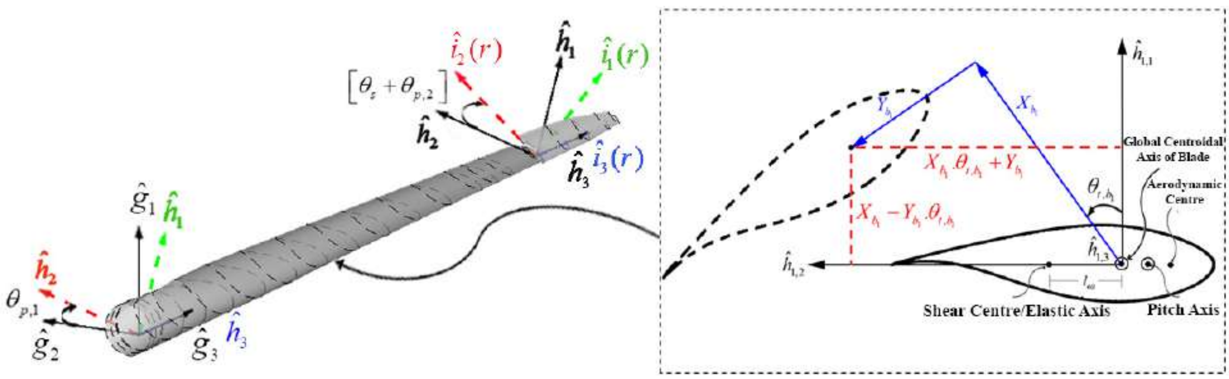

Figure 7.1: Double pitched blade and Blade sectional view undergoing coupled deformation (inset)

Once the position vectors of blade nodes are defined, the total angular and linear velocities [i.e., $\omega_{b_1}(r)$ & $v_{b_1}(r)$, respectively] can be obtained from the velocities of the low-speed shaft and local blade element. These angular and linear velocities can be expressed in their partial form $\omega_{i,b_1}(r)$ and $v_{i,b_1}(r)$. Readers may refer to Eq. 2.48a and Eq. 2.48b of chapter 2 for the details of these partial velocities. The components of partial angular and linear acceleration, i.e., $\boldsymbol{\alpha_{i,b_1}(r)} = \frac{d}{dt}\boldsymbol{\omega_{i,b_1}(r)}$ and $\boldsymbol{a_{i,b_1}(r)} = \frac{d}{dt}\boldsymbol{v_{i,b_1}(r)}$, are obtained from the time derivatives of the partial velocities. Hence, the expression for the generalized inertia force associated with the blade is given by

$$\begin{aligned}\boldsymbol{F^*_{i,b_1}} = &\int_0^{R_{b_1}} \mu_{b_1}(r).\boldsymbol{v_{i,b_1}(r).a_{b_1}(r)}.dr + \int_0^{R_{b_1}} \boldsymbol{\omega_{i,b_1}(r).\bar{I}_{b_1}(r).\alpha_{b_1}(r)}.dr \\ &+ \int_0^{R_{b_1}} \boldsymbol{\omega_{i,b_1}(r)}.\left\{\boldsymbol{\omega_{b_1}(r)} \times \boldsymbol{\bar{I}_{b_1}(r).\omega_{b_1}(r)}\right\}.dr\end{aligned} \tag{7.7}$$

In this equation, R_{b_1} denotes the blade length while $\mu_{b_1}(r)$ and $\boldsymbol{\bar{I}_{b_1}(r)}$ denote its distributed mass and inertia dyadic, respectively. The nodal linear and angular accelerations are given by $\boldsymbol{a_{b_1}(r)}$ and $\boldsymbol{\alpha_{b_1}(r)}$, while the distributed inertia of the blade has the following form

$$\boldsymbol{\bar{I}_{b_1}(r)} = I^F_{b_1}(r).\hat{i}_{1,1}.\hat{i}_{1,1} + I^E_{b_1}(r).\hat{i}_{1,2}.\hat{i}_{1,2} + \{\rho_{b_1}(r).I^p_{b_1}(r) + \mu_{b_1}(r).l^2_{cg,b_1}(r)\}.\hat{i}_{1,3}.\hat{i}_{1,3} \tag{7.8}$$

where $I^F_{b_1}(r)$, $I^E_{b_1}(r)$ and $I^p_{b_1}(r)$ denote the flapwise, edgewise, and rotational inertia, respectively. Also, $\mu_{b_1}(r)$ and l_{cg,b_1} denote the nodal mass density and offset of the airfoil center of gravity from the blade centroidal axis. Eq. 7.7 can be rearranged using the expressions of velocities, accelerations, mass distribution, and inertial properties, which leads to the following mass matrix

$$\begin{aligned}\boldsymbol{M_{i,j;b_1}(u,t)} = \int_0^{R_{b_1}} \mu_{b_1}(r).\boldsymbol{v_{i,b_1}(r).v_{j,b_1}(r)}.dr + \int_0^{R_{b_1}} \boldsymbol{\omega_{i,b_1}(r).\bar{I}_{b_1}(r).\omega_{j,b_1}(r)}.dr \\ \text{for } \; i,j = 1...11\end{aligned} \tag{7.9}$$

while the remaining part of the generalized inertia force is given by

$$\begin{aligned}\boldsymbol{\bar{F}^*_{i,b_1}(\dot{u},u,t)} = &\int_0^{R_{b_1}} \mu_{b_1}(r).\boldsymbol{v_{i,b_1}(r)}.\left(\sum_{i=1}^{11}\frac{d}{dt}\{\boldsymbol{v_{i,b_1}(r)}\}.\dot{u}_i\right).dr \\ &+ \int_0^{R_{b_1}} \boldsymbol{\omega_{i,b_1}(r)}.\left[\boldsymbol{\bar{I}_{b_1}(r)}.\left\{\sum_{i=1}^{11}\frac{d}{dt}\{\boldsymbol{\omega_{i,b_1}(r)}\}.\dot{u}_i\right\} + \boldsymbol{\omega_{b_1}(r)} \times \boldsymbol{\bar{I}_{b_1}(r).\omega_{b_1}(r)}\right].dr \\ &\text{for } \; i,j = 1...11\end{aligned} \tag{7.10}$$

Once the inertia force is determined, the remaining part of Eq. 7.3 consists of elastic, damping, and external force vectors. All these forces contribute to the generalized active force acting on the system. The model used in this study also includes the effect of elastic coupling between the bending and torsional modes. Aerodynamic and gravitational forces are the external forces acting on the system. The details of the generalized active force vector can be found in §2.2.4 of chapter 2.

7.3 External Loads on Double-Pitched Turbine

A land-based wind turbine undergoes various forces, encompassing aerodynamic forces acting on both the blades and tower, along with gravitational pull affecting all its components. The comprehensive explanation of these aerodynamic and gravitational loads, employed for modeling and analysis in this research, is provided in §2.2.5 and §2.2 of Chapter 2. Consequently, these details are not reiterated here.

7.4 Centralized PID Based Double-Pitch Control

Traditionally, power output regulation of a horizontal axis wind turbine relies on two different control strategies - either generator-torque control or full-span rotor-collective blade-pitch control. Among these two options, the first one is configured below the rated speed, while the second option operates above it. The present study focuses on the second category as they become critical with the increase in wind speed. A full-span blade pitch controller is a single variate system where the controller modifies the blade pitch angle to minimize the fluctuation of generator speed. The actuator force demand for a full-blade pitch controller is generally higher. To address this issue a double-pitch rotor system is considered in this chapter, whose model has been developed in the previous section. In this section, a centralized multi-variate controller is proposed for the double-pitched smart rotor. The schematics of this control are shown in Fig. 7.2. This configuration aims to control the generator speed and subsequently attenuate blade vibration, i.e., flapwise, edgewise, and torsional deformations. For this purpose, firstly the PID algorithm is chosen for its effectiveness and popularity in the industry. The proposed blade-pitch control algorithm uses generator speed as feedback,

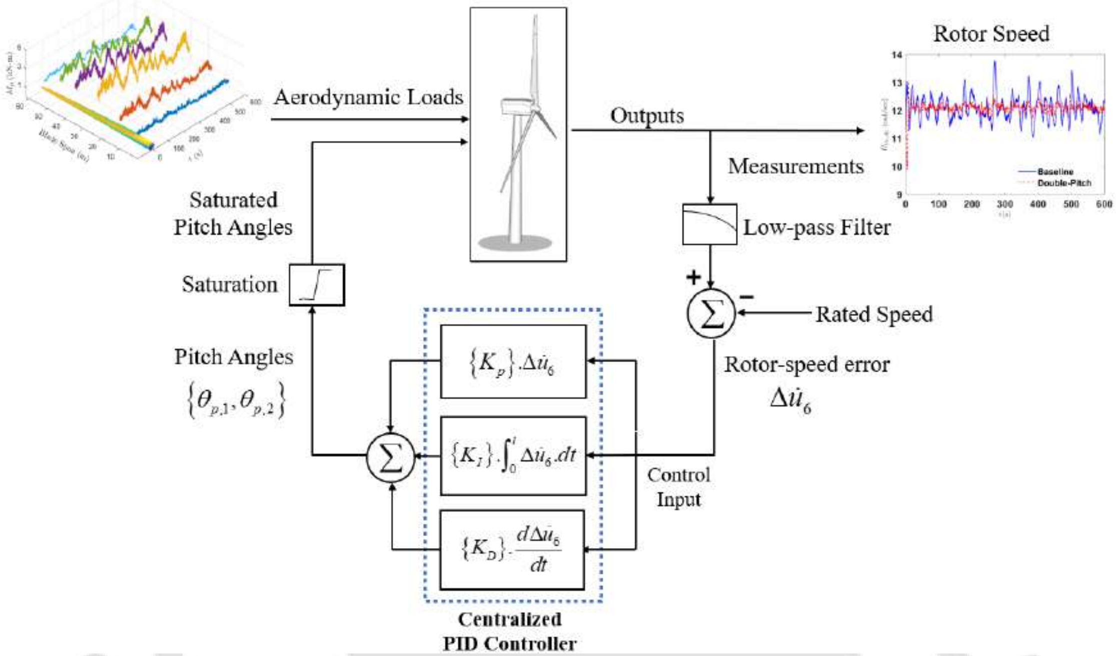

Figure 7.2: Simplified schematic diagram of the centralized control system

and a recursive, single-pole low-pass filter with exponential smoothing is used to filter the generator speed while minimizing high-frequency excitation, as also recommended by NREL [5]. The generator torque is inversely proportional to its speed to keep the power output constant above the rated wind speed, i.e.,

$$T_{gn} = \frac{P_0}{G_{br}.\dot{u}_6} \tag{7.11}$$

Here, G_{br} is the gearbox ratio and u_6 is the azimuth of the low-speed shaft, where the time derivative (i.e., $\dot{u}_6$) represents the rotor speed. The term P_0 refers to the rated power of the turbine. The first-order Taylor series expansion of Eq. 7.11 with respect to a reference point $\dot{u}_6^*$ has the following form

$$T_{gn} \approx \left.\frac{P_0}{G_{br}.\dot{u}_6}\right|_{\dot{u}_6^*=\Omega_0} + (\dot{u}_6 - \dot{u}_6^*).\left.\frac{\partial T_{gn}}{\partial \dot{u}_6}\right|_{\dot{u}_6^*=\Omega_0} = \frac{P_0}{G_{br}.\Omega_0} - \frac{P_0}{G_{br}.\Omega_0^2}.\Delta\dot{u}_6 \tag{7.12}$$

In the above equation, Ω_0 is the rated speed of the low-speed shaft. The aerodynamic torque exerted on the drive shaft is a function of collective pitch angles ($\theta_{p,1}$, $\theta_{p,2}$) of the smart rotor proposed in this study, i.e.,

$$T_{aero}(\Omega_0, \theta_{p,1}, \theta_{p,2}) = \frac{P(\Omega_0, \theta_{p,1}, \theta_{p,2})}{\Omega_0} \tag{7.13}$$

Here, P denotes the power produced by the turbine at a particular time instant. Using first-order Taylor series expansion similar to Eq. 7.12, Eq. 7.13 can be expressed as

$$T_{aero} \approx \frac{P_0}{.\Omega_0} + \frac{1}{\Omega_0}.\left(\frac{\partial P}{\partial \theta_{p,1}}\right).\Delta\theta_{p,1} + \frac{1}{\Omega_0}.\left(\frac{\partial P}{\partial \theta_{p,2}}\right).\Delta\theta_{p,2} \tag{7.14}$$

In this expression, the perturbation of the pitch angles around their operating point is denoted by $\Delta\theta_{p,i}$, which is correlated to the rotor speed fluctuation (i.e., $\Delta\dot{u}_6$) through the following relation

$$\Delta\theta_{p,i} = K_{P,i}.G_{br}.\Delta\dot{u}_6 + K_{I,i}\int_0^t G_{br}.\Delta\dot{u}_6.dt + K_{D,i}.G_{br}.\Delta\ddot{u}_6 \qquad \text{for } i = 1,2 \tag{7.15}$$

Thus, the centralized controller has proportional, integral, and derivative gains for both the pitch angles, which are denoted by $K_{P,i}$, $K_{I,i}$, and $K_{D,i}$, respectively. It may be noted that the dynamics of the drive-train can be modeled by the following expression [5]

$$T_{aero} - G_{br}.T_{gn} = I_{DT}.\Delta\ddot{u}_6 \tag{7.16}$$

Parameter $I_{DT} = I_{rotor} + {G_{br}}^2.I_{gn}$ in the above equation is the inertia of the drive-train. Substituting Eq. 7.12, Eq. 7.14 and Eq. 7.15 into Eq. 7.16 and rearranging them lead to the following second-order equation of motion for the rotor-speed fluctuation

$$\begin{aligned}&\left[I_{DT} - \tfrac{G_{br}}{\Omega_0}\left\{\tfrac{\partial P}{\partial\theta_{p,1}}.K_{D,1} + \tfrac{\partial P}{\partial\theta_{p,2}}.K_{D,2}\right\}\right].\ddot{\phi} + \left[-\tfrac{G_{br}}{\Omega_0}\left\{\tfrac{\partial P}{\partial\theta_{p,1}}.K_{P,1} + \tfrac{\partial P}{\partial\theta_{p,2}}.K_{P,2}\right\} - \tfrac{P_0}{\Omega_0^2}\right].\dot{\phi}\\ &+\left[-\tfrac{G_{br}}{\Omega_0}\left\{\tfrac{\partial P}{\partial\theta_{p,1}}.K_{I,1} + \tfrac{\partial P}{\partial\theta_{p,2}}.K_{I,2}\right\}\right].\phi = 0\end{aligned} \tag{7.17}$$

The term $\dot{\phi}$ in this formulation is used as a substitute for $\Delta\dot{u}_6$ for simplification purposes only. As shown in Eq. 7.17, the idealized double-pitch PID-controlled rotor-speed fluctuation behaves as a second-order system with a natural frequency of ω_ϕ and a damping ratio of η_ϕ, i.e.,

$$\omega_\phi = \sqrt{\frac{\left[-\tfrac{G_{br}}{\Omega_0}\left\{\tfrac{\partial P}{\partial\theta_{p,1}}.K_{I,1} + \tfrac{\partial P}{\partial\theta_{p,2}}.K_{I,2}\right\}\right]}{\left[I_{DT} - \tfrac{G_{br}}{\Omega_0}\left\{\tfrac{\partial P}{\partial\theta_{p,1}}.K_{D,1} + \tfrac{\partial P}{\partial\theta_{p,2}}.K_{D,2}\right\}\right]}} \tag{7.18a}$$

$$\eta_\phi = \frac{\left[-\tfrac{G_{br}}{\Omega_0}\left\{\tfrac{\partial P}{\partial\theta_{p,1}}.K_{P,1} + \tfrac{\partial P}{\partial\theta_{p,2}}.K_{P,2}\right\} - \tfrac{P_0}{\Omega_0^2}\right]}{2.\left[I_{DT} - \tfrac{G_{br}}{\Omega_0}\left\{\tfrac{\partial P}{\partial\theta_{p,1}}.K_{D,1} + \tfrac{\partial P}{\partial\theta_{p,2}}.K_{D,2}\right\}\right].\omega_\phi} \tag{7.18b}$$

The derivative term increases the effective inertia of the drive-train. At the same time, the proportional term introduces damping while the integral term provides restoring force with positive controller gain. Also, since the generator torque decreases as the speed increases (i.e., to maintain constant power) above the rated flow, the generator-torque controller develops negative damping in the response as indicated by the term $\frac{P_0}{\Omega_0^2}$ in Eq. 7.17. The proportional term in the blade-pitch controller must compensate for this negative damping. The derivative term in this case is smaller compared to the drive-train inertia. The negative damping and derivative term in Eq. 7.17 may be neglected for all practical purposes as recommended by NREL [13]. It also recommends $\omega_\phi = 0.6$ rad/s and $\eta_\phi = 0.7$ for the smooth operation of 5MW benchmark turbine used in this study. This assumption leads to the simplification of Eq. 7.18, which can be rearranged in the following format

$$\frac{-\tfrac{G_{br}}{\Omega_0}\left\{\tfrac{\partial P}{\partial\theta_{p,1}}.K_{I,1} + \tfrac{\partial P}{\partial\theta_{p,2}}.K_{I,2}\right\}}{I_{DT}} = 0.36 \tag{7.19a}$$

$$\frac{-\tfrac{G_{br}}{\Omega_0}\left\{\tfrac{\partial P}{\partial\theta_{p,1}}.K_{P,1} + \tfrac{\partial P}{\partial\theta_{p,2}}.K_{P,2}\right\}}{I_{DT}} = 0.84 \tag{7.19b}$$

The four unknowns, i.e., $K_{P,i}$ and $K_{I,i}$ for $i = 1,2$ in the above equations, need to be determined for optimal performance of the pitch controller. A full-span collective pitch controller in Eq. 7.19 has two unknowns (i.e., K_P and K_I). Moreover, if the blade-pitch sensitivity ($\frac{\partial P}{\partial\theta_p}$) is known, the optimal values of K_P and K_I can be determined directly from Eq. 7.19.

As for the present case, only two equations are available for the four unknowns. Thus, two additional equations are proposed to solve for optimal gain, which are developed using two additional parameters α_1 and α_2 as given in the following expressions

$$K_{P,i} = \alpha_i.K_P \qquad \text{for } i = 1,2 \tag{7.20a}$$

$$K_{I,i} = \alpha_i . K_I \qquad \text{for} \;\; i = 1, 2 \tag{7.20b}$$

In this proposal, K_P and K_I are the optimal gains for a full-blade pitching system. The formulation in Eq. 7.20 leads to an optimization problem, where the unknown parameters α_1 and α_2 are solved, minimizing the rotor speed fluctuations and subsequently the blade vibration. Without loss of generality, the controller gains (i.e., $K_{P,i}$ and $K_{I,i}$) at the rotor hub in the proposed double-pitched system are kept the same as for a full-blade controller (i.e., $\alpha_1 = 1$) and optimize the gain factor for the second part (i.e., α_2). Here, the parameters $K_{P,i}$ and $K_{I,i}$ for the primary pitch actuator are designed as per the baseline controller given by NREL [5]. In this context, it should be noted that the gain scheduling is conducted based on the variation of the pitch sensitivity of the rotor with respect to different wind speeds. The secondary pitch controller also has a similar nature of pitch sensitivity variation with increasing wind speed. Hence, this study proposes that the double-pitch controller gains can be optimized as a scalar multiple of baseline controller gains. Due to this reason, the nature of variation of the parameters $K_{P,i}$ and $K_{I,i}$ is similar to that of a single-pitch turbine. The details of this multi-objective optimization are discussed in § 7.6.2 later.

7.5 Collective Double Pitch Control Using LQR Algorithm

The major contribution of this work is the development of the detailed mathematical model and, subsequently, PID and LQR algorithm for the double-pitch rotor; the latter is described in this section. A centralized multi-variate controller for the double-pitched rotor is suggested in this section, whose schematics are displayed in Fig. 7.3. This setup aims to reduce the generator speed fluctuations and subsequently affect blade vibration in flapwise, edgewise, and torsional directions. The LQR algorithm has been selected for this task due to its efficiency and optimality.

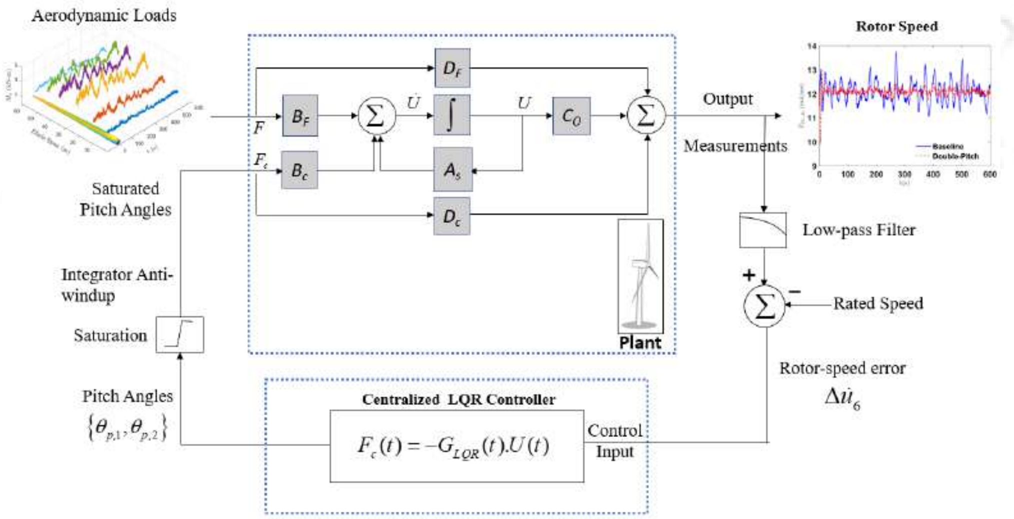

Figure 7.3: Schematic diagram of the centralized LQR Double-Pitch control system

The generator speed is used as feedback in the proposed blade-pitch control algorithm, and as advised by Jonkman et al. [5], the generator speed is filtered while minimizing high-frequency excitation using a recursive, single-pole low-pass filter with exponential smoothing. Starting from the equation of the drive-train dynamics (refer Eq. 7.16), the Eq. 7.12, and Eq. 7.14 can be substituted into Eq. 7.16 and rearranging them in the general state-space form $\dot{U}(t) = A_s.U(t) + B_c.F_c(t)$ lead to the following equation of motion for the rotor-speed fluctuation

$$\begin{aligned} \underbrace{\begin{Bmatrix} \Delta\dot{u}_6 \\ \Delta\ddot{u}_6 \end{Bmatrix}}_{\dot{U}(t)} &= \underbrace{\begin{bmatrix} 0 & 1 \\ 0 & \frac{P_0}{I_{DT}{\Omega_0}^2} \end{bmatrix}}_{A_s} . \underbrace{\begin{Bmatrix} \Delta u_6 \\ \Delta\dot{u}_6 \end{Bmatrix}}_{U(t)} \\ &+ \underbrace{\frac{1}{I_{DT}\Omega_0} \begin{bmatrix} 0 & 0 \\ \frac{\partial P}{\partial\theta_{p,1}} & \frac{\partial P}{\partial\theta_{p,2}} \end{bmatrix}}_{B_c} . \underbrace{\begin{Bmatrix} \Delta\theta_{p,1} \\ \Delta\theta_{p,2} \end{Bmatrix}}_{F_c(t)} \end{aligned} \tag{7.21}$$

In this state-space form, A_s consists of system matrices, where the generator-torque controller imposes negative damping $\frac{P_0}{\Omega_0^2}$ on the system. In contrast, B_c is the sensitivity matrix that correlates the control output $F_c(t)$ to the appropriate degrees of freedom. Now, applying LQR theory, the Algebric Riccati Equation (ARE) of matrix P_{LQR} can be formed considering weight matrices Q and R on the states and control effort, respectively, which has the following form

$$P_{LQR}.A_s + {A_s}^T.P_{LQR} - P_{LQR}.B_c.R^{-1}.{B_c}^T.P_{LQR} + Q = 0 \tag{7.22}$$

where P_{LQR} is a symmetric, and positive definite matrix. The solution for P_{LQR} is stored and used to compute the control force in forward time. As a result, the optimal solution for the control force can be expressed as

$$F_c(\theta, t) = -R^{-1}.{B_c}^T.P_{LQR}.U = -G_{LQR}(\theta, t).U(t) \tag{7.23}$$

In the above expression, G_{LQR} is the feedback gain matrix corresponding to Q, R, and the terminal penalty matrix S^f. Also, the sensitivity matrix B_c plays a crucial role in gain-scheduling due to the terms $\frac{\partial P}{\partial \theta_{p,1}}$ and $\frac{\partial P}{\partial \theta_{p,2}}$. Hence, this study proposes an optimal gain scheduling based on pitch sensitivity and weight matrices discussed in the following sections. Finally, the control output at any time step is obtained by multiplying the gain with the state vector.

7.6 Numerical Results and Discussion

This section demonstrates the numerical response simulation of a benchmark wind turbine considering aerodynamic pitching moment and bending-torsion coupling. For this purpose, the National Renewable Energy Laboratory (NREL) 5MW onshore wind turbine parameters are used [5]. Sandia National Laboratory (SNL) [229] developed the basic composite structural layup of the blade for this turbine, which met the design guidelines stipulated by International Electrotechnical Commission (IEC) standard [87] and NREL [5]. PreComp [221] is used to obtain the structural parameters, such as mass per unit length, stiffness, and elastic axis offset of the blade. The MATLAB [232] code with a full-span baseline pitch control as recommended by NREL [5] over its complete operating range is already validated in §2.3.3 of chapter 2. Hence, the details of this benchmark turbine and its validation exercise are not repeated here. Since this study uses a benchmark 5MW turbine of NREL, the blade's structural layout, shape, and other modal characteristics, i.e., mode shapes, are the same. Only a part of the blade near the tip is modified with an additional pitch angle for better control. For the purposes of the study, a length ratio γ (i.e., the ratio of the length of the blade-tip part to the overall length) of 0.1 is chosen for tuning the controller. However, the modeling described in this work is general and capable of integrating a secondary pitch at any point along the length of the blade with tailor-made blade data. However, the numerical value of the secondary actuator mass is not included in this modeling, even though the blade mass distribution can be modified to incorporate this effect where the formulation has no restriction. In this context, it may be noted that the length ratio is kept minimal to avoid significant actuator mass for the second pitch angle. Only the performance of the proposed control algorithms for the double-pitched rotor under bending-torsion coupling is presented in the following subsection. Different response quantities (e.g., u_{B1_OOP}, u_{B1_IP}, and u_{B1_T}, $\dot{u}_{Ge\_Az}$) are considered for comparison, where out-of-plane, in-plane, and torsional deformation of the blade are represented by the second subscripts OOP, IP, and T, respectively. Subscript Ge_Az is used here to represent the azimuth angle of the low-speed shaft $\dot{u}_6$, for better clarity in understanding.

The properties of the benchmark turbine are already given in Table 2.3 where subscripts ci, r, and co refer to cut-in, rated, and cut-out, respectively. The generator is assumed to be running at 94.4% efficiency in this numerical simulation, as recommended by NREL. The NREL report [5] also provides the properties of the baseline controller (i.e., collective single pitch system) and other actuator parameters (e.g., maximum and minimum pitch angle, maximum absolute pitch rate) used in this study for comparison. The details of the baseline pitch control are presented in §2.3.2 of chapter 2.

TurbSim [85] is used to model steady and turbulent wind fields for different mean values corresponding to rated, above-rated, and cut-out speeds at 90m hub height. IEC [87] Kaimal spectrum is used for wind field simulation with an onshore power-law exponent of 0.14 for steady wind and different turbulence intensities. Two sample wind fields developed in this study are shown in Fig. 7.4 for rated and cut-out conditions. Using these simulated wind fields, the response of the multi-body system is obtained and subsequently used for optimal pitch control of the proposed smart rotor.

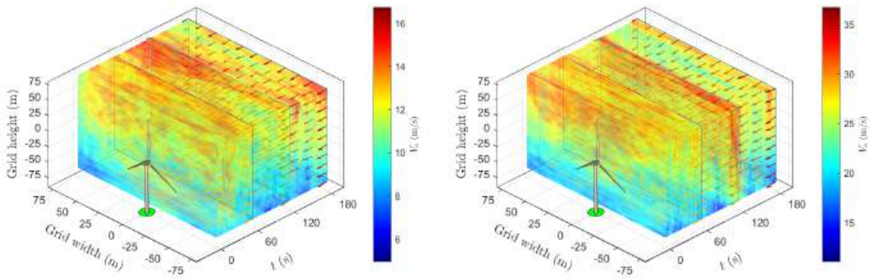

(a) (b)

Figure 7.4: Simulated wind fields for 10% turbulence at hub height for; (a) 11.4m/s (i.e., rated speed), (b) 25m/s (i.e., cut-out condition). (N.B.: Turbine diagram is not to scale)

7.6.1 Steady State Characteristics of the Double-Pitched Rotor

Studying the steady state behavior of such double-pitched systems is essential before designing the controller. Hence, this section highlights the equilibrium combination of two different pitch angles that produce the rated power (inherently the rated RPM) for different values of steady wind speed. For this purpose, a number of simulations are carried out at a given steady wind and within a range of $\theta_{p,1}$ and $\theta_{p,2}$ over the complete operating range of the double-pitch controller (i.e., rated to cut-out speed). The power law exponent of the steady wind field is taken as 0.2 for these simulations. The steady-state rpm produced by the combination of the pitch angles is shown in Fig. 7.5a-Fig. 7.5c for three different wind speed values, where the red line denotes the equilibrium pitch combination for generating the rated power.

It is notable from these figures that the range of these equilibrium pitch angles changes with increasing wind speed. Hence, it is possible to plot these equilibrium pitch angles as a function of wind speed, as shown in Fig.. 7.6. The diagram clearly demonstrates that achieving the same aerodynamic torque is possible with various pairs of $\theta_{p,1}$ and $\theta_{p,2}$ values for a given wind speed. The line highlighted in red in Fig. 7.6 denotes the equilibrium values of the base-pitch angle ($\theta_{p,1}$) when the tip-pitch angle ($\theta_{p,2}$) is zero. This marginal of the surface (i.e., $\theta_{p,1}$ as a function of wind speed) is further used in this study to schedule the controller gains in the following section. Also, using the base-pitch angle ($\theta_{p,1}$) rather than the wind speed as the basis for scheduling the controller gains offers the significant benefit of omitting the requirement of sensors to measure the inflowing wind speed directly. The controller stores the previously applied value of the base-pitch angle and schedules the gains accordingly for the next time-step, regardless of the applied tip-pitch angle and inflowing wind. This approach leads to a more straightforward solution to the controller design problem, beginning with an initial setting of zero pitch angles (i.e., both $\theta_{p,1}$ and $\theta_{p,2}$) at the rated speed.

7.6.2 Proposed Optimal Design of PID Controller Gains

The performance of the proposed optimal control algorithm above the rated speed is demonstrated in this section. NREL [5] provides the optimal values of K_P and K_I for a baseline full-blade collective pitch controller and gain correction factors for the benchmark turbine using linear perturbation analysis. The newly defined parameters α_1 and α_2 denote the distribution of K_P and K_I in a double-pitch system. For a controller operating in field conditions, the optimization problem must satisfy multiple design objectives, e.g., rotor speed fluctuation and blade vibration, among many others. Optimal control for power fluctuation does not always ensure the reduction of blade vibration if only rotor speed fluctuation is chosen as the objective function (i.e., single objective) and vice-versa. Thus, all these criteria together lead to multi-objective optimization of the parameters α_1 and α_2 in Eq. 7.20. The parametric study in this section is conducted initially to study the sensitivity of α_1 and α_2 over the primary control objectives. It is possible to optimize the two variables for the given objective functions from these sensitivity surfaces. However, the multi-objective optimization reveals that the smooth Pareto front is only obtainable when the variable α_1 is fixed at a certain value. In this context, the designer may select a different combination of α_1 to generate a different Pareto front to achieve the same goal through a different path. Also, in this study, it is proposed that the gains for the primary pitch controller are the same as the baseline controller designed by NREL, and the gains of the secondary pitch controller are a scalar multiple of the primary gains, which simplifies the optimization and design process for the double-pitched controller and avoids the risk of conflict. As

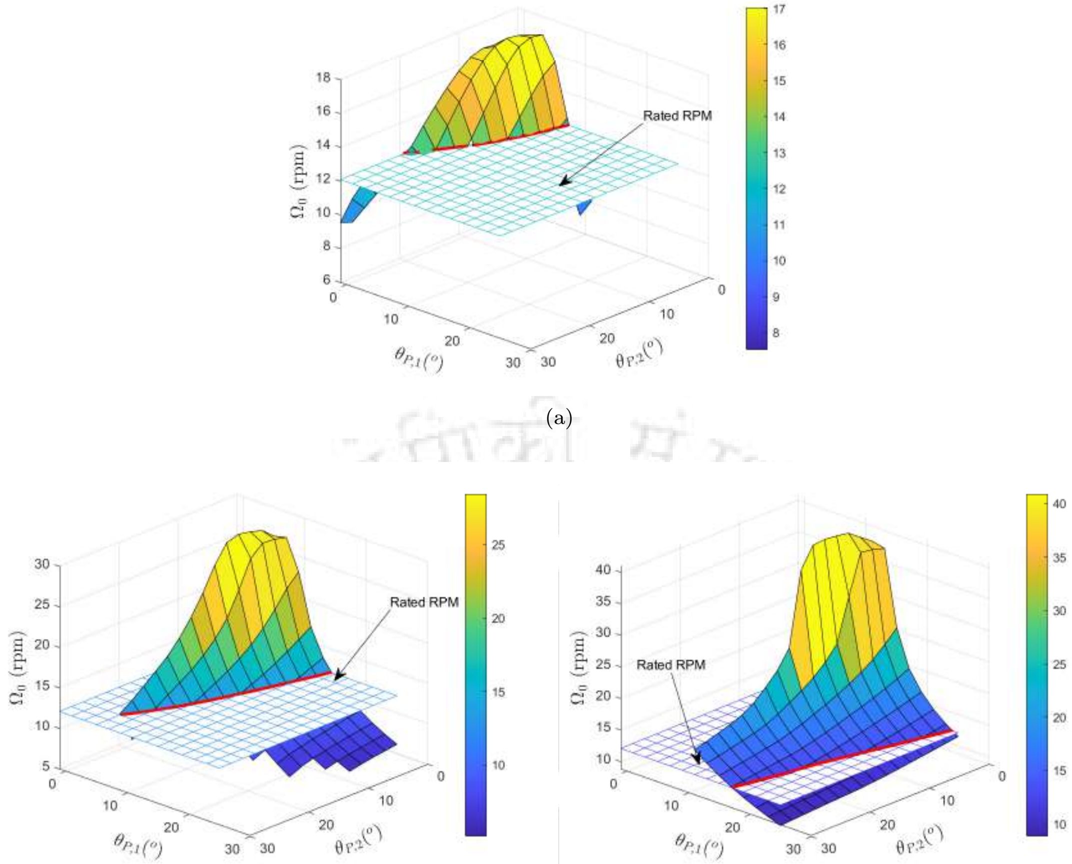

(a)

(b) (c)

Figure 7.5: Steady-state rpm of the double-pitched rotor; (a) at 13 m/s wind speed, (b) at 17 m/s wind speed & (c) at 25 m/s wind speed. (N.B.: The red line represents the set of equilibrium pitch angles required to achieve the rated power.)

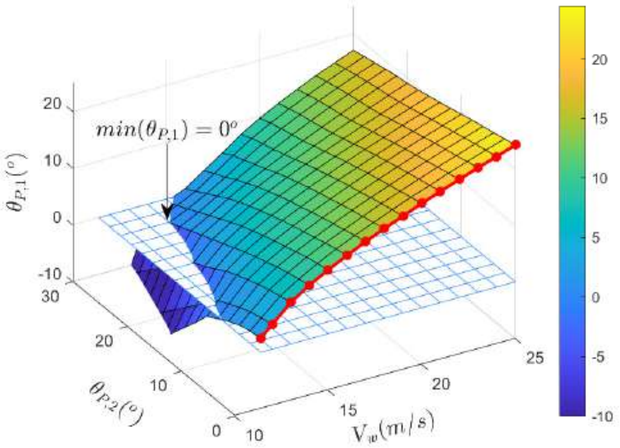

Figure 7.6: Equilibrium pitch angles plotted as a function of wind speed. (N.B.: The red line represents the set of equilibrium base-pitch angles required to achieve the rated power when the tip-pitch angle is zero.)

mentioned earlier, the proposed optimization scheme keeps the controller gains at the rotor hub the same as that of a full-blade controller (i.e., $\alpha_1 = 1$ leading to $K_{P,1} = K_P$ and $K_{I,1} = K_I$). Hence, the gains (i.e., $K_{P,2}$ and $K_{I,2}$) for the second part near the blade tip are optimized using multi-objective performance functions, with the main aim to stabilize the generator speed (which, in turn, stabilizes power output) and blade responses simultaneously. The following equation demonstrates the optimization problem solved in the proposed control strategy

$$\begin{aligned} &Obj(\alpha_1, \alpha_2) = \min\left(\left|\sigma_{\dot{u}_{GeAz}}\right|, \left|\mu_{u_{B1\_OOP}}\right|, \left|\mu_{u_{B1\_IP}}\right|\right) \\ &s.t. \quad ll \leq \alpha_1, \alpha_2 \leq ul \end{aligned} \tag{7.24}$$

where ll, and ul represent the lower and upper limit of the parameters, respectively, which may vary for α_1, and α_2. On the other hand, μ and σ denote the mean and standard deviation of the respective response quantities. In this context, it may be noted that the torsional stiffness of the blade is, in general, significantly higher compared to its flap and edgewise bending stiffness. Hence, the objective function is envisaged to be dominated by its flap and edgewise response. The mean wind speed varies from rated to cut-out condition (i.e., when the pitch controller is engaged) to replicate the ideal settings for the multiple objectives covering the complete operating range. The length ratio γ (i.e., length of the tip part to the overall blade length) is kept at 0.1 for this numerical simulation and also during the performance evaluation in subsequent sections unless stated otherwise. The impact of γ on the controller's performance is also investigated separately at the end.

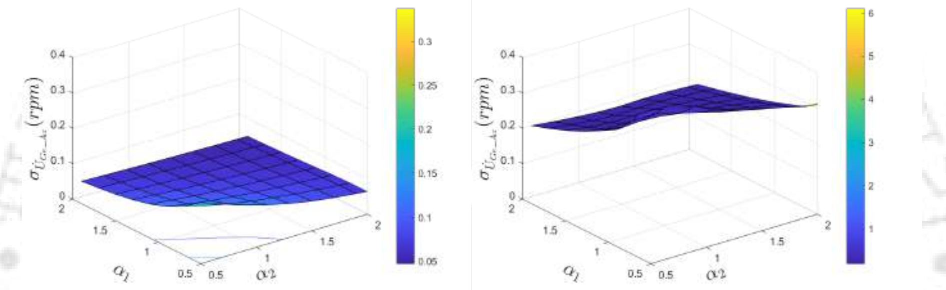

(a) (b)

Figure 7.7: Standard deviation of rotor speed; (a) 14m/s, (b) 24m/s wind speed.

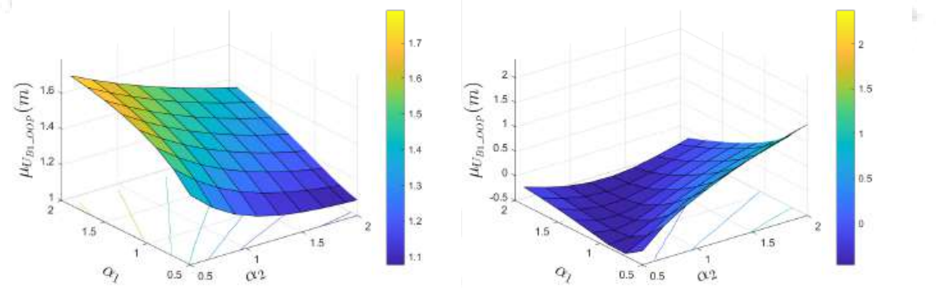

(a) (b)

Figure 7.8: Mean out-of-plane displacement of blade; (a) 14m/s, (b) 24m/s wind speed.

The variations of the three response quantities (i.e., the standard deviation of rotor speed, mean blade out-of-plane, and in-plane deflection) mentioned in Eq. 7.24 due to the changes in control parameters are presented in Fig. 7.7, Fig. 7.8, and Fig. 7.9, for two different mean wind speeds near the rated and cut-out value (i.e., 14m/s and 24m/s), respectively. These figures reveal the optimal points for three different objective functions in Eq. 7.24 (i.e., $\left|\sigma_{\dot{u}_{GeAz}}\right|, \left|\mu_{u_{B1\_OOP}}\right|, \left|\mu_{u_{B1\_IP}}\right|$) are different. Fig. 7.7 shows that rotor speed fluctuation decreases as α_2 increases. However, increasing α_2 may adversely affect the mean blade response at different mean wind speeds; (refer to Fig. 7.8 and Fig. 7.9). All these together advocated simultaneous optimization of the objective functions identified in Eq. 7.24, which leads to the Pareto optimal solution. This multi-objective optimization is solved using an in-built pattern-search algorithm [234–236] within the MATLAB optimization toolbox. The bounds in Eq. 7.24 are fixed based on the preliminary

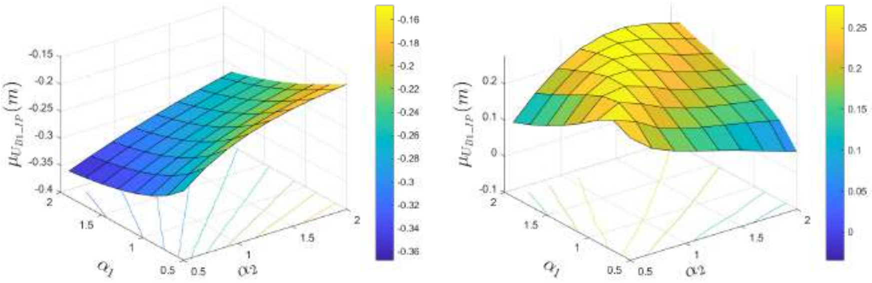

(a) (b)

Figure 7.9: Mean in-plane displacement of blade; (a) 14m/s, (b) 24m/s wind speed.

studies that ensure the effective range of parameters, which in this case are found to be 0.5 to 2. Using these bounds, the optimization problem is solved with a tolerance of 1e-4.

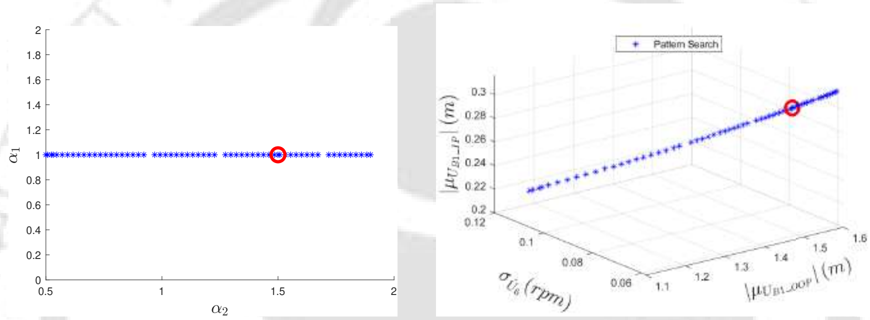

(a) (b)

Figure 7.10: (a) Pareto optimal design points control parameters and (b) Objective function values at design points for 14m/s wind speed.

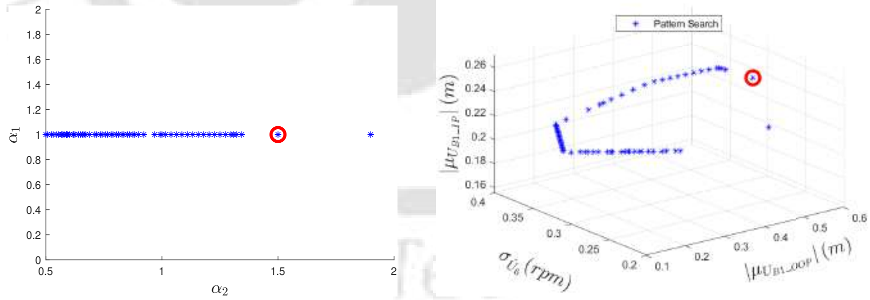

(a) (b)

Figure 7.11: (a) Pareto optimal design points control parameters and (b) Objective function values at design points for 24m/s wind speed.

Fig. 7.10a and Fig. 7.11a show the Pareto-optimal points for 14m/s, and 24m/s wind speed, respectively, while their corresponding objective function values are presented in Fig. 7.10b and Fig. 7.11b. Any point on the Pareto optimal front can be chosen for tuning the gain parameter. However, without loss of generality, a point marked red in Fig. 7.10 (and also in Fig. 7.11) corresponding to $\alpha_1 = 1$ and $\alpha_2 = 1.5$ is considered for further performance evaluation. Fig. 7.12 shows the proportional and integral gains for this optimal point as a function of $\theta_{p,1}$ and corresponding mean wind speed. It is evident that the blade tip actuator requires a higher gain than the other actuator at the rotor hub. Here, it may be noted that optimal α_2 is time-invariant, as shown in Eq. 7.20 in the proposed algorithm. It only signifies the proportional distribution of controller gains between the two actuators.

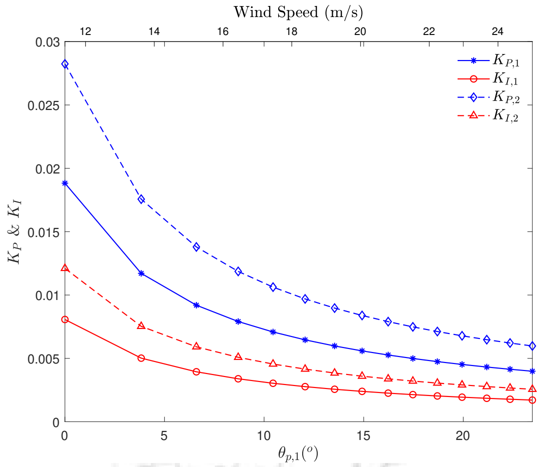

Figure 7.12: Optimal PI gains for the double-pitch system

7.6.3 PID Controller Performance Evaluation

Once the PID controller is optimized, it is further used to evaluate the performance of the proposed double-pitched rotor. As the pitch controller works above the rated speed, a reference wind speed of 17m/s is chosen for demonstration purposes. Fig. 7.13 shows the impact of the proposed double-pitched system on the rotor speed and actuator demand. Fig. 7.13a shows the rotor speed at different time instances, where the double-pitched system is compared with the baseline controller of NREL [5]. The term *baseline* refers to the full-blade collective pitch controller presented in §2.3.2.2. The standard deviation (σ) of this time history represents the rotor speed variation, which ultimately reflects power fluctuation. The value of σ for a full-blade collective pitch control is found to be 0.207 rpm, while the same parameter for the double pitch system is 0.124 rpm, indicating a reduction of 40.38%. This reduction of rpm variation and subsequent power fluctuation by the double-pitched system with respect to the baseline controller is significant where the increased pitch angle of the tip part reduces the aerodynamic load as a natural consequence. It is observed that the pitch demand for the first segment is also reduced compared to a full blade baseline controller, as shown in Fig. 7.13b. Here it may be noted that the maximum pitch angle imposed by the baseline control in the NREL report [5] is 17.25^o, which is reduced to 12.13^o at the hub, signifying a 29.68% reduction of the primary actuator demand. Fig. 7.13c shows the pitch initiated by the actuator for the blade tip, where the maximum pitch demand is 18.19^o in the proposed system.

Fig. 7.14 shows the blade response due to turbulent wind for two different controllers. This figure shows the response reduction in the out-of-plane, in-plane, and torsional direction of the blade. The horizontal line in Fig. 7.14a and Fig. 7.14b represent the mean response, which demonstrates the impact of the proposed control strategy. The mean response along the out-of-plane and in-plane directions are found to reduce by 67.68% and 76.78%, respectively. The absolute peak responses along these DOFs are reduced by 31.47%, and 24.50%, respectively. Besides lateral deflection, performance along the torsional DOF is also improved, as shown in Fig. 7.14c, where an 8.55% reduction of peak value is observed. Hence, it is evident that the double-pitched system improves blade performance in addition to its main aim for power regulation.

Here, it may be noted that higher wind speed and turbulence intensity generally increase rotor speed fluctuation, affecting power output. Thus, a sensitivity analysis is carried out to investigate it further. Table. 7.1 shows the performance of the double-pitched system for different flow conditions. In general, rotor speed fluctuation increases with mean wind speed and turbulence intensity. However, the proposed smart rotor offers 27.78% more control of rotor speed fluctuation even at higher mean wind speed (i.e., 21 m/s) with significant turbulence (i.e., 15%) on top of the performance offered by the baseline controller. In addition to this remarkable performance, the percentage reduction of blade vibration consistently increases with the mean wind speed and turbulence level. This is due to the fact that aerodynamic load (which increases towards the free end) is significantly reduced by the optimal tuning of the outboard pitch angle $\theta_{p,2}$, resulting in less blade vibration. These results indicate the superiority of the double-pitched system with respect to the baseline option at different speeds and turbulence intensities.

Further, the performance envelope of this controller is evaluated for different wind speeds at higher turbulence intensity (i.e., 15%). Fig. 7.15a portrays the performance of the double-pitched system over the complete operating range of the turbine. All three design parameters are significantly reduced by the

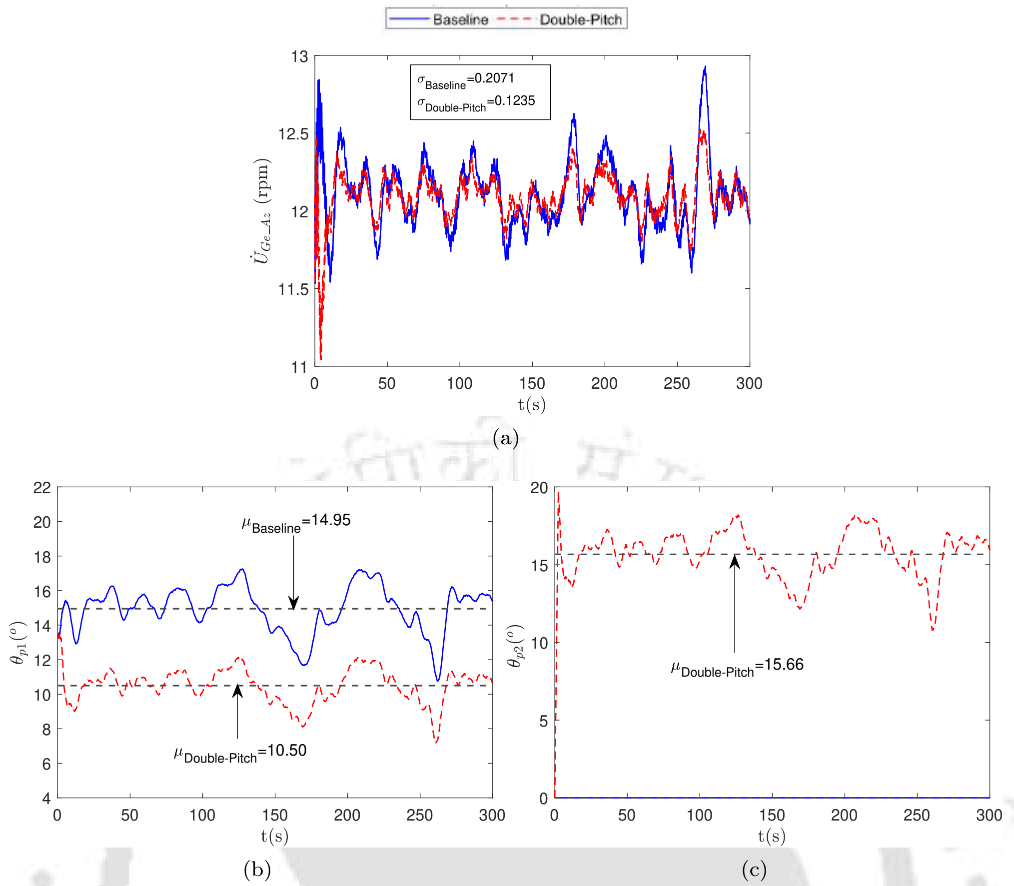

Figure 7.13: Response of low-speed shaft and blade pitch angles at 17 m/s wind speed with 10% turbulence at hub height; (a) Low-speed shaft rotational speed, (b) base-pitch & (c) tip-pitch. (N.B.: The '–' line represents the mean value of the corresponding time history.)

Table 7.1: Response due to difference in turbulence at different wind speeds and corresponding percentage reduction

Wind Speed (m/s)	Turbulence Intensity (%)	Baseline			Double-Pitch		
		$\sigma_{\dot{U}_{Ge\_Az}}(rpm)$	$\mu_{U_{B1\_OOP}}$ (m)	$\mu_{U_{B1\_IP}}$ (m)	$\sigma_{\dot{U}_{Ge\_Az}}(rpm)$	$\mu_{U_{B1\_OOP}}$ (m)	$\mu_{U_{B1\_IP}}$ (m)
14	5	0.080	2.017	0.399	0.045 [43.91]	1.430 [29.12]	0.255 [36.20]
	10	0.160	1.954	0.393	0.091 [42.97]	1.348 [31.01]	0.242 [38.58]
	15	0.245	1.898	0.385	0.141 [42.53]	1.277 [32.71]	0.227 [41.18]
17	5	0.104	1.359	0.353	0.062 [39.86]	0.481 [64.61]	0.096 [72.68]
	10	0.207	1.304	0.342	0.123 [40.38]	0.421 [67.68]	0.080 [76.78]
	15	0.311	1.248	0.330	0.184 [40.87]	0.387 [68.98]	0.065 [80.31]
21	5	0.142	0.770	0.245	0.104 [27.28]	0.051 [93.35]	0.082 [66.38]
	10	0.283	0.715	0.228	0.205 [27.51]	0.097 [86.46]	0.083 [63.79]
	15	0.424	0.657	0.210	0.306 [27.78]	0.140 [78.69]	0.083 [60.28]

N.B.: The values in [.] refer to percentage reduction with respect to baseline control.

proposed strategy. The highest reduction (i.e., 42.53%) of rotor speed variation is observed at 14m/s wind speed. In contrast, the maximum reduction of blade vibrations (i.e., 45.33% in out-of-plane and 26.1% in the in-plane direction) is observed at 22m/s mean wind speed. Finally, the study continues to analyze the effect of length ratio γ on the controller performance, which is shown in Fig. 7.15b. This bar diagram shows the percentage reduction of the rotor speed fluctuations over the complete operating range for different γ. Here, it should be noted that the controller is designed in such a way that it has to be re-tuned for each length ratio. However, the variation in the optimal value of α_2 is observed to be very insignificant in the range of the selected length ratio γ (0.07 - 0.17), and hence, it is not reported separately here. It can be observed that the controller performance improves as γ increases for obvious reasons. However, a higher length ratio is not recommended as the weight of the tip part increases, which in turn demands a heavy actuator for α_2.

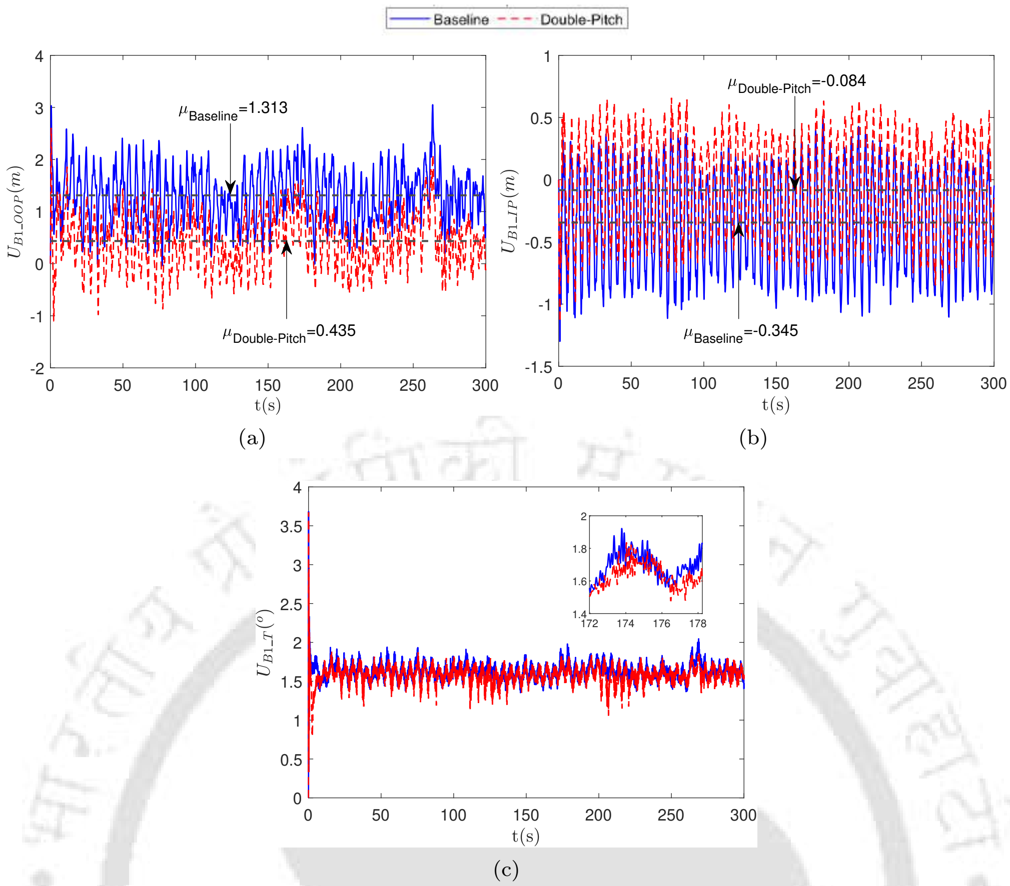

Figure 7.14: Response of the blade at 17 m/s wind speed with 10% turbulence at hub height; (a) out-of-plane, (b) in-plane & (c) torsional. (N.B.: The '–' line represents the mean value of the corresponding time history.)

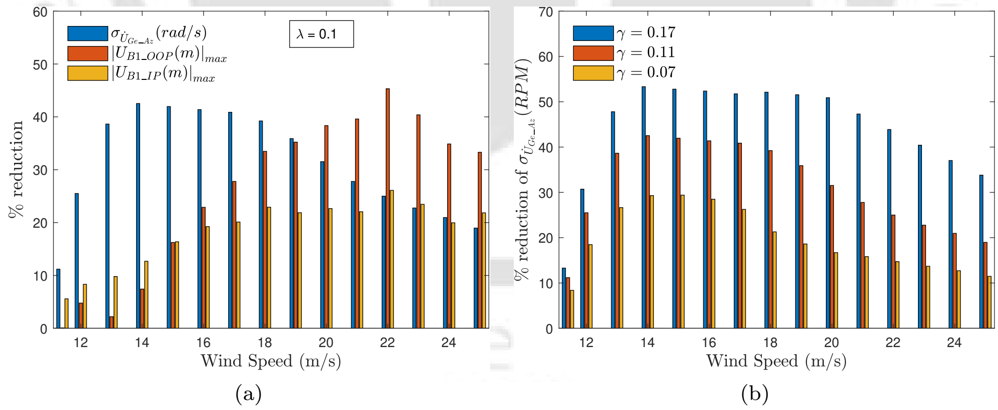

Figure 7.15: Performance characteristics of the proposed controller for 15% turbulence at hub height (a) different DOFs for $\lambda = 0.1$ & (b) rotor speed fluctuation for different length ratio. N.B. % reduction is defined with respect to the baseline controller.

Here, it may be noted that the rationale behind the selection of $\gamma = 0.17$ is that the mass ratio (i.e., mass of the tip part to the overall blade mass) remains within 5%. The same ratio for $\gamma = 0.1$ is 2.9%, which is recommended in this study to keep the weight of the outward part of the rotor minimum.

Based on these results, it can be inferred that the PID-controlled double-pitched rotor has a considerable positive impact on the power regulation and dynamic response of the blade when it is optimally tuned, as proposed in the study. However, the performance of the double-pitched rotor can be further improved by the weight-optimized LQR algorithm, which is discussed in the following subsections.

7.6.4 Optimal Gain-Scheduling for the LQR Double-Pitch Controller

As discussed in the earlier section, the LQR gain matrix G_{LQR} can be estimated once the weight matrices (Q and R) and the sensitivity of aerodynamic power to the blade pitch angles, i.e., $\frac{\partial P}{\partial \theta_{p,i}}$ are known. The blade-pitch sensitivity of a rotor is an aerodynamic property that is affected by wind speed, rotor speed, and blade-pitch angle. It is estimated using different steady wind speeds in the operating region of the pitch controller, keeping rated rotor speed (12.1 rpm) constant, and at the corresponding first blade pitch angle ($\theta_{p,1}$) that generate the rated power ($P_0 = 5.296610$ MW). The initial operating point of the outboard pitch angle ($\theta_{p,2}$) is kept at zero during this optimization for all wind speeds. Unless otherwise specified, the length ratio γ (i.e., length of the tip component to the entire blade length) is maintained at 0.1 for this simulation and also throughout the performance analysis in the following sections. The reason behind this restriction is to keep the mass ratio (i.e., the mass of the tip part to the entire blade mass) under 3%. However, the methodology for the optimal LQR controller gains of a double-pitched rotor can be extended for a different length ratio, if need be. The analysis of determining the pitch sensitivity involves perturbing the rotor-collective blade-pitch angles (both $\theta_{p,1}$ and $\theta_{p,2}$) at each operating point and determining the subsequent fluctuation in aerodynamic power using a central-difference-perturbation technique. The results are presented in Table 7.2.

Table 7.2: Blade Pitch Sensitivity

Wind Speed (m/s)	**Base Pitch Angle** (^{o})	$\frac{\partial \mathbf{P}}{\partial \theta_{\mathbf{p},\mathbf{1}}}$ (watt/rad)	$\frac{\partial P}{\partial \theta_{p,2}}$ (watt/rad)
11.4 (Rated)	0.00	4.07E+06	2.78E+06
12	3.83	-1.36E+07	-9.96E+05
13	6.60	-2.65E+07	-3.73E+06
14	8.70	-3.54E+07	-5.67E+06
15	10.45	-4.29E+07	-7.26E+06
16	12.06	-4.98E+07	-8.67E+06
17	13.54	-5.62E+07	-9.97E+06
18	14.92	-6.25E+07	-1.13E+07
19	16.23	-6.88E+07	-1.26E+07
20	17.47	-7.47E+07	-1.36E+07
21	18.70	-8.04E+07	-1.46E+07
22	19.94	-8.67E+07	-1.61E+07
23	21.18	-9.35E+07	-1.74E+07
24	22.35	-9.99E+07	-1.84E+07
25 (Cut-out)	23.47	-1.06E+08	-1.95E+07

For classical LQR-based pitch control, the weighting matrix $Q = \begin{bmatrix} Q_{11} & 0 \\ 0 & Q_{22} \end{bmatrix}$ is a diagonal matrix chosen to give more importance to controlling rotor speed fluctuations. The parameters Q_{11} and Q_{22} can heavily influence the performance of the LQR controller. Hence, they are further optimized in this study using a performance function given below

$$\begin{aligned} &Obj(Q_{11}, Q_{22}) = \min\left(\sigma_{\dot{u}_6}\right) \\ &s.t. \quad Q_{11} \in \{0.02 \le Q_{11} \le 0.6\} \\ &\qquad Q_{22} \in \{0.2 \le Q_{22} \le 1.6\} \end{aligned} \tag{7.25}$$

where $\sigma_{\dot{u}_6}$ represents the standard deviation of rotor speed from its rated value. The lower and upper limits of Q_{11} and Q_{22} in Eq. 7.25 are selected following a thorough sensitivity analysis to find out the range of the parameters where the proposed controller is most effective. For this purpose, the weight matrix R (the weight on control effort) is kept as $R_{11} = 1$ to ensure lesser importance on the control effort than the state. The variations of the response quantity (i.e., $\sigma_{\dot{u}_6}$) due to the changes in control parameters Q_{11} and Q_{22}

are presented in Fig. 7.16 for the rated wind speed with two different turbulence intensity levels, i.e., 10% (Fig. 7.16a) and 15% (Fig. 7.16b), where the minima of the response surface are marked in red. It is observed

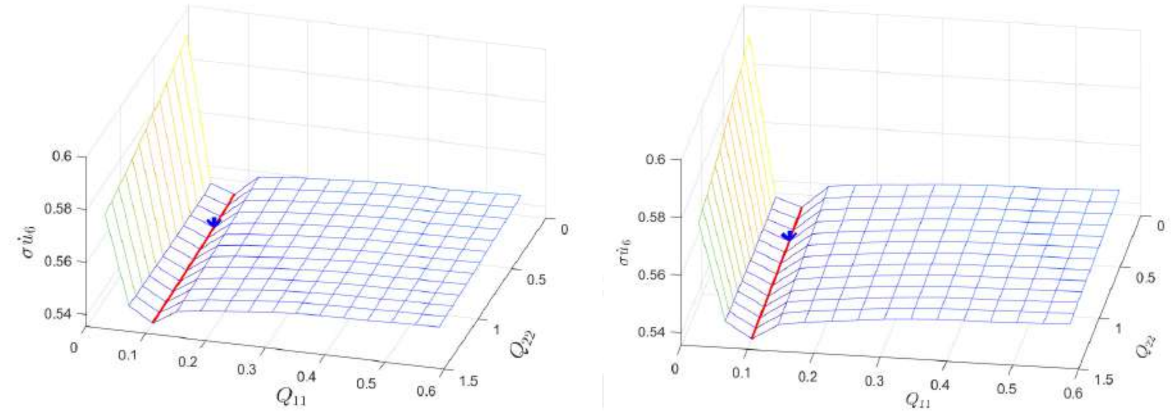

(a) (b)

Figure 7.16: Influence of $[Q]$ on the standard deviation of rotor speed for rated wind; (a) for turbulence level 10% & (b) for turbulence level 15%

that the change in the turbulence intensity levels does not influence the optimal weight parameters, and the position of the minimal line remains the same for both cases. Hence, any point on this minimal line can be chosen for tuning the gain matrix. However, for further evaluation of the controller performance, the point corresponding to $Q_{11} = 0.1$ and $Q_{22} = 0.5$ (marked in blue in Fig.7.16) is chosen to tune the LQR controller. With these parameters of the weight matrix Q, the penalty on the control effort R_{22} is optimized for the double-pitched case. For this purpose, the value of R_{11} is kept at 1, and R_{22} is varied within a predefined range of $0.05 - 0.2$. The variation of rotor speed fluctuation is measured for different levels of mean wind speed, as shown in Fig. 7.17. It is observed that a lower penalty near the value 0.06 (i.e., marked with the red line in Fig. 7.17) on the secondary pitch actuator improves the controller's performance in most of the cases. However, near the cut-out wind speed, it leads to over-saturation of the pitch actuator. The time

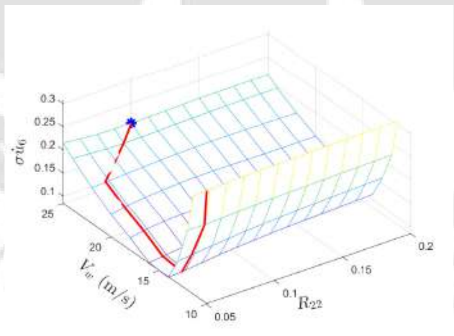

Figure 7.17: Influence of R_{22} on the standard deviation of rotor speed

history plot of the applied pitch rate at 25m/s mean wind speed for the value of $R_{22} = 0.06$ is shown in Fig. 7.18. Additionally, the actuator saturation limit of $8^o/s$ is also marked in the same figure. Under these conditions, the commanded pitch rate reaches the actuator limit in multiple instances, which subsequently affects the control performance. On the other hand, the minima of $\sigma_{\dot{u}_6}$ is observed for the value of $R_{22} = 0.1$ considering 25m/s mean wind speed (i.e., cut-out value). Hence, the optimal value of $R_{22} = 0.1$ (marked in blue in Fig. 7.17) is selected here for tuning the double-pitch controller gains. Finally, the gain matrix $G_{LQR}(\theta, t)$ is formed with the optimized weight parameters and pitch sensitivity at each operating point. These optimized LQR gains are then used in the simulation to evaluate the effectiveness of the proposed configuration, which is presented in the section below.

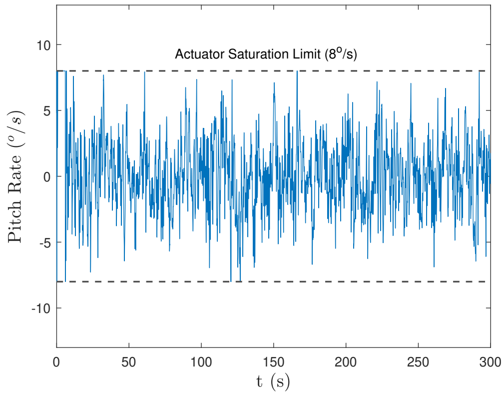

Figure 7.18: Applied pitch rate at 25m/s wind speed for $R_{22} = 0.06$

7.6.5 LQR Double-Pitch Controller Performance Evaluation

This section presents the performance of the proposed control algorithm for a double-pitched rotor. Comparison is made between different response quantities (e.g., U_{B1_OOP}, U_{B1_IP}, $\dot{U}_{Ge\_Az}$), where the second subscripts OOP and IP represent out-of-plane and in-plane direction, respectively. The subscript Ge_Az represents the azimuth angle of the generator, i.e., the low-speed shaft. Before the performance of the proposed controller is investigated, the optimized parameters are selected using the optimization scheme mentioned in the previous section. These parameters are utilized to evaluate the performance of the double-pitched rotor compared to a single-pitch rotor with the same LQR algorithm and the baseline single-pitch controller given in NREL report [5]. A reference wind speed of 16m/s is selected to assess performance, as the pitch controller operates beyond the rated speed. Fig. 7.19 illustrates the blade response to turbulent wind, comparing the double-pitched system to NREL's baseline controller. This figure demonstrates the effectiveness of the proposed method in decreasing out-of-plane and in-plane blade vibrations, with peak responses along these degrees of freedom reduced by 36.02% and 34.28%, respectively, with respect to the baseline control. Here, it can be observed from Fig. 7.19c that the double-pitch system has little impact on the blade-torsional response, as also expected from the formulation. It can be inferred that the reduction of aerodynamic loads by applying a second pitch at the blade tip neither improves nor adversely affects blade-torsional response. Hence, the reduction in the mean response of this DOF is observed to be only about 1%. These response reductions are expected to benefit other associated degrees of freedom, such as the torsion of the low-speed shaft. The peak value of this response of the drive train is found to be reduced by 3.67% more in the case of a double-pitched rotor when compared to its single-pitch version. However, the nature of the time history is similar to the single-pitch case, and hence it is not shown here to avoid repetition.

Finally, Fig. 7.20 illustrates the effect of the controller on the rotor speed and actuator demand. The rotor speed fluctuation is reduced by 65.44% compared to the baseline controller when the proposed double-pitched rotor is used (refer to Fig. 7.20a). The reduction in rotor speed variation is bound to affect the power fluctuation. Fig. 7.20b displays the instantaneous power produced by the turbine, where a 20.83% reduction in the standard deviation is observed. The decrease in rotor speed fluctuation, in turn, reduces stresses in the electrical equipment as a natural consequence, and hence, it is bound to decrease downtime for maintenance.

Fig. 7.20c and Fig. 7.20d show the pitch induced by the hub and blade-tip actuators, respectively. This regulation of pitch aids in stabilizing power output fluctuations, thereby enhancing the lifespan of the gearbox and other electrical and mechanical components. The maximum pitch angle proposed by the baseline controller in NREL report [5] is further reduced from 17.09^o to 12.34^o at the hub, which indicates a 27.79% decrease in primary actuator demand. These numerical values indicate that the primary actuator's pitch demand is lower with the proposed method than with a full-blade single-pitch controller. This is due to the fact that the double-pitched controller reduces aerodynamic loads significantly. However, the blade tip portion (i.e., secondary pitch) requires a maximum pitch angle of 24.13^o in the proposed double-pitch architecture. As the blade-tip region is relatively small, a slightly higher pitch angle at this location does not significantly impact the overall actuator demand. In general, this arrangement results in a more responsive and efficient control system.

Additionally, the controller's performance envelope is assessed across various wind speeds and turbulence intensity levels. The results of this evaluation are presented in Table 7.3, which highlights the performance

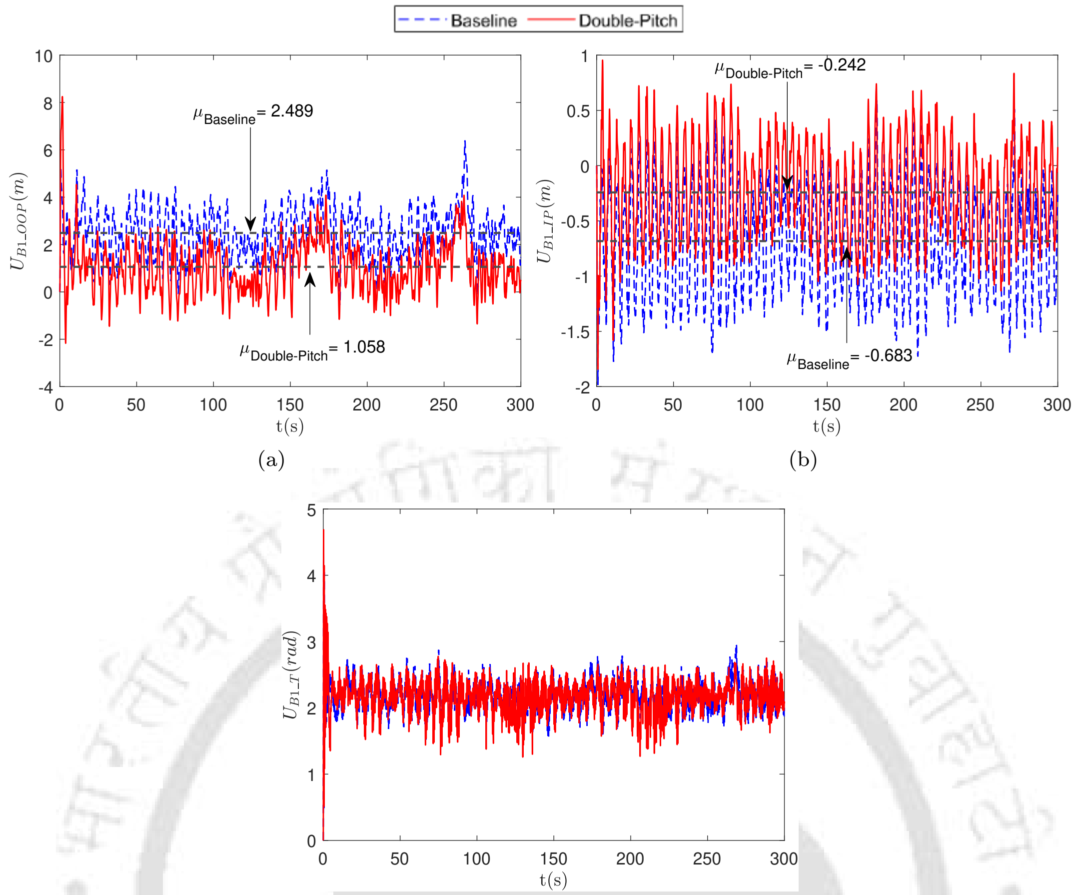

Figure 7.19: Response of the blade at 16 m/s wind speed with 15% turbulence; (a) out-of-plane, (b) in-plane & (c) torsion

Table 7.3: Performance evaluation of the proposed controller under different operating conditions

Wind Speed (m/s)	Turb. Intensity (%)	% reduction of different response quantities compared to baseline controller					
		LQR Single-Pitch			LQR Double-Pitch		
		$\mu_{U_{B1\_OOP}}$	$\mu_{U_{B1\_IP}}$	$\sigma_{\dot{U}_{Ge\_Az}}$	$\mu_{U_{B1\_OOP}}$	$\mu_{U_{B1\_IP}}$	$\sigma_{\dot{U}_{Ge\_Az}}$
11.4 (Rated)	5	-0.08	-0.16	-0.64	0.48	0.91	2.94
	10	-0.17	-0.17	6.33	2.99	5.56	8.12
	15	-0.31	-0.29	5.99	4.87	9.50	7.91
16	5	0.04	-0.03	56.24	55.21	60.02	64.41
	10	0.01	-0.19	56.26	58.05	63.10	64.94
	15	0.05	-0.41	56.22	59.18	65.29	65.44
20	5	0.53	0.46	61.81	68.38	85.13	62.66
	10	0.86	0.56	61.90	65.54	84.06	63.64
	15	1.32	0.74	61.89	61.72	82.56	63.97
25	5	2.64	3.65	60.31	11.00	98.98	60.14
	10	3.92	5.55	60.43	9.15	94.77	60.68
	15	5.31	7.74	60.42	7.96	88.65	60.83

of the double-pitched rotor in terms of critical performance parameters. The values in the table correspond to the absolute mean and standard deviation (i.e., $|\mu|$ and σ) of the response quantities indicated by the subscripts. It can be observed from this table that the proposed gain-scheduled LQR algorithm outperforms the classical baseline controller and PID controller in all the cases in terms of controlling rotor speed fluctuation (i.e., $\sigma_{\dot{U}_{Ge\_Az}}$). Furthermore, adding a second pitch angle at the blade tip improves the performance compared to a full-span single-pitch controller. The proposed smart rotor utilizes differential pitch angles

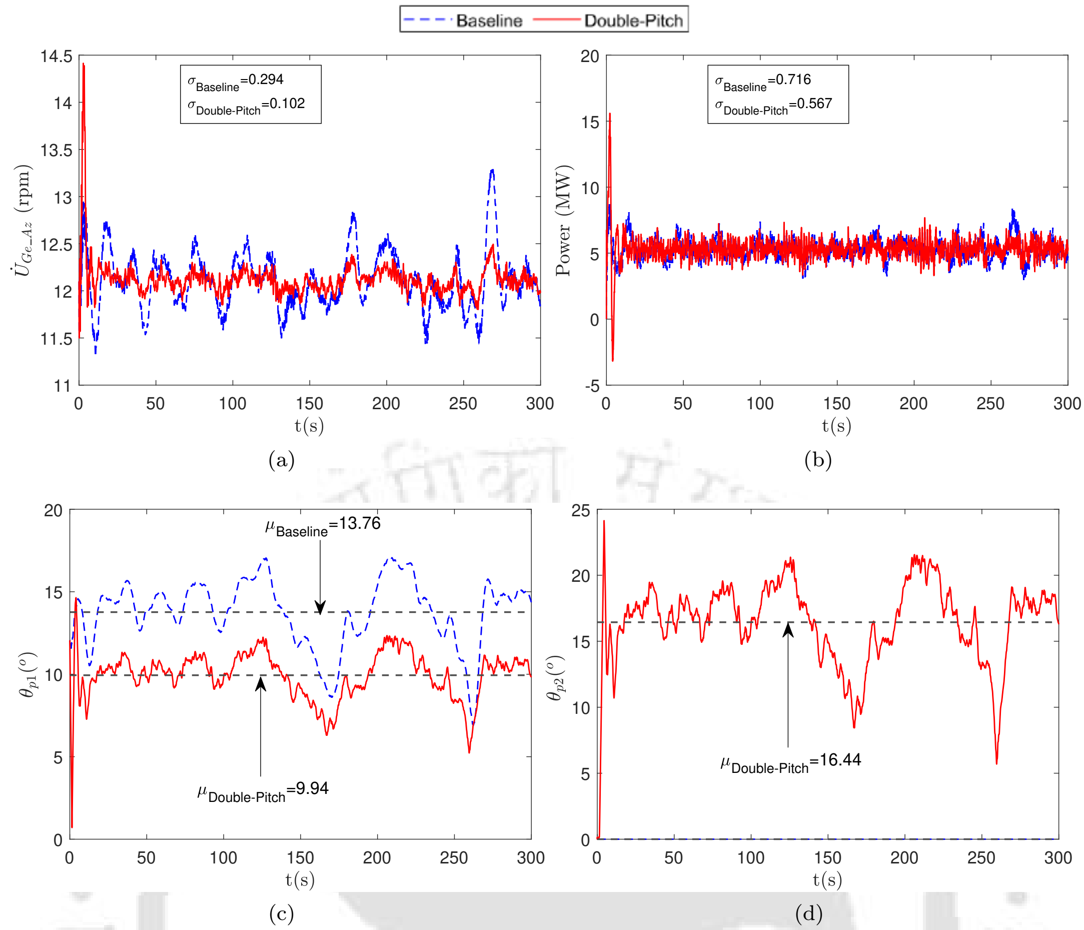

Figure 7.20: Response of low-speed shaft and blade pitch angles at 16 m/s wind speed with 15% turbulence; (a) Low-speed shaft rotational speed, (b) Generated power,(c) base-pitch & (d) tip-pitch

to decrease aerodynamic loads, resulting in varying performance along different degrees of freedom with increasing wind speed.

According to the table, the proposed rotor demonstrates optimal control of rotor speed fluctuations at a mean wind speed of approximately 16 m/s, with a reduction of 56.22% compared to the baseline response. This reduction indicates the impact of the proposed controller on power regulation. Furthermore, the mean out-of-plane blade response exhibits similar behavior, with a maximum reduction of 68.38% occurring at a wind speed of 20 m/s. The mean blade response in the in-plane direction demonstrates a maximum reduction of 98.98% near the cut-out value. The controller's performance across different degrees of freedom is also influenced by turbulence intensity levels. Here, it should be mentioned that the controller is designed and optimized using only the objective function of rotor speed errors, whereas the reduction of blade responses occurs as a secondary effect due to reduced aerodynamic loads. Hence, the controller becomes more efficient in suppressing rotor speed fluctuations as the turbulence intensity increases. Based on this investigation, it is clear that using an LQR controller in combination with a double-pitched rotor produces impressive results. At first, it successfully reduces power fluctuations, improving the system's overall performance and stability. Secondly, the double-pitched rotor coupled with LQR control affects the overall dynamic response, improving aerodynamic performance and damping characteristics. These are possible due to the rotor's improved design and intelligent pitch adjustment. As a result, the turbine can maintain structural integrity and operational efficiency owing to the better reactivity of the smart rotor to external disturbances.

7.7 Summary

The multi-body dynamics of a double-pitch rotor and its optimal tuning in controlling different turbine responses are the main contributions of this work. The model developed in this study is generic and considers coupling between bi-directional bending and torsional vibration while modeling the double-pitched rotor.

The effects of different pitch angles under a 3D turbulent wind field are modeled for proper aerodynamic damping and load estimation, which, in turn, influence the rotor speed and blade vibration. The aero-servo-elastic model is developed using Kane's approach, and optimal PID and LQR control strategy is designed considering multiple performance objectives. Different aerodynamic conditions are simulated, ranging from the rated to cut-out wind speed. The numerical results presented in this paper show substantial improvement in overall turbine performance, particularly in terms of power regulation compared to the existing baseline controller. The most important findings from this study are summarised below.

- Development of a High-fidelity model of a horizontal axis wind turbine with a double-pitched rotor in a multi-body dynamic framework is the main theme of this chapter. Proper aero-elastic simulation for the complete system (i.e. interactions between the rotor, drive-train, and tower) with collective double-pitch control of the blade experiencing bending-torsion coupling is first time attempted to demonstrate the advantage of this smart rotor. The model can accurately predict the behavior of the double-pitched rotor under varied operating situations, which is critical for the design of different structural, and mechanical components of the turbine. Overall, this study offers insightful information about complex wind turbine modeling and control system architecture that are essential for safe and sustained operation and power generation.

- The PID controlled double-pitched system proposed in this study offers a significant enhancement of rotor performance than a collective full blade baseline pitch controller available in literature [5]. The optimal tuning following the proposed methodology can provide more than 40% reduction of rotor speed fluctuation with respect to the baseline controller over the operating range of the turbine besides significant blade vibration control, which is an additional benefit.

- Sensitivity analysis reveals that the length ratio (γ) is one of the critical parameters for a double-pitched system. Although the rotor speed stabilizes more with an increased length ratio, it may not be feasible beyond a realistic limit. With this in view, $\gamma = 0.1$ is recommended in this study.

- The LQR controlled double-pitched rotor system offers further enhancement of turbine performance than a single full-blade pitch controller and PID double-pitch controller. The optimal design of the proposed method can provide more than 50% reduction of rotor speed fluctuation, which ultimately regulates power production. Subsequently, the structural responses along different DOFs are also improved, which is an additional benefit.

- Choosing optimal controller weightage is a critical aspect of designing an LQR pitch controller. It is observed that the proposed gain scheduled LQR algorithm outperforms the baseline controller available in the literature [5], even in a single-pitch configuration. The increased performance is achieved by appropriate actuation of pitch angles, ultimately reducing the effect of aerodynamic turbulence.

- Although not reported in this study, the blade fatigue life and reliability are bound to increase as a natural consequence due to reduced vibration (and subsequently stress/strain level) along different blade DOFs as reported in other literature [161, 267]. A detailed study of the effect of the proposed controller on these derived quantities can be a further extension of the present work.

Finally, to summarize the work, it can be stated that the proposed optimization methodology of the LQR-controlled double-pitched rotor has demonstrated high efficiency. The proposed approach particularly performs well in controlling rotor speed fluctuation (subsequently power generation) and structural vibration of the blades simultaneously. The above observation clearly highlights the superiority of the proposed method over a conventional single-pitch baseline controller in the operation of modern horizontal-axis wind turbines.

Chapter 8

Power Regulation and Vibration Control of Floating Offshore Wind Turbine with Wavelet-LQR based Double-Pitched Rotor

8.1 Introduction

This chapter introduces a wavelet-based Linear Quadratic Regulator (LQR) control strategy for double-pitched rotor systems of spar-type floating offshore horizontal axis wind turbines. A comprehensive aero-servo-elastic model incorporating bending-torsion coupling is developed to assess the performance of the proposed controller under combined turbulent wind and wave loading. The weight matrices of the classical LQR algorithm are optimized using a nonlinear optimization scheme. Additionally, frequency-dependent gain scheduling is proposed using wavelet transform where the analytic Morse wavelet serves as the basis function. The resulting LQR algorithm operates in the time-frequency domain and solves scale-dependent Algebric Riccati Equation (ARE) to determine optimal gains. Numerical simulations demonstrate the superior performance of the proposed gain scheduling compared to the classical LQR approach. The effectiveness of the algorithm is evaluated across various flow conditions and wind-wave misalignments, with benchmark results used for performance comparison.

8.2 Mathematical Model of Spar-Type Floating Wind Turbine (FWT) with a Double-Pitched Rotor

A horizontal-axis wind turbine can be modeled as a group of multiple bodies interacting with one another either in Lagrangian framework [161] or using Kane's approach [12]. In this study, the second option is utilized, which employs 25 degrees of freedom (DOFs) to simulate the entire system with a double-pitched rotor. These DOFs represent the spar, tower, nacelle, drive-train, and blades, i.e.,

$$u = \{\underbrace{u_1, ...u_6,}_{Spar}\underbrace{u_7, ...u_{10},}_{Tower}\ \underbrace{u_{11},}_{Nacelle}\ \underbrace{u_{12}, u_{13},}_{DriveTrain}\ \underbrace{u_{14}, ...u_{25}}_{Blades}\}^T \tag{8.1}$$

Table 4.1 in chapter 4 provides details of the degrees of freedom (DOFs) and coordinate systems employed in this study. The fixed global reference frame $\hat{x}$ is situated at the base of the tower for the complete system. In addition to the specified reference frame, each component has its own global and local coordinates as listed in Table 4.1 and illustrated in Fig. 8.1. The offshore spar-supported turbine considered in this study

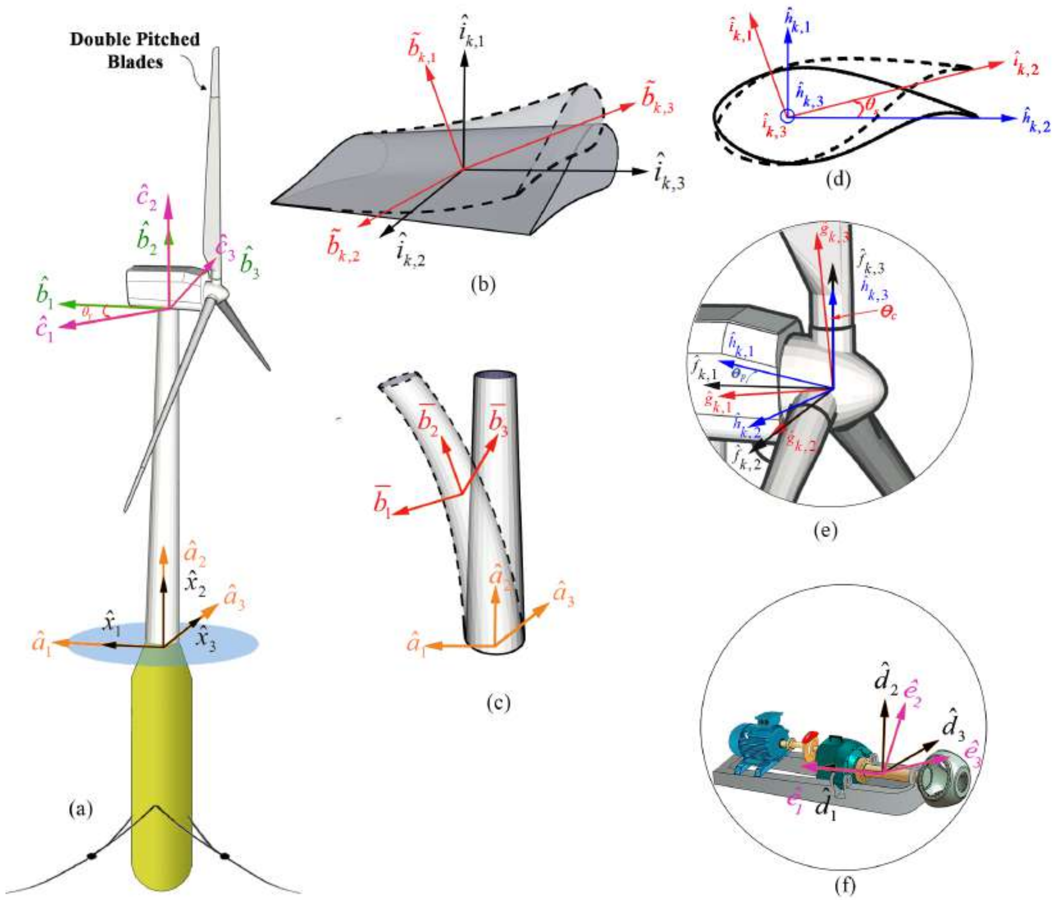

Figure 8.1: Schematic diagram of Offshore HAWT and associated coordinates; (a) combined multi-body system, (b) deformed blade element, (c) deformed tower, (d) local twist of blades, (e) cone and pitch & (f) drive-train

experiences rigid body rotation at the base. Therefore, reference system $\hat{a}$ is utilized to account for this motion. The nacelle coordinate system $\hat{c}$ is located at the centre of the tower top base plate, but its orientation changes with the nacelle-yaw angle (θ_Y). The coordinate system for the low-speed shaft $\hat{d}$ has its origin at the intersection of the shaft and tower centre line, and it is tilted and skewed with the low-speed shaft. The coordinate system $\hat{e}$ is fixed at the same origin and orientation as $\hat{d}$ but azimuthally rotates with the low-speed shaft, thereby accounting for the rotation of the blades. The blade coordinate system has a subscript k to represent the blade number (e.g., $\hat{g}_k$ for $k = 1, 2, 3$) with a secondary subscript along the three orthogonal directions for a specific blade. It also includes a global coordinate system $\hat{f}_k$, which starts at the rotor apex and passes through the blade's centroidal axis. This coordinate system is also coned (i.e., by angle θ_C) and pitched (i.e., by angle θ_p) to form two other coordinate systems $\hat{g}_k$ and $\hat{h}_k$, respectively. The twisted coordinate system $\hat{i}_k$ is placed at each blade node and aligned with its structural twist (θ_s). Additionally, two extra elemental coordinate systems are employed for aeroelastic simulation, namely the blade element coordinate ($\tilde{b}_k$) and fixed airfoil reference for aerodynamic loads ($\hat{a}_{e_k}$). This study adopts a fixed airfoil reference frame ($\hat{a}_{e_k}$) to determine aerodynamic loads (i.e., normal/tangential to the rotor plane and torsional moments). These reference frames are parallel to the blade-coned reference frame ($\hat{g}_k$) in three orthogonal directions. The primary difference between these two reference frames is that the fixed airfoil reference frame ($\hat{a}_{e_k}$) is located at each node of a specific blade k, which undergoes different rotations during vibration. Therefore, different transformation matrices are used at each node, whereas the reference frame $\hat{g}_k$ is global for the whole blade. Suitable transformations are employed to convert between these coordinates (i.e., local to global).

The position vectors are expressed using the DOFs and coordinate systems to quantify the linear and angular velocities and accelerations of each deformed component. According to Newton's law of motion, these quantities are then used to determine the forces acting on each component. After defining the internal and external forces, the force equilibrium of the turbine can be represented in the following form within a holonomic multi-body dynamic framework

$$\boldsymbol{F_i} - \boldsymbol{F_i^*} = 0 \quad for \quad i = 1, 2, ..., n \tag{8.2}$$

The number of degrees of freedom in the equation above is represented by an integer n, which is equal to 25 in this case. The active and inertia forces are represented by $\boldsymbol{F_i}$ and $\boldsymbol{F_i^*}$, respectively. The equation of motion can be expressed in matrix notation using the constituents of $\boldsymbol{F_i}$ and $\boldsymbol{F_i^*}$ from Eq. 8.2, as follows

$$[\boldsymbol{M}(\boldsymbol{u}, \boldsymbol{t})] . \{\ddot{\boldsymbol{u}}\} + \left\{\bar{\boldsymbol{F}}(\dot{\boldsymbol{u}}, \boldsymbol{u}, \boldsymbol{t})\right\} = 0 \tag{8.3}$$

The vector $\bar{\boldsymbol{F}}(\dot{\boldsymbol{u}}, \boldsymbol{u}, \boldsymbol{t})$ represents stiffness, damping, and externally applied forces in the above equation. The primary focus of this study is to develop an optimal Wavelet-LQR control strategy for the double-pitched blade. To achieve this objective, a double-pitched rotor system is incorporated into the multi-body aeroelastic code previously developed in chapter 4. The bending-torsionally coupled blade model with two different pitch angles is also previously described in §7.2.1 of chapter 7. Other details, including multi-body dynamics of the spar, tower, nacelle, drive-train, and hub, may be found in §4.2 of chapter 4 and §2.2 of chapter 2 hence, they are omitted here.

8.3 External Loads on Offshore Turbine

A floating wind turbine is exposed to various external loads, which can affect its stability, performance, and safety. These loads include aerodynamic load, hydrodynamic load, gravitational load, and mooring forces. The interaction of the wind with the turbine blades and tower produces the aerodynamic load. The hydrodynamic load is caused by the interaction of the turbine spar with the water waves, while mooring forces are caused by the anchoring cables that connect the turbine to the seabed. Previous studies have proposed various techniques to model these loads accurately, which are already available in literature [15,166]. Therefore, to avoid too many details, only the necessary information on modeling these loads is presented here for completeness.

- The blades of a wind turbine experience both aerodynamic lift and drag forces and pitching moment, while only the drag force acts on the tower. A modified Blade Element Momentum (BEM) theory proposed by Ning [99] has been employed to estimate these forces while ensuring convergence. The wind acting on the blades varies over time and was estimated through a rotational sampling of the 3D turbulent wind field simulated in TurbSim [85]. Here, the one-dimensional flow has been modeled using International Electrotechnical Commission (IEC) Kaimal spectrum [87]. Additional details on the simulation of aerodynamic loads can be found in §2.2.5 of chapter 2.

- For the hydrodynamic load, the ocean wave profile is simulated using Pearson-Moskowitch (PM) spectrum [101], which represents a developed sea state. Morison's equation is used to estimate the linear wave inertia force and non-linear viscous drag force acting on the spar. It assumes that viscous drag force dominates the total drag force and damping due to radiation is negligible. These assumptions are valid as the spar undergoes small rotations, and the cylindrical shape has a small diameter compared to the wavelengths of the ocean waves [278]. The added mass associated with spar heave motion is also taken into account [199]. Details on the simulation of hydrodynamic loads are presented in §4.3 of chapter 4.

- The gravitational load applies a vertical force downward on all structural elements, i.e., the blades, nacelle, hub, generator, tower, and spar, corresponding to the negative $\hat{x}_2$ axis as shown in Fig. 8.1. However, the in-plane bending moment of the blade caused by gravity varies as it rotates, reaching a maximum when the blade is in a horizontal position. Readers may refer to chapter 2 for a detailed explanation of the equations governing the generalized active forces due to gravity.

- For the mooring loads, an open-source mooring line simulation program, MoorDyn [263,264], is used to compute the dynamic loads on the spar. This program accounts for the forces due to internal axial stiffness and damping, weight, buoyancy, hydrodynamic forces from Morison's equation, and vertical spring-damper forces arising from contact with the seabed. The wave kinematics on the mooring cable are not considered because the fairleads of the spar-type FWT are deep below the water surface.

In summary, all environmental loads acting on the spar-type floating turbine are considered for detailed analysis. The necessary details of modeling these loads are presented to help readers understand the complete load modeling process. Further details can be found in the sections cited above.

8.4 Collective Double-Pitch Control Using Wavelet-LQR Algorithm

Horizontal Axis Wind Turbine (HAWT)s are often regulated using rotor-collective blade-pitch or generator-torque control. The former operates above the rated speed, while the latter operates below it. As wind speed increases, the pitch controller becomes increasingly important and is, therefore, the focus of this study. Generally, a single variate system, known as a full-span blade pitch controller, changes the blade pitch angle and reduces generator speed variability due to incoming turbulence. However, a full-blade pitch controller is slow to respond and requires more actuator force. Thus, to address this issue, a double-pitch rotor system is proposed here, and the model has been thoroughly discussed in the preceding section, which is further used in this section for controller design. The classical LQR approach is initially used to formulate the feedback gain matrix, which is further updated in the time-frequency domain using wavelet transform. The proposed control strategy is detailed below.

8.4.1 Development of Classical LQR Algorithm for the Control of Double-Pitched Rotor

This section describes a centralized multi-variate controller for the double-pitched rotor, aiming to reduce generator speed fluctuations and, subsequently, blade vibration in flapwise, edgewise, and torsional directions. The LQR algorithm is selected for this task due to its efficiency and widespread use. In this blade-pitch control algorithm, the generator speed serves as feedback. Following the recommendation of [5], the generator speed is filtered while minimizing high-frequency excitation with a recursive, single-pole low-pass filter with exponential smoothing. The drive-train dynamics is modeled using the following equation [5]

$$T_{aero} - G_{br}.T_{gn} = I_{DT}.\Delta\ddot{u}_{12} \tag{8.4}$$

In this equation, G_{br} and $I_{DT} = I_{rotor} + {G_{br}}^2.I_{gn}$ denote the gearbox ratio and the inertia of the drive-train, respectively. The terms T_{aero} and T_{gn} correspond to the aerodynamic torque produced by the rotor and the torque produced by the generator, respectively. The variable u_{12} represents the degree of freedom corresponding to the azimuth angle of the low-speed shaft of the drive train. The second-order time derivative of u_{12}, denoted by $\ddot{u}_{12}$, represents the rotor acceleration. In the region where the pitch controller operates (i.e., above the rated wind speed), the generator torque is inversely proportional to its speed to maintain constant power output, which can be expressed as

$$T_{gn} = \frac{P_0}{G_{br}.\dot{u}_{12}} \tag{8.5}$$

The time derivative of the rotor speed is denoted by $\dot{u}_6$ in this equation. The expression P_0 corresponds to the rated power of the turbine. The first-order Taylor series expansion of Eq. 8.5 around a reference point $\dot{u}_{12}^*$ can be written as

$$T_{gn} \approx \left.\frac{P_0}{G_{br}.\dot{u}_{12}}\right|_{\dot{u}_{12}^*=\Omega_0} + (\dot{u}_{12} - \dot{u}_{12}^*) . \left.\frac{\partial T_{gn}}{\partial \dot{u}_{12}}\right|_{\dot{u}_{12}^*=\Omega_0} = \frac{P_0}{G_{br}.\Omega_0} - \frac{P_0}{G_{br}.\Omega_0^2}.\Delta\dot{u}_{12} \tag{8.6}$$

where Ω_0 is the rated speed of the low-speed shaft. The aerodynamic torque produced by the rotor can be denoted as a function of the blade-pitch angles ($\theta_{p,1}$, $\theta_{p,2}$) of the double-pitched rotor proposed in this study, i.e.,

$$T_{aero}(\Omega_0, \theta_{p,1}, \theta_{p,2}) = \frac{P(\Omega_0, \theta_{p,1}, \theta_{p,2})}{\Omega_0} \tag{8.7}$$

The above equation represents the instantaneous power produced by the turbine and is denoted by P. Similar to Equation 8.6, Equation 8.7 can also be expressed using a first-order Taylor series expansion, which is given by

$$T_{aero} \approx \frac{P_0}{.\Omega_0} + \frac{1}{\Omega_0}.\left(\frac{\partial P}{\partial \theta_{p,1}}\right).\Delta\theta_{p,1} + \frac{1}{\Omega_0}.\left(\frac{\partial P}{\partial \theta_{p,2}}\right).\Delta\theta_{p,2} \tag{8.8}$$

The above equation represents the pitch angles' deviation from their operating point, represented by $\Delta\theta_{p,i}$. Substituting Eq.8.8 into Eq. 8.4 and reordering them into the general state-space form, i.e., $\dot{U}(t) = A_s.U(t) + B_c.F_c(t)$, leads to the following equation for the rotor-speed fluctuation

$$\underbrace{\left\{ \Delta\dot{u}_{12}\Delta\ddot{u}_{12} \right\}}_{\dot{U}(t)} = \underbrace{\begin{bmatrix} 0 & 1 \\ 0 & \frac{P_0}{I_{DT}{\Omega_0}^2} \end{bmatrix}}_{A_s} . \underbrace{\begin{Bmatrix} \Delta u_{12} \\ \Delta\dot{u}_{12} \end{Bmatrix}}_{U(t)} + \underbrace{\frac{1}{I_{DT}\Omega_0}\begin{bmatrix} 0 & 0 \\ \frac{\partial P}{\partial\theta_{p,1}} & \frac{\partial P}{\partial\theta_{p,2}} \end{bmatrix}}_{B_c} . \underbrace{\begin{Bmatrix} \Delta\theta_{p,1} \\ \Delta\theta_{p,2} \end{Bmatrix}}_{F_c(t)} \tag{8.9}$$

$$\underbrace{\begin{Bmatrix} \Delta\dot{u}_6 \\ \Delta\ddot{u}_6 \end{Bmatrix}}_{\dot{U}(t)} = \underbrace{\begin{bmatrix} 0 & 1 \\ 0 & \frac{P_0}{I_{DT}{\Omega_0}^2} \end{bmatrix}}_{A_s} . \underbrace{\begin{Bmatrix} \Delta u_6 \\ \Delta\dot{u}_6 \end{Bmatrix}}_{U(t)} + \underbrace{\frac{1}{I_{DT}\Omega_0}\begin{bmatrix} 0 & 0 \\ \frac{\partial P}{\partial\theta_{p,1}} & \frac{\partial P}{\partial\theta_{p,2}} \end{bmatrix}}_{B_c} . \underbrace{\begin{Bmatrix} \Delta\theta_{p,1} \\ \Delta\theta_{p,2} \end{Bmatrix}}_{F_c(t)} \tag{8.10}$$

where A_s is a matrix consisting of system matrices. The generator-torque controller imposes negative damping $\frac{P_0}{\Omega 0^2}$ on the system. The sensitivity matrix B_c correlates the control output $F_c(t)$ to the appropriate degrees of freedom. Using traditional LQR theory, the ARE of the matrix P_{LQR} can be formed by considering weight matrices Q and R on the states and control effort, respectively, which is given by

$$P_{LQR}.A_s + {A_s}^T.P_{LQR} - P_{LQR}.B_c.R^{-1}.{B_c}^T.P_{LQR} + Q = 0 \tag{8.11}$$

The matrix P_{LQR} in this equation is positive definite and symmetric. It is possible to obtain a solution for P_{LQR} to evaluate the control force. Thus, the optimal control force can be expressed as

$$F_c(\theta, t) = -R^{-1}.{B_c}^T.P_{LQR}.U = -G_{LQR}(\theta, t).U(t) \tag{8.12}$$

The above expression shows the control force computed using the feedback gain matrix G_{LQR}, which is determined by the weight matrices Q, R, and the terminal penalty matrix S^f. The sensitivity matrix B_c is crucial for gain-scheduling, as it contains the terms $\frac{\partial P}{\partial\theta_{p,1}}$ and $\frac{\partial P}{\partial\theta_{p,2}}$. This study proposes the rationale behind the proposed optimal gain scheduling using pitch sensitivity and weight matrices (see section 8.6). The control output at any time step can be obtained by multiplying the gain matrix with the state vector

8.4.2 Integration of Continuous Wavelet Transform in the LQR Algorithm

The time-frequency content of the input (i.e., rotor speed error in this formulation) can be utilized to schedule the feedback gain matrix. In this section, the frequency-dependent gain scheduling of the double-pitched rotor is introduced, which is based on the wavelet-LQR approach. In this regard, the continuous wavelet transform is employed to decompose the input signal into distinct frequency scales.

The continuous wavelet transform is the inner product of a finite energy signal with the scaled and translated versions of a basis function. Unlike the Fourier transformation, it facilitates the extraction of instantaneous features of any signal and, hence, has an inherent advantage. The detailed formulation of the continuous wavelet transform is extensively documented in §5.4.2 of chapter 5; hence, it is not reiterated here. This study utilizes the analytic Morse wavelet, a complex-valued wavelet with only positive real Fourier transform [271]. The analytic Morse wavelet is advantageous in representing signals with varying amplitude and frequency content over time [272,273]. The amplitude spectrum of this wavelet in the frequency domain is given by

$$\Psi_{\beta,\nu}(\omega) = \mathrm{H}(\omega) a_{\beta,\nu} \omega^{\beta} e^{-\omega^{\nu}} \tag{8.13}$$

The above equation includes $\mathrm{H}(\omega)$, i.e., the Heaviside step function, and a normalizing constant $a_{\beta,\nu} = 2\left(\frac{e\nu}{\beta}\right)^{\frac{\beta}{\nu}}$. The parameters β and ν represent the compactness and symmetry of this wavelet [274], respectively, and can be selected according to the specific requirements. The resulting wavelet's time-bandwidth product is expressed as $P^2 = \beta\nu$. MATLAB [232] provides efficient algorithms developed by Lilly [275] to calculate Morse wavelet coefficients, which is employed in this study. It is worth noting that the Morse wavelet's skewness equals zero when the symmetry parameter $\nu = 3$. Therefore, the default parameter values of $\nu = 3$ and $P^2 = 60$ are used in this study. Using these parameters, the state-space model of the system, as in Eq. 8.9, is transformed into the wavelet domain to determine the ideal control force. Therefore, taking wavelet transform of both sides of Eq. 8.9 using basis function $\psi(t)$ with scale parameter a and translation parameter b leads to the following expression

$$\frac{\partial}{\partial b} W_\psi U(a,b) = A_s.W_\psi \left[U(t)\right](a,b) + B_c.W_\psi \left[F_c(t)\right](a,b) \tag{8.14}$$

Using the definition of continuous wavelet transform, the first term on the right side of the above equation for a time interval of $[t_0, t]$ can be expressed as follows

$$W_\psi[U(b)] = \frac{1}{\sqrt{|a|}} \int_b U(b).\psi^* \left(\frac{t-b}{a}\right) db \tag{8.15}$$

The ARE for the optimal controller gain corresponding to scale a is formed by following the same procedure as described in subsection 8.4.1, which is given by

$$P_a + {A_s}^T.P_a - P_a.B_c.R_a^{-1}.{B_c}^T.P_a + Q_a = 0 \tag{8.16}$$

The weight matrices in this equation, Q_a and R_a, are determined based on the scale parameter a. The optimal solution for the control force in the wavelet domain can be expressed by the following equation, obtained by solving the ARE

$$W_\psi F_c(\theta, a, b) = -R_a^{-1}.{B_c}^T.P_a.W_\psi U(a,b) = -G_a(\theta, b).W_\psi U(a,b) \tag{8.17}$$

Here it should be noted that the gain matrix G_a is scale a dependent, which is inversely related to the frequency. Hence, a frequency-dependent gain matrix can be obtained for different scales. To evaluate the frequency-dependent gain matrix, weight matrices corresponding to frequency scales with the highest, mean, and lowest energy are selected first. Next, the relative energy in each scale is computed using the decomposed signal in the wavelet domain. Finally, the gain matrix is interpolated between the maximum, mean, and minimum values to schedule it for individual scales based on the energy arrival of the input.

Once the gain matrix is obtained, the control force in the time domain can be obtained by invoking the inverse wavelet transform of Eq. 8.17, i.e.,

$$F_c(\theta, t) = \frac{1}{2\pi C_\Psi} \int_a \int_b \frac{1}{a^2} \left[W_\psi F_c(\theta, a, b)\right].\tilde{\psi} \left(\frac{t-b}{a}\right) db.da \tag{8.18}$$

Figure 8.2 shows the proposed control system, where the estimated pitch angles are saturated using actuator limits before being sent back to the plant.

8.5 Offshore Wind Turbine Characteristics and Environmental Conditions

The properties of a benchmark National Renewable Energy Laboratory (NREL)-5MW turbine are utilized in this study. Table 2.3 provides an overview of the turbine's basic properties, where the subscripts ci, r, and co denote cut-in, rated, and cut-out, respectively. The blades are made up of eight distinct airfoils, each with unique properties such as chord length, aero-twist, lift and drag coefficients, and blade structural properties, including mass per unit length and stiffness. These properties are obtained from the NREL report [5]. The drivetrain comprises a gear tooth ratio of 97, with torsional stiffness and generator inertia values of 867637kN-m/rad and 534kg-m^2, respectively. The OC3-Hywind spar is 120m deep and has three mooring lines, and the fundamental properties of the spar and mooring cable are presented in Table 4.4. TurbSim is used to simulate the steady and turbulent wind fields for various mean velocities (i.e., 11.4-25m/s), corresponding to the active region between rated and cut-out speeds at 90m hub height. The power-law exponent of 0.2

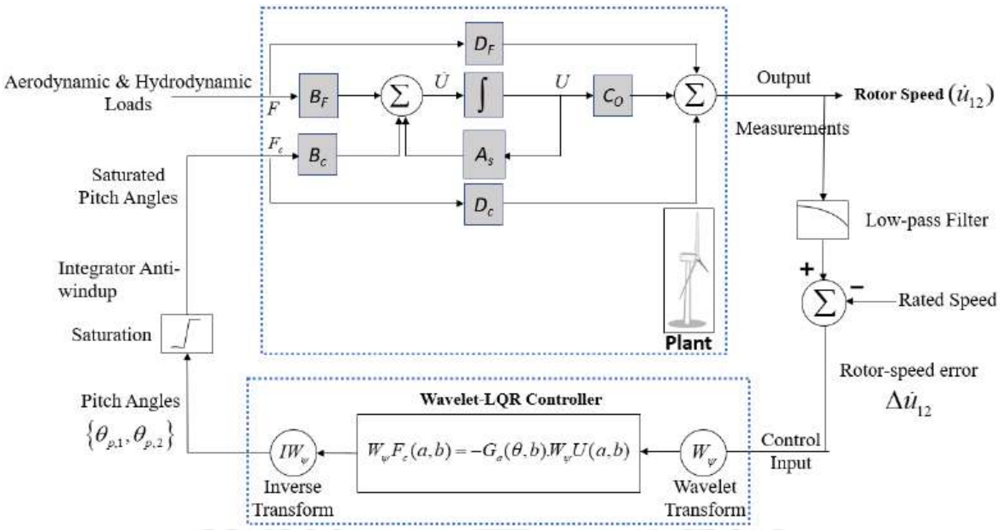

Figure 8.2: Schematic diagram of the centralized Wavelet-LQR Double-Pitch control system

for steady wind and 10% turbulence with IEC Kaimal spectra are used for wind field simulation since the marine environment has less turbulence compared to onshore [14].

The joint probability distribution of mean wind speed at 10m height along with significant height and peak period of the wave presented by Johannessen et al. [265] is used to generate wave acceleration and velocities at different depths from the Pierson-Moskowitch spectrum, as mentioned in §4.3. Three additional cases of wind-wave misalignment ranging from 0^o to 60^o are considered for different marine states to study the effectiveness of the proposed control strategy (refer to Table. 6.1). Fig. 6.3a displays the wind field generated by TurbSim corresponding to the rated speed with 10% turbulence, while Fig. 6.3b displays one of the sample time histories of simulated waves along surge corresponding to a significant wave height of 3.1m at different depths without misalignment. Here, it may be mentioned that the model of an offshore spar-type single-pitch wind turbine has already been developed and validated in chapter 4; hence, the validation exercise is not repeated here. In this chapter, the structural properties and environmental loads of the combined double-pitch system (i.e., the new addition) are used to determine the optimal gains for the proposed wavelet-LQR controller and then evaluate its effect on the dynamic response of the turbine.

8.6 Optimal Gain-Scheduling for the Wavelet-LQR Based Double-Pitch Rotor

This section provides the procedure of the optimal gain matrix evaluation for the double-pitched rotor described earlier. Two scenarios are simulated, in which the performance of the traditional LQR algorithm is compared to the proposed algorithm using wavelet transform. The selection of weight matrices is crucial during the active tuning process, and their selection for each scenario is detailed below.

i. **LQR Control**: As previously mentioned, once the weight matrices (Q and R) and the blade-pitch sensitivity to aerodynamic power ($\frac{\partial P}{\partial \theta_{p,i}}$) are known, the LQR gain matrix G_{LQR} can be estimated for the double-pitched rotor. The blade-pitch sensitivity is an aerodynamic property that depends on wind speed, rotor speed, and blade-pitch angle and is evaluated at different steady wind speeds within the operating region of the pitch controller. The corresponding blade base pitch angles ($\theta_{p,1}$) to generate the rated power (P_0 = 5.296610 MW) are taken as the operating points, while the rotor speed is kept constant at the rated speed of 12.1 rpm. The outboard pitch angle ($\theta_{p,2}$) is set to zero initially for all wind speeds during optimization. In this simulation and in all subsequent performance analyses, the length ratio γ (i.e., the length of the tip component to the entire blade length) is kept at 0.1 to minimize the weight of the rotor's outermost portion and maintain the mass ratio (i.e., the mass of the tip part to the entire blade mass) under 3%. However, a different length ratio may be opted for a different scenario, following the same methodology for designing optimal controller gains for the double-pitched rotor. To determine the pitch sensitivity, the rotor-collective blade-pitch angles (both $\theta_{p,1}$ and $\theta_{p,2}$) are perturbed at each operating point, and the resulting fluctuation in aerodynamic power is calculated using the central-difference-perturbation technique. Table 7.2 in chapter 7 shows the results from this analysis.

In classical LQR-based pitch control, the weighting matrix $Q = \begin{bmatrix} Q_{11} & 0 \\ 0 & Q_{22} \end{bmatrix}$ is chosen to be a diagonal matrix that gives more importance to controlling rotor speed fluctuations. The parameters Q_{11} and Q_{22} heavily influence the performance of the LQR controller and are, therefore, further optimized in this study using the following performance function.

$$\begin{aligned} &Obj(Q_{11}, Q_{22}) = \max\left(\left|\frac{\sigma_{\dot{u}_{12}}^{Baseline} - \sigma_{\dot{u}_{12}}^{LQR}}{\sigma_{\dot{u}_{12}}^{Baseline}}\right| \times 100\right) \\ &s.t.\ \ Q_{11}\ \{1e-5 \leq Q_{11} \leq 1e-2\} \\ &Q_{22}\ \{1e-3 \leq Q_{22} \leq 1e-1\} \end{aligned} \tag{8.19}$$

Here the performance function is selected to be the percentage reduction of the standard deviation of the rotor speed using the LQR algorithm ($\sigma_{\dot{u}_{12}}^{LQR}$), compared to a baseline single-pitch controller ($\sigma_{\dot{u}_{12}}^{Baseline}$). The range of these parameters that yielded the best results for the proposed controller was identified as the lower and upper limits in Eq. 8.19. During the sensitivity analysis, the weight on control effort R_{11} was held constant at a value of 1 to ensure that it was given less importance than the states. In Fig. 8.3, the objective function is shown to vary with changes in the control parameters Q_{11} and Q_{22} for the rated wind speed with 5% (Fig. 8.3a), 10% (Fig. 8.3b) and 15% (Fig. 8.3c) turbulence intensity levels and corresponding wave parameters (given in Table. 6.1) considering no misalignment. Finally, the optimization problem described in Eq. 8.19 is solved using the "fmincon" function in MATLAB [232], which utilizes the interior point nonlinear-optimization algorithm [279]. A total of 35 sample points distributed in a logarithmic scale are used in the optimization process. It converged at an interior point where the objective function is non-decreasing in feasible directions satisfying the optimality tolerance (i.e., 1%) and constraint tolerance (i.e., 1e-6). The blue points marked in Fig. 8.3a, Fig. 8.3b and Fig. 8.3c corresponding to $Q_{11} = 1e-3$ and $Q_{22} = 0.03$ is optimal in this scenario. It is observed that the alteration in turbulence intensity levels has no impact on the optimal weight parameters, and the optimal value remains constant for both scenarios. As a result, the point corresponding to $Q_{11} = 1e-3$ and $Q_{22} = 0.03$ is chosen for fine-tuning the gain matrix Q.

Next, the penalty on the control effort R is optimized for the double-pitched case by keeping R_{11} at 1 and varying R_{22} in the range of 0.025 to 0.1. In this case, a similar objective function is formed, where the controller's performance is evaluated at each operating wind speed for the selected range of R_{22}. Fig. 8.4 illustrates the variation of % reduction with mean wind speed for different values of R_{22}. It is observed that a lower penalty on the secondary pitch actuator improves the controller's performance. The optimization is carried out at each operating point with the same function parameters in MATLAB. The red line in Fig. 8.4 traces out the optimal value of R_{22} at each wind speed. After this analysis, it is observed that a lower penalty on the secondary pitch actuator near the value of 0.05 (indicated by the red line in Fig. 8.4) generally improves the controller's performance. However, near the cut-out wind speed, it recommends very high values of pitch angles to the actuators, ultimately impacting the controller's performance. On the other hand, near the cut-out speed, the value of $R_{22} = 0.07$ results in a faster controller response during turbulence, thereby controlling rotor speed fluctuations more efficiently (indicated by the red line in Fig. 8.4). Therefore, the optimal value of $R_{22} = 0.07$ (marked in blue in Fig. 8.4) is chosen for tuning the double-pitch controller gains. Finally, the gain matrix $G_{LQR}(\theta, t)$ is formed with the optimized weight parameters and pitch sensitivity at each operating point. These gains are then used in a time history simulation of the turbine to assess the effectiveness of the proposed configuration, which is discussed in the following sections.

ii. **Wavelet-based LQR Double-Pitch Control**:

Section 8.4.2 described how the state feedback is transformed into the wavelet domain, where different scales are utilized. This transformation is achieved using the analytic Morse wavelet as the basis function (as discussed in §8.4.2), and the relative energy corresponding to each scale is obtained from the wavelet coefficients. The gain matrix is scheduled proportionally in each scale based on the energy levels, where the optimal weight matrix Q and R identified earlier are associated with the mean levels of the relative energy scale, respectively. However, the weight Q for the scales with the highest and lowest

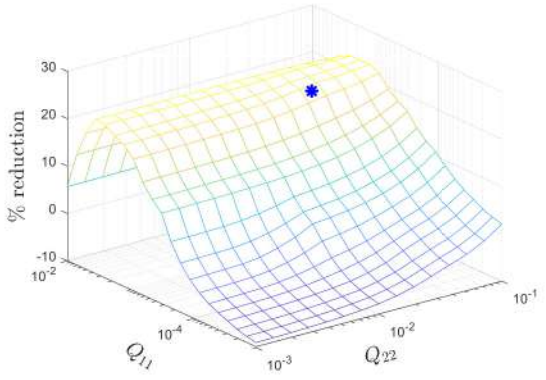

(a)

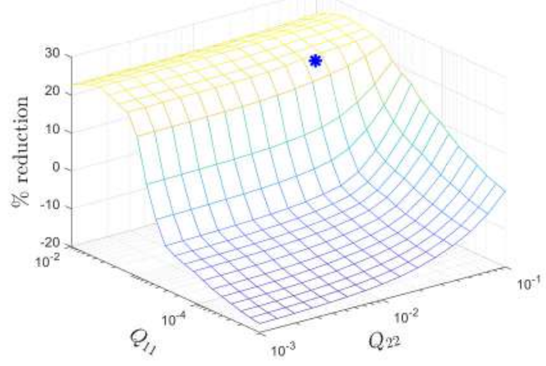

(b)

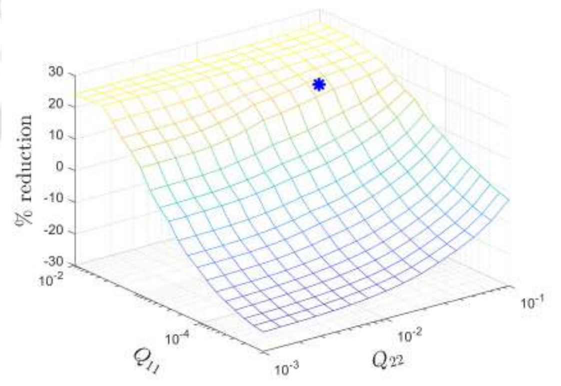

(c)

Figure 8.3: Variation of the objective function with the weight parameters for rated wind; (a) for turbulence level 5%, (b) for turbulence level 10% & (c) for turbulence level 15% (N.B. The optimal points are shown in blue)

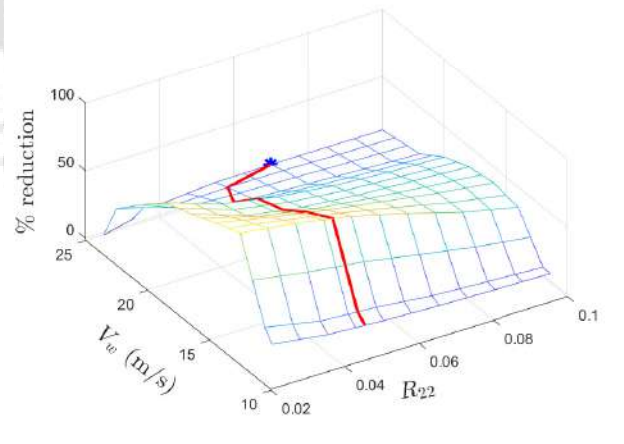

Figure 8.4: Influence of R_{22} on the objective function

energy is multiplied by factors 10 and 100, respectively. Following that, the gain is interpolated based on the relative energy content of different frequency levels. This approach ensures that the decomposed signal with the highest and lowest energy receives a higher gain to avoid the insignificance of the control force at that scale. The frequency-dependent gain matrix is obtained using this distribution, which is multiplied by the decomposed signal to obtain the control force in the wavelet domain. Finally, the control force is transformed back into the time domain before being applied through a closed loop.

8.7 Controller Performance Evaluation

This section evaluates the performance of the proposed LQR and wavelet-LQR control algorithms for a double-pitched rotor with bending-torsion coupling. The responses of various degrees of freedom, namely $\dot{U}_{Ge\_Az}$, U_{B1_OOP}, U_{B1_IP}, U_{B1_T}, U_{s_R}, and U_{s_P}, are compared. These degrees of freedom correspond to the generator azimuth angle, blade deflection in out-of-plane and in-plane directions, blade torsional degree of freedom, and spar roll and pitch degrees of freedom, respectively. The time histories of these responses collectively demonstrate the overall performance of the controller in suppressing vibrations across different degrees of freedom while maintaining platform stability. Before assessing the controller's performance, the optimized parameters are selected using the scheme described in the previous section. Once optimized, the controller is employed to evaluate the performance of the double-pitched rotor compared to the baseline single-pitch controller provided by NREL [5]. Each simulation runs for 360 seconds, with the wavelet controller activated after the initial 60 seconds to avoid transience. The wavelet controller utilizes the past 15 seconds of feedback data on rotor speed error states (Δu_{12} and $\Delta \dot{u}_{12}$) at each time step to calculate the optimal gain based on the energy levels in different frequency scales. This ensures fast and efficient operation of the algorithm, preventing it from becoming progressively slower over time.

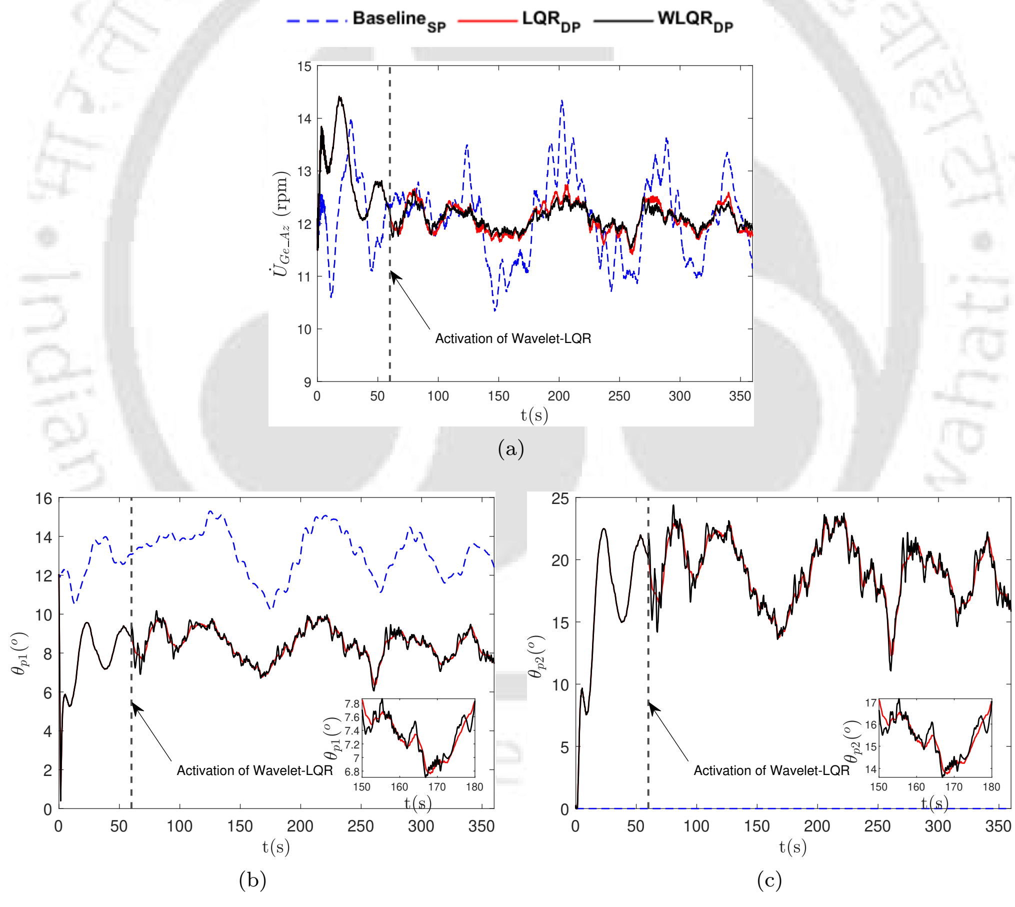

Figure 8.5: Response of low-speed shaft and blade pitch angles at 16 m/s wind speed with 10% turbulence and no misalignment; (a) Low-speed shaft rotational speed, (b) base-pitch & (c) tip-pitch. (N.B.: The inset represents an enlarged view of the corresponding time history.)

A reference wind speed of 16 m/s with 10% turbulence is selected for demonstration, along with corresponding wave parameters as specified in Table 6.1, assuming no misalignment to evaluate the controller's performance. Fig. 8.5 shows the impact of the controller on the rotor speed and actuator demand. The standard deviation (σ) of the rotor speed time history (refer to Fig. 8.5a) represents the variation in rotor speed, which directly reflects power fluctuation. The reduction in rotor speed fluctuation is observed to be

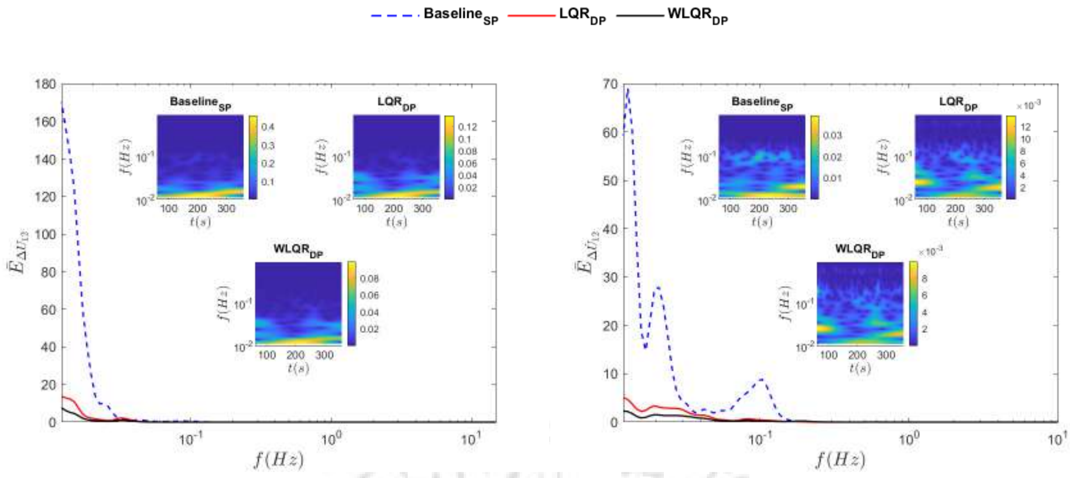

(a) (b)

Figure 8.6: Energy distribution in state errors; (a) Δu_{12} and (b) $\Delta \dot{u}_{12}$ (N.B.: Scalograms for different control algorithms are shown in inset)

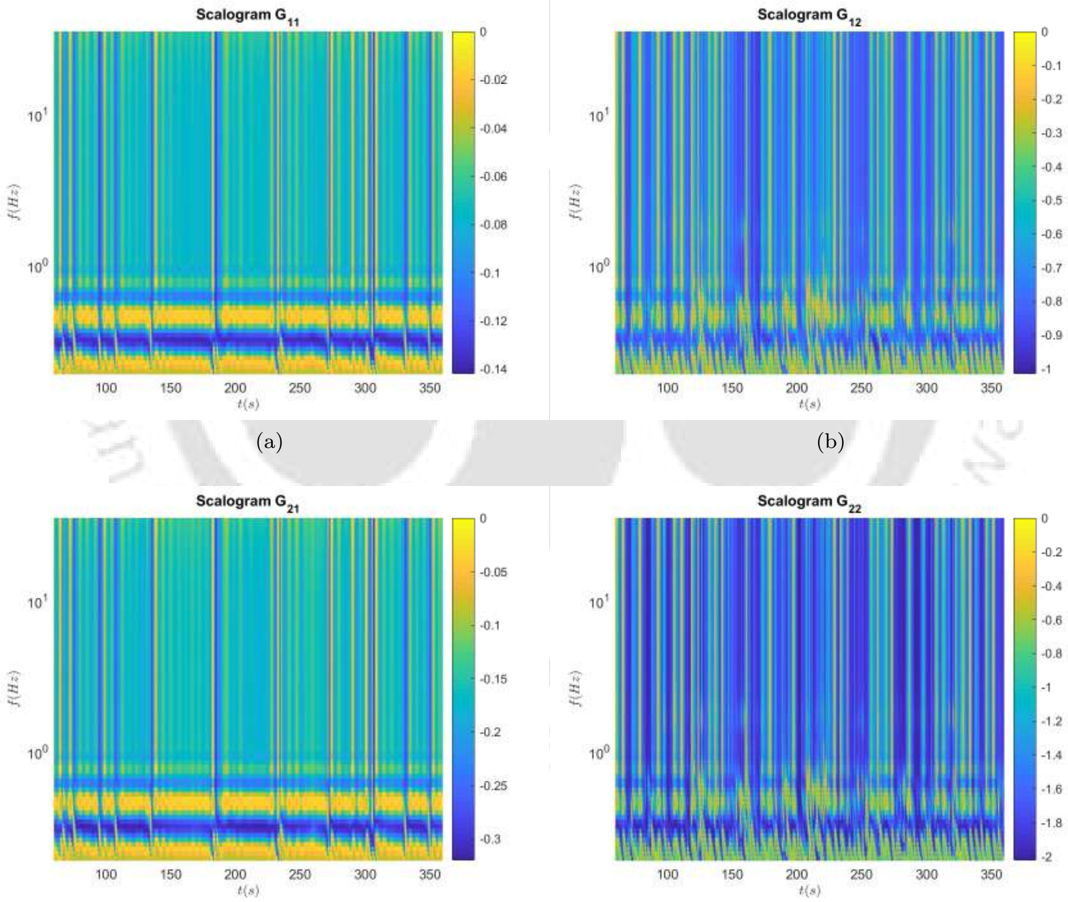

(a) (b)

(c) (d)

Figure 8.7: Time-frequency representation of wavelet-LQR controller gain matrix for two different pitch angles; (a) G_{11}, (b) G_{12}, (c) G_{21} and (d) G_{22}

67.53% compared to the baseline controller when using the classical LQR for the double-pitched rotor. The proposed wavelet-LQR algorithm further reduces the variation, achieving an impressive 76.53% reduction compared to the baseline control. This enhanced performance of the wavelet-LQR algorithm is achieved by scheduling higher gains based on frequency scales with maximum and minimum energy levels, ensuring significant control output at low energy scales. Fig. 8.6 illustrates the relative energy distribution of the error states, while the wavelet scalogram in insets depicts the energy variation under different control algorithms. In the legends of these figures, the subscripts SP and DP represent single-pitch and double-pitch controllers, respectively. Fig. 8.7 shows the elements of the gain matrix for the two pitch actuators, where the scheduled gain complies with the energy levels shown in Fig. 8.6.

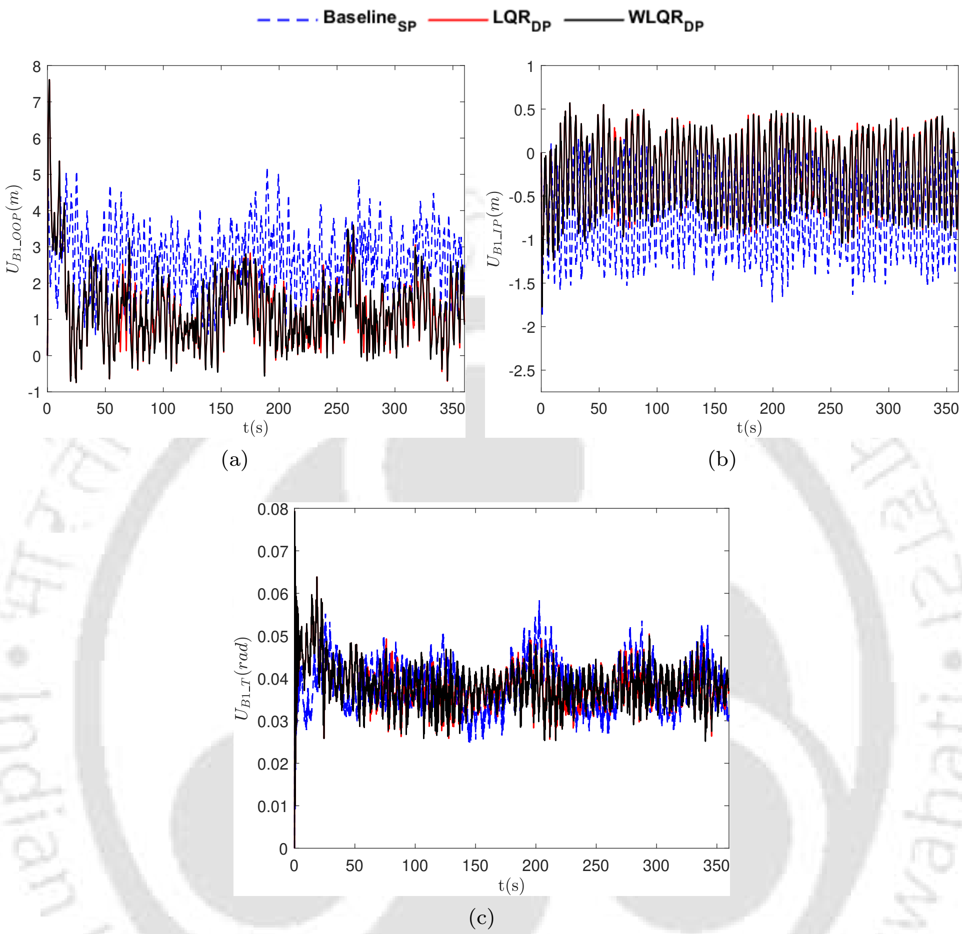

Figure 8.8: Response of the blade at 16 m/s wind speed with 10% turbulence and no misalignment; (a) out-of-plane, (b) in-plane & (c) torsional.

The proposed method exhibits lower pitch demands for the primary actuator compared to a single full-blade pitch controller due to the double-pitched controller's ability to minimize aerodynamic loads. Fig. 8.5b and Fig. 8.5c illustrate the pitch induced by the hub and blade-tip actuators, respectively. This pitch regulation helps stabilize power output fluctuations, thereby improving the longevity of the gearbox and other components. The LQR double-pitch control algorithm reduces the maximum pitch angle at the hub from 15.29^o (baseline controller) to 9.87^o, i.e., a 35.51% decrease in primary actuator demand. The wavelet-LQR double-pitch controller achieves a similar maximum pitch angle at the hub of 9.97^o but performs better by providing faster pitch actuation based on state frequencies. At the blade tip, a maximum pitch angle of 23.43^o is required (refer to Fig. 8.5c) by the wavelet-LQR controller. However, since the blade-tip region is relatively small, slightly higher pitch angles in this area do not significantly burden the actuators. This behavior reduces the overall pitch rate and actuator power requirement, resulting in a more responsive and efficient control system. The insets of Fig. 8.5b and Fig. 8.5c provide an enlarged view of the pitch angles produced by the two controllers, highlighting the differences between the algorithms. It should be noted that although the wavelet-LQR controller requires faster pitch actuation, the maximum pitch rate remains well within the actuator saturation limit of 8^o/sec.

The impact of the proposed controller on other degrees of freedom of the turbine was further investigated. Fig. 8.8 compares the blade response to turbulent wind between the double-pitched systems and NREL's baseline controller. These results demonstrate the effectiveness of the proposed method in reducing out-of-plane and in-plane blade vibrations. The peak responses along these DOFs are reduced by 31.35% and 39.64%, respectively, by the classical LQR double-pitch controller. The wavelet controller achieves similar results, with peak blade deformation in the out-of-plane and in-plane directions reduced by 30.64% and 39.50%, respectively, showing efficiency at par with the classical LQR. Additionally, both the LQR and wavelet-LQR controllers lead to approximately 13.61% and 14.32% reduction in peak blade torsional response, as shown in Fig. 8.8c. These findings indicate that the double-pitch system reduces the blade's torsional response significantly.

The reduction in blade responses discussed earlier is expected to positively affect the rotational degrees of freedom of the spar, specifically its roll and pitch motions. These rotational motions are crucial for offshore turbines as they impact the overall stability of the structure. Fig. 8.9a illustrates the rolling motion of the spar, which remains largely unaffected by both the LQR and wavelet-LQR algorithms. However, the double-pitch controller significantly reduces the variability in the pitching motion of the spar. Fig. 8.9b shows the time history of the pitch DOF of the spar, with the wavelet-LQR double-pitch control achieving a remarkable 44.61% reduction in the standard deviation. The classical LQR controller performs similarly in this aspect. The improved stability of the spar's pitching motion ensures the safety and reliability of the proposed control scheme when deployed in an offshore environment.

The controller's performance was further evaluated under various wind and wave misalignment conditions within its operational range. The results of this analysis are summarized in Table 8.1, which presents key performance parameters for the double-pitched rotor. The table includes the absolute peak,i.e., $|.|_{max}$, and standard deviation σ values for the respective response quantities indicated by the subscripts. It is evident from the table that the optimized double-pitch algorithm consistently outperforms the classical baseline controller in all cases. Moreover, the inclusion of the proposed wavelet-based gain scheduling further enhances the control performance in mitigating rotor speed fluctuations. The intelligent use of differential pitch angles of the smart rotor helps reduce aerodynamic loads, leading to varying performance across different degrees of freedom as wind speed increases.

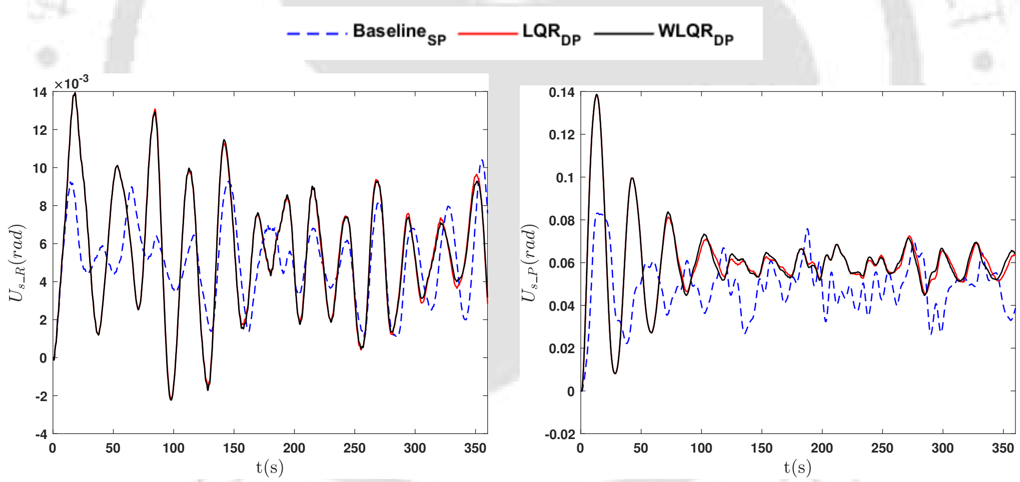

(a) (b)

Figure 8.9: Response of the spar at 16 m/s wind speed with 10% turbulence and no misalignment; (a) roll and (b) pitch

The proposed rotor demonstrates optimal control of rotor speed fluctuations at a mean wind speed of approximately 16 m/s and no misalignment, achieving a significant reduction of 76.53% compared to the baseline response. This reduction highlights the effectiveness of the proposed controller in regulating power output. Similarly, the peak out-of-plane blade response shows a maximum decrease of 46.66% at a wind speed of 20 m/s, while the peak in-plane blade response exhibits a maximum reduction of 45.16% around the same wind speed. The table also indicates that the standard deviation of the spar's pitching motion slightly increases by 8.73% with the wavelet-LQR controller near the rated speed, compared to the baseline response. However, the movement of the spar in this degree of freedom is significantly low near the rated speed, hence the slight increase in standard deviation is inconsequential to the turbine's dynamics. Moreover, as the wind speed increases, the wavelet-LQR control algorithm performs better in suppressing spar pitching motion, achieving a maximum reduction of 44.61% at a wind speed of 16 m/s.

The present controller demonstrates superior performance in various aspects compared to the system

Table 8.1: Performance evaluation of the proposed controller under different operating conditions

Wind Speed	**Wave Direction**	**% reduction of different response quantities compared to Baseline Control**							
		LQR Double-Pitch				**Wavelet-LQR Double-Pitch**			
(m/s)	(^{o})	$\lvert U_{B1\_OOP}\rvert_{max}$	$\lvert U_{B1\_IP}\rvert_{max}$	$\sigma_{U_{Spar\_Pitch}}$	$\sigma_{\dot{U}_{Ge\_Az}}$	$\lvert U_{B1\_OOP}\rvert_{max}$	$\lvert U_{B1\_IP}\rvert_{max}$	$\sigma_{U_{Spar\_Pitch}}$	$\sigma_{\dot{U}_{Ge\_Az}}$
	0.00	2.26	12.62	2.76	32.45	0.90	12.06	-8.73	36.16
11.4	30.00	1.18	12.39	2.09	31.97	-0.21	12.57	-9.74	35.56
(Rated)	60.00	-2.65	11.11	0.92	30.79	-3.77	11.07	-11.05	34.20
	0.00	31.35	39.64	46.32	67.53	30.64	39.50	44.61	76.53
16	30.00	29.66	38.80	45.41	67.24	27.97	39.95	43.81	76.32
	60.00	24.93	36.31	43.48	66.58	22.14	38.41	42.12	75.84
	0.00	47.18	45.52	37.45	62.34	46.66	45.16	43.05	72.40
20	30.00	42.88	41.88	36.02	61.55	42.30	41.54	41.76	71.79
	60.00	35.05	39.54	32.67	59.74	34.26	39.16	38.70	70.37
	0.00	20.87	43.34	12.96	52.29	21.06	41.87	23.02	66.95
25	30.00	10.81	43.41	7.26	50.86	11.05	43.50	18.51	65.92
(Cut-out)	60.00	5.00	39.40	-8.87	48.07	5.99	38.49	5.06	63.99

described in the literature [199], which utilizes a wavelet-based individual single-pitch control system for spar-type offshore turbines. For example, the maximum reduction in peak out-of-plane blade response achieved by the system in literature [199] was 50%, observed at the cut-out wind speed. In contrast, the present controller achieves a comparable reduction of 46.6% at a wind speed of 20 m/s. However, the previous system [199] achieved this blade response reduction at the expense of a maximum 42.14% increase in the standard deviation of rotor speed. The present controller, on the other hand, reduces rotor speed fluctuations by up to 76.53% at a wind speed of 16 m/s, and overall, the standard deviation of rotor speed is reduced across the entire operating range. Another previous study [217] proposed a different individual pitch control algorithm that addressed the issue of rotor speed variability. In that case, the maximum reduction in the rotor speed RMS value was 30%, which is still less than what the present controller achieves. Additionally, the present controller performs equally well or even better in controlling blade out-of-plane and in-plane loads.

The performance of the controller across different degrees of freedom is also influenced by wind-wave misalignment. It is important to note that the controller is designed and optimized based on the objective function of rotor speed errors. As a result, the reduction in blade responses occurs as a secondary effect due to decreased aerodynamic loads. Therefore, the controller remains equally effective in suppressing rotor speed fluctuations as the wind-wave misalignment increases. However, the performance in controlling other degrees of freedom, such as blade and spar response, is slightly affected by the increased misalignment. In summary, the wavelet-LQR-controlled double-pitched rotor significantly impacts power fluctuation and the dynamic response of the blades and spar as a secondary effect when optimally tuned.

8.8 Summary

This chapter introduces detailed modeling of the double-pitched rotor for spar-type floating wind turbines, which to the best of the author's knowledge, has not been reported in the literature. It also evaluates the effectiveness of this smart rotor in controlling power fluctuation and structural responses of offshore horizontal axis wind turbines. All these are achieved by developing an aero-servo-elastic multi-body dynamic model using Kane's approach and designing an optimal wavelet-LQR control strategy for two pitching actuators considering bending-torsion coupling. Simulations are performed under different wind conditions, and the results show substantial improvements in overall response, especially in power regulation. The key findings of this study are summarized below.

- This study presented the development of a comprehensive multi-body dynamic model for an offshore spar-supported horizontal axis wind turbine with a double-pitched rotor, considering dynamic bending-torsion coupling. This model predicts the turbine's behavior and performance in diverse marine environments. In this context, it may be noted that the inclusion of dynamic bending-torsion coupling is essential for the accurate estimation of aerodynamic and structural responses. The study provides valuable insights into the modeling and control system architecture of offshore double-pitched wind turbines, contributing to the development of reliable and efficient wind energy systems.

- The proposed formulation in this study eliminates the need for scheduling weight matrices, as also seen in previous works such as Sarkar et al. [199] and Fitzgerald et al. [198] for single-pitched rotor.

However, these approaches rely on reduced-order modeling schemes and time-independent system matrices, invariably introducing modeling and estimation errors. In contrast, the present study avoids these approximations by selecting optimal controller weights while using a high-fidelity model for the double-pitched wind turbine system. The results show that the proposed optimal wavelet-LQR algorithm consistently outperforms both the baseline controller described in NREL[5] and the classical LQR controller under different environmental conditions. This improved performance is achieved through faster pitch angle actuation, effectively reducing the impact of aerodynamic turbulence.

- Compared to a full-blade pitch controller, a double-pitched rotor system offers significant improvements in turbine performance. Optimal rotor design can result in a reduction of over 50% in rotor speed fluctuation, leading to improved power regulation. In this context, previous literature reported degraded responses across various turbine DOFs when implementing wavelet-based pitch controllers in offshore environments [199,217]. However, the control methodology proposed in this study not only enhances power regulation but also improves structural responses along different DOFs of the benchmark turbine, providing additional benefits in terms of stability and sustainability.
- The scale-dependent gain scheduling in the time-frequency plane, utilizing the energy content of the feedback, improves controller performance compared to the classical LQR algorithm. Numerical results showcased the performance of this control strategy across the entire operating spectrum of the turbine, including different wind-wave misalignments. Moreover, the reductions in rotor speed variability are substantial in all the load cases.

In summary, the proposed optimization of weight matrices and frequency-based gain scheduling for the LQR-controlled double-pitched rotor have shown excellent performance in regulating rotor speed fluctuations and structural responses. The superiority of this approach over a conventional single-pitch baseline controller and classical LQR controller underscores its effectiveness.

Chapter 9

Concluding Remarks

The work presented in this thesis primarily contributes to the mathematical development of a multi-body dynamic model of onshore/offshore Horizontal Axis Wind Turbine (HAWT) with complete aero-servo-elastic coupling between its components. Bending-torsion coupling in blades and Soil-Structure Interaction (SSI) in monopiles are considered while developing the tightly coupled mathematical framework. Overall, the performance of the turbine is investigated in different operating conditions to study the behavior of its modal, dynamic, fatigue characteristics, and design life. The model is further extended to accommodate several novel control techniques for mitigating vibrations of turbine components. For example, the beneficial effects of bending-torsion coupling are utilized via the optimal design of blade skin fibre angles to improve its dynamic characteristics. Bi-directional active Tuned Mass Damper (TMD) is designed inside the nacelle using a wavelet-based Linear Quadratic Regulator (LQR) algorithm to control tower vibration of onshore turbines during seismic events. For spar-supported offshore turbines, the hydrodynamic loads are isolated through a novel configuration of spar-torus, which, in turn, reduces the dynamic response of the spar and the tower top, particularly in the side-to-side directions. Finally, the performance of double-pitched rotors is investigated for both onshore and offshore turbines using different advanced control algorithms (i.e., multi-objective optimal Proportional Integral Derivative (PID), weight-optimized LQR, and wavelet-based LQR) to effectively mitigate rotor speed fluctuations and blade vibrations simultaneously. The following sections will detail the significant contributions of this study, as well as their potential future developments, keeping this perspective in mind.

9.1 Conclusions

The investigation into the multi-body dynamic modeling, fatigue analysis, and vibration control of wind turbine components has made some important contributions in this domain. The key contributions and findings of this study are summarized below and presented in chronological order as outlined in the preceding chapters. The recent trends in research within the wind energy industry are highlighted in Chapter 1. A few key objectives are defined within the several gap areas that were identified in the literature review. With those in mind, a mathematical model of an onshore horizontal axis wind turbine has been developed in the 2^{nd} chapter, capturing the complex interaction between blade bending, torsion, and aerodynamic forces. It reveals how bending-torsion coupling and aerodynamic pitching significantly affect turbine vibrations and structural stresses, especially at high wind speeds. Furthermore, optimizing the blade skin's fiber angle enhances the turbine's dynamic performance by leveraging the positive effects of bending-torsion coupling. The key conclusions drawn from this work are as follows

- A comprehensive aero-servo-elastic multi-body model of a horizontal axis wind turbine has been created using Kane's method, taking into account the interaction between the bi-axial bending and torsion of the blade. This detailed model allows for unrestricted modeling of sub-systems and their seamless integration into the overall framework. It incorporates various types of coupling, including dynamic and elastic, and examines the effect of composite layer orientation across the turbine's operating range. This modeling approach addresses the limitations found in existing models documented in the literature, offering a thorough dynamic analysis of the entire system.

- The dynamic bending-torsion coupling and aerodynamic pitching moment predominantly influence the tower's fore-aft movement and the blade's response in two orthogonal directions (out-of-plane and in-plane), potentially causing significant vibrations, especially at higher wind speeds. Overlooking these effects may result in an inaccurate assessment of strains and the resulting stresses within various structural components.

- The impact of elastic bending-torsion coupling in blades on the turbine's dynamic response can vary between beneficial and adverse, depending on their orientation, such as twist-to-feather or twist-to-stall. Notably, the twist-to-feather orientation is advantageous because it decreases the angle of attack during this effect, leading to reduced aerodynamic loads on the blade. Consequently, this behavior can be harnessed for the effective design of airfoils.

- A positive fiber angle in the blade skin results in a positive coupling effect on flap-torsional stiffness and creates structural bending-torsion coupling in the twist-to-feather direction. Additionally, the optimal principal material orientation for the blade skin is found within this same area. Therefore, optimally leveraging bending-torsion coupling in a blade can significantly enhance the dynamic performance of a wind turbine.

The 3^{rd} chapter presents a study on the development of a multi-body dynamic model tailored for monopile-supported offshore wind turbines, with a particular focus on soil-structure interaction. Through numerical analyses, the study uncovers the conditions leading to maximum damage from aerodynamic and hydrodynamic forces, emphasizing the significance of the rated wind speed over the turbine's lifetime. Additionally, it investigates stiffness degradation and its implications on monopile performance in marine environments, offering valuable design insights for ensuring compliance with serviceability standards. The following findings highlight the critical role of stress-based modeling and soil-structure interaction in the fatigue design of monopile foundations.

- A multi-body dynamic model focusing on soil-structure interaction for offshore wind turbines has been formulated to aid in fatigue design and assess long-term performance. This model employs Kane's method, integrating equivalent monopile properties derived from an in-depth substructure analysis. It applies Winkler's beam theory for modeling the soil layers, characterized by their specific p-y curves. The model's accuracy is confirmed using the parameters of a benchmark turbine subjected to turbulent wind conditions, showing strong concordance with results from FAST. This model is further applied to explore soil-structure interactions within offshore conditions.

- The numerical findings underscore the importance of incorporating stress-based modeling with soil-structure interaction in the fatigue design of monopile foundations, following International Electrotechnical Commission (IEC) guidelines [87]. These analyses reveal that maximum damage is observed when aerodynamic and hydrodynamic forces align, with minimal effects at sixty degrees of misalignment. Short-term maximum damage arises at the cut-out wind speed, whereas the rated wind speed is the primary contributor to lifetime damage. Thus, the long-term fatigue impact is predominantly determined by the rated speed, given the turbine's extensive operational time under this condition.

- The study also explores factors affecting damage-equivalent stress and their role in fulfilling strict serviceability standards, showing how stiffness degradation impacts the long-term performance of monopiles in marine settings. It provides design curves for turbines of specific power ratings, emphasizing the relationship between diameter, thickness, and water depth. The dimensions derived from these curves meet fatigue life and serviceability requirements, making them useful for designing similar structures and planning projects in comparable marine environments.

The 4^{th} chapter presents the development of a multi-body dynamic model for spar-supported floating offshore wind turbines, with a focus on wind-wave interaction. The key highlights from this chapter are as follows.

- An extensive aero-servo-elastic model for spar-type floating offshore turbines has been constructed within a multi-body framework using Kane's method, taking into account the interaction between various structural elements. This model addresses the impact of external forces such as aerodynamic, hydrodynamic, and gravitational loads, simulating a range of environmental conditions the turbine might face during its operational life.

- Additionally, the temporal behavior of different structural components is simulated and validated using FAST results utilizing the data of a benchmark turbine.

Chapter 5 unveils a novel method aimed at enhancing vibration control in onshore horizontal axis wind turbine towers, addressing the challenges posed by turbulent winds and seismic activities. Through a pioneering integration of a multi-body dynamic framework and Kane's method, the study develops a mathematical model featuring an active TMD with time-dependent system matrices. It also introduces a wavelet-based time-frequency analysis to navigate the complexities of applying the LQR algorithm to systems influenced by time-varying frequencies, such as seismic events. This approach circumvents the limitations of previous methods, offering a more accurate and efficient solution for tuned mass dampers, as evidenced by its superior performance across a wide range of operating conditions and against various seismic loads. The key conclusions from this study are listed below.

- This study introduces an innovative approach for controlling vibrations in onshore horizontal axis wind turbine towers under turbulent wind and seismic activity. It features a mathematical model for the turbine and an active TMD, developed in a multi-body dynamic framework using Kane's method, where system matrices like mass, stiffness, and damping are time-dependent. Given the challenge of applying a standard LQR algorithm to systems with time-varying frequency inputs, such as earthquakes, the study proposes using wavelet-based time-frequency analysis. This technique reformulates the LQR problem into a time-frequency domain, enabling the development of a scale-dependent Differential Riccati Equation (DRE) for effective gain scheduling and tuning the active mass damper.
- The proposed method eliminates the need for estimating equivalent system matrices for active mass damper tuning, a requirement in previous approaches like those by Lackner and Rotea [108, 119] or FAST-SC [276], which use equivalent linearization and face inherent modeling errors. Unlike these methods, which introduce white noise to solve inverse problems, adding layers of modeling and estimation inaccuracies, the present approach avoids such approximations, leading to more efficient and accurate tuning of mass dampers for wind turbine towers. This results in a method that is not only mathematically precise but also superior in performance.
- The proposed method utilizes scale-dependent gain scheduling in the time-frequency domain, focusing on the energy content of the feedback to accurately estimate the control force. This approach outperforms traditional LQR algorithms, like those in FAST-SC, in reducing vibrations more effectively. Demonstrated across the turbine's entire operating range from rated to parked conditions and against various earthquake ground motions, the numerical results show significant reductions in peak, peak-to-peak (P2P), and Root Mean Square (RMS) responses in the tower's fore-aft direction. These outcomes collectively affirm the effectiveness of the proposed wavelet-LQR-based gain scheduling in actively tuning the mass damper for enhanced vibration control of onshore horizontal axis wind turbine towers.

Chapter 6 introduces a novel vibration control strategy for spar-type floating wind turbines utilizing a modified torus to dampen wave energy, thereby improving the dynamics of the spar supporting the turbine. This approach, distinct from traditional tuned mass dampers, integrates with the Floating Wind Turbine (FWT) without compromising the structure's weight or integrity, all while operating passively. The conclusions drawn from this chapter are given below.

- This study introduces an innovative approach of vibration control for spar-type floating wind turbines through the use of a modified torus. This modification is designed to absorb wave energy, thus influencing the dynamics of the spar that supports the blade-tower setup. Unlike a tuned mass damper, which can add extra weight and affect the main structure, the modified torus system integrates seamlessly with a spar-type FWT without altering its primary structure or increasing its weight. The proposed Modified Spar-Torus Combination (MSTC) positioned as a floating mass external to the main structure avoids these issues. To evaluate the effectiveness of this system, an aero-servo-elastic multi-body dynamic model is developed using Kane's method.
- The reduction in peak response for both the spar and tower was observed to exceed 60%, influenced by factors such as wind speed, turbulence intensity, significant wave heights, and the alignment between wind and waves. As a passive system, the proposed controller operates without the need for power or real-time monitoring, offering a significant benefit in deep-sea environments.
- Increments in the wind-wave misalignment angle enhance the effectiveness of the MSTC in managing the spar's sway and the nacelle's lateral movements. These outcomes align with the primary goals of this research, as excessive motion in either the sway or lateral directions can harm the drivetrain's delicate electro-mechanical components.

The 7^{th} chapter introduces a high-fidelity model of a horizontal axis wind turbine equipped with a double-pitched rotor framed within a multi-body dynamic analysis that addresses bending-torsion coupling. Moreover, the implementation of multi-objective optimal PID control and a weight-optimized LQR algorithm for the onshore double-pitched system substantially surpasses traditional pitch control methods in reducing rotor speed fluctuations and controlling blade vibrations. The following points highlight the findings of this study.

- One of the key contributions of this thesis is the creation of a high-fidelity model for a horizontal axis wind turbine featuring a double-pitched rotor within a multi-body dynamic framework. Although DTU's HAWC2 and Siemens-Gamesha's BHAWC can simulate the dynamics of double-pitched rotors with Lagrangian methods, this model is able to conduct accurate aero-elastic simulations of the entire system within Kane's multi-body dynamic framework, including the interactions among the rotor, drivetrain, and tower, with collective double-pitch control of the blade that undergoes bending-torsion coupling. Hence, it effectively surpasses NREL's ElastoDyn module, which lacked a complete representation of the system within Kane's framework. This effort illustrates the benefits of employing a smart rotor design. The model's ability to precisely predict the performance of the double-pitched rotor across various operational scenarios is essential for designing the turbine's structural and mechanical components.

- The double-pitched system governed by multi-objective optimal PID control introduced in this research significantly outperforms the collective full-blade baseline pitch control documented in existing studies. By adhering to the tuning process suggested here, it's possible to achieve a reduction in rotor speed fluctuation over 40% compared to the baseline controller [5] across the turbine's operating range. Moreover, this approach also offers considerable control over blade vibrations, presenting an extra advantage.

- The sensitivity analysis indicates that the length ratio (γ) plays a pivotal role in the performance of a double-pitched system. While a higher length ratio contributes to more stable rotor speeds, exceeding a practical threshold may not be viable. Therefore, this study suggests adopting a length ratio of $\gamma = 0.1$, or less.

- The double-pitched rotor system managed by LQR control significantly boosts turbine efficiency beyond what is achievable with a single full-blade pitch controller or PID double-pitch controller. The optimally designed approach detailed in this study is capable of reducing rotor speed fluctuations over 50%, thereby stabilizing power output. Additionally, it enhances structural performance across various degrees of freedom, offering further advantages.

- Selecting the optimal weights for the controller plays a vital role in the design of an LQR pitch controller. The gain-scheduled LQR algorithm proposed in this study surpasses the performance of the baseline controller documented in the literature, even when implemented in a single-pitch setup. This improvement is realized through the precise actuation of pitch angles, effectively mitigating the impact of aerodynamic turbulence.

In the 8^{th} chapter, a sophisticated multi-body dynamic model for an offshore spar-supported horizontal axis wind turbine is developed, integrating an offshore double-pitched rotor with dynamic bending-torsion coupling, a novel aspect not previously studied in detail. This model provides accurate predictions of turbine performance and efficiency under diverse marine conditions, underlining the importance of dynamic bending-torsion coupling for accurate aerodynamic and structural predictions. Introducing a new method that simplifies the optimization of controller weights without the inaccuracies of past approaches, this study demonstrates the superiority of an optimized wavelet-LQR algorithm over traditional control methods. The key contributions of this chapter are listed below.

- This study introduces a new approach that avoids the complexities of scheduling weight matrices, a limitation seen in earlier methods for single-pitched rotors [198, 199], which relied on simplified models, leading to inaccuracies. By selecting optimal controller weights for a detailed double-pitched wind turbine model, this research circumvents such errors. The findings reveal that the optimized wavelet-LQR algorithm surpasses standard baseline [5] and classical LQR controllers, achieving superior performance by rapidly adjusting pitch angles to diminish the effects of aerodynamic turbulence.

- The study reveals that, in offshore environments, a double-pitched rotor system substantially outperforms traditional full-blade pitch controls, enhancing turbine efficiency. By optimizing the rotor's design, it's possible to achieve more than a 50% decrease in rotor speed variability, which translates to better power management. Previous research has shown that wavelet-based pitch controls could lead to degraded turbine performance across various degrees of freedom (DOFs) under offshore conditions [199, 217]. Nonetheless, the control strategy introduced in this research not only boosts power management but also benefits the structural performance across the turbine's DOFs, thereby offering improved stability and long-term durability.

- The scale-dependent gain scheduling within the time-frequency domain enhances controller efficiency over the traditional LQR method utilizing the energy content in feedback. Numerical analyses demonstrate the effectiveness of this approach throughout the turbine's full operational range, accommodating various wind-wave alignments. Additionally, significant reductions in rotor speed fluctuations were observed across all load scenarios.

Considering the points discussed above, it can be summarized that the high-fidelity multi-body dynamic model developed in the study is essential for designing horizontal-axis wind turbines and their associated control systems. The advancement in the modeling made in this thesis offers insights into the different coupling effects observed between turbine components and external environments. In this context, the code developed in MATLAB does not take any abnormal time compared to FAST, and hence, it was never a matter of inquiry. On the other hand, the advanced control systems proposed in this study offer significant improvements in the dynamic performance of the turbine components (i.e., tower, blade, and generator), thereby ensuring its safe and sustained operation.

9.2 Future Work

The preceding discussion highlights the significant contributions of this research in the multi-body dynamic modeling of horizontal axis wind turbines and the vibration control for better performance. While the performance analyses presented are promising, there is room for further advancement in the proposed strategies. Considering this, several areas have been identified for future investigation, which are listed below.

1. **Finite Element Modeling and Validation:** The intersection of Finite Element Method (FEM) in a Lagrangian framework with the incorporation of spinning effects and multi-body interactions, validated through the models developed using Kane's vector approach, opens a broad avenue for research in the area of wind turbine simulation and design optimization. Below are several potential research topics that deal with this intricate field:
    - Developing a comprehensive multi-body dynamic model of HAWTs in the Lagrangian framework poses several challenges, as indicated earlier. However, with improving computing technologies, the capability of developing such multi-physics models in ANSYS or similar software and validating them with the present model can be a potential area of research.
    - Research could focus on the integration of more sophisticated aerodynamic loading models into the FEM framework. This would involve developing and validating models that accurately reflect the complex wind flow patterns and their impact on turbine blades, considering both steady-state and transient wind conditions.
    - For offshore wind turbines, the research could delve into the coupled aeroelastic and hydrodynamic modeling within the FEM framework. This would entail validating the model against the present simulations that consider the interaction between aerodynamic forces on the turbine and hydrodynamic forces on the supporting structure.
2. **Advanced Aeroelastic Modeling:** In this study, the performance of the turbine and the proposed controllers are investigated based on aerodynamic loads generated through Blade Element Momentum (BEM) theory. A comprehensive performance evaluation can be carried out using advanced techniques such as unsteady aerodynamics or Computational Fluid Dynamics (CFD) via software platforms such as ANSYS or equivalent tools. Several potential research topics focused on advanced aeroelastic modeling of wind turbines are given in the following
    - Research on advanced aerodynamic modeling could help to bridge the gap between the relatively simple BEM theory and the more detailed but computationally intensive CFD simulations. The major difference between BEM and CFD is that BEM does not include 3D effects that might

happen in the flow field. By integrating these approaches, the study could offer a more accurate and efficient method for predicting the aerodynamic performance and structural loads on turbine blades under operating conditions. It is also acknowledged that incorporating advanced aerodynamic factors, such as vortices, wind shear and turbulence bubbles, and individual double-pitch control and detailed fatigue analysis could enhance the system's performance and accuracy.

- Developing systems that use aeroelastic models in conjunction with sensor data from operational turbines to perform real-time monitoring and determine structural loads and stresses. This could help identify potential issues before they lead to significant damage or downtime, thereby improving the reliability and efficiency of wind energy production. Also, the sensor data can be used to improve the aeroelastic models further.
- Integrate aeroelastic models with advanced weather forecasting systems to predict how incoming weather conditions will affect turbine performance and structural integrity. Such an approach could enable more proactive and optimized turbine management, adjusting operational parameters in anticipation of changes in the wind field.
- Specifically focusing on the unique challenges faced by offshore wind turbines, including the impact of wave loading, wind-wave-current interaction, and saltwater corrosion on aeroelastic behavior. This research could explore novel materials, designs, and operational strategies tailored to the offshore environment.

3. **Advanced Soil-Structure Interaction Modeling:** Exploring the soil-structure interaction across various seabed foundation types beyond monopiles, like tripods or gravity-based foundations, represents a natural extension of this research. Research could be focused on enhancing modeling techniques in terms of accuracy and runtime to predict the long-term effects of cyclic loads on foundation integrity and turbine stability. A few research topics that could significantly contribute to the field of advanced soil-structure interaction modeling for wind turbines are listed below

   - Research could focus on creating more accurate and computationally efficient high-fidelity numerical models that capture the complex behaviors between soil and various offshore wind turbine foundation types under dynamic loading conditions. Enhancements could include better representation of soil anisotropy, nonlinear behavior, and the effects of prolonged cyclic loading.
   - Investigating how changing climate patterns, such as rising sea levels and increased frequency of severe weather events, could affect the soil-structure interaction of wind turbine foundations in marine environments. This research would aim to predict future challenges and develop strategies to mitigate risks associated with climate change.
   - Conducting detailed studies on the properties of marine soils and their behavior under the specific conditions faced by offshore wind turbines. This could involve the development of new in-situ testing methods or the application of advanced sensing technologies to gather more accurate soil data for use in SSI models.
   - Utilizing advanced SSI models to explore and optimize different foundation designs for efficiency and resilience. This could include investigating alternative foundation concepts or configurations that may offer improved performance or cost-effectiveness in specific marine soil conditions.

4. **Non-Linear and Stochastic Modeling:** Wind turbines experience non-linear deformations, particularly under non-stationary aerodynamic loads. Thus, the non-linear analysis of wind turbines, considering various uncertainties in non-stationary loading conditions, warrants further exploration. In addition to uncertainties in excitation, there are inherent uncertainties in modeling. For instance, the drivetrain discussed in this study has undergone significant enhancements over time. Similarly, the baseline controller has been updated to manage increasingly complex scenarios. These aspects merit additional in-depth research in terms of uncertainties and reliability.

   - Focus on developing comprehensive dynamic models that accurately reflect the non-linear behavior of wind turbines under a range of wind speeds and directions, including turbulent and gusty conditions. It would involve a deep dive into the non-linear properties of materials, structural components, and their interactions under non-stationary loads. With the advent of faster counting systems, the Lagrangian formulation or Finite Element Analysis (FEA) in non-linear multi-body dynamics can prove to be an important tool to focus on the development of such computationally demanding models.

- Aim to incorporate randomness and uncertainty directly into the models of wind turbine loads and responses. This could include the variability in wind speed, direction, density, and turbulence intensity, as well as uncertainties in material properties and structural damping. Advanced probabilistic methods and statistical techniques could be used to predict the reliability and performance of turbines under real-world conditions.
- Focus on the drivetrain complexities, including gear backlash, bearing stiffness, and the non-linear behavior of drivetrain components under varying loads. This research should also consider the stochastic nature of wind variability and seek to enhance model accuracy and predictive capability.
- Conducting rigorous uncertainty analyses to identify and quantify the sources of uncertainty in wind turbine models, from aerodynamic loading to material properties and structural behavior. This could involve the use of techniques such as Monte Carlo simulations, Polynomial Chaos Expansion (PCE), or Bayesian methods to assess and improve the reliability of turbine models.

5. **Development of Advanced Control Algorithms**: Control techniques that can adapt to the non-linear and stochastic nature of wind turbine operation can be developed. Also, the performance of different controllers can be enhanced by investigating and validating robust control algorithms that are specifically designed for onshore or offshore wind turbines. This includes optimizing control algorithms in terms of safety and performance to minimize the impact of wave, wind, or seismically induced motions. A few research objectives under this domain are listed below.

    - Developing advanced control techniques for blade vibration and flutter instability of large turbines will remain an open problem throughout the future of the wind energy industry. As the demand for larger rotors increases, developing their efficient control techniques would pose different challenges. A few promising flow control algorithms are Dielectric Barrier Discharge (DBD) plasma, trailing edge flaps, sliding mode control of pitch angles, advanced double-pitch controlled rotors, etc. Further research in this domain would lead to new possibilities in terms of rotor speed stability and load control.
    - Apart from blade vibration and rotor speed stability, advanced generator torque control can prove to be very important in capturing maximum power during low wind speed. The model presented in this study can be extended to adapt different torque control algorithms and simulate their performance.
    - Tower vibration can also create a nuisance as it becomes more evident for long and slender towers. Recent works in advanced materials such as carbon fibre and steel composites, Shape Memory Alloy (SMA) patches, and tendons can help improve the strength properties of the structure. Also the latest active and semi-active vibration control devices can also be integrated into the present model and analyzed for their efficiency.

6. **Development and Validation Through Experiments:** The theoretical model presented in this thesis demonstrates promising control performance; however, it necessitates validation through suitable experiments through scaled models or in test turbines. This research would include the design of experiments to test these algorithms in real-world conditions, evaluating their performance in enhancing turbine efficiency and reducing wear and tear on components. A few research objectives in this domain are

    - Design and execute experimental studies using scaled models or full-scale test turbines to validate the developed model and control strategies. This would involve comparing theoretical predictions with observed behaviors under controlled and uncontrolled conditions, focusing on response patterns.
    - Develop non-linear aeroelastic models and validate their feasibility in predicting non-linear deformation through experimental studies. This research will focus on gathering sensor data on aerodynamic loads and induced strains in structural components such as the blades or the tower. The experimental results should serve as a benchmark in validating the developed mathematical models and checking their accuracy.
    - Utilize advanced sensors and real-time data analysis to improve the responsiveness and effectiveness of wind turbine control systems under nonlinear and uncertain conditions. This could include the development of algorithms that predictively adjust to anticipated load changes based on sensor input, enhancing safety and performance.

7. **Advanced Materials for Blade Design:** The wind turbine industry is constantly reviewing its materials in an effort to identify substitutes for the existing thermoset composite technology. Blades are a key component of wind turbines, and modern designs call for larger blades hence material selection has become more important. This selection process emphasizes various critical factors such as reduced weight, lower cost, enhanced performance, extended lifespan, simplified processing, and recyclability. The present work can lay the groundwork for investigating the development and integration of smart materials into the blade design, such as composites reinforced with nanomaterials, SMA, among many others. For example, carbon nanotubes are cylindrical carbon molecules with special properties that may be useful in wind turbine blades. These carbon nanotubes can be reinforced with different resins to exhibit different properties. These materials should aim to enhance the bending-torsion coupling effects beneficially and withstand the dynamic loads experienced by the blades over their operational life, potentially leading to greater efficiency and durability of wind turbines. Outlines for possible future research works within this domain are given below

   - Investigate the physical and chemical properties of various nanomaterials, focusing on their compatibility with composite resin systems used in blade manufacturing. Developing formulations for nanomaterials-reinforced composites and optimizing the dispersion of nanomaterials within the resin matrix to achieve the desired mechanical properties can be a viable area of research.
   - Conduct comprehensive studies on various SMA compositions to identify those with optimal mechanical properties for wind turbine blade applications. The SMA can be used in composite skin layup of the blades or as a tendon through the spar to enhance the stiffness and dynamic properties of the blade. FEA can be utilized to design blades that leverage the unique properties of SMAs for improved performance. Thereby finding the coupled mode shapes and stiffness properties of such blades.
   - With the known material properties, the multi-body dynamic model presented in this study can be further extended to simulate the behavior of advanced materials in blades under varying operating conditions, aiming to predict their performance and identify areas for material optimization in light of bending-torsion coupling.
   - Design and implement control systems that can dynamically adjust the shape and stiffness properties of the smart material-enhanced blades in response to real-time data on wind speed, direction, and turbine operational status.
   - Conduct testing of the prototype blades in controlled and real-world conditions to evaluate their performance, load reduction, and efficiency improvements over conventional designs. The real-time test data can be further used to tune the mathematical model and reduce inherent errors.

8. **Fatigue and Reliability Based Blade Design:** The intricate relationship between fatigue life, reliability of wind turbine blades, and the dynamics of their vibrations presents a fertile ground for advanced research. Such studies not only aim to enhance the operational efficiency and lifespan of wind turbines but also minimize maintenance costs and maximize energy output simultaneously. The blade fatigue life and reliability are bound to increase as a natural consequence due to reduced vibration (and subsequently stress/strain level) along different blade DOFs as reported in other literature [161, 267]. A detailed study of these derived quantities can be a further extension of the present work. Below are proposed future research works that delve into the domain of fatigue and reliability-based blade design, focusing on the potential impact of innovative design strategies

   - Investigating new materials or composites that offer superior resistance to fatigue. This research could involve the creation and testing of new alloys or composite materials that are lighter, stronger, and more resilient to the cyclic loads experienced by blades.
   - Developing or improving predictive models for the fatigue life of materials used in blade construction. This includes enhancing the accuracy of these models through the integration of real-world data from operational turbines or experimental setups, considering variables like environmental conditions and manufacturing defects.
   - Investigating blade design modifications or additions (such as winglets, vortex generators, or serrations) that could reduce the aerodynamic loads on blades, thereby reducing fatigue stress and extending their operational life.
   - Focusing on the development of multiscale models to better understand and predict how fatigue affects composite materials at different scales, from the microscopic (fiber-matrix interactions)

to the macroscopic (whole blade behavior). This research can help in designing more durable composite blades.

- Examine how different manufacturing techniques affect the reliability and fatigue life of blades. This could involve comparing traditional manufacturing methods with newer, potentially more efficient techniques such as additive manufacturing or investigating the effects of manufacturing-induced defects on fatigue life.

9. **Hybrid Energy Systems Integration:** Explore the integration of wind turbines with other renewable energy sources to create hybrid systems capable of providing more stable and reliable power output and simultaneously reducing vibrations in turbine components, thereby increasing its life. This could involve studying the dynamic interactions between wind turbines and other components like integrated solar panels, piezoelectric patches, or wave-energy converters in offshore environments. Below are several research topics focused on the exploration of hybrid energy systems integration:

   - Develop comprehensive models to simulate the dynamic interactions between wind turbines and wave-energy converters in offshore environments. This topic could include studying the synergies between these technologies in terms of energy capture and load balancing, as well as assessing the impact on the structural integrity and lifespan of offshore wind turbines.
   - Focus research on the integration of piezoelectric patches into wind turbine structures for dual purposes: harvesting energy from vibrations and simultaneously reducing vibration levels to extend the turbine's operational life. Research could include material optimization, placement strategies, and the development of control systems for maximizing energy conversion efficiency.
   - Examine the technical, economic, and environmental feasibility of deploying hybrid renewable energy systems in remote or off-grid locations. This could involve case studies comparing different hybrid system configurations, including wind, solar, and energy storage components, to identify optimal solutions for specific geographical and climatic conditions.
   - Investigate the optimal design and operational strategies for integrating wind turbines with solar photovoltaic (PV) panels in blades and towers. This research could explore how to maximize total energy output and smooth power supply variations through advanced control algorithms that consider the variability of both wind and solar resources.

10. **Predictive Maintenance and Health Monitoring:** Artificial Intelligence-based algorithms such as Machine Learning (ML) or Artificial Neural Networks (ANN) can be implemented to analyze data from high-fidelity multi-body dynamic models and real-world operational data. The goal would be to monitor the turbine's health and predict potential failures or maintenance needs, thereby reducing downtime and extending the lifespan of wind turbine components. A number of research objectives that delve into the application of AI for the predictive maintenance and health monitoring of wind turbines are listed below.

    - Investigate advanced signal processing techniques and data fusion strategies to enhance the quality and interpretability of data collected from wind turbine sensors. By applying ML algorithms to this enriched data, researchers could improve the sensitivity and specificity of health monitoring systems.
    - Implement artificial neural networks to process real-time data from sensors across the turbine structure and powertrain. The research could investigate how ANNs can be used to predict and adapt to changing load conditions, thereby preventing overstressing components and extending their useful life.
    - Explore the combination of different AI techniques, such as ML, ANN, and Deep Learning, to improve the accuracy and reliability of fault diagnosis and prognosis. This could involve developing models that can learn from a combination of simulated data and real-world operational anomalies to predict future maintenance needs more accurately.
    - Utilize artificial neural networks to process and interpret data from structural health monitoring sensors embedded in wind turbine blades. The focus should be on detecting early signs of wear, fatigue cracks, or other forms of damage, facilitating timely maintenance actions to prevent catastrophic failures.
    - Creating and training machine learning models to analyze vibration, temperature, and acoustic data for early detection of gearbox anomalies. This research could explore various ML algorithms and feature extraction techniques to improve prediction accuracy and reduce false alarm rates.

- Develop AI-based models that optimize maintenance strategies across an entire wind farm. This research would consider the logistical and operational complexities of managing multiple turbines to maximize overall efficiency and minimize downtime.

Each of these topics highlights a novel approach to harnessing the true potential of the wind energy sector. Further research on these above-mentioned topics based on the theoretical groundwork presented in this thesis can significantly enhance the reliability, efficiency, and economic viability of wind turbine operations by improving the accuracy and timeliness of maintenance decisions.

Appendix A

Coordinate Transformation

The coordinates used in this chapter can be converted from one form to another using a linear transformation following a small-angle approximation, which is independent of the rotation sequence. Hence, the generalized transformation matrix T_{xa}, which correlates coordinate system $\hat{a}$ with $\hat{x}$, has the following form

$$T_{xa} = \begin{bmatrix} \cos\theta_{x_1a_1} & \cos\theta_{x_1a_2} & \cos\theta_{x_1a_3} \\ \cos\theta_{x_2a_1} & \cos\theta_{x_2a_2} & \cos\theta_{x_2a_3} \\ \cos\theta_{x_3a_1} & \cos\theta_{x_3a_2} & \cos\theta_{x_3a_3} \end{bmatrix} \tag{A.1}$$

Here, the term $\theta_{x_1a_1}$, for example, represents the angle between its subscripts, where the first subscript corresponds to the unit vector $\hat{x}_1$ while the second one represents the same along $\hat{a}_1$ direction. In this manner, the coordinate system $\hat{x}$ can be transformed into $\hat{a}$ by the following expression

$$\begin{Bmatrix} \hat{a}_1 \\ \hat{a}_2 \\ \hat{a}_3 \end{Bmatrix} = T_{xa} \begin{Bmatrix} \hat{x}_1 \\ \hat{x}_2 \\ \hat{x}_3 \end{Bmatrix} \tag{A.2}$$

For example, the tower top coordinate system $\hat{b}$ can be rotated by yaw angle θ_Y in the $\hat{b}_2$ direction to obtain the nacelle coordinate system $\hat{c}$, which can be expressed as

$$\begin{Bmatrix} \hat{c}_1 \\ \hat{c}_2 \\ \hat{c}_3 \end{Bmatrix} = \begin{bmatrix} \cos\theta_Y & 0 & -\sin\theta_Y \\ 0 & 1 & 0 \\ -\sin\theta_Y & 0 & \cos\theta_Y \end{bmatrix} \begin{Bmatrix} \hat{b}_1 \\ \hat{b}_2 \\ \hat{b}_3 \end{Bmatrix} \tag{A.3}$$

Similarly, other coordinates can be transformed using the angles between them.

References

[1] W. De Goeij, M. Van Tooren, A. Beukers, Implementation of bending-torsion coupling in the design of a wind-turbine rotor-blade, Applied Energy 63 (3) (1999) 191–207.

[2] J. Jonkman, S. Butterfield, P. Passon, T. Larsen, T. Camp, J. Nichols, J. Azcona, A. Martinez, Offshore code comparison collaboration within IEA wind annex XXIII: phase II results regarding monopile foundation modeling, Tech. rep., National Renewable Energy Lab.(NREL), Golden, CO (United States) (2008).

[3] M. Lee, K.-T. Bae, I. W. Lee, M. Yoo, Cyclic py curves of monopiles in dense dry sand using centrifuge model tests, Applied Sciences 9 (8) (2019) 1641.

[4] DNVGL-RP-0005:2014-06, RP-C203: Fatigue design of offshore steel structures, Det Norske Veritas.

[5] J. Jonkman, S. Butterfield, W. Musial, G. Scott, Definition of a 5-mw reference wind turbine for offshore system development, Tech. rep., National Renewable Energy Lab.(NREL), Golden, CO (United States) (2009).

[6] J. Jonkman, Definition of the floating system for phase iv of oc3, Tech. rep., National Renewable Energy Lab.(NREL), Golden, CO (United States) (2010).

[7] R. T. Watson, Intergovernmental panel on climate change (ipcc) third assessment report. climate change 2001: Synthesis report (2001).

[8] B. Metz, O. Davidson, H. De Coninck, et al., Carbon dioxide capture and storage: special report of the intergovernmental panel on climate change, Cambridge University Press, 2005.

[9] T. Burton, N. Jenkins, D. Sharpe, E. Bossanyi, Wind energy handbook, John Wiley and Sons, 2011.

[10] D. Roberts, These huge new wind turbines are a marvel. they're also the future, vox. com.

[11] J. Winters, Z. Saunders, The largest wind turbine ever, Mechanical Engineering 140 (12) (2018) 31–31.

[12] T. R. Kane, D. A. Levinson, Dynamics, theory and applications, McGraw Hill, 1985.

[13] J. M. Jonkman, Modeling of the uae wind turbine for refinement of fast_ad, Tech. rep., National Renewable Energy Lab., Golden, CO (US) (2003).

[14] A. Mitra, S. Sarkar, A. Chakraborty, S. Das, Sway vibration control of floating horizontal axis wind turbine by modified spar-torus combination, Ocean Engineering 219 (2021) 108232.

[15] M. M. Sajeer, A. Mitra, A. Chakraborty, Multi-body dynamic analysis of offshore wind turbine considering soil-structure interaction for fatigue design of monopile, Soil Dynamics and Earthquake Engineering 144 (2021) 106674.

[16] J. C. Houbolt, G. W. Brooks, Differential equations of motion for combined flapwise bending, chordwise bending, and torsion of twisted nonuniform rotor blades, Vol. 1346, National Advisory Committee for Aeronautics, 1957.

[17] D. H. Hodges, E. H. Dowell, Nonlinear equations of motion for the elastic bending and torsion of twisted nonuniform rotor blades, Tech. rep. (1974).

[18] D. H. Hodges, R. A. Ormiston, D. A. Peters, On the nonlinear deformation geometry of euler-bernoulli beams, Tech. rep. (1980).

[19] D. H. Hodges, Nonlinear equations for dynamics of pretwisted beams undergoing small strains and large rotations, Tech. rep. (1985).

[20] B. Panda, I. Chopra, Dynamics of composite rotor blades in forward flight., VERTICA. 11 (1) (1987) 187–209.

[21] R. Chandra, I. Chopra, Structural response of composite beams and blades with elastic couplings, Composites Engineering 2 (5-7) (1992) 347–374.

[22] A. Fasana, S. Marchesiello, Rayleigh-ritz analysis of sandwich beams, Journal of sound and vibration 241 (4) (2001) 643–652.

[23] D. H. Hodges, Vibration and response of nonuniform rotating beams with discontinuities, Journal of the American Helicopter Society 24 (4) (1979) 43–50.

[24] J. Banerjee, Development of an exact dynamic stiffness matrix for free vibration analysis of a twisted timoshenko beam, Journal of Sound and Vibration 270 (1-2) (2004) 379–401.

[25] J. Banerjee, H. Su, Dynamic stiffness formulation and free vibration analysis of a spinning composite beam, Computers & structures 84 (19-20) (2006) 1208–1214.

[26] J. Banerjee, H. Su, C. Jayatunga, A dynamic stiffness element for free vibration analysis of composite beams and its application to aircraft wings, Computers & Structures 86 (6) (2008) 573–579.

[27] H. H. Yoo, J. H. Park, J. Park, Vibration analysis of rotating pre-twisted blades, Computers & Structures 79 (19) (2001) 1811–1819.

[28] I. Goulos, V. Pachidis, P. Pilidis, Lagrangian formulation for the rapid estimation of helicopter rotor blade vibration characteristics, The Aeronautical Journal 118 (1206) (2014) 861–901.

[29] I. Goulos, V. Pachidis, P. Pilidis, Helicopter rotor blade flexibility simulation for aeroelasticity and flight dynamics applications, Journal of the American Helicopter Society 59 (4) (2014) 1–18.

[30] G. Zhao, Z. Wu, Coupling vibration analysis of rotating three-dimensional cantilever beam, Computers & Structures 179 (2017) 64–74.

[31] A. Castillo Pardo, I. Goulos, V. Pachidis, Modelling and analysis of coupled flap-lag-torsion vibration characteristics helicopter rotor blades, Proceedings of the Institution of Mechanical Engineers, Part G: Journal of Aerospace Engineering 231 (10) (2017) 1804–1823.

[32] Y. Oh, H. H. Yoo, Vibration analysis of a rotating pre-twisted blade considering the coupling effects of stretching, bending, and torsion, Journal of Sound and Vibration 431 (2018) 20–39.

[33] M. M. Abdel Hafeez, A. A. El-Badawy, Effect of mass and shear center offset on the dynamic response of a rotating blade, Journal of Vibration and Control 23 (14) (2017) 2235–2255.

[34] Y. Bichiou, A. Abdelkefi, M. Hajj, Nonlinear aeroelastic characterization of wind turbine blades, Journal of Vibration and Control 22 (3) (2016) 621–631.

[35] S. Kessentini, S. Choura, F. Najar, M. Franchek, Modeling and dynamics of a horizontal axis wind turbine, Journal of Vibration and Control 16 (13) (2010) 2001–2021.

[36] N. Kang, S. Chul Park, J. Park, S. N. Atluri, Dynamics of flexible tower-blade and rigid nacelle system: dynamic instability due to their interactions in wind turbine, Journal of Vibration and Control 22 (3) (2016) 826–836.

[37] R. Rafiee, M. Tahani, M. Moradi, Simulation of aeroelastic behavior in a composite wind turbine blade, Journal of Wind Engineering and Industrial Aerodynamics 151 (2016) 60–69.

[38] A. R. Stäblein, M. H. Hansen, D. R. Verelst, Modal properties and stability of bend–twist coupled wind turbine blades, Wind Energy Science 2 (1) (2017) 343–360.

[39] D. Lobitz, D. Laino, Load mitigation with twist-coupled hawt blades, in: 37th Aerospace Sciences Meeting and Exhibit, 1999, p. 33.

[40] M. O. Gözcü, A. Kayran, Investigation of the effect of bending twisting coupling on the loads in wind turbines with superelement blade definition, in: Journal of physics: conference series, Vol. 524, IOP Publishing, 2014, p. 012040.

[41] K. Hayat, A. G. M. de Lecea, C. D. Moriones, S. K. Ha, Flutter performance of bend–twist coupled large-scale wind turbine blades, Journal of Sound and Vibration 370 (2016) 149–162.

[42] P. Shakya, M. R. Sunny, D. K. Maiti, A parametric study of flutter behavior of a composite wind turbine blade with bend-twist coupling, Composite Structures 207 (2019) 764–775.

[43] S. Adhikari, S. Bhattacharya, Vibrations of wind-turbines considering soil-structure interaction, Wind and Structures 14 (2) (2011) 85.

[44] S. Bisoi, S. Haldar, Dynamic analysis of offshore wind turbine in clay considering soil–monopile–tower interaction, Soil Dynamics and Earthquake Engineering 63 (2014) 19–35.

[45] H. Zuo, K. Bi, H. Hao, Dynamic analyses of operating offshore wind turbines including soil-structure interaction, Engineering Structures 157 (2018) 42–62.

[46] S. Bisoi, S. Haldar, Design of monopile supported offshore wind turbine in clay considering dynamic soil–structure-interaction, Soil Dynamics and Earthquake Engineering 73 (2015) 103–117.

[47] X. N. Rong, R. Q. Xu, H. Y. Wang, S. Y. Feng, Analytical solution for natural frequency of monopile, Wind and Structures 25 (5) (2017) 459–474.

[48] S. Bhattacharya, Design of foundations for offshore wind turbines, Wiley Online Library, 2019.

[49] A. Banerjee, T. Chakraborty, V. Matsagar, M. Achmus, Dynamic analysis of an offshore wind turbine under random wind and wave excitation with soil-structure interaction and blade tower coupling, Soil Dynamics and Earthquake Engineering 125 (2019) 105699.

[50] E. Kementzetzidis, S. Corciulo, W. G. Versteijlen, F. Pisano, Geotechnical aspects of offshore wind turbine dynamics from 3D non-linear soil-structure simulations, Soil Dynamics and Earthquake Engineering 120 (2019) 181–199.

[51] L. J. Prendergast, K. Gavin, A comparison of initial stiffness formulations for small-strain soil–pile dynamic Winkler modelling, Soil Dynamics and Earthquake Engineering 81 (2016) 27–41.

[52] L. Prendergast, W. Wu, K. Gavin, Experimental application of FRF-based model updating approach to estimate soil mass and stiffness mobilised under pile impact tests, Soil Dynamics and Earthquake Engineering 123 (2019) 1–15.

[53] J. Li, X. Wang, Y. Guo, X. B. Yu, The loading behavior of innovative monopile foundations for offshore wind turbine based on centrifuge experiments, Renewable Energy 152 (2020) 1109–1120.

[54] G. Katsikogiannis, E. E. Bachynski, A. M. Page, Fatigue sensitivity to foundation modelling in different operational states for the DTU 10MW monopile-based offshore wind turbine, Journal of Physics: Conference Series 1356 (1) (2019) 012019.

[55] S. Schafhirt, A. M. Page, G. R. Eiksund, M. Muskulus, Influence of soil parameters on the fatigue lifetime of offshore wind turbines with monopile support structure, Energy Procedia 94 (2016) 347–356.

[56] R. Rezaei, P. Fromme, P. Duffour, Fatigue life sensitivity of monopile-supported offshore wind turbines to damping, Renewable Energy 123 (2018) 450–459.

[57] W. Carswell, J. Johansson, F. Løvholt, S. Arwade, C. Madshus, D. DeGroot, A. Myers, Foundation damping and the dynamics of offshore wind turbine monopiles, Renewable energy 80 (2015) 724–736.

[58] S. Aasen, A. M. Page, K. S. Skau, T. A. Nygaard, Effect of foundation modelling on the fatigue lifetime of a monopile-based offshore wind turbine, Wind Energy Science 2 (2017) 361–376.

[59] E. Marino, A. Giusti, L. Manuel, Offshore wind turbine fatigue loads: The influence of alternative wave modeling for different turbulent and mean winds, Renewable Energy 102 (2017) 157–169.

[60] R. De Risi, S. Bhattacharya, K. Goda, Seismic performance assessment of monopile-supported offshore wind turbines using unscaled natural earthquake records, Soil Dynamics and Earthquake Engineering 109 (2018) 154–172.

[61] I. B. Løken, A. M. Kaynia, Effect of foundation type and modelling on dynamic response and fatigue of offshore wind turbines, Wind Energy 22 (12) (2019) 1667–1683.

[62] A. Jacob, A. Mehmanparast, R. D'Urzo, J. Kelleher, Experimental and numerical investigation of residual stress effects on fatigue crack growth behaviour of S355 steel weldments, International Journal of Fatigue 128 (2019) 105196.

[63] V. Igwemezie, A. Mehmanparast, Waveform and frequency effects on corrosion-fatigue crack growth behaviour in modern marine steels, International Journal of Fatigue 134 (2020) 105484.

[64] S. B. Kim, G. L. Yoon, H. Y. Jin, J. H. Lee, Reliability analysis of laterally loaded piles for an offshore wind turbine support structure using response surface methodology, Wind and Structures, An International Journal 21 (6) (2015) 597–607.

[65] J. H. Yi, S. B. Kim, G. L. Yoon, L. V. Andersen, Natural frequency of bottom-fixed offshore wind turbines considering pile-soil-interaction with material uncertainties and scouring depth, Wind and Structures 21 (6) (2015) 625–639.

[66] S. Haldar, J. Sharma, D. Basu, Probabilistic analysis of monopile-supported offshore wind turbine in clay, Soil Dynamics and Earthquake Engineering 105 (2018) 171–183.

[67] R. Teixeira, M. Nogal, A. O'Connor, J. Nichols, A. Dumas, Stress-cycle fatigue design with kriging applied to offshore wind turbines, International Journal of Fatigue 125 (2019) 454–467.

[68] J. Velarde, C. Kramhøft, J. D. Sørensen, Global sensitivity analysis of offshore wind turbine foundation fatigue loads, Renewable energy 140 (2019) 177–189.

[69] M. Jimenez-Martinez, Fatigue of offshore structures: A review of statistical fatigue damage assessment for stochastic loadings, International Journal of Fatigue 132 (2020) 105327.

[70] F. G. Nielsen, T. D. Hanson, B. Skaare, Integrated dynamic analysis of floating offshore wind turbines, in: International conference on offshore mechanics and arctic engineering, Vol. 47462, 2006, pp. 671–679.

[71] Y. Bazilevs, M.-C. Hsu, J. Kiendl, R. Wüchner, K.-U. Bletzinger, 3d simulation of wind turbine rotors at full scale. part ii: Fluid–structure interaction modeling with composite blades, International Journal for numerical methods in fluids 65 (1-3) (2011) 236–253.

[72] M. K. Al-Solihat, M. Nahon, K. Behdinan, Dynamic modeling and simulation of a spar floating offshore wind turbine with consideration of the rotor speed variations, Journal of Dynamic Systems, Measurement, and Control 141 (8) (2019) 081014.

[73] J. O'Brien, T. Young, D. O'Mahoney, P. Griffin, Horizontal axis wind turbine research: A review of commercial cfd, fe codes and experimental practices, Progress in Aerospace Sciences 92 (2017) 1–24.

[74] M. B. Ageze, Y. Hu, H. Wu, et al., Wind turbine aeroelastic modeling: basics and cutting edge trends, International Journal of Aerospace Engineering 2017.

[75] Z. Ullah, N. Muhammad, D.-H. Choi, Effect of hydrostatic nonlinearity on the large amplitude response of a spar type floating wind turbine, Ocean Engineering 172 (2019) 803–816.

[76] J. M. Jonkman, M. L. Buhl Jr, et al., Fast user's guide, Tech. rep., National Renewable Energy Lab.(NREL), Golden, CO (United States) (2005).

[77] X. Li, C. Zhu, Z. Fan, X. Chen, J. Tan, Effects of the yaw error and the wind-wave misalignment on the dynamic characteristics of the floating offshore wind turbine, Ocean engineering 199 (2020) 106960.

[78] R. Kyle, Y. C. Lee, W.-G. Früh, Propeller and vortex ring state for floating offshore wind turbines during surge, Renewable Energy 155 (2020) 645–657.

[79] L. Li, Y. Liu, Z. Yuan, Y. Gao, Dynamic and structural performances of offshore floating wind turbines in turbulent wind flow, Ocean Engineering 179 (2019) 92–103.

[80] L. Liu, H. Bian, Z. Du, C. Xiao, Y. Guo, W. Jin, Reliability analysis of blade of the offshore wind turbine supported by the floating foundation, Composite Structures 211 (2019) 287–300.

[81] Y. Chevillotte, Y. Marco, G. Bles, K. Devos, M. Keryer, M. Arhant, P. Davies, Fatigue of improved polyamide mooring ropes for floating wind turbines, Ocean Engineering 199 (2020) 107011.

[82] H.-D. Pham, F. Schoefs, P. Cartraud, T. Soulard, H.-H. Pham, C. Berhault, Methodology for modeling and service life monitoring of mooring lines of floating wind turbines, Ocean Engineering 193 (2019) 106603.

[83] NWTC Information Portal (IECWind), https://nwtc.nrel.gov/IECWind, [Last modified 28-September-2014 ; Accessed 01-April-2020].

[84] NWTC Information Portal (TurbSim), https://nwtc.nrel.gov/TurbSim, [Last modified 14-June-2016; Accessed 13-November-2019] (2008).

[85] B. J. Jonkman, TurbSim user's guide: Version 1.50, Tech. rep., National Renewable Energy Laboratory (NREL), Golden, CO (United States) (2009).

[86] I. E. Commission, et al., Iec 61400-1: Wind turbines part 1: Design requirements, International Electrotechnical Commission.

[87] IEC-61400-3, Wind turbines - part 3: Design requirements for offshore wind turbines, International Electrotechnical Commission.

[88] R. W. Thresher, A. Wright, E. Hershberg, A computer analysis of wind turbine blade dynamic loads, Journal of solar energy engineering 108 (1) (1986) 17–25.

[89] A. Wright, M. Buhl, R. Thresher, Flap (force and loads analysis program) code development and validation, Tech. rep., Solar Energy Research Inst., Golden, CO (USA) (1988).

[90] M. Robinson, M. Hand, D. Simms, S. Schreck, Horizontal axis wind turbine aerodynamics: three-dimensional, unsteady, and separated flow influences, Tech. rep., National Renewable Energy Lab., Golden, CO (US) (1999).

[91] Y. Song, CFD simulation of the flow around NREL phase VI wind turbine.

[92] E. P. Duque, M. D. Burklund, W. Johnson, Navier-Stokes and comprehensive analysis performance predictions of the NREL phase VI experiment, J. Sol. Energy Eng. 125 (4) (2003) 457–467.

[93] N. Goundarzi, Computational fluid dynamics methods for wind turbines performance analysis, in: Advanced Wind Turbine Technology, Springer, 2018, pp. 47–58.

[94] NWTC information portal (AeroDyn), https://nwtc.nrel.gov/AeroDyn, [Last modified 25-May-2017; Accessed 04-December-2019].

[95] H. Glauert, The analysis of experimental results in the windmill brake and vortex ring states of an airscrew, HM Stationery Office, 1926.

[96] M. L. Buhl Jr, New empirical relationship between thrust coefficient and induction factor for the turbulent windmill state, Tech. rep., National Renewable Energy Lab.(NREL), Golden, CO (United States) (2005).

[97] Z. Du, M. Selig, A 3D stall-delay model for horizontal axis wind turbine performance prediction, in: 1998 ASME Wind Energy Symposium, 1998, p. 21.

[98] A. Eggers, K. Chaney, R. Digumarthi, An assessment of approximate modeling of aerodynamic loads on the UAE rotor, in: ASME 2003 Wind Energy Symposium, American Society of Mechanical Engineers Digital Collection, 2003, pp. 283–292.

[99] S. A. Ning, A simple solution method for the blade element momentum equations with guaranteed convergence, Wind Energy 17 (9) (2014) 1327–1345.

[100] W. J. Pierson Jr, L. Moskowitz, A proposed spectral form for fully developed wind seas based on the similarity theory of SA Kitaigorodskii, Journal of geophysical research 69 (24) (1964) 5181–5190.

[101] K. Hasselmann, T. Barnett, E. Bouws, H. Carlson, D. Cartwright, K. Enke, J. Ewing, H. Gienapp, D. Hasselmann, P. Kruseman, et al., Measurements of wind-wave growth and swell decay during the Joint North Sea Wave Project (JONSWAP), Ergänzungsheft 8-12.

[102] P. Jamieson, T. Camp, D. Quarton, Wind turbine design for offshore, in: Proceedings of the Offshore Wind Energy in Mediterranean and European Seas Conference, CEC/EWEA/IEA Sicily, 2000, pp. 405–414.

[103] M. H. Hansen, Aeroelastic instability problems for wind turbines, Wind Energy: An International Journal for Progress and Applications in Wind Power Conversion Technology 10 (6) (2007) 551–577.

[104] K. Thomsen, J. T. Petersen, E. Nim, S. Øye, B. Petersen, A method for determination of damping for edgewise blade vibrations, Wind Energy: An International Journal for Progress and Applications in Wind Power Conversion Technology 3 (4) (2000) 233–246.

[105] V. Riziotis, S. Voutsinas, E. Politis, P. Chaviaropoulos, Aeroelastic stability of wind turbines: the problem, the methods and the issues, Wind Energy: An International Journal for Progress and Applications in Wind Power Conversion Technology 7 (4) (2004) 373–392.

[106] P. Murtagh, B. Basu, B. Broderick, Along-wind response of a wind turbine tower with blade coupling subjected to rotationally sampled wind loading, Engineering structures 27 (8) (2005) 1209–1219.

[107] Z. L. Zhang, J. B. Chen, J. Li, Theoretical study and experimental verification of vibration control of offshore wind turbines by a ball vibration absorber, Structure and Infrastructure Engineering 10 (8) (2014) 1087–1100.

[108] M. A. Lackner, M. A. Rotea, Passive structural control of offshore wind turbines, Wind energy 14 (3) (2011) 373–388.

[109] P. H. Kirkegaard, S. R. Nielsen, B. Poulsen, J. Andersen, L. Pedersen, B. Pedersen, Semiactive vibration control of a wind turbine tower using an mr damper, in: Structural Dynamics: EURODYN 2002, CRC Press/Balkema, 2002, pp. 1575–1580.

[110] J.-L. Chen, C. T. Georgakis, Spherical tuned liquid damper for vibration control in wind turbines, Journal of Vibration and Control 21 (10) (2015) 1875–1885.

[111] A. F. Mensah, L. Dueñas Osorio, Improved reliability of wind turbine towers with tuned liquid column dampers (TLCDs), Structural Safety 47 (2014) 78–86.

[112] S. Colwell, B. Basu, Tuned liquid column dampers in offshore wind turbines for structural control, Engineering Structures 31 (2) (2009) 358–368.

[113] Z. Zhang, B. Basu, S. R. Nielsen, Tuned liquid column dampers for mitigation of edgewise vibrations in rotating wind turbine blades, Structural Control and Health Monitoring 22 (3) (2015) 500–517.

[114] F. Ricciardelli, A. Occhiuzzi, P. Clemente, Semi-active tuned mass damper control strategy for wind-excited structures, Journal of Wind Engineering and Industrial Aerodynamics 88 (1) (2000) 57–74.

[115] B. Ollgaard, S. P. Jensen, Wind turbine tower having a damper, uS Patent 9,657,717 (May 23 2017).

[116] ESM Tuned Mass Dampers, https://www.esm-gmbh.de/en/products/#tuned-mass-dampers, accessed: 2021-09-03.

[117] Xi Engineering Consultants, Tuned Mass Dampers, https://xiengineering.com/technologies/tuned-mass-dampers-2/, accessed: 2021-09-03.

[118] P. Murtagh, A. Ghosh, B. Basu, B. Broderick, Passive control of wind turbine vibrations including blade/tower interaction and rotationally sampled turbulence, Wind Energy 11 (4) (2008) 305–317.

[119] M. A. Lackner, M. A. Rotea, Structural control of floating wind turbines, Mechatronics 21 (4) (2011) 704–719.

[120] M. Rezaee, A. M. Aly, Vibration control in wind turbines for performance enhancement: A comparative study, Wind and Structures 22 (1).

[121] C. Sun, V. Jahangiri, Bi-directional vibration control of offshore wind turbines using a 3d pendulum tuned mass damper, Mechanical Systems and Signal Processing 105 (2018) 338–360.

[122] M. Asareh, I. Prowell, Seismic loading for fast, Contract 303 (275) (2011) e3000.

[123] J. Yang, E. He, Coupled modeling and structural vibration control for floating offshore wind turbine, Renewable Energy.

[124] Z. Jiang, The impact of a passive tuned mass damper on offshore single-blade installation, Journal of Wind Engineering and Industrial Aerodynamics 176 (2018) 65–77.

[125] S. Sarkar, B. Fitzgerald, Vibration control of spar-type floating offshore wind turbine towers using a tuned mass-damper-inerter, Structural Control and Health Monitoring 27 (1) (2020) e2471.

[126] S. Xie, X. Jin, J. He, C. Zhang, Structural responses suppression for a barge-type floating wind turbine with a platform-based TMD, IET Renewable Power Generation 13 (13) (2019) 2473–2479.

[127] J. Yang, E. He, Y. Hu, Dynamic modeling and vibration suppression for an offshore wind turbine with a tuned mass damper in floating platform, Applied Ocean Research 83 (2019) 21–29.

[128] M. Ghassempour, G. Failla, F. Arena, Vibration mitigation in offshore wind turbines via tuned mass damper, Engineering Structures 183 (2019) 610–636.

[129] I. Enevoldsen, K. Mørk, Effects of a vibration mass damper in a wind turbine tower, Journal of Structural Mechanics 24 (2) (1996) 155–187.

[130] J.-l. Chen, Y. Zhao, O. Cong, M.-j. He, Vibration control using double-response damper and site measurements on wind turbine, Structural Control and Health Monitoring 25 (9) (2018) e2200.

[131] J. Chen, Y. Wang, Y. Zhao, Y. Feng, Experimental research on design parameters of basin tuned and particle damper for wind turbine tower on shaker, Structural Control and Health Monitoring 26 (11) (2019) e2440.

[132] R. R. Gerges, B. J. Vickery, Wind tunnel study of the across-wind response of a slender tower with a nonlinear tuned mass damper, Journal of Wind Engineering and Industrial Aerodynamics 91 (8) (2003) 1069–1092.

[133] B. Fitzgerald, B. Basu, Active tuned mass damper control of wind turbine nacelle/tower vibrations with damaged foundations, in: Key Engineering Materials, Vol. 569, Trans Tech Publ, 2013, pp. 660–667.

[134] A. Hemmati, E. Oterkus, Semi-active structural control of offshore wind turbines considering damage development, Journal of Marine Science and Engineering 6 (3) (2018) 102.

[135] B. Fitzgerald, B. Basu, S. R. Nielsen, Active tuned mass dampers for control of in-plane vibrations of wind turbine blades, Structural Control and Health Monitoring 20 (12) (2013) 1377–1396.

[136] M. L. Brodersen, A. S. Bjørke, J. Høgsberg, Active tuned mass damper for damping of offshore wind turbine vibrations, Wind Energy 20 (5) (2017) 783–796.

[137] S. Sarkar, A. Chakraborty, Optimal design of semiactive MR-TLCD for along-wind vibration control of horizontal axis wind turbine tower, Structural Control and Health Monitoring 25 (2) (2018) e2083.

[138] Y. Hu, E. He, Active structural control of a floating wind turbine with a stroke-limited hybrid mass damper, Journal of Sound and Vibration 410 (2017) 447–472.

[139] P. Martynowicz, M. Rosół, Wind turbine tower-nacelle system with mr tuned vibration absorber: Modelling, test rig, and identification, in: 2019 20th International Carpathian Control Conference (ICCC), IEEE, 2019, pp. 1–6.

[140] B. Fitzgerald, S. Sarkar, A. Staino, Improved reliability of wind turbine towers with active tuned mass dampers (ATMDs), Journal of Sound and Vibration 419 (2018) 103–122.

[141] F. Madsen, T. Nielsen, T. Kim, H. Bredmose, A. Pegalajar-Jurado, R. Mikkelsen, A. Lomholt, M. Borg, M. Mirzaei, P. Shin, Experimental analysis of the scaled dtu10mw tlp floating wind turbine with different control strategies, Renewable Energy 155 (2020) 330–346.

[142] C. Han, R. Nagamune, Platform position control of floating wind turbines using aerodynamic force, Renewable Energy 151 (2020) 896–907.

[143] C. Sun, Mitigation of offshore wind turbine responses under wind and wave loading: Considering soil effects and damage, Structural Control and Health Monitoring 25 (3) (2018) e2117.

[144] J. He, X. Jin, S. Xie, L. Cao, Y. Lin, N. Wang, Multi-body dynamics modeling and tmd optimization based on the improved afsa for floating wind turbines, Renewable Energy 141 (2019) 305–321.

[145] M. C. Smith, Synthesis of mechanical networks: the inerter, IEEE Transactions on automatic control 47 (10) (2002) 1648–1662.

[146] M. J. Muliawan, M. Karimirad, T. Moan, Z. Gao, Stc (spar-torus combination): a combined spar-type floating wind turbine and large point absorber floating wave energy converter—promising and challenging, in: International Conference on Offshore Mechanics and Arctic Engineering, Vol. 44946, American Society of Mechanical Engineers, 2012, pp. 667–676.

[147] M. J. Muliawan, M. Karimirad, T. Moan, Dynamic response and power performance of a combined spar-type floating wind turbine and coaxial floating wave energy converter, Renewable energy 50 (2013) 47–57.

[148] M. J. Muliawan, Z. Gao, T. Moan, Application of the contour line method for estimating extreme response in mooring lines of a two-body floating wave energy converter, in: International Conference on Offshore Mechanics and Arctic Engineering, Vol. 44915, American Society of Mechanical Engineers, 2012, pp. 429–439.

[149] M. J. Muliawan, M. Karimirad, Z. Gao, T. Moan, Extreme responses of a combined spar-type floating wind turbine and floating wave energy converter (stc) system with survival modes, Ocean Engineering 65 (2013) 71–82.

[150] L. Wan, Z. Gao, T. Moan, Model test of the stc concept in survival modes, in: International Conference on Offshore Mechanics and Arctic Engineering, Vol. 45530, American Society of Mechanical Engineers, 2014, p. V09AT09A010.

[151] N. Ren, Z. Ma, B. Shan, D. Ning, J. Ou, Experimental and numerical study of dynamic responses of a new combined tlp type floating wind turbine and a wave energy converter under operational conditions, Renewable Energy 151 (2020) 966–974.

[152] M. Yue, Q. Liu, C. Li, Q. Ding, S. Cheng, H. Zhu, Effects of heave plate on dynamic response of floating wind turbine spar platform under the coupling effect of wind and wave, Ocean Engineering 201 (2020) 107103.

[153] T. Sant, D. Buhagiar, R. N. Farrugia, Evaluating a new concept to integrate compressed air energy storage in spar-type floating offshore wind turbine structures, Ocean Engineering 166 (2018) 232–241.

[154] J.-M. Choung, S.-I. Jeon, M.-S. Lee, Fatigue design of mooring lines of floating type combined renewable energy platforms, International Journal of Ocean System Engineering 1 (3) (2011) 171–179.

[155] N. Ren, Z. Gao, T. Moan, L. Wan, Long-term performance estimation of the spar–torus-combination (stc) system with different survival modes, Ocean engineering 108 (2015) 716–728.

[156] V. Jaksic, C. Wright, J. Murphy, C. Afeef, S. Ali, D. Mandic, V. Pakrashi, Dynamic response mitigation of floating wind turbine platforms using tuned liquid column dampers, Philosophical Transactions of the Royal Society A: Mathematical, Physical and Engineering Sciences 373 (2035) (2015) 20140079.

[157] S. Sarkar, A. Chakraborty, Development of semi-active vibration control strategy for horizontal axis wind turbine tower using multiple magneto-rheological tuned liquid column dampers, Journal of Sound and Vibration 457 (2019) 15–36.

[158] J. Chen, C. Yuan, J. Li, Q. Xu, Semi-active fuzzy control of edgewise vibrations in wind turbine blades under extreme wind, Journal of Wind Engineering and Industrial Aerodynamics 147 (2015) 251–261.

[159] H. Biglari, V. Fakhari, Edgewise vibration reduction of small size wind turbine blades using shunt damping, Journal of Vibration and Control 26 (3-4) (2020) 186–199.

[160] A. Staino, B. Basu, S. R. Nielsen, Actuator control of edgewise vibrations in wind turbine blades, Journal of Sound and Vibration 331 (6) (2012) 1233–1256.

[161] M. M. Sajeer, A. Mitra, A. Chakraborty, Spinning finite element analysis of longitudinally stiffened horizontal axis wind turbine blade for fatigue life enhancement, Mechanical Systems and Signal Processing 145 (2020) 106924.

[162] P. Haghdoust, A. L. Conte, S. Cinquemani, N. Lecis, Investigation of shape memory alloy embedded wind turbine blades for the passive control of vibrations, Smart Materials and Structures 27 (10) (2018) 105012.

[163] S. Das, M. M. Sajeer, A. Chakraborty, Vibration control of horizontal axis offshore wind turbine blade using SMA stiffener, Smart Materials and Structures 28 (9) (2019) 095025. doi:10.1088/1361-665x/ab1174.

[164] S. Das, M. Mohamed Sajeer, A. Chakraborty, S. Sarkar, Shape memory alloy-based centrifugal stiffening for response reduction of horizontal axis wind turbine blade, Structural Control and Health Monitoring 28 (3) (2021) e2669.

[165] W. Tao, B. Basu, J. Li, Reliability analysis of active tendon-controlled wind turbines by a computationally efficient wavelet-based probability density evolution method, Structural Control and Health Monitoring 25 (3) (2018) e2078.

[166] A. Mitra, A. Chakraborty, Multi-objective optimization of composite airfoil fibre orientation under bending–torsion coupling for improved aerodynamic efficiency of horizontal axis wind turbine blade, Journal of Wind Engineering and Industrial Aerodynamics 221 (2022) 104881.

[167] T. Ekelund, Yaw control for reduction of structural dynamic loads in wind turbines, Journal of Wind Engineering and Industrial Aerodynamics 85 (3) (2000) 241–262.

[168] X. Lachenal, S. Daynes, P. M. Weaver, A zero torsional stiffness twist morphing blade as a wind turbine load alleviation device, Smart Materials and Structures 22 (6) (2013) 065016.

[169] S. Daynes, P. Weaver, Design and testing of a deformable wind turbine blade control surface, Smart Materials and Structures 21 (10) (2012) 105019.

[170] S. S. Govindan, A. E. X. Santiago, Optimized dielectric barrier discharge-plasma actuator for active flow control in wind turbine, Structural Control and Health Monitoring 26 (12) (2019) e2454.

[171] W. H. A. Lio, Blade-pitch control for wind turbine load reductions, Springer, 2018.

[172] O. Apata, D. Oyedokun, An overview of control techniques for wind turbine systems, Scientific African 10 (2020) e00566.

[173] R. Gao, Z. Gao, Pitch control for wind turbine systems using optimization, estimation and compensation, Renewable Energy 91 (2016) 501–515.

[174] L. Mackowski, T. Carolus, Wind turbine trailing edge noise: Mitigation of normal amplitude modulation by individual blade pitch control, Journal of Sound and Vibration 510 (2021) 116279.

[175] E. Mohammadi, R. Fadaeinedjad, G. Moschopoulos, Implementation of internal model based control and individual pitch control to reduce fatigue loads and tower vibrations in wind turbines, Journal of sound and vibration 421 (2018) 132–152.

[176] K. Kim, H.-G. Kim, C.-j. Kim, I. Paek, C. L. Bottasso, F. Campagnolo, Design and validation of demanded power point tracking control algorithm of wind turbine, International Journal of Precision Engineering and Manufacturing-Green Technology 5 (2018) 387–400.

[177] V. Petrović, M. Jelavić, M. Baotić, Advanced control algorithms for reduction of wind turbine structural loads, Renewable Energy 76 (2015) 418–431.

[178] A. Kusiak, W. Li, Z. Song, Dynamic control of wind turbines, Renewable energy 35 (2) (2010) 456–463.

[179] A. D. Wright, M. J. Balas, Design of state-space-based control algorithms for wind turbine speed regulation, J. Sol. Energy Eng. 125 (4) (2003) 386–395.

[180] E. Bossanyi, Wind turbine control for load reduction, Wind Energy: An International Journal for Progress and Applications in Wind Power Conversion Technology 6 (3) (2003) 229–244.

[181] N. Bao, Z. Ye, Active pitch control in larger scale fixed speed horizontal axis wind turbine systems part i: Linear controller design, Wind Engineering 25 (6) (2001) 339–351.

[182] I. P. Girsang, J. S. Dhupia, Collective pitch control of wind turbines using stochastic disturbance accommodating control, Wind Engineering 37 (5) (2013) 517–533.

[183] M. M. Hand, Variable-speed wind turbine controller systematic design methodology: a comparison of non-linear and linear model-based designs, Tech. rep., National Renewable Energy Lab., Golden, CO (US) (1999).

[184] H. Habibi, H. R. Nohooji, I. Howard, Adaptive pid control of wind turbines for power regulation with unknown control direction and actuator faults, IEEE Access 6 (2018) 37464–37479.

[185] M. Mirzaei, C. Tibaldi, M. H. Hansen, Pi controller design of a wind turbine: evaluation of the pole-placement method and tuning using constrained optimization, in: Journal of Physics: Conference Series, Vol. 753, IOP Publishing, 2016, p. 052026.

[186] A. Staino, B. Basu, Emerging trends in vibration control of wind turbines: a focus on a dual control strategy, Philosophical Transactions of the Royal Society A: Mathematical, Physical and Engineering Sciences 373 (2035) (2015) 20140069.

[187] K. A. Naik, C. P. Gupta, E. Fernandez, Advanced type-2 fuzzy logic–based pitch-angle control strategy for wind energy system, Wind Engineering 44 (1) (2020) 75–92.

[188] S. Sahoo, B. Subudhi, G. Panda, Torque and pitch angle control of a wind turbine using multiple adaptive neuro-fuzzy control, Wind Engineering 44 (2) (2020) 125–141.

[189] J. Qi, Y. Liu, Pid control in adjustable-pitch wind turbine system based on fuzzy control, in: 2010 The 2nd International Conference on Industrial Mechatronics and Automation, Vol. 2, IEEE, 2010, pp. 341–344.

[190] Y. Song, Control of wind turbines using memory-based method, Journal of Wind Engineering and Industrial Aerodynamics 85 (3) (2000) 263–275.

[191] Z. Yang, Y. Li, J. E. Seem, Individual pitch control for wind turbine load reduction including wake modeling, Wind Engineering 35 (6) (2011) 715–738.

[192] C. E. Riboldi, On the optimal tuning of individual pitch control for horizontal-axis wind turbines, Wind Engineering 40 (4) (2016) 398–416.

[193] T. Kallen, J. Zierath, S. Dickler, T. Konrad, U. Jassmann, D. Abel, Repetitive individual pitch control for load alleviation at variable rotor speed, in: Journal of physics: Conference series, Vol. 1618, IOP Publishing, 2020, p. 022055.

[194] R. Manikandan, N. Saha, A control algorithm for nonlinear offshore structural dynamical systems, Proceedings of the Royal Society A: Mathematical, Physical and Engineering Sciences 471 (2184) (2015) 20150605.

[195] C. Tutivén, Y. Vidal, J. Rodellar, L. Acho, Acceleration-based fault-tolerant control design of offshore fixed wind turbines, Structural Control and Health Monitoring 24 (5) (2017) e1920.

[196] G. Noshirvani, J. Askari, A. Fekih, Fractional-order fault-tolerant pitch control design for a 2.5 mw wind turbine subject to actuator faults, Structural Control and Health Monitoring 26 (10) (2019) e2411.

[197] B. Basu, S. Nagarajaiah, A wavelet-based time-varying adaptive lqr algorithm for structural control, Engineering Structures 30 (9) (2008) 2470–2477.

[198] B. Fitzgerald, A. Staino, B. Basu, Wavelet-based individual blade pitch control for vibration control of wind turbine blades, Structural Control and Health Monitoring 26 (1) (2019) e2284.

[199] S. Sarkar, L. Chen, B. Fitzgerald, B. Basu, Multi-resolution wavelet pitch controller for spar-type floating offshore wind turbines including wave-current interactions, Journal of Sound and Vibration 470 (2020) 115170.

[200] R. Lanzafame, M. Messina, Design and performance of a double-pitch wind turbine with non-twisted blades, Renewable Energy 34 (5) (2009) 1413–1420.

[201] R. D. Corrigan, J. C. Glasgow, P. J. Sirocky, Measured performance of a tip-controlled, teetered rotor with an naca 64/sub 3/-618 tip airfoil, Tech. rep., NASA Lewis Research Center, Cleveland, OH (United States) (1982).

[202] J. A. White, Performance analysis of a tip-controlled wind turbine utilizing a helical vortex wake model, Ph.D. thesis, University of Toledo (1983).

[203] A. A. Afjeh, T. G. Keith Jr, A simple computational method for performance prediction of tip-controlled horizontal axis wind turbines, Journal of Wind Engineering and Industrial Aerodynamics 32 (3) (1989) 231–245.

[204] R. Agarwala, P. I. Ro, Separated pitch control at tip: innovative blade design explorations for large mw wind turbine blades, Journal of Wind Energy 2015.

[205] B. Chen, X. Hua, Z. Zhang, S. R. Nielsen, Z. Chen, Active flutter control of the wind turbines using double-pitched blades, Renewable Energy 163 (2021) 2081–2097.

[206] A. P. Bernhard, I. Chopra, Analysis of a bending-torsion coupled actuator for a smart rotor with active blade tips, Smart Materials and Structures 10 (1) (2001) 35.

[207] W. Xie, P. Zeng, L. Lei, A novel folding blade of wind turbine rotor for effective power control, Energy Conversion and Management 101 (2015) 52–65.

[208] B. S. Linscott, J. T. Dennett, L. H. Gordon, Mod-2 wind turbine development project, Tech. rep., NASA Lewis Research Center, Cleveland, OH (United States) (1981).

[209] P. Grabau, M. Friedrich, Wind turbine and an associated control method, us patent US20120288371A1 (Nov. 2012).

[210] M. Friedrich, A. V. Rebsdorf, Partial pitch wind turbine with floating foundation, us patent US9732730B2 (Jul. 2014).

[211] F. K. Sen, High-speed wind turbine, germany patent DE917540C (Jun. 1954).

[212] V. Arramounet, C. de Winter, N. Maljaars, S. Girardin, H. Robic, Development of coupling module between bhawc aeroelastic software and orcaflex for coupled dynamic analysis of floating wind turbines, in: Journal of Physics: Conference Series, Vol. 1356, IOP Publishing, 2019, p. 012007.

[213] T. J. Larsen, A. M. Hansen, How 2 HAWC2, the user's manual, Risø National Laboratory, 2007.

[214] I. IEC 61400-24., Wind turbine generator systems–part 24: Lightning protection for wind turbines".

[215] E. Bossanyi, GH bladed user manual, Garrad Hassan and Partners Ltd 701.

[216] J. De Vaal, T. Nygaard, 3DFloat user manual, Institute for Energy Technology, Norway.

[217] S. Sarkar, B. Fitzgerald, B. Basu, Individual blade pitch control of floating offshore wind turbines for load mitigation and power regulation, IEEE Transactions on Control Systems Technology 29 (1) (2020) 305–315.

[218] J. M. Jonkman, M. L. Buhl Jr, et al., FAST user's guide, Tech. rep. (2005).

[219] S. Sarkar, B. Fitzgerald, Use of kane's method for multi-body dynamic modelling and control of spar-type floating offshore wind turbines, Energies 14 (20) (2021) 6635.

[220] R. Clough, J. Penzien, Dynamics of Structures, McGraw Hill, New York, 1993.

[221] G. S. Bir, User's guide to precomp (pre-processor for computing composite blade properties), Tech. rep., National Renewable Energy Lab.(NREL), Golden, CO (United States) (2005).

[222] M. Capellaro, M. Kühn, Boundaries of bend twist coupling, The Science of Making Torque from Wind, Crete, Greece 5.

[223] V. Fedorov, C. Berggreen, Bend-twist coupling potential of wind turbine blades, in: Journal of Physics: Conference Series, Vol. 524, IOP Publishing, 2014, p. 012035.

[224] O. K. G. Tietjens, L. Prandtl, Applied hydro-and aeromechanics: based on lectures of L. Prandtl, Vol. 2, Courier Corporation, 1957.

[225] R. P. Coleman, A. M. Feingold, C. W. Stempin, Evaluation of the induced-velocity field of an idealized helicoptor rotor, Tech. rep., National Aeronautics and Space Administration Hampton Va Langley Research Center (1945).

[226] J. M. Drees, A theory of airflow through rotors and its application to some helicopter problems, J. Helicopter Association of Great Britain 3 (2) (1949) 79–104.

[227] M. McWilliam, C. Crawford, The behavior of fixed point iteration and newton-raphson methods in solving the blade element momentum equations, Wind Engineering 35 (1) (2011) 17–31.

[228] I. Masters, J. C. Chapman, M. R. Willis, J. A. C. Orme, A robust blade element momentum theory model for tidal stream turbines including tip and hub loss corrections, Journal of Marine Engineering & Technology 10 (1) (2011) 25–35.

[229] B. R. Resor, Definition of a 5mw/61.5 m wind turbine blade reference model, Albuquerque, New Mexico, USA, Sandia National Laboratories, 2013-2569.

[230] G. Bir, User's guide to bmodes (software for computing rotating beam-coupled modes), Tech. rep., National Renewable Energy Lab.(NREL), Golden, CO (United States) (2005).

[231] S. W. Smith, et al., The scientist and engineer's guide to digital signal processing.

[232] MATLAB, version 9.6.0 (R2019a), The MathWorks Inc., Natick, Massachusetts, 2019a.

[233] J. C. Berg, B. R. Resor, Numerical manufacturing and design tool (numad v2. 0) for wind turbine blades: user's guide., Tech. rep., Sandia National Laboratories (SNL), Albuquerque, NM, and Livermore, CA ... (2012).

[234] A. L. Custódio, J. A. Madeira, A. I. F. Vaz, L. N. Vicente, Direct multisearch for multiobjective optimization, SIAM Journal on Optimization 21 (3) (2011) 1109–1140.

[235] P. Bratley, B. Fox, Implementing sobols quasirandom sequence generator (algorithm 659), ACM Transactions on Mathematical Software 29 (1) (2003) 49–57.

[236] M. Fleischer, The measure of pareto optima applications to multi-objective metaheuristics, in: International Conference on Evolutionary Multi-Criterion Optimization, Springer, 2003, pp. 519–533.

[237] K. Deb, Multi-objective optimization using evolutionary algorithms, Vol. 16, John Wiley & Sons, 2001.

[238] Y. Censor, Pareto optimality in multiobjective problems, Applied Mathematics and Optimization 4 (1) (1977) 41–59.

[239] N. Da Cunha, E. Polak, Constrained minimization under vector-valued criteria in finite dimensional spaces, Journal of Mathematical Analysis and Applications 19 (1) (1967) 103–124.

[240] M. Sajeer, A. Mitra, A. Chakraborty, Spinning finite element analysis of longitudinally stiffened horizontal axis wind turbine blade for fatigue life enhancement, Mechanical Systems and Signal Processing 145 (2020) 106924. doi:10.1016/j.ymssp.2020.106924.

[241] J. N. Reddy, An introduction to the finite element method, New York: McGraw-Hill, 2004.

[242] RP2A-WSD, API, Recommended practice for planning, designing and constructing fixed offshore platforms–working stress design, Houston: American Petroleum Institute.

[243] I. Møller, T. Christiansen, Laterally loaded monopile in dry and saturated sand-static and cyclic loading: experimental and numerical studies, Masters Project, Aalborg University Esbjerg.

[244] C. Desai, M. Zaman, Advanced geotechnical engineering: Soil-structure interaction using computer and material models, CRC Press, 2013.

[245] DNVGL-ST-0126, Support structures for wind turbines, Det Norske Veritas.

[246] R. W. Boulanger, C. J. Curras, B. L. Kutter, D. W. Wilson, A. Abghari, Seismic soil-pile-structure interaction experiments and analyses, Journal of geotechnical and geoenvironmental engineering 125 (9) (1999) 750–759.

[247] Y. W. Choo, D. Kim, Experimental development of the p-y relationship for large-diameter offshore monopiles in sands: Centrifuge tests, Journal of Geotechnical and Geoenvironmental Engineering 142 (1) (2016) 04015058.

[248] M. O. Hansen, Aerodynamics of wind turbines, Routledge, 2015.

[249] T. Burton, D. Sharpe, N. Jenkins, Handbook of wind energy, John Wiley and Sons, 2001.

[250] S. Das, M. M. Sajeer, A. Chakraborty, Vibration control of horizontal axis offshore wind turbine blade using SMA stiffener, Smart Materials and Structures 28 (9) (2019) 095025. doi:10.1088/1361-665x/ab1174.

[251] S. D. Downing, D. Socie, Simple rainflow counting algorithms, International journal of fatigue 4 (1) (1982) 31–40.

[252] J. Goodman, Mechanics applied to engineering, Longmans, Green, 1918.

[253] N. Veritas, Guidelines for design of wind turbines, Wind Energy Department, RisøNational Laboratory, 2002.

[254] A. Palmgren, Die lebensdauer von kugellagern (life length of roller bearings. in german), Zeitschrift des Vereines Deutscher Ingenieure (VDI Zeitschrift), ISSN (1924) 0341–7258.

[255] M. Miner, et al., Cumulative fatigue damage, Journal of applied mechanics 12 (3) (1945) A159–A164.

[256] G. Hayman, Mlife theory manual for version 1.00, National Renewable Energy Laboratory, Golden, CO 74 (75) (2012) 106.

[257] R. L. Little, J. L. Briaud, Full scale cyclic lateral load tests on six single piles in sand, Tech. rep., Texas A and M Univ College Station Dept of Civil Engineering (1988).

[258] S. S. Lin, J. C. Liao, Permanent strains of piles in sand due to cyclic lateral loads, Journal of geotechnical and geoenvironmental engineering 125 (9) (1999) 798–802.

[259] M. Achmus, Y. S. Kuo, K. Abdel Rahman, Behavior of monopile foundations under cyclic lateral load, Computers and Geotechnics 36 (5) (2009) 725–735.

[260] T. Fischer, W. De Vries, B. Schmidt, UpWind design basis (WP4: Offshore foundations and support structures), Upwind.

[261] DNV-OS-B101, Metallic materials, Det Norske Veritas.

[262] M. Hall, Moordyn user's guide, Department of Mechanical Engineering, University of Maine: Orono, ME, USA 15.

[263] M. Hall, A. Goupee, Validation of a lumped-mass mooring line model with deepcwind semisubmersible model test data, Ocean Engineering 104 (2015) 590–603.

[264] G. Vissio, B. Passione, M. Hall, M. Raffero, Expanding iswec modelling with a lumped-mass mooring line model, in: Proceedings of the European Wave and Tidal Energy Conference, Nantes, France, 2015, pp. 6–11.

[265] K. Johannessen, T. S. Meling, S. Hayer, Joint distribution for wind and waves in the northern north sea, in: ISOPE International Ocean and Polar Engineering Conference, ISOPE, 2001, pp. ISOPE–I.

[266] T. Sawaragi, Chapter 2 wave interactions with structures and hydrodynamic forces, Dev. Geotech. Eng 78 (1995) 67–149.

[267] M. M. Sajeer, A. Chakraborty, Long-term fatigue reliability enhancement of horizontal axis wind turbine blade, Wind and Structures 33 (2) (2021) 169–185.

[268] A. Mallik, S. Chatterjee, Principles of passive and active vibration control, East West Press (2014) 8176710989.

[269] M. Lackner, M. Rotea, R. Saheba, Active structural control of offshore wind turbines, in: 48th AIAA aerospace sciences meeting including the new horizons forum and aerospace exposition, 2010, p. 1000.

[270] Y. Chan, Wavelet basics, Springer Science and Business Media, 1994.

[271] S. C. Olhede, A. T. Walden, Generalized morse wavelets, IEEE Transactions on Signal Processing 50 (11) (2002) 2661–2670.

[272] J. M. Lilly, S. C. Olhede, Higher-order properties of analytic wavelets, IEEE Transactions on Signal Processing 57 (1) (2008) 146–160.

[273] J. M. Lilly, S. C. Olhede, On the analytic wavelet transform, IEEE transactions on information theory 56 (8) (2010) 4135–4156.

[274] J. M. Lilly, S. C. Olhede, Generalized morse wavelets as a superfamily of analytic wavelets, IEEE Transactions on Signal Processing 60 (11) (2012) 6036–6041.

[275] J. Lilly, A data analysis package for matlab, v. 1.6. 2. 2016, URL- http://www. jmlilly. net/jmlsoft.html.

[276] M. A. Lackner, FAST-SC, https://www.umass.edu/windenergy/research/software/fastsc, accessed: 2021-09-03.

[277] M. J. Muliawan, M. Karimirad, T. Moan, Z. Gao, Stc (spar-torus combination): a combined spar-type floating wind turbine and large point absorber floating wave energy converter—promising and challenging, in: International Conference on Offshore Mechanics and Arctic Engineering, Vol. 44946, American Society of Mechanical Engineers, 2012, pp. 667–676.

[278] I. R. Young, Wind generated ocean waves, Elsevier, 1999.

[279] R. H. Byrd, J. C. Gilbert, J. Nocedal, A trust region method based on interior point techniques for nonlinear programming, Mathematical programming 89 (2000) 149–185.

Index